



HAL
open science

Sorption of Radionuclides in Reinforced Cementitious Barriers

Bin Ma

► **To cite this version:**

Bin Ma. Sorption of Radionuclides in Reinforced Cementitious Barriers. Material chemistry. Université Grenoble Alpes, 2017. English. NNT : 2017GREAU027 . tel-01961482

HAL Id: tel-01961482

<https://theses.hal.science/tel-01961482>

Submitted on 20 Dec 2018

HAL is a multi-disciplinary open access archive for the deposit and dissemination of scientific research documents, whether they are published or not. The documents may come from teaching and research institutions in France or abroad, or from public or private research centers.

L'archive ouverte pluridisciplinaire **HAL**, est destinée au dépôt et à la diffusion de documents scientifiques de niveau recherche, publiés ou non, émanant des établissements d'enseignement et de recherche français ou étrangers, des laboratoires publics ou privés.

THÈSE

Pour obtenir le grade de

DOCTEUR DE LA COMMUNAUTÉ UNIVERSITÉ GRENOBLE ALPES

Spécialité : **Science de la Terre, de l'Univers et de
l'Environnement**

Arrêté ministériel : 7 août 2006

Présentée par

Bin MA

Thèse dirigée par **Prof. Laurent CHARLET** et
codirigée par **Dr. Alejandro FERNANDEZ-MARTINEZ**

préparée au sein du **l'Institut des Sciences de la Terre**
dans **l'École Doctorale Terre - Univers - Environnement**

Sorption de Radionucléides dans des Barrières Cimentaires Renforcées

Thèse soutenue publiquement le **19 Décembre 2017**,
devant le jury composé de :

M. Bernd GRAMBOW

PR. Université de Nantes (Rapporteur)

Mme Barbara LOTHENBACH

DR. Swiss Federal Laboratories for Materials Science and
Technology (Empa) (Rapporteuse)

M. Laurent CHARLET

PR. Université Grenoble Alpes (Directeur)

M. Alejandro FERNANDEZ-MARTINEZ

CR. Université Grenoble Alpes, CNRS (Co-Directeur)

M. Erich WIELAND

DR. Paul Scherrer Institute (PSI) (Examineur)

M. Bruno LANSON

DR. Université Grenoble Alpes, CNRS (Examineur, Président du
Jury)

M. Benoît MADE

DR. agence nationale pour la gestion des déchets radioactifs
(Andra) (Examineur)



Sorption of Radionuclides in Reinforced Cementitious Barriers

Bin MA

Cotutelle

Université Grenoble-Alpes, Institut des Science de la Terre (ISTerre), Equipe Géochimie 4D
Ecole doctorale: TUE (Terre, Univers, Environnement)

Abstract

Sorption and redox reactions of radionuclides (RNs) are critical processes for a nuclear waste disposal repository safety assessment. In geological repositories, these process may occur in (i) canister (steel) corrosion layer, (ii) reinforced concrete, e.g. on hydrated cement and (iii) argillite, e.g. on pyrite and clays or granite. Both steel corrosion products and pyrite act as local reducing buffers, controlling the redox potential (Eh) and thus the sorption behavior of redox-sensitive RNs. In contrast, sorption of RNs not involving redox processes may occur on clays, iron oxides and cement hydration products, and often involve surface adsorption, ion exchange, or co-precipitations processes. In this PhD thesis, minor but highly reactive cementitious AFm phases (AFm-Cl₂ or AFm-SO₄ solids, belonging to CaAl LDHs) were employed to adsorb MoO₄²⁻ and SeO₃²⁻ at various surface loadings. A combination of PHREEQC chemical equilibrium modelling and synchrotron-based X-ray techniques (e.g., in-situ time-resolved XRD, PDF, and XAFS) reveals that multiple sorption sites, including two types of edge sites, interlayer ion exchange sites, and a Ca-rich phase precipitation, are active processes in the RNs retention on AFm phases. A linear relationship is shown to link AFm basal spacing and hydrated intercalated anion radius. Co-sorption of U and Mo on Fe⁰-reinforced hydrated cement-core has also been investigated by micro-probe mapping, showing U to be instantly immobilized by cement materials while Mo is preferentially sorbed on Fe reaction products. The Eh value prevailing in concrete is hard to be determined. Here, redox-sensitive RNs (e.g., U^{VI}, Se^{IV}, Mo^{VI}, and Sb^V) are employed as probes, to measure in-situ Eh values, by computing the Nernst equation in the following way. Reduced species concentration were measured based on the total concentration of reductively precipitated RN and on speciation among these reduced species as obtained by LCF analysis of XANES data. The experimentally determined Eh values obtained that way were remarkably closed for all RNs with centered values of -446.4±78.0 mV for cement pore water (CPW) equilibrated with Fe⁰ and values of -346 to -509 mV for CPW equilibrated with corrosion products Fe-oxides couples (magnetite/hematite or magnetite/goethite) at pH ~13.5. Neither the Eh value computed for these couples or for Fe⁰/Fe(OH)₂ match these data. Instead, the redox potential appear to be controlled by amorphous Fe(OH)₂/Fe(OH)₃ or (Fe_{1-x},Ca_x)(OH)₂/Fe(OH)₃ couples. Finally, within clay or granite far field, several factors may critically affect the surface reactivity of pyrites, namely element impurities in pyrite lattice and presence of Fe³⁺ and S²⁻ at the pyrite surface. Element impurities and presence of S²⁻ on the pyrite surface were shown to largely speed up U(VI) reduction. The experimental results obtained above could provide fundamental data for the safety assessment of nuclear waste disposal.

Résumé

La sorption et les réactions redox des radionucléides (RN) sont des processus critiqués pour une évaluation de la sécurité des dépôts de déchets nucléaires. Dans les dépôts géologiques, ces procédés peuvent se produire dans (i) une couche de corrosion (acier), (ii) un béton armé, par exemple, sur le ciment hydraté et (iii) l'argilite, sur la pyrite et les argiles ou le granit. Les produits de corrosion de l'acier et la pyrite agissent comme des tampons de réduction locaux, contrôlant le potentiel redox (Eh) et donc le comportement de sorption des RN sensibles au redox. En revanche, la sorption de RN n'impliquant pas de processus redox peut se produire sur des argiles, des oxydes de fer et des produits d'hydratation de ciment et impliquent souvent des processus d'adsorption de surface, d'échange d'ions ou de co-précipitations. Dans cette thèse de doctorat, des phases d'AFm cimentaires mineures, mais hautement réactives (acides gras AFm-Cl₂ ou AFm-SO₄, appartenant aux LDH CaAl) ont été utilisées pour adsorber MoO₄²⁻ et SeO₃²⁻ à diverses charges de surface. Une combinaison de la modélisation de l'équilibre chimique PHREEQC et des techniques de rayons X à base de synchrotron (par exemple, XRD, PDF et XAFS résolus dans le temps) révèle que les sites de sorption multiples, y compris deux types de sites de bord, des sites d'échange d'ions intercalaires et une précipitation de phase riche en Ca, sont des processus actifs dans la rétention des RN sur les phases AFm. Une relation linéaire permet de lier l'espacement basal AFm et le rayon d'anion intercalé hydraté. La co-sorption de U et Mo sur le ciment-ciment hydraté renforcé par Fe⁰ a également été étudiée par cartographie micro-sonde, montrant que U doit être immobilisé instantanément par des matériaux de ciment tandis que Mo est préférentiellement sorbé sur des produits de réaction de Fe. La valeur Eh prédominant dans le béton est difficile à déterminer. Ici, les RN sensibles à la réduction rénale (par exemple, U^{VI}, Se^{IV}, Mo^{VI} et Sb^V) sont utilisées comme sondes, pour mesurer les valeurs Eh in-situ, en calculant l'équation de Nernst de la manière suivante. La concentration des espèces réduites a été mesurée en fonction de la concentration totale de RN précipitée par réduction et de la spéciation parmi ces espèces réduites, tel qu'obtenu par l'analyse LCF des données XANES. Les valeurs Eh déterminées expérimentalement obtenues de cette façon étaient remarquablement fermées pour toutes les RN avec des valeurs centrées de -368 à -524 mV pour l'eau de pore de ciment (CPW) équilibrée avec Fe⁰ et des valeurs de -346 à -509 mV pour CPW équilibrées avec des produits de corrosion Fe - couples d'oxydes (magnetite / hématite ou magnetite / goethite) à pH ~ 13,5. Ni la valeur Eh calculée pour ces couples ni pour Fe⁰ / Fe(OH)₂ correspond à ces données. Au lieu de cela, le potentiel redox semble être contrôlé par le couple amorphe Fe(OH)₂/Fe(OH)₃ or (Fe_{1-x},Ca_x)(OH)₂/Fe(OH)₃. Enfin, dans le domaine de l'argile ou du granit, plusieurs facteurs peuvent affecter réactivité superficielle des pyrites, à savoir les impuretés élémentaires dans le réseau de pyrite et de la présence de Fe³⁺ et S²⁻ à la surface de la pyrite. Les impuretés des éléments et la présence de S²⁻ sur la surface de la pyrite ont largement accéléré la réduction des U (VI). Les résultats expérimentaux obtenus ci-dessus pourraient fournir des données fondamentales pour l'évaluation de la sécurité de l'élimination des déchets nucléaires.

Acknowledgment

Time flies. I still clearly remember the first time when I stepped on beautiful Grenoble. It is the autumn of 2014. My supervisor, Prof. Laurent Charlet, kindly picked me up at the railway station, drove me to the restaurant and my dormitory. That day I also met with my co-supervisor, Dr. Alejandro Fernandez-Martinez, who also greatly helped me in the following three PhD years.

Firstly, I would like to express my sincere gratitude to my two supervisors. I was ever hesitating in the massive ocean of academia. It is my two kind and knowledgeable supervisors who point me out a clear research direction. They always instruct me how to do a good science, from making a comprehensive literature survey, to formulating reasonable experimental plans, to performing experiments in synchrotron facilities, to treating any difficult experimental data, to preparing nice presentations for conferences, to scientific writing finally. Meantime, they also set for me a target: to be independent as much and soon as I can. In my following academic career, I will keep going with this target.

Besides my supervisors, I would like to thank all my colleagues working together at ISTerre: Dr. Antoine Géhin, Dr. Ayumi Koishi, Dr. Phan Van, Dr. Ekaterina Markelova, Dr. Ana Elena Pradas Del Real, Dr. Géraldine Sarret, Mr. Nathaniel Findling, Ms. Delphine Tisserand, Ms. Sarah Bureau, Ms. Valérie Magnin.

I am also very grateful to Dr. Christophe Tournassat, Dr. Sylvain Grangeon, Dr. Francis Claret, and Dr. Nicolas C. M. Marty from BRGM, for their strong support, collaboration and encouragement for my PhD research. I benefited a lot on cement knowledge from them.

Great gratitude to Dr. Benoît Madé for the financial support from ANDRA. I also really appreciate the powerful scientific support on XAFS from Dr. Fabrizio Bardelli, Dr. Eduardo Salas-Colera and Dr. Olivier Proux.

My sincere thanks also goes to Prof. Bernd Grambow, Dr. Barbara Lothenbach, Dr. Erich Wieland, Dr. Bruno Lanson, and Dr. Benoît Madé for accepting the invitation to be the referees of my thesis.

Last but not the least, I would like to thank my family: my parents and brother for supporting me all the time spiritually and the encouragement from my girlfriend throughout the thesis writing.

Publications during PhD thesis (2014-2017)

1. **B. Ma**, A. Fernandez-Martinez, S. Grangeon, C. Tournassat, N. Findling, F. Claret, A. Koishi, N. Marty, D. Tisserand, S. Bureau, E. Salas-Colera, E. Elkaim, C. Marini, L. Charlet. Evidence of multiple sorption modes in layered double hydroxides using Mo as structural probe. *Environmental Science & Technology*, 2017, 51(10): 5531-5540.
2. * C. Wang, **B. Ma**, S. Xu, D. Li, S. He, Y. Zhao, J. Han, M. Wei, D. G. Evans, X. Duan. Visible-light-driven overall water splitting with a largely-enhanced efficiency over a Cu₂O@ZnCr-layered double hydroxide photocatalyst. *Nano Energy*, 2017, 32, 463-469.
3. * J. He, **B. Ma (co-first author)**, M. Kang, C. Wang, Z. Nie, C. Liu. Migration of ⁷⁵Se(IV) in crushed Beishan granite: Effects of the iron content. *Journal of Hazardous Materials*, 2017, 324, 564-572.
4. M. Kang, F. Bardelli, **B. Ma**, L. Charlet, F. Chen, Y. Yang. The influence of pH and reaction time on the formation of FeSe₂ upon selenite reduction by nano-sized pyrite-graigite. *Radiochimica Acta*, 2016, 104(9), 649-656.
5. **B. Ma**, A. Fernandez-Martinez, S. Grangeon, C. Tournassat, N. Findling, S. Carrero, D. Tisserand, S. Bureau, E. Elkaim, C. Marini, G. Aquilanti, A. Koishi, N. Marty, L. Charlet. Selenite uptake by CaAl LDH: a description of intercalated anion coordination geometries. *Environmental Science & Technology* (minor revision).
6. * C. Wang, **B. Ma**, X. Cao, S. He, J. Han, M. Wei, D. G. Evans, X. Duan. Largely enhanced overall water splitting by precise interface optimization on Cu₂O@ZnCr-layered double hydroxide heterostructure. *Chemistry of Materials* (under review).
7. **B. Ma**, A. Fernandez-Martinez, B. Madé, N. Findling, E. Markelova, D. Tisserand, S. Bureau, E. Salas-Colera, L. Charlet. XANES-based determination of redox potentials imposed by steel corrosion products in cement-based media. *Environmental Science & Technology* (in preparation).
8. **B. Ma**, M. Kang, A. Fernandez-Martinez, A.R. Lewis, T.G.G. Maffei, E. Salas-Colera, D. Tisserand, L. Charlet. The influence of surface impurities on the reactivity of pyrite toward aqueous U(VI). *Geochimica et Cosmochimica Acta* (in preparation).
9. **B. Ma**, L. Charlet, A. Fernandez-Martinez, M. Kang, B. Madé. Multiple barrier concept applied to redox-sensitive radionuclides. *Applied Geochemistry* (in preparation).

* Not related to the PhD topic, but done in collaboration.

Résumé étendu

Le stockage géologique des déchets nucléaires est largement acceptée comme la solution préférentielle pour le stockage à long terme des déchets radioactifs de niveau intermédiaire (IL) et haut (HL) à vie longue (-LL). Au contraire, les déchets radioactifs de moyenne activité à vie courte (IL-SL) et de faible niveau (LL) seront traités par stockage près de la surface, du sol ou dans des cavités souterraines (à quelques dizaines de mètres). Dans le concept de stockage géologique profond, un système de barrières multiples (Figure I) est généralement proposé pour isoler les déchets de la biosphère pendant des siècles. Les barrières multiples comprennent généralement des contenants en béton ou en métal (par exemple, en acier ou cuivre) contenant les déchets radioactifs vitrifiés, le tampon et / ou les matériaux de remblai de ciment ou d'argile (bentonite) et les roches hôtes du dépôt (p. ou tuf volcanique).

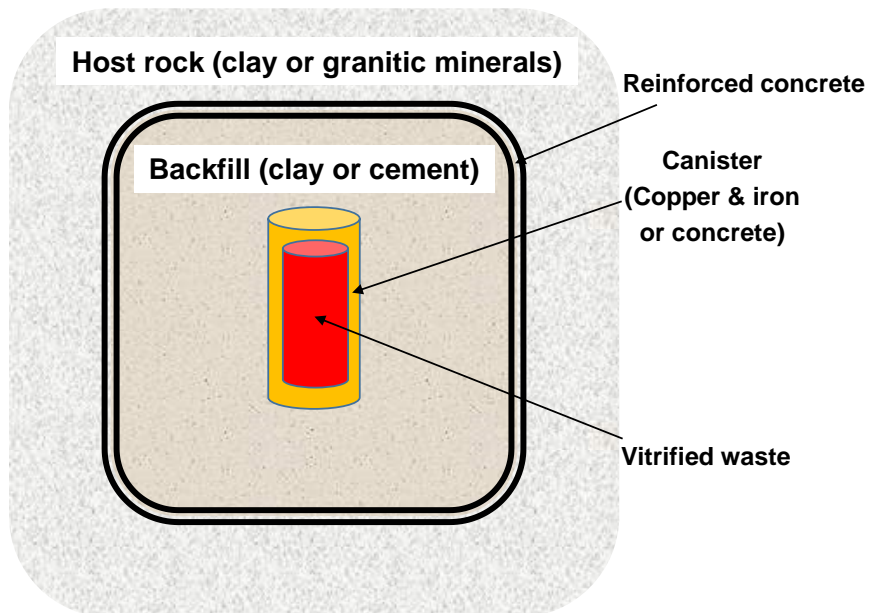


Figure I. Dessin schématique du système de barrières multiples constitué de barrières artificielles et naturelles (géologiques).

En France et en Suisse, des ouvrages riches en béton armé sont prévus pour le soutènement et le remblai des tunnels, les conteneurs de déchets et matrices de déchets, qui sont considérés comme des barrières empêchant la mobilité des radionucléides (RNs) en cas de fuite éventuelle. Plusieurs facteurs de retard peuvent être efficaces pour l'immobilisation des RNs du champ proche au champ lointain : matériau vitrifié, fer et cuivre dans les cartouches avec leurs produits de corrosion, matériaux argileux et cimentaires, acier incorporé dans les bétons

et ses produits de corrosion, et phases actives (p. ex. pyrite, smectite et annite) présents dans l'argile hôte et les matériaux granitiques.

Dans le cas où les RN diffusent à travers des conteneurs, ils rencontreront des matériaux de remblai / tampon et plus loin avec ceux tunnels et alvéoles de béton dans leur. En plus de mécanisme de précipitation réductrice, la structure cimentaire, en tant que barrière, devrait retarder la diffusion des RN par l'intermédiaire de mécanismes d'adsorption de surface, d'échange d'ions ou de coprécipitation. En particulier pour les cations de RNs, le mécanisme de co-précipitation pourrait entraîner un retard d'efficacité dans les conditions inhérentes à l'hypercalcalinisme imposées par le ciment hydraté. Dans notre projet, les anions radionucléides, SeO_3^{2-} , MoO_4^{2-} , et $\text{Sb}(\text{OH})_6^-$, ainsi que l'uranium, ont été étudiés.

Parmi les produits d'hydratation, les aluminates de calcium hydratés AFm appartenant à la famille des hydroxydes doubles couches (LDH), ont été étudiés considérés comme des phases efficaces pour immobiliser les contaminants anioniques à des valeurs de pH élevées. Les LDH se réfèrent à une famille d'hydroxydes mixtes lamellaires avec une formule chimique générique $\text{M}^{\text{II}}_{6-x}\text{M}^{\text{III}}_x\text{O}_6\text{]}^{x+}(\text{A}^{n-})_{x/n}\cdot m\text{H}_2\text{O}$. Dans le cas de la phase AFm (AFm- SO_4) dans le ciment, M^{II} , M^{III} et A^{n-} représentent Ca^{II} , Al^{III} et SO_4^{2-} , respectivement. Pour AFm- Cl_2 , A^{n-} denotes Cl^- .

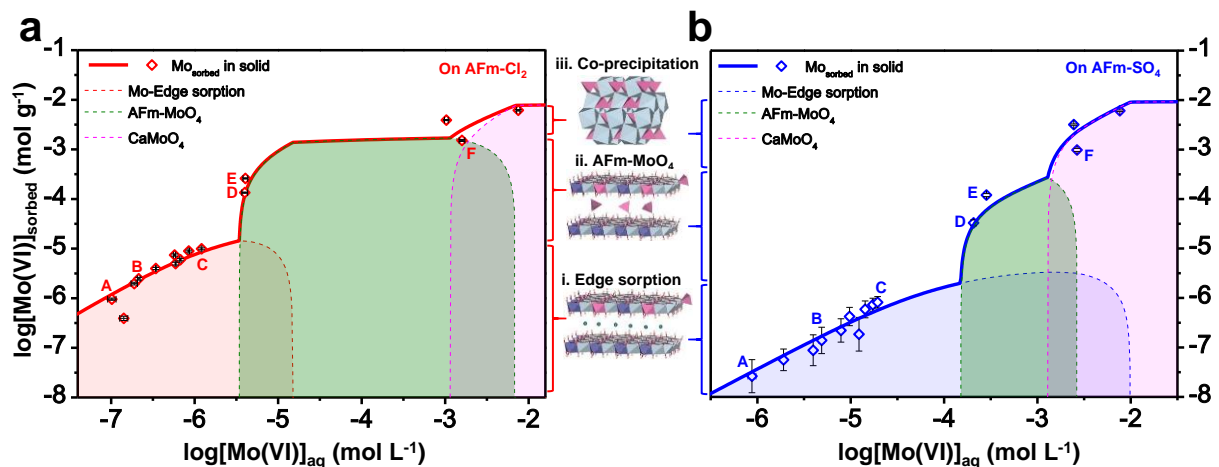


Figure II. Isotherme de sorption du molybdate après 48 h d'équilibration. (a) Sur AFm- Cl_2 . De l'étape de sorption sur les bords à celle de la précipitation du Ca, les capacités sont de 8×10^{-5} , 2×10^{-3} et 8×10^{-3} mol g^{-1} , respectivement. (b) Sur AFm- SO_4 . Les trois types de capacités de sorption correspondantes sont respectivement 8×10^{-6} , 2×10^{-3} et 8×10^{-3} mol g^{-1} . Les courbes pleines en gras sont les résultats modélisés concernant la quantité de Mo sorbée sur le solide. Chaque zone sous la courbe représente le sorbant solide dominant, à chaque stade de sorption. Les produits d'adsorption sélectionnés pour l'étude par les techniques de spectroscopie aux rayons X sur chaque phase AFm sont désignés les points par A à F, et correspondent à des charges croissantes en molybdate. La représentation schématique de trois mécanismes de rétention est montrée dans le panneau du milieu.

Ces phases micro- et nano-poreuses ont une structure unique composée de couches chargées positivement et d'anions intercalaires chargés négativement, avec possibilité de substitution cationique dans la couche cristalline et échange d'anions avec les anions hôtes intercalés faibles. Cependant, dans le cas de la fuite d'RN à partir des déchets nucléaires, sous forme de traces d'anions RN, les mécanismes d'absorption préférentiels sont encore en discussion. Dans notre projet, une combinaison d'expériences isothermes et de techniques de rayons X a été utilisée pour examiner les mécanismes de sorption de MoO_4^{2-} sur des phases AFm synthétiques, les AFm-SO₄ et AFm-Cl₂, avec des charges croissantes d'anions RN hôtes. Comme le montre la Figure II, l'isotherme de sorption, c'est-à-dire la couverture superficielle accrue en fonction de l'activité de cette même espèce, peut être reproduite de manière adéquate par une modélisation thermodynamique incluant trois mécanismes de rétention : la formation d'AFm-MoO₄, et enfin la décomposition des structures de LDH se transformant en précipitation de CaMoO₄.

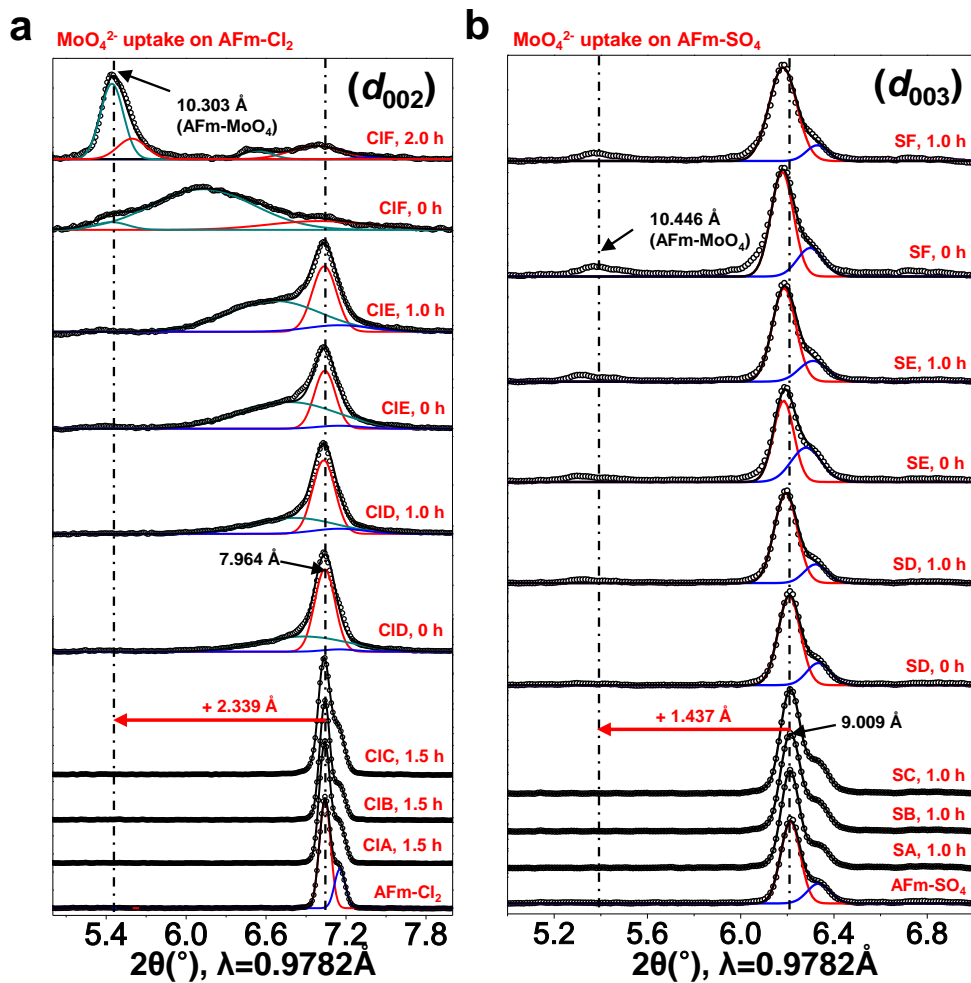


Figure III. Modèles in-situ résolus dans le temps et détails de pics inter-couches. (a) Les modèles DRX recueillis l'absorption de molybdate sur AFm-Cl₂. (b) les modèles obtenus avec AFm-SO₄. Les données expérimentales, tracées en cercles noirs, sont par des fonctions

Gaussienne (indiquées par des courbes en couleur). Les courbes noires représentent les courbes ajustées totales. Le temps d'équilibre correspondant à chaque spectre est indiqué après le nom de l'échantillon.

Des mesures DRX et in-situ résolues en temps ont été réalisées pour vérifier la présence d'éventuelles transitions structurales, et de modifications de composition de l'espace inter-couche (par un changement de la distance couche-couche) lors de l'augmentation de la concentration de molybdate. Mo a été ajouté en six étapes, comme dans les expériences de chimie humide de A à F. Comme le montre la Figure III, à des concentrations solides supérieures à celles du réacteur C, l'intensité du pic correspondant à la distance entre les couches augmente en raison de l'échange de MoO_4^{2-} avec les anions présents dans l'intercalaire. Finalement, une distance inter-couches de 10,3 Å est observée. Cependant, l'absence de gonflement des LDH à de faibles concentrations confirme que d'autres mécanismes d'adsorption et d'incorporation de Mo existent dans des conditions pertinentes naturelles, reflétant un paysage complexe de modes de sorption dans les LDH. Les résultats de XRD in situ concordent remarquablement avec l'isotherme de sorption.

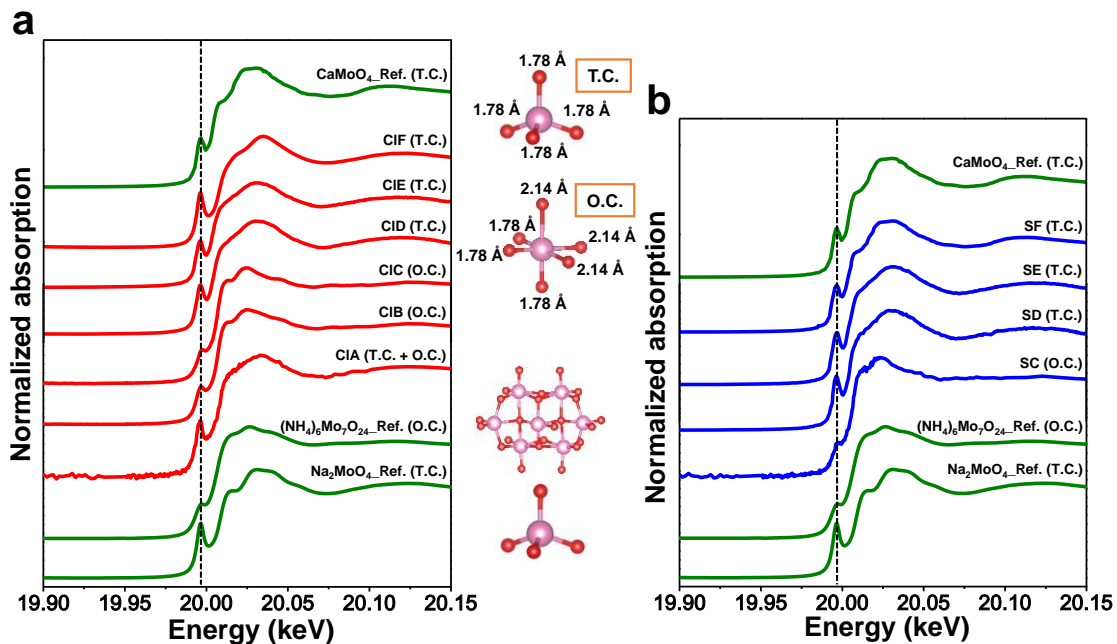


Figure IV. Spectres expérimentaux XANES Mo K-edge de produits de sorption sélectionnés AFm-Cl₂ (a) et AFm-SO₄ (b) provenant d'expériences de sorption discontinue et de composés de référence (en bas). La représentation schématique de la géométrie du molybdène dans une coordination différente est montrée dans le panneau du milieu.

L'absorption des rayons X près de la spectroscopie de bord (XANES) permet de distinguer les atomes de Mo à coordination tétraédrique (TC) de ceux à coordination octaédrique (OC), principalement par le niveau d'intensité du pré-pic (plus intense pour le molybdate TC). Les

spectres XANES de Mo au K-edge des échantillons correspondant à ceux de la Figure II sont donnés avec ceux avec les standards TC et OC de la Figure IV indiquent que la coordination du molybdate dans les produits de sorption évolue avec le degré de couverture de surface de TC (échantillon A) à OC déformé (échantillons B et C), puis retour à TC (échantillon F), suggérant une évolution complexe du mécanisme d'absorption. On peut donc conclure que la sorption du molybdate sur les phases AFm à des couvertures relativement faibles passe par deux types de complexation de sites de surface de bordure: complexation tétraédrique et octaédrique sur le bord.

Sur les particules AFm ayant réagi sur leur bord avec du molybdate, certaines nanoparticules ont été observées principalement sur ces bords par microscopie électronique à transmission (MET). Ces NP ont une composition de type katoïte ($\text{Ca}_3\text{Al}_2(\text{OH})_{12}$) d'après l'analyse par spectroscopie à rayons X à dispersion d'énergie (EDX). Le molybdate était plus concentré dans ces NP de katoïte, cela a été interprété comme un processus de déstabilisation du bord AFm- Cl_2 , suivi d'une coprécipitation d'une katoïte porteuse de Mo. Cette vision moléculaire détaillée montre que différents mécanismes d'absorption: sorption, dissolution-reprécipitation interfaciale et contrôlent l'absorption d'anions dans des conditions environnementales pertinentes, ce qui contraste avec la vision classique de l'échange d'anions comme mécanisme principal de rétention sur LDH. Ce travail met tous ces mécanismes en perspective, offrant un nouvel aperçu de l'interaction complexe entre mécanismes d'absorption d'anions par les phases AFm, en utilisant les changements de géométrie du Mo comme sonde moléculaire.

Différentes géométries de coordination du Mo absorbé sur les bords de phase AFm ont été détectées, comme décrit ci-dessus. La géométrie d'anions intercalés pourrait également être modifiée une fois que le processus d'échange d'anions a eu lieu. La capacité d'échange d'anions peut contribuer au potentiel d'élimination des anions RN par la phase AFm. L'absorption de Se(IV) par divers LDH a été rapportée précédemment par d'autres auteurs, mais l'environnement structural de complexation du sélénium intercalé était objet de débats auquel manquaient une discussion détaillée, basée sur des mesures faites au niveau moléculaire, sur les configurations structurales des anions intercalés dans les phases AFm. Le présent travail porte sur le processus d'échange par les oxyanions Se(IV), les anions présents dans les phases AFm, dans les ciments et susceptible d'agir comme barrières dans le stockage de déchets nucléaires.

La comparaison de SeO_3^{2-} avec d'autres anions, Cl^- , SO_4^{2-} et MoO_4^{2-} , intercalés dans des LDH CaAl, a permis d'établir une relation entre la structure des anions présents dans l'inter-

couches et l'espace interfeuillet a été établie, la stabilité de ces phases. Cette approche intégrée permet un compte rendu détaillé des processus d'échange anionique à l'œuvre dans les LDH CaAl, basé sur la cinétique que sur la thermodynamique d'équilibre.

Ici, l'absorption des phases SeO_3^{2-} par AFm a été étudiée en fonction de la concentration de Se. La modélisation des isothermes par sorption discontinue montre que l'échange d'anions dépend du niveau de concentration, et non du mécanisme dominant contrôlant la rétention de Se aux chargements moyens. AFm-Cl₂ montre une affinité beaucoup plus forte et une plus grande capacité de sorption ($R_d \sim 17800 \text{ L kg}^{-1}$) envers SeO_3^{2-} que AFm-SO₄ ($R_d \sim 705 \text{ L kg}^{-1}$). Les changements de distance couche-à-couche ($d_{\text{interlayer}}$), provoqués par l'intercalation des anions dans les phases AFm, ont été suivis en temps réel grâce à une étude in-situ des réflexions XRD. Comme l'illustre la Figure V, à la charge stoechiométrique de SeO_3^{2-} , la nouvelle phase AFm-SeO₃ se traduit par deux distances inter-couches, $11,01 \pm 0,01 \text{ \AA}$ et $9,99 \pm 0,01 \text{ \AA}$, différant de celle de AFm-MoO₄, une valeur unique de $10,37 \pm 0,07 \text{ \AA}$ observé (Figure III). Ces deux distances peuvent résulter de différentes configurations de complexation du SeO_3^{2-} intercalé, plutôt que d'autres anions intercalés possibles ou de polytypes et groupes spatiaux différents de phases AFm.

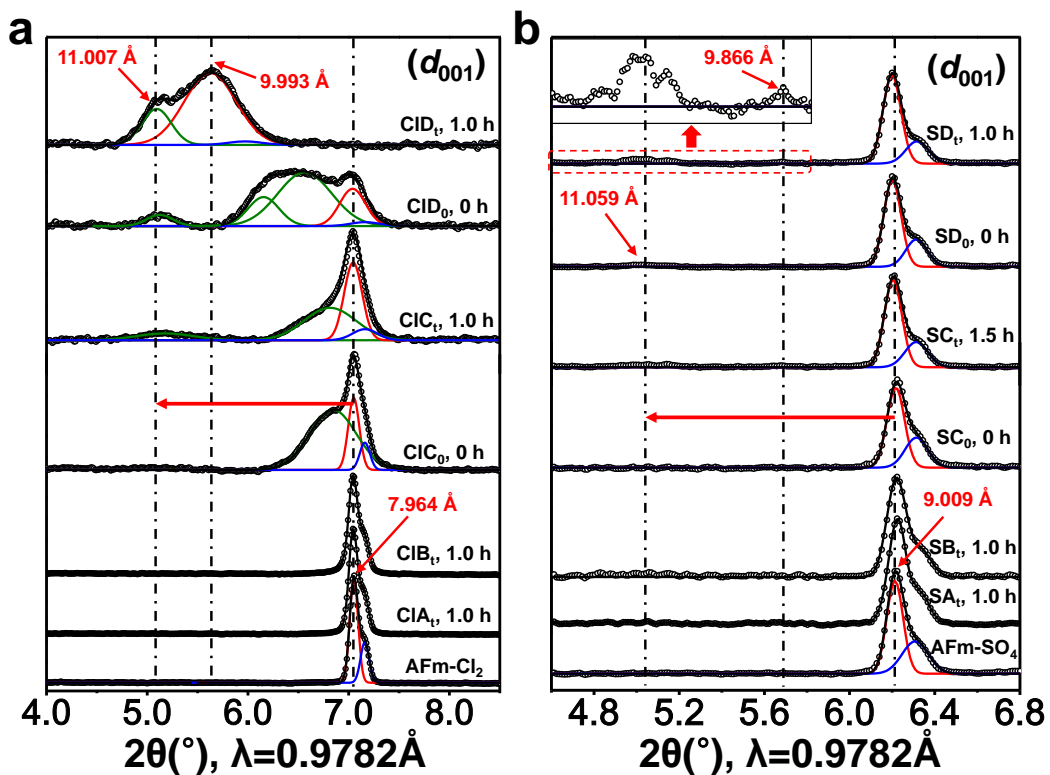


Figure V. Spectres et XRD résolus dans le temps in-situ des détails de pics inter-couches. (a) Les profils XRD collectés pour l'absorption de sélénite sur AFm-Cl₂. (b) Spectres et XRD sur AFm-SO₄. L'encart est les motifs partiellement agrandis d'écart-type, avec le signal d'origine marqué avec des lignes pointillées rouges. Les données expérimentales, tracées avec des

cercles noirs, sont modélisées par une fonction gaussienne (indiquée par les courbes en couleur). Les courbes noires représentent la somme des courbes ajustées. Le temps d'équilibre pour chaque étape est donné après le nom de l'échantillon. Les petits épaulements de pics inter-feuillets à des valeurs 2θ légèrement plus élevées, affichées en bleu, peuvent être attribués à différents niveaux de gonflement des couches cristallines empilées.

Les spectres de structure fine d'absorption de rayons X étendus de Se K-edge (EXAFS) indiquent que les formes intercalées de SeO_3^{2-} forment non seulement des complexes, comme attendu de la part d'un échange d'anions, mais également des complexes binucléaires bidentés de sphère interne avec les couches Ca-Al-O. L'unique fréquence d'oscillation observée dans les spectres EXAFS à S K-edge pondérés par k^3 du SO_4^{2-} intercalé suggère que SO_4^{2-} entre les couches de Ca-Al-O préfère l'environnement de complexation de la sphère. La taille d'anions hydratés focalisés, c'est-à-dire Cl^- , SO_4^{2-} , SeO_3^{2-} , et MoO_4^{2-} , sont données dans le Tableau I.

Tableau I. Espacement basal des LDH CaAl et des rayons des anions hydratés^a.

Anions	Espacement basal (Å)	Moyenne $X \cdots O_w$ (Å)	R_{stokes} (Å)
Cl^-	7.96(1)	3.16, 3.20	1.81+0.43
SO_4^{2-}	9.03(2)	3.61	2.32, 2.40+0.38
MoO_4^{2-}	10.37(7)	4.06	2.68+0.29
SeO_3^{2-}	11.03(3)&9.93(6)	3.87(2)&4.36(8)	2.49

^a $X \cdots O_w$: distance entre l'atome central de l'anion et l'atome d'oxygène des molécules d'eau liées par l'hydrogène. Pour SeO_3^{2-} , 3.87 et 4.36 Å sont les distances $\text{Se} \cdots O_w$ correspondent à la moyenne des aux molécules d'eau se liant via l'hydrogène aux oxygènes du sélénite et de celle correspondant à m'extérieur de la paire d'électrons solitaire, respectivement. R_{stokes} représente le rayon de Stokes, qui est égal à la somme du rayon d'ions et de la largeur de la coque d'hydratation. Les incertitudes sont données par le nombre entre parenthèses sur le dernier chiffre, c'est-à-dire que 9.03 (2) représente 9.03 ± 0.02 .

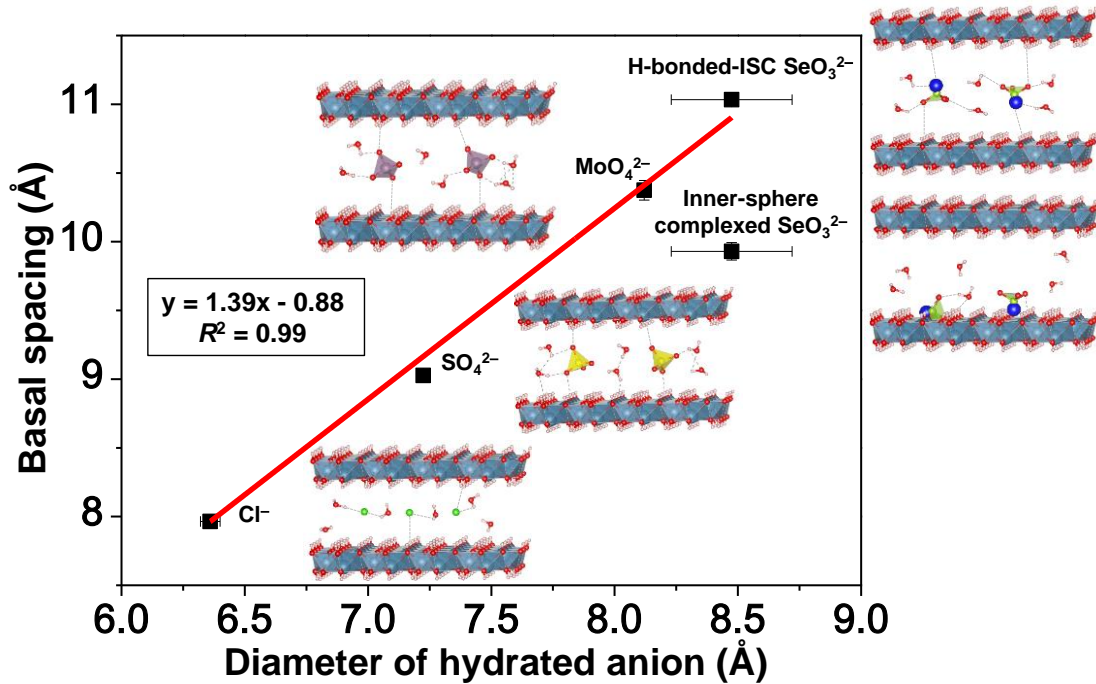


Figure VI. Relation linéaire entre l'espacement interfoliaire et les diamètres des anions hydratés. Représentation schématique d'une coupe de la structure des LDH CaAl correspondant à chaque type d'anion intercalé. La sphère bleue se fixant sur l'anion sélénite représente sa paire d'électrons solitaire. Dans le cas de Se, le diagramme supérieur correspond aux anions échangeables OSC, le diagramme inférieur aux anions "échangeables" ISC présents dans l'intercouche.

En utilisant les distances entre atomes centraux et molécules d'eau d'hydratation, au lieu de R_{Stokes} , l'espacement basal des phases AFm dans des conditions d'humidité de 100% (en solution aqueuse) montre une relation linéaire remarquable avec le diamètre des anions distance de liaison (Figure VI). L'espacement de 11,03 Å dans les échantillons de sorption de Se devrait résulter du SeO_3^{2-} intercalé librement hydraté, alors que la plus petite valeur d'espacement de 9,93 Å, déviant fortement de la relation linéaire, peut provenir du complexe SeO_3^{2-} sphère interne confirmé par Se K-edge bord des données EXAFS. Ces analyses confirment la coexistence de SeO_3^{2-} intercalé libre et lié.

Examinée par XRD résolue en temps in-situ, la phase avec SeO_3^{2-} intercalée par OSC libre est favorisée cinétiquement mais thermodynamiquement instable, comparée à AFm- SeO_3 avec SeO_3^{2-} lié par ISC. Ce travail offre de nouvelles perspectives dans une approche rapide mais fiable pour déterminer l'environnement de complexation des anions intercalés via des analyses DRX, et plus loin la stabilité de la structure des LDH. Par exemple, les valeurs d'espacement basal sous la ligne d'ajustement (Figure 5) montreraient des structures plus stables et donc une biodisponibilité plus faible des contaminants, par rapport aux valeurs sur ou au-dessus de la ligne. Ce travail fournit également un aperçu du contrôle cinétique contre thermodynamique

sur les configurations préférées d'anions, formant potentiellement des complexes de sphères internes (par exemple, SeO_3^{2-} , SO_3^{2-} et AsO_2^-) quand ils sont soumis à l'absorption par les LDH par des mécanismes d'échange anionique. En conclusion, les phases AFm pourraient agir comme un puit efficace pour SeO_3^{2-} via une variété de mécanismes en fonction de la couverture de surface, retardant ainsi potentiellement la diffusion du ^{79}Se hors d'un site de stockage de dépôt de déchets nucléaires et de ses infrastructures à base de ciment.

On s'attend à ce que l'acier incorporé (à pH élevé) dans le béton armé (ainsi que Fe^0 présent dans les scories de béton) contrôle le potentiel redox (Eh) dans un site de stockage de déchets nucléaires riche en ciment et retarde la migration des RN. Paramètre critique contrôlant le comportement et la migration des RN sensibles au redox, le Eh dans le béton armé est contrôlé par la corrosion du fer, qui produit un film mince (de quelques microns) de Fe^{II} -oxyhydroxides / magnétite / Fe^{III} -oxyhydroxides -film en "sandwich". En outre, le H_2 généré après la fermeture des alvéoles du site de stockage pourrait potentiellement être un donneur d'électrons pour de nombreuses espèces RN oxydées (par exemple, U^{VI} , Se^{IV} , Mo^{VI} et Sb^{V}) présentes dans les déchets. En raison de l'interface de corrosion complexe et de la contribution peu claire du H_2 aux processus d'oxydo-réduction dans le béton, le Eh réel qui prévaudra dans les alvéoles reste encore indéterminé. Les deux conditions d'hyper alcalinité et de H_2 excluraient l'utilisation de la mesure directe par électrode de Pt du interfacial Eh. Dans la présente étude, une nouvelle méthode de mesure des potentiels redox a été explorée pour la première fois, basée en partie de mesures XANES, sur NZVI et sur Fe-oxyhydroxy des dans l'eau de porosité du ciment (CPW). Nous cherchons à déterminer de cette manière une valeur expérimentale "in-situ" du Eh imposé par l'acier (modélisé ici par NZVI) et par ses couples de produits de corrosion, comme les couples : magnétite / hématite (en abrégé M / H) et magnétite / goethite (abrégé en M / G), en utilisant des RN sensibles à l'oxydoréduction, c'est-à-dire U, Se, Mo et Sb, en tant que sondes redox.

Grâce à l'utilisation de couples Redox de ses RN dans l'eau de porosité du ciment, sous une atmosphère de 8 bar H_2 ou 1 bar N_2 , l'Eh interfacial de l'acier corrodé a été mesurée expérimentalement. Les RN (U^{VI} , Se^{IV} , Mo^{VI} , Sb^{V}) ont été introduits séparément, leurs concentrations en espèces solides réduites ont été obtenues par soustraction entre RN apporté et RW présent dans l'eau potable à l'équilibre, puis au sein de la phase solide par ajustement linéaire linéaire (LCF) des spectres XANES échantillon solide à l'énergie d'absorption des rayons X pour chaque RN. La spéciation de la solution a montré que la concentration aqueuse totale en RN (obtenue par HPLC-ICP-MS et des méthodes colorimétriques) était toujours

celle d'une espèce oxydée. Les couples de produits de corrosion de l'acier (magnétite / hématite et magnétite / goethite) et surtout Fe^0 ont montré une bonne affinité pour les RNs, entraînant une diminution de la teneur en solution suivant un K_d pour $\text{U} > \text{Sb} > \text{Se} > \text{Mo}$ dans des atmosphères N_2 et H_2 . Basé sur les LCF des spectres de XANES de U, Se, et Sb, on a démontré que ces éléments sont et réduits en UO_2 , U_4O_9 , FeSe , FeSe_2 , Se^0 , Sb^0 et Sb_2O_3 . La présence de H_2 n'augmente manifestement pas le taux d'élimination des RN aqueux, mais elle favorise la formation des espèces les plus réduites, par exemple FeSe (sur FeSe_2 et Se^0) ou Sb^0 (sur Sb_2O_3). Les valeurs E_h expérimentales peuvent alors être obtenues en utilisant l'équation de Nernst :

$$E_h = -\frac{\Delta_r G^0}{nF} - \frac{RT}{nF} \ln \frac{a_{\text{Red}}}{a_{\text{Ox}}} \quad (\text{i})$$

Où R et F sont respectivement la constante des gaz parfaits et la constante de Faraday, et où n est le nombre de moles d'électrons transférés, et a est l'activité chimique des espèces correspondants et $\Delta_r G^0$ l'énergie libre de Gibbs de réaction standard.

Comme le montre la Figure VII, les valeurs E_h expérimentales de tous les systèmes NZVI sont remarquablement convergentes et centrées dans une gamme étroite de E_h , avec comme valeur moyenne de $-446,4 \pm 78,0$ mV à $\text{pH} \sim 13,5$. Pour les réacteurs avec le couple redox M/H, les valeurs E_h obtenues se situent entre $\sim -346,2$ mV et $\sim -509,4$ mV, avec une valeur moyenne de ~ -430 mV. Les valeurs de E_h dans les réacteurs M/G sont légèrement plus élevées, ce qui est probablement dû à un E_h plus élevé (valeur moyenne de $-576,0$ mV) imposé par M/G, comparé au couple M/H ($-649,4$ mV). Selon les spectres HE-XRD analysés par fonction de distribution de paires (PDF) et présentés dans la Figure VIII, la phase amorphe de $\text{Fe}(\text{OH})_2$ ou sa couche co-précipitée $(\text{Fe}_{1-x}, \text{Ca}_x)(\text{OH})_2$ sont présentes et pourraient être caractérisé par un produit de solubilité plus grand (K_{sp}), donc par un $\Delta_r G^0$ plus grand que les phases cristallines correspondantes.

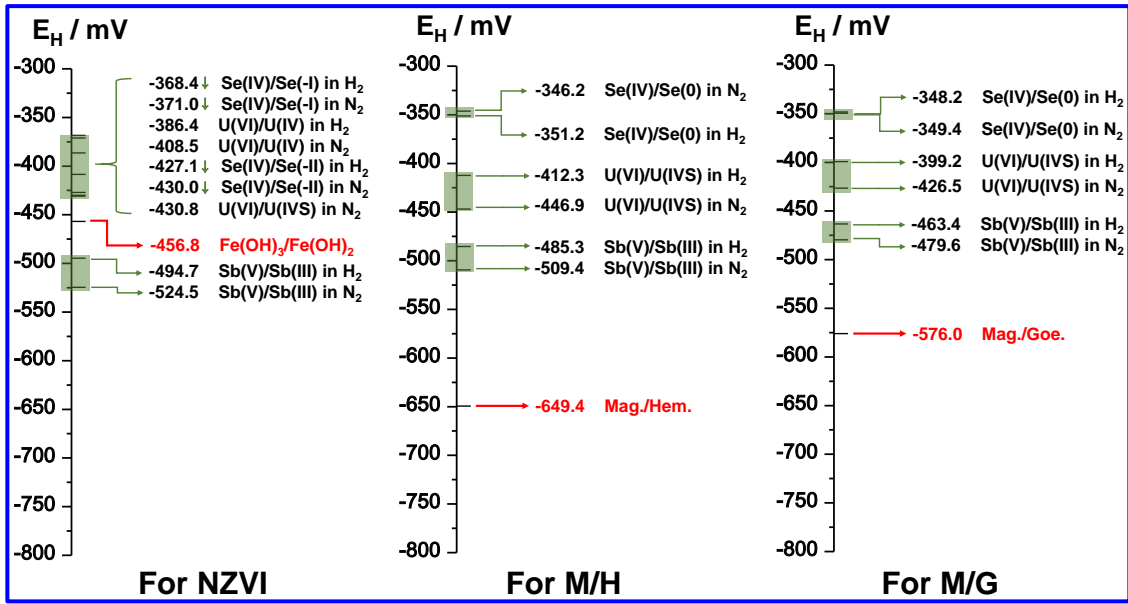


Figure VII. Valeurs expérimentales Eh obtenues "in-situ" pour tous les systèmes de RN, et valeurs Eh imposées théoriquement par les couples Fe-oxyhydroxydes dans le domaine de stabilité de l'eau. Les flèches vers le bas placées sur Se (IV) / Se (-II) et Se (IV) / Se (-I) indiquent des valeurs de Eh encore plus basses dues à du Fe(OH)₃⁻ éventuellement plus dilué.

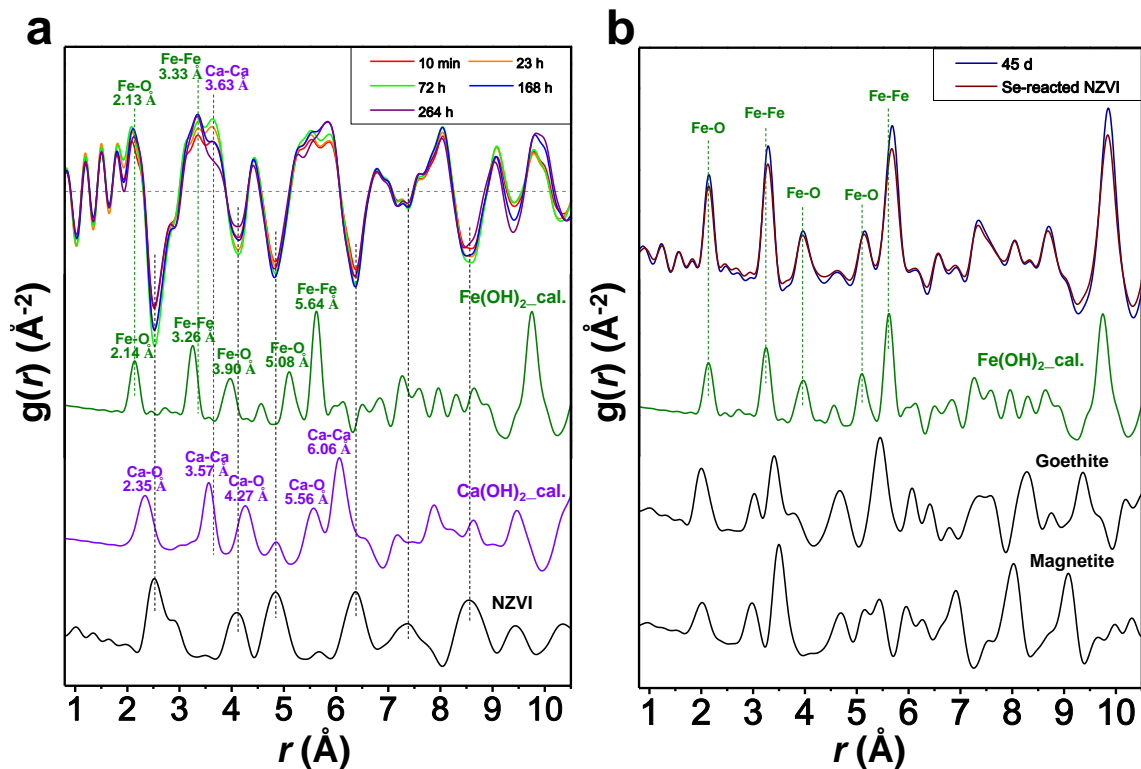


Figure VIII. Modèles différentiels PDF (*d*-PDF) et PDF de NZVI ayant réagi avec CPW avec différents temps de réaction. (a) PDF expérimental de NZVI vierge et *d*-PDF de NZVI ayant réagi ; Références PDF calculées pour Fe(OH)_{2(cr)} et Ca(OH)₂. (b) Les références PDF sont dérivées du Fe Fe(OH)_{2(cr)} calculé, de la goethite synthétisée et de la magnétite. Le PDF expérimental de NZVI ayant réagi avec CPW à 45 jours et NZVI ayant réagi avec Se^{IV} est montré en haut.

En utilisant les valeurs de $\Delta_f G^0$ du $\text{Fe}(\text{OH})_2$ et du $\text{Fe}(\text{OH})_3$ amorphes, on a calculé que l'Eh théorique imposé par le couple $\text{Fe}(\text{OH})_2/\text{Fe}(\text{OH})_3$ est égale à -456.8 mV, une valeur très proche des valeurs expérimentales obtenues pour les réacteurs avec NZVI. Les valeurs théoriques Eh des couples M / H (-649,4 mV) et M / G (-576,0 mV) étaient significativement plus faibles que les valeurs expérimentales obtenues à partir des demi-réactions des RN. Les contributions à l'énergie de surface et l'effet d'hydratation de surface des particules nanométriques conduisent à une augmentation de $\Delta_f G^0$ et peuvent expliquer dans une large mesure les valeurs de Eh mesurées. Une autre explication de la distribution expérimentale des valeurs de Eh observés dans les réacteurs M/H et M/G peut être le contrôle par les couples formés en surface $\text{Fe}(\text{OH})_2/\text{Fe}(\text{OH})_3$ ou $(\text{Fe}_{1-x}, \text{Ca}_x)(\text{OH})_2/\text{Fe}(\text{OH})_3$ amorphe, plutôt que par les couples Fe-oxyhydroxydes ajoutés à l'origine.

Dans la littérature, des désaccords sont souvent observés entre les valeurs Eh théorique et celles mesurées avec une électrode, attribués soit à des réactions redox n'ayant pas atteint l'équilibre (cas des couples avec Nets), soit à des défauts analytiques à l'interface Pt-électrode-eau (pire dans le cas de l'électrode Pt est exposée à des lixiviats hyperalcalins). En revanche, l'approche décrite montre une bonne cohérence interne entre les valeurs de toutes les demi-réactions et semble donc être une nouvelle méthode fiable pour calculer Eh dans le béton, ainsi que dans d'autres systèmes où la mesure directe n'est pas réalisable. Notre approche pourrait ouvrir la voie à une cartographie de la spéciation des RN dans de vrais blocs de béton armé et à une description plus poussée du gradient Eh (les résolutions spatiales dépendant de la taille des pixels de balayage du faisceau de rayons X, soit $\sim \mu\text{m}$).

Les structures cimentaires renforcées dans les sites de stockage géologiques de déchets nucléaires agiront comme des barrières limitant le transfert des radionucléides (RN). En France, le ciment CEM-V/A, préféré est composé de 30% de laitier de haut fourneau (pouvant contenir jusqu'à 35% de sulfure d'oxydes de Cd, Cu, Fe ..., Fe^0 et Fe (II) / (III)) et 20% de cendres volantes (également très riches en impuretés, en particulier en sulfures de divers métaux). Ce ciment présente l'avantage d'avoir un pH interne plus élevé et avoir une meilleure résistance à l'attaque des sulfates. Ici, nous avons étudié le comportement de sorption des RN (Se, Mo, Sb) sur la pâte de ciment hydratée CEM-V/A (HCP) en présence au nom des phases Fe (NZVI, magnétite, hématite, goethite, magnétite / hématite et magnétite / goethite). En outre, nous avons tenté de déterminer les sites potentiels de sorption active pour les RNs et de cartographier la distribution de chaque RN au cours de sa diffusion à travers un HCP CEM-V/A renforcé par du NZVI (modèle de l'acier). Les résultats ont montré que le

ciment hydraté contenant du NZVI possède une capacité d'élimination des RN plus élevée et que le ciment hydraté vierge avait une meilleure capacité d'absorption que le ciment contenant des Fe- (hydr) oxydes. Tous les types de ciment présentaient une forte affinité pour Sb (V) et U (VI), avec des Rd de $Sb > U > Se > Mo$. La formation de nanoparticules colloïdales de type Clarkeite pourraient prédominer dans les mécanismes de sorption sur ciment, tandis que la coprécipitation avec des sites de surface de matériaux riche en Ca pourrait être la voie d'absorption la plus efficace concernant Sb (V). L'analyse des spectres (XANES) a mis en évidence l'existence d'espèces S réductrices, comme le soufre natif et FeS_2 , qui peuvent donc à leur tour agir comme réducteur de RN. LCF des spectres XANES au seul Se a montré que l'absorption de Se (IV) se faisait par complexation avec des sites Ca et par précipitation après réduction des Se par NZVI et par les sulfures, révélant que même le ciment CEM-V/A hydraté blanc était un bon réducteur en vers Se (VI). En outre, l'analyse PDF des spectres HE-XRD a montré qu'après corrosion par SeO_3^{2-} , le NZVI se transformait complètement en $Fe(OH)_2$ et le pont tétraèdre-octaèdre ferreux de la magnétite disparaissait en raison de l'oxydation par Se (IV). Aucune réduction de molybdate n'a été détectée. L'analyse de Mo K-edge XAS a révélé que $AFm-SO_4$ et Fe^0 étaient les deux phases les plus efficaces pour l'élimination du MoO_4^{2-} dans le ciment armé.

Des échantillons solides de ciment hydraté contenant du fer en présence de RN ont été analysés par micro-sonde électronique (EMPA). D'après la cartographie des éléments (présenté dans la Figure IX), U est concentré à la surface des phases riches en Ca alors que la distribution Mo présentait une forte corrélation avec celles de phases Fe. Fe^0 a toujours montré une forte affinité pour tous les RN étudiés, tandis que les phases de ciment hydraté présentaient une certaine sélectivité capacité de complexation des RN avec Ca. En conclusion les RN ont une affinité forte pour le ciment CEM-V/A hydraté et les résultats expérimentaux obtenus dans un environnement de béton armé simulé devraient fournir des données fondamentales pour cette affinité prédire.

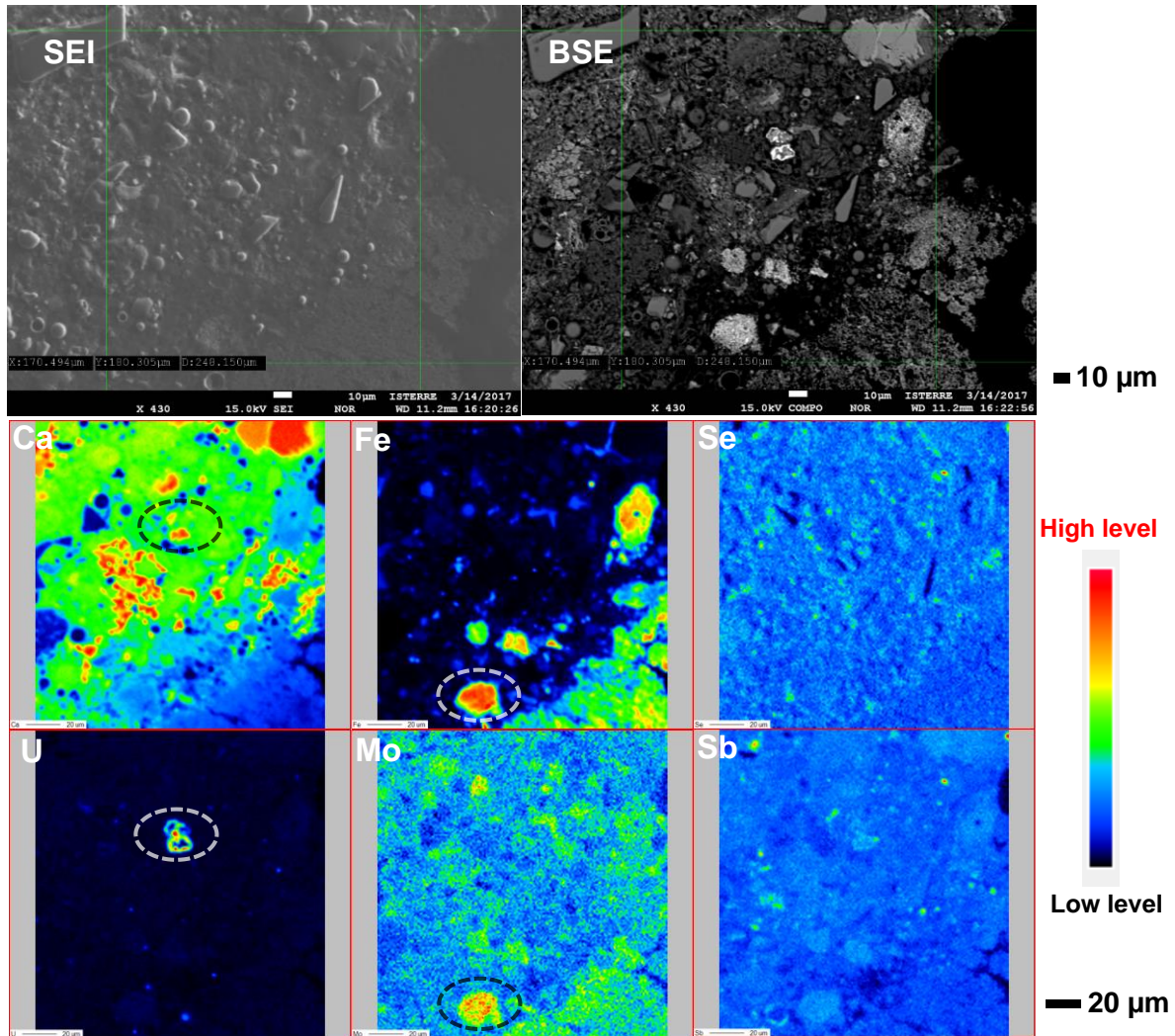


Figure IX. Image d'électrons secondaires (SEI) par électrons rétrodiffusés (BSE) et cartographie d'éléments de la section sélectionnée pour l'échantillon NZVI. La barre d'échelle pour SEI et BSE est de 10 µm, celle pour la cartographie est de 20 µm. De la couleur noire à la couleur rouge, le niveau de concentration des éléments augmente dans les images de cartographie.

Les sulfures de fer, par exemple la pyrite (FeS_2) et le mackinawite (FeS), sont largement présents non seulement dans le ciment CEM-V/A, mais également dans les barrières naturelles d'argilites et de roches granitiques comme pièges potentiels des RN dans les sites géologiques de stockage des déchets nucléaires. Dans cette étude, les facteurs influençant la réduction de l'U(VI) par la pyrite ont été étudiés. On a utilisé de la pyrite ayant des impuretés en Pb, As et Si. Les résultats ont montré que la pyrite contenant As est généralement plus réactive que la pyrite contenant du Pb, mais que le SiO_2 coexistant peut améliorer la réactivité de la pyrite contenant du Pb. De plus, la pyrite broyée fraîchement (pyrite de Type II) contenant Pb et As présentait une réactivité beaucoup plus élevée envers l'U(VI) aqueux, tandis que la réaction d'oxydoréduction était inhibée dans la plupart des conditions pH, quand

la pyrite de Type I (Figure X). Une quantité considérable de soufre élémentaire présent à la surface a été détectée lors de l'oxydation de la pyrite broyée fraîchement par du U(VI) aqueux conduisant à une diminution de la concentration en S aqueux.

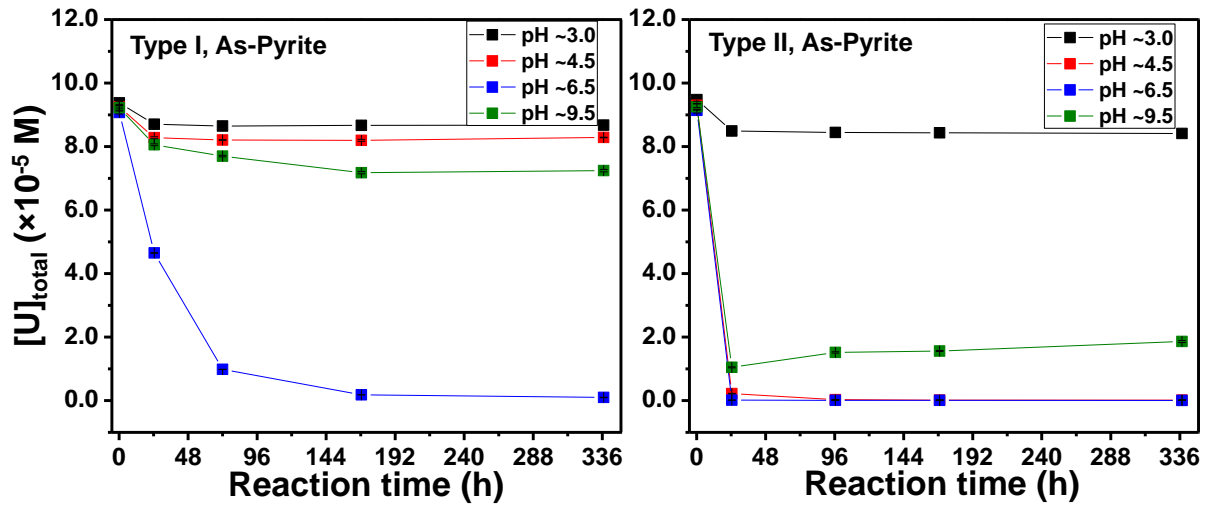


Figure X. Évolution de la concentration en U, Fe et S aqueux totaux en fonction temps de réaction, dans des réacteurs contenant de la pyrite riche en As de Type I et de Type II à pH ~ 3,0, ~ 4,5, ~ 6,5 et ~ 9,5.

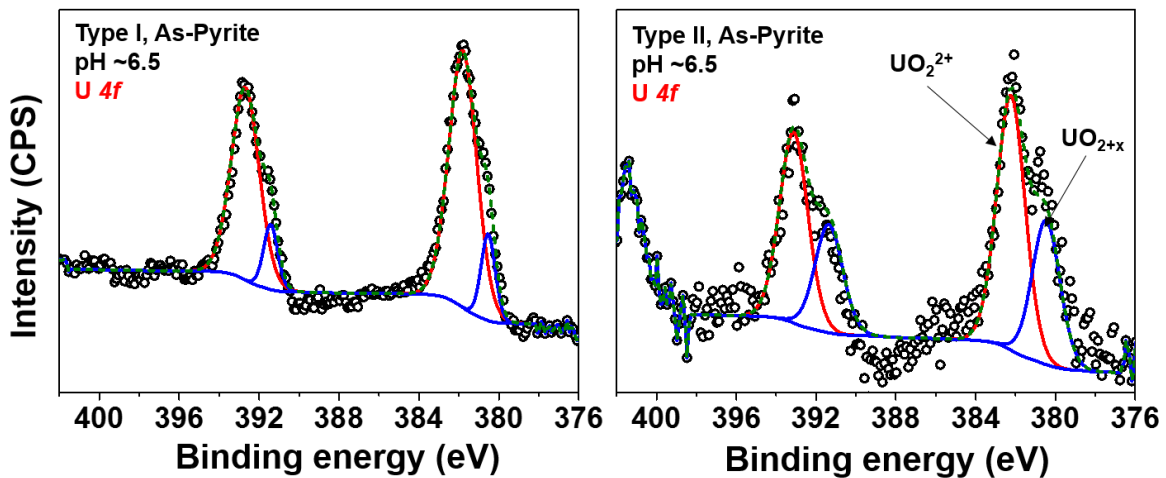


Figure XI. Spectres XPS ajustés de Fe (2p), S (2p) et U (4f) pour la pyrite riche en As de Type I (gauche) et de Type II (droit) ayant réagi avec U (VI) à un pH d'environ 6,5.

Les produits de sorption d'As-pyrite de Type I et de Type II ayant à pH ~ 6,5, ont été analysés par spectroscopie de photoélectrons X (XPS). Une plus grande quantité d'espèces U réduit, UO_{2+x} , a été détectée sur la pyrite de Type II, comme le montre la Figure XI. Les images MEB (Figure XII) ont de plus montré que la réduction de U(VI) aqueux se produisait principalement aux sites de surface enrichis en Pb et As. Nous en avons conclu que la solubilité des pyrites pourrait augmenter en partie sur ces taches d'impureté. Suite à des

défauts du réseau. Cela conduirait à la présence d'une plus grande quantité d'espèces soufrées plus réactive que au sein de la structure, comme S^{2-} et S_2^{2-} . Par conséquent, plus de U (VI) peut être réduit et précipité sur ces sites riches en impuretés.

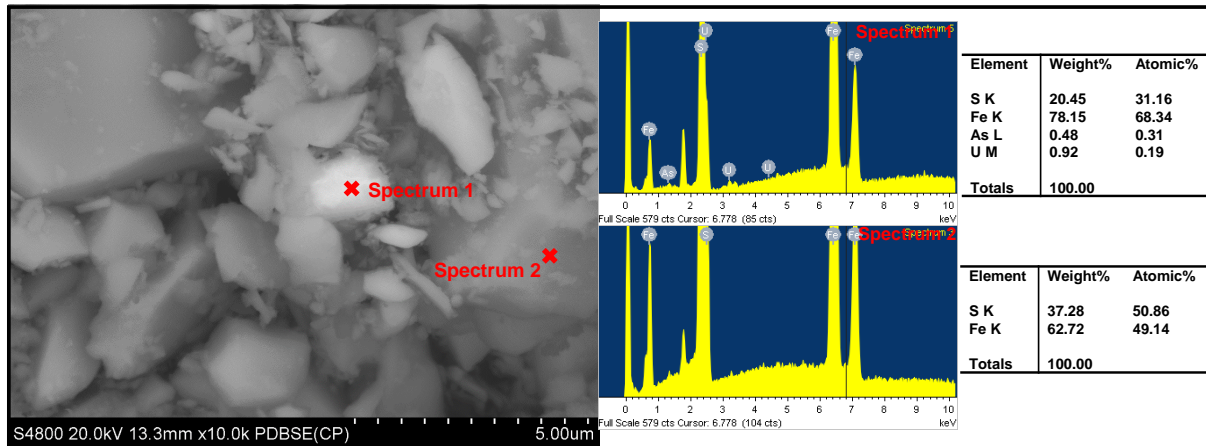


Figure XII. Images MEB d'As-pyrite de Type II ayant réagi avec U (VI) à pH ~ 3,0. Les spectres EDS correspondants et le contenu élémentaire des points sélectionnés sont indiqués sur la droite de chaque image SEM.

Nous avons proposé que la réactivité de la pyrite dépend largement des impuretés hébergées dans la pyrite et de la teneur en S^{2-} réactif présent à la surface de la pyrite, et résultant de la rupture des liaisons Fe-S durant le processus de broyage. Les résultats de cette étude conduisent à une meilleure compréhension du rôle de la pyrite dans la contrôle de la mobilité de l'uranium dans l'environnement.

L'étude ci-dessus contribue avec des données fondamentales à l'évaluation du comportement de migration des RN dans un système à barrières multiples. Lorsque les RN traversent des boîtes en métal ou de béton renforcés et de roches hôtes riches en pyrite, les processus d'interaction entre les RN et barrières, comme l'adsorption, la réaction redox, la coprécipitation et les échanges d'anions peuvent participer à leur retour. Dans cette thèse de doctorat, des phases d'AFm cimentaires mineures, mais hautement réactives (acides gras AFm-Cl₂ ou AFm-SO₄, appartenant aux LDH CaAl) ont été utilisées pour adsorber MoO₄²⁻ et SeO₃²⁻ à diverses charges de surface. Une combinaison de la modélisation de l'équilibre chimique PHREEQC et des techniques de rayons X à base de synchrotron (par exemple, XRD, PDF et XAFS résolus dans le temps) révèle que les sites de sorption multiples, y compris deux types de sites de bord, des sites d'échange d'ions intercalaires et une précipitation de phase riche en Ca, sont des processus actifs dans la rétention des RN sur les phases AFm. Une relation linéaire permet de lier l'espacement basal AFm et le rayon d'anion intercalé hydraté.

La co-sorption de U et Mo sur le ciment-ciment hydraté renforcé par Fe⁰ a également été étudiée par cartographie micro-sonde, montrant que U doit être immobilisé instantanément par des matériaux de ciment tandis que Mo est préférentiellement sorbé sur des produits de réaction de Fe. La valeur Eh prédominant dans le béton est difficile à déterminer. Ici, les RN sensibles à la réduction rénale (par exemple, U^{VI}, Se^{IV}, Mo^{VI} et Sb^V) sont utilisées comme sondes, pour mesurer les valeurs Eh in-situ, en calculant l'équation de Nernst de la manière suivante. La concentration des espèces réduites a été mesurée en fonction de la concentration totale de RN précipitée par réduction et de la spéciation parmi ces espèces réduites, tel qu'obtenu par l'analyse LCF des données XANES. Les valeurs Eh déterminées expérimentalement obtenues de cette façon étaient remarquablement fermées pour toutes les RN avec des valeurs centrées de -368 à -524 mV pour l'eau de pore de ciment (CPW) équilibrée avec Fe⁰ et des valeurs de -346 à -509 mV pour CPW équilibrées avec des produits de corrosion Fe - couples d'oxydes (magnetite / hématite ou magnetite / goethite) à pH ~ 13,5. Ni la valeur Eh calculée pour ces couples ni pour Fe⁰ / Fe (OH)₂ correspond à ces données. Au lieu de cela, le potentiel redox semble être contrôlé par le couple amorphe Fe(OH)₂/Fe(OH)₃ or (Fe_{1-x},Ca_x)(OH)₂/Fe(OH)₃ . Enfin, dans le domaine de l'argile ou du granit, plusieurs facteurs peuvent affecter réactivité superficielle des pyrites, à savoir les impuretés élémentaires dans le réseau de pyrite et de la présence de Fe³⁺ et S²⁻ à la surface de la pyrite. Les impuretés des éléments et la présence de S²⁻ sur la surface de la pyrite ont largement accéléré la réduction des U (VI). Cette thèse permet d'apprécier l'importance de ces processus.

Table of content

Acknowledgment	iii
Publications during PhD thesis (2014-2017)	iv
Résumé étendu	I
Chapter 1. Introduction-Barriers around geologic nuclear waste repositories.....	1
1.1. Geological nuclear waste disposal.....	1
1.2. Multi-barrier systems.....	2
1.3. Sorption behavior of radionuclides in potential barriers	3
1.3.1. On iron phases existing in canisters and steel reinforcements.....	4
1.3.2. On hydrated cement phases existing in backfills and tunnels.....	5
1.3.3. On clays	12
1.3.4. On granitic minerals.....	13
1.4. Objectives of the thesis.....	13
Chapter 2. Evidence of multiple sorption modes in AFm phases using Mo as structural probe	15
2.1. Introduction	16
2.2. Materials and methods.....	17
2.2.1. Materials and Chemicals.....	17
2.2.2. Adsorption Experiments.	18
2.2.3. Aqueous Data Modelling.	19
2.2.4. In-situ X-ray Diffraction.	19
2.2.5. Solid Phase Characterization.	20
2.3. Results and discussion	22
2.3.1. Wet Chemistry Experiments.	22
2.3.2. In-situ Time Resolved X-ray Diffraction.....	24
2.3.3. Local Geometry of Adsorbed Molybdate.	26
2.3.4. Mo Distribution in Reacted LDHs Particles.	27
2.3.5. Complexation environment around adsorbed Mo.....	29
2.3.6. Estimation of edge sites density.....	31
2.3.7. Environmental implications.	32
Supporting Information	34
Chapter 3. Selenite uptake by AFm phases: a description of intercalated anion coordination geometries	51
3.1. Introduction	52
3.2. Materials and methods.....	53

3.2.1. Materials and chemicals.....	53
3.2.2. Adsorption experiments.....	54
3.2.3 Aqueous data modelling.....	55
3.2.4 In-situ time-resolved XRD.....	55
3.2.5 Solid phase characterization.....	55
3.3. Results and discussion.....	56
3.3.1 Batch sorption isotherm.....	56
3.3.2. In-situ time resolved XRD.....	58
3.3.3. Sorbed Se coordination.....	60
3.3.4. Sulfur K-edge EXAFS results.....	62
3.3.5. Linear relationship between basal spacing and hydrated anions' radii.....	63
3.3.6. Structural stability of AFm-SeO ₃	64
3.3.7. Environmental Implications.....	65
Supporting Information.....	67
Chapter 4. Determination of redox potentials imposed by steel corrosion products in cement-based media.....	80
4.1. Introduction.....	81
4.2. Materials and methods.....	82
4.2.1. Materials and chemicals.....	82
4.2.2. Synthesis and characterization of Fe-bearing phases.....	83
4.2.3. Batch sorption experiments.....	83
4.2.4. XANES spectroscopy.....	84
4.2.5. PDF spectroscopy.....	85
4.3. Results and discussion.....	85
4.3.1. Aqueous phase results.....	85
4.3.2. Surface Se and Sb species.....	88
4.3.3. Surface U and Mo species.....	90
4.3.4. PDF analysis of reacted NZVI.....	91
4.3.5. "In-situ" experimental Eh values.....	93
4.3.6. Environmental implications.....	96
Supporting Information.....	98
Chapter 5. RNs (i.e., U, Se, Mo, and Sb) sorption behavior on hydrated Fe-bearing CEM-V/A cement.....	113
5.1. Introduction.....	114
5.2. Materials and methods.....	115
5.2.1. Materials and chemicals.....	115

5.2.2. Preparation of powder samples of hydrated Fe-bearing cement products.....	115
5.2.3. Synthesis of each separated CEM-V/A cement hydration product.	116
5.2.4. Kinetics experiments.....	116
5.2.5. Batch sorption experiments.....	116
5.2.6. Preparation of RNs-containing Fe ⁰ -bearing cement cores.....	117
5.2.7. Polishing of RNs-containing cement cores and Micro-probe analysis.	118
5.2.8. Sulfur K-edge, Selenium K-edge, and Molybdenum K-edge XANES-EXAFS spectroscopy.....	119
5.2.9. PDF analysis.	120
5.3. Results and discussion	120
5.3.1. XRD characterization and dissolution kinetics of Fe-bearing hydrated cement...	120
5.3.2. U(VI) sorption on hydrated CEM-V/A cement particles.....	122
5.3.3. Se(IV) sorption on hydrated CEM-V/A cement particles.....	124
5.3.4. Mo(VI) sorption on hydrated CEM-V/A cement particles.	134
5.3.5. Sb(V) sorption on hydrated CEM-V/A cement particles.....	138
5.3.6. Microprobe mapping on Fe ⁰ /cement interface in presence of RNs.	139
5.4. Conclusions	145
Chapter 6. The influence of surface impurities on the reactivity of pyrite toward aqueous U(VI).....	146
6.1. Introduction	147
6.2. Materials and methods.....	148
6.2.1 Materials	148
6.2.2 Batch sorption experiments.....	149
6.2.3 Spectroscopic and Microscopic Analyses.....	150
6.3. Results and discussion	151
6.3.1 Pyrite Characterization.....	151
6.3.2 Aqueous phase analysis for Type I pyrite suspension	152
6.3.3 Aqueous phase analysis for Type II pyrite suspension.....	153
6.3.4. XPS Surface features	156
6.3.5. XAS Characterization on uranium speciation.....	159
6.3.6. SEM surface morphology	161
6.3.7. Influencing factors on pyrite reactivity.....	162
6.4. Conclusions	163
Supporting information.....	164
General conclusions	173
Retention of MoO ₄ ²⁻ on AFm phases.	173

SeO ₃ ²⁻ uptake by CaAl LDH.	173
Determination of Eh values imposed by steel corrosion products in cement-based media.	174
RNs sorption behaviors on hydrated Fe-bearing CEM-V/A cement.....	175
The influence of surface impurities on the reactivity of pyrite toward aqueous U(VI).	176
Perspectives.....	177
Dissolution of spent nuclear fuel (UO ₂) in silica-rich fluids.....	177
Uranium(VI) colloidal nanoparticles in cement leachate.....	177
Sorption behaviors of RN oxyanions on LDHs' surface.....	177
Intercalated anion's size vs. LDHs' basal spacing.	178
Sorption competition of RNs on corrosion products of reinforced Fe ⁰	179
Synchrotron-based X-ray analysis of Fe ⁰ -reinforced cement cores.	179
U(VI) retention on synthetic trace elements doped pyrite.....	180
Thermodynamic predictions of secondary phases in cementitious repositories.....	181
References	182

Chapter 1. Introduction-Barriers around geologic nuclear waste repositories

1.1. Geological nuclear waste disposal

Geological disposal was defined in a 1995 Collective Opinion of the Nuclear Energy Agency (NEA) Radioactive Waste Management Committee entitled “The Environmental and Ethical Basis of Geological Disposal”[1]. A deep geological repository is a nuclear waste repository excavated deep within a stable geologic environment (typically below 300 m or 1000 feet). Nowadays, deep geological disposal has been widely adopted in many countries to be the preferential solution for final disposing of intermediate-level long-lived (IL-LL) and high-level (HL) radioactive waste, at depths between 250 m and 1000 m for mined repositories, or 2000 m to 5000 m for boreholes. On the other hand, intermediate-level short-lived (IL-SL) and low-level (LL) radioactive waste will be disposed in the near-surface, at ground level, or in caverns below ground level (at depths of tens of meters). As shown in Figure 1.1, a multiple barriers principle is applied for the disposal of HL radioactive waste in Sweden.

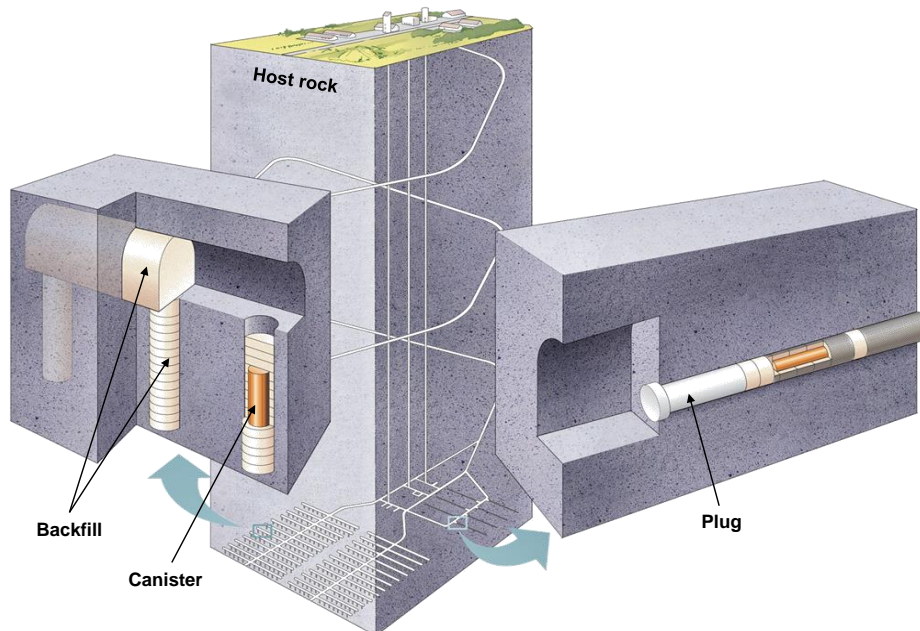


Figure 1.1. The proposed KBS-3 nuclear waste repository concept from Swedish Nuclear Fuel and Waste Management Co (SKB). Illustrator: Jan Rojmar.

The International Atomic Energy Agency (IAEA) estimates that up to the early 2000s, low- and intermediate-level radioactive waste worldwide has been generated up to a cumulative

volume of $7.3 \times 10^6 \text{ m}^3$, and the produced cumulative volume of HL waste has reached $8.3 \times 10^5 \text{ m}^3$ [2]. However, nearly 0% of HL waste is in disposal, with ~80% of LL/IL-SL waste and ~20% of IL waste in disposal. Thus, the disposal of high-level radioactive waste is extremely urgent and a sustainable disposal of low- and intermediate-level radioactive waste should be also supported in the long term.

1.2. Multi-barrier systems

A mined repository is the most widely proposed option within the deep geological disposal concept, generally relying on a multi-barrier system to isolate the waste from the biosphere for centuries. This multi-barrier principle creates an overall system robustness that enhances confidence that the waste will be successfully contained. The multiple barriers typically comprises metal (e.g., iron or copper) or concrete canisters/casks containing the vitrified radioactive waste, cement or clay (e.g., bentonite) buffer and/or backfill materials, and repository host rocks (e.g., Callovo-Oxfordian clay[3], Boom clay[4], or Opalinus clay[5], granite[6], welded volcanic tuff rocks[7], and layered salt strata or domes). The choice of waste container materials and design, as well as the buffer/backfill material varies depends on the type of waste to be contained and the nature of the host rock-type available.

In France, about 80% of the electricity is generated from its 58 nuclear power plants, being a world leader in the technology. The French radioactive waste disposal agency, ANDRA, is designing a deep geological repository, Cigéo project, in a clay formation at Bure, in eastern France. This will host vitrified HL waste and long-lived IL waste. With the grey 150-million-year-old Callovo-Oxfordian argillaceous rock as the host rock, the disposal concept in France is to use the reinforced concrete, stainless steel casks, and glass as the engineered barrier system (EBS). The specially formulated Fe-reinforced cement backfill material would provide a long-lasting alkaline environment that contributes to containment of the waste by preventing many radionuclides from dissolving in the groundwater. Similar cement-based schemes have been proposed in Switzerland, Czech Republic, Finland, Sweden, Germany, Spain, UK, and US[8].

Besides, huge amounts of cementitious materials are also used for IL waste disposal in France, with an approximately three-time volume of the waste. In the repositories, reinforced cementitious materials are used for tunnel support and backfill, waste containers and waste matrixes, which are considered as barriers that inhibit the mobility of RNs in case of eventual leakage.

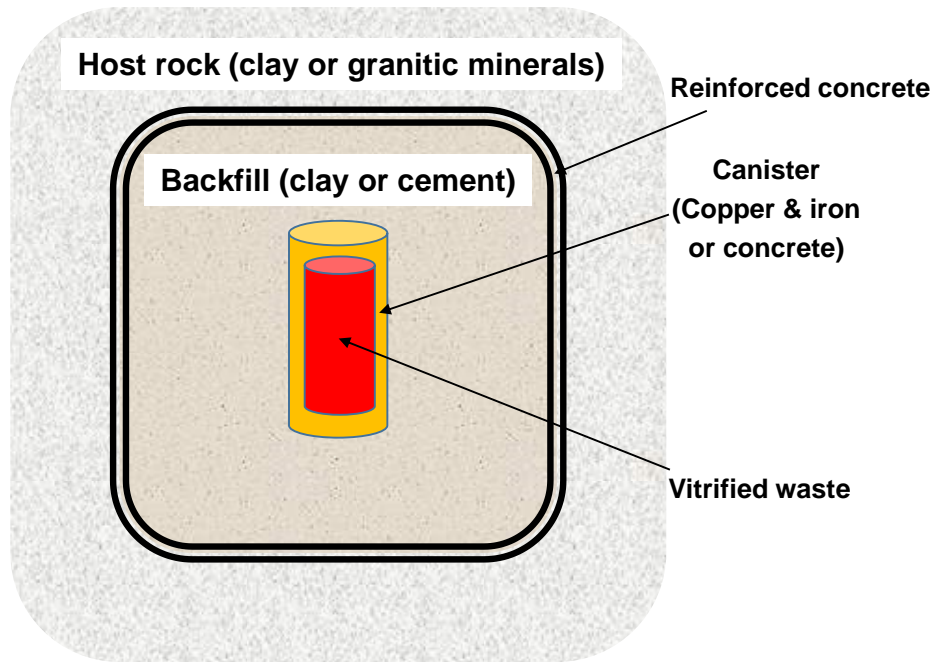


Figure 1.2. Schematic drawing of the multi-barrier system consisting of engineered and natural (geological) barriers.

In any nuclear waste repository with the multi-barrier system concept, as shown in Figure 1.2, several retardation factors can be effective for the immobilization of radionuclides (RNs) from the near field to the far field: vitrified materials, iron and copper in canisters along with their corrosion products, clay and cementitious materials, embedded steel and its corrosion products, and active phases (e.g., pyrite, smectite, and annite) in host clay and granitic minerals.

1.3. Sorption behavior of radionuclides in potential barriers

The mobility of radionuclides (RN) is a key issue regarding the safety assessment of nuclear waste repositories, governed by the geochemical interaction with each barrier. To a large extent, the extremely low mobility of the most radiotoxic RNs, the actinides, increases the reliability of long-term safety of deep nuclear waste repositories. However, a few RNs, mainly anionic species like I^{129} , Cl^{36} , Se^{79} , and Tc^{99} , would diffuse fast and contribute to the ultimate radioactive exposure risks to the biosphere, according to leakage scenarios[9]. Less mobile RN on barriers will result in a larger distribution coefficient (K_d). Figure 1.3 shows the effect that even a small K_d value would have on ^{129}I fluxes and retention time at the top of the Callovo-Oxfordian GBS[10]. In the spent fuel, 96% of the mass is the remaining uranium: most of the original ^{238}U and a little ^{235}U . Thus, uranium migration behavior in multi-barrier system is also of essence when evaluating nuclear waste disposal options. A detailed

scientific understanding of the chemical form of solid phase associated RNs, and of the possible sorption mechanisms at work, constitutes a priority research area to enhance our confidence for repository safety.

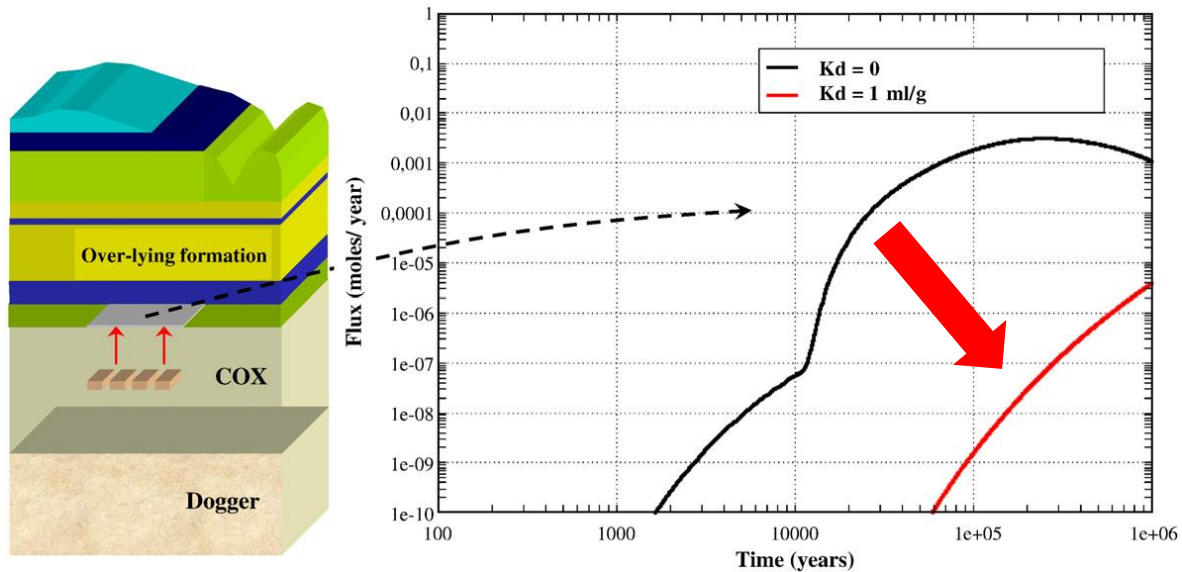


Figure 1.3. Reactive transport model showing an example of the retardation effect of a non-null K_d on ^{129}I fluxes (mol/year) exiting the upper surface of the Callovo-Oxfordien GBS[11].

1.3.1. On iron phases existing in canisters and steel reinforcements

Iron phases, including the iron canister (at low pH) and embedded steel (at high pH) in EBS, are expected to retard the migration of RNs through different interactions. Besides, iron corrosion products, such as, magnetite (Fe_3O_4), hematite (Fe_2O_3), goethite (FeOOH), and siderite (FeCO_3), can also contribute to the RNs immobilization. Vital to the migration behaviors of redox-sensitive radionuclides (RNs)[12], the redox potential (Eh) in EBS will be governed by the corrosion of iron, producing a thin (over a few microns) film based on the dynamic Fe^{II} -oxyhydroxides/magnetite/ Fe^{III} -oxyhydroxides thin-film “sandwich” structure[13]. Under aerobic conditions, Fe_3O_4 is the intermediate oxidation product on the steel surface while $\text{Fe}(\text{OH})_2$ is the intermediate product under anaerobic conditions[14]. Previous studies have reported that the oxidized RNs species can be immobilized by Fe^0 and Fe-oxyhydroxides via reductive precipitation and surface adsorption. For instance, aqueous U^{VI} can be reduced by nanoscale zero-valent iron (NZVI)[15] into UO_2 . Reductive precipitation can also occur on colloidal hematite with Fe^{2+} [16] and nanocrystalline magnetite [17, 18]. Besides, Fe^{III} -oxyhydroxides, e.g., goethite, can also remove aqueous U^{VI} by surface complexation[19]. Uranium co-precipitation with iron oxide minerals (e.g., hematite and goethite) indicates that U^{6+} is incorporated in the Fe oxides as uranate until a

point of saturation is reached, not as UO_2^{2+} ion, the one with large ionic radius ($\sim 1.8 \text{ \AA}$) [20]. Furthermore, selective and highly efficient UO_2^{2+} adsorption, separating from Ln^{3+} at $\text{pH} \sim 3$, is observed on a magnetic nanocomposite, $\text{Fe}_3\text{O}_4@\text{ZIF-8}$ [21]. Regarding aqueous Se^{IV} , reduced species, e.g., Se^0 , FeSe , and FeSe_2 , could be also obtained on these Fe-oxyhydroxides [22]. In addition, the presence of sorbed Fe(II) can enhance Se(IV) sorption on calcite compared to that of Fe-free pure calcite, resulting in half immobilized Se reducing into $\text{Se}(0)$. Selenite can be reduced into FeSe by Fe/ FeC_3 ultrasmall particles according to a previous report [23]. Antimonate ($\text{Sb}(\text{OH})_6^-$) also belongs to the mobile anions in repositories. In reducing environments, lower oxidation state Sb species, such as Sb^{III} and Sb^0 , can be formed. For instance, magnetite can reduce Sb^{V} into Sb^{III} and the reduction increases with pH values [24]. Sb^{III} was also found present at the surface of Fe-bearing rims [25]. In addition, Sb^0 was detected in soil samples from Swiss shooting ranges, probably derived from reduction by Pb^0 into PbSb alloy-containing unweathered bullet fragments [26]. Thus, Fe^0 , with even lower standard reduction potential than Pb^0 , can also generate Sb^0 [27]. Fe-oxyhydroxides [24] also show strong sorption affinity to Sb^{V} , resulting in reductive precipitates (e.g., Sb_2O_3) and structural incorporation [26, 28]. In contrast, molybdate (MoO_4^{2-}) is much more difficult to be reduced, even by NZVI [29], and non-redox sorption occurred prevalingly on Fe-oxyhydroxides systems [30, 31]. In contrast, ferrihydrite [32], with much higher specific surface area, is proven to be a good sorbent to molybdate [31, 33] via structural incorporation mechanisms during phase transformations. Besides, aqueous selenium oxyanions [34] and Sb(V) [28] can also be removed efficiently during the ferrihydrite-hematite or ferrihydrite-goethite recrystallization. Regarding embedded steel (Fe^0) in cement-based medium, the hyperalkaline condition ($\text{pH} \sim 13$) would heavily influent both steel corrosion processes and the redox potential imposed, and thus sorption behavior of RN anions on the resulting Fe-oxyhydroxides, which are still not well-documented.

1.3.2. On hydrated cement phases existing in backfills and tunnels

Backfill/buffer materials and cementitious materials from the tunnels and alveolis can act as secondary barriers in the case of RN leakage from canisters. Unlike redox-reactive iron oxides, the cementitious structure can add potentially a retardation factor for RNs diffusion via surface adsorption, ion exchange, or co-precipitation reactions. Regarding ordinary Portland cement (OPC), its hydration products include crystalline portlandite, amorphous calcium silicate hydrate phases (CSH, the major component in hydrated cement) [35], and other minor

phases - hydrogarnet, hydrotalcite, ettringite[36, 37] and AFm phases[38, 39], gypsum, calcite, metal sulfides from blast furnace slags, and possibly pyrite.

1.3.2.1. On portlandite and CSH phase

It can be foreseen that the extremely alkaline environment imposed by portlandite will dramatically decrease the mobility of cationic RNs, due to their enhanced adsorption at high pH. Furthermore, CSH phase, referred to as “cement gel”, is expected to have a high density of sorption sites for both cations and anions due to its low crystallinity and imperfect “structure”[40]. The electrostatic sorption of alkali metal ions (including Cs⁺) on negatively charged CSH was found to increase inversely in proportion to the Stokes radius of the hydrated ions for cements with various Ca:Si ratios[41]. Tits et al.[42] have shown that the sorption process controlling the retention of Th(IV) and Eu(III) on CSH is fast. Related sorption mechanisms were investigated[43, 44], indicating that the surface complexed or co-precipitated Eu can be attributed to a Eu-substitution for Ca in the framework of the CSH and a high hydroxylated environment. Sorption of anions, such as Cl⁻ and I⁻, is found to be directly related to the surface charge of CSH phases below millimolar level[45] and Noshita et al.[46] concluded that electrostatic sorption may dominate I⁻ uptake. Besides, CSH materials could be one of the cementitious phases controlling U(VI) uptake in degraded cement pastes[47]. Sorption of UO₂²⁺ [48] on hardened cement paste (HCP) has been also studied, showing that precipitation of calcium-uranate predominates.

1.3.2.2. On AFm phases

Numerous studies have reported RNs sorption behavior on cement hydration products[49]. Through hardened cement paste (HCP), anionic RNs will diffuse much faster than the cations due to the hyperalkaline condition, thus, more intriguing research topic is the sorption behavior of anions. Among the hydration products, AFm phases, hydrated calcium aluminates belonging to layered double hydroxides (LDHs)[38], have been considered as effective phases for the remediation of aquatic environments, to remove anionic contaminants. LDHs refer to a family of lamellar mixed hydroxides with a generic chemical formula $[M^{II}_{6-x}M^{III}_xO_6]^{x+}(A^{n-})_{x/n} \cdot mH_2O$. In the case of the AFm phase (AFm-SO₄) in cement, M^{II}, M^{III}, and Aⁿ⁻ represent Ca^{II}, Al^{III}, and SO₄²⁻, respectively. When concrete is subject to Cl⁻ corrosion (e.g., exposed to sea water, or deicing salt), or when Cl-bearing mixing water, aggregate and admixtures are used to produce it [50, 51], AFm-Cl₂ ($[Ca_4Al_2O_6]^{2+} \cdot (Cl^-)_2 \cdot mH_2O$) can also be present in cement hydration products. These micro- and nano-porous phases have a unique structure

composed of positively charged main layers and negatively charged interlayers, being tolerant of oxyanions substitution in the crystalline layer and anion exchange with weak-binding intercalated anions. As widespread artificial LDHs around the world, AFm phases can be detected or thermodynamically predicted to occur in bottom ash [52, 53] and Class C coal fly ash (CFA) [54-56], which are two of the main coal combustion products (CCPs) with a global production of over 750 million tonnes per year [57]. AFm phases have strong ability to remove toxic soluble anions via surface adsorption and anion exchange processes. It is found that only the AFm-SO₄ phase, competing with ettringite, hydrotalcite, chloride- and carbonate- containing AFm phases, can take up trace levels of iodide. The preferential uptake mechanisms are figured out by co-precipitation experiments, indicating the formation of a solid solution between AFm-I₂ and AFm-SO₄ for the I-SO₄ mixtures (Figure 1.4) [39].

Besides, AFm phase also shows a good affinity for selenium oxyanions, especially for selenate, which is immobilized by anion exchange with intercalate sulfate. On the other hand, sorption mechanisms of selenite are dominated by surface adsorption and Ca co-precipitation, at low and high loadings, respectively [58, 59]. Non-specific interaction of selenium oxyanions with the surface of the cement minerals, and no direct bonding to neighboring atoms can be detected by X-ray absorption spectroscopy[60]. In addition, aqueous arsenic(V) can also be removed efficiently by monosulfate via anion exchange, causing the transformation of monosulfate to ettringite [61].

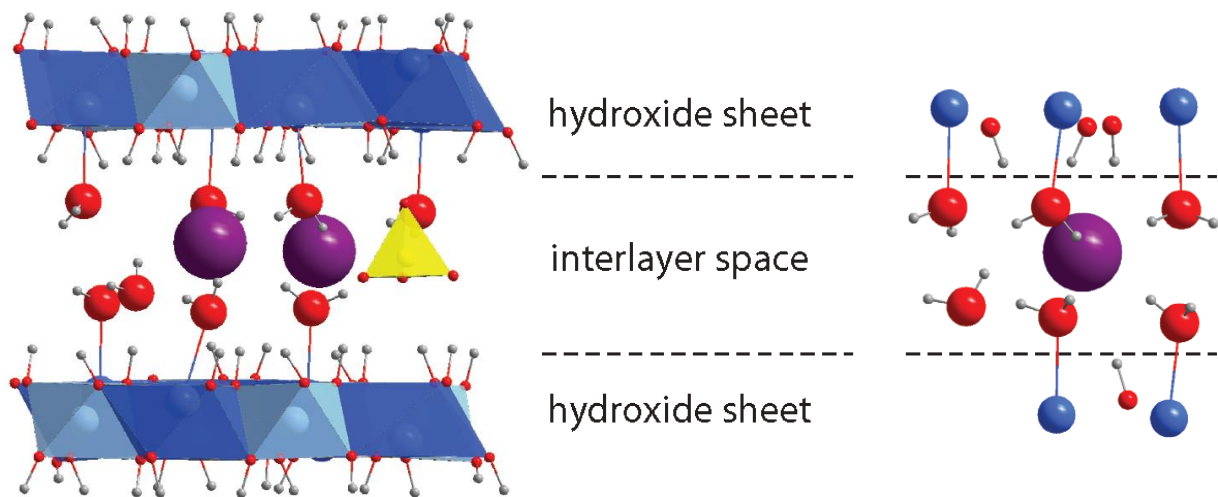


Figure 1.4. Coordination environment of iodine as obtained by geometry optimization based on ab initio simulations for AFm-I-(SO₄)_{0.5}. I, O, H atoms are in violet, red, and gray, respectively. Ca and Al polyhedra are displayed in blue and light blue, respectively. A sulfate molecule is shown as yellow tetrahedron[39].

1.3.2.3. On ettringite (AFt) phase

Ettringite, with a general formula of $[\text{Ca}_3(\text{Al,Fe})(\text{OH})_6 \cdot 12\text{H}_2\text{O}]\text{X}_3 \cdot \text{H}_2\text{O}$ where X denotes a double-charged anion (typically sulfate) or two units of a single-charged anion, occurs in natural alkaline environments, associated with other phases like portlandite, gypsum or afwillite. However, a non-natural analogue of ettringite also occurs during the early hydration of Portland cements in the presence of gypsum[62]. Portland and modified Portland cements are widely used in nuclear waste repositories, thus ettringite is assumed to play a key role in the RNs immobilization processes. The unit cell of ettringite consists of a column part $([\text{Ca}_6[\text{Al}(\text{OH})_6]_2 \cdot 24\text{H}_2\text{O}]^{6+})$ with the inter-column spaces occupied by 3 units of SO_4^{2-} ions and 2 units of H_2O molecules, which hold the columns together through electrostatic forces[63].

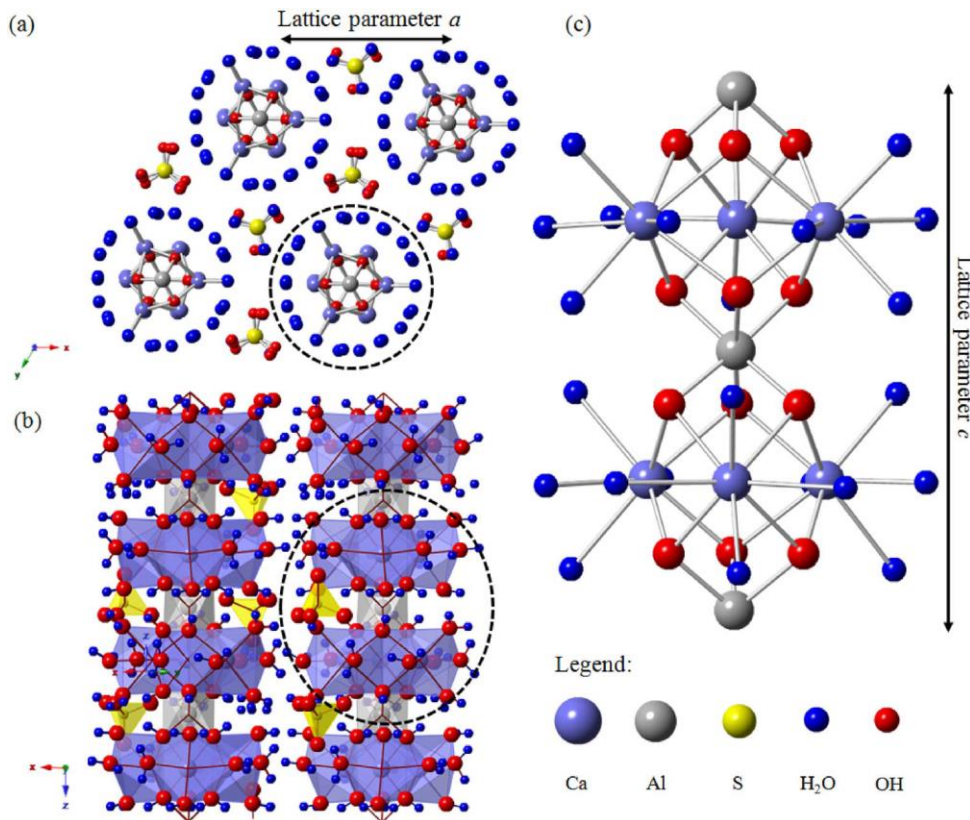


Figure 1.5. Structure of ettringite. (a) Perpendicular to c-axis shown columns and channels, (b) projection of ettringite structure, (c) expanded the dash line regions in (a) and (b)[64].

Ettringite is an anion exchanger and it has been shown that partial or full replacement of SO_4^{2-} (Figure 1.5) is possible in the case of $\text{SeO}_4^{2-}/\text{SeO}_3^{2-}$ [58, 60, 64, 65], MoO_4^{2-} [66], and $\text{Sb}(\text{OH})_6^-$ [67]. Anionic contaminant removal mechanisms can take place in two different ways: i) adsorption in the interchannels of already formed ettringite structure; ii) structural

incorporation into ettringite lattice[68, 69]. Furthermore, ettringite particle surfaces exhibit a net negative charge, so anion substitution with trivalent and divalent cations in the bulk[70] is probably more important than surface adsorption[71]. It is proved that the incorporation mechanism of SeO_4^{2-} in ettringite depends on coexisting SO_4^{2-} in aqueous environments. Without SO_4^{2-} , SeO_4^{2-} -substituted AFm phase was formed as an intermediate [65]. Anion exchange with structural SO_4^{2-} is the main mechanism for immobilization of SeO_4^{2-} . In contrast, SeO_3^{2-} is easily immobilized to form inner-sphere complexes in ettringite[64]. Besides, a consistent observation is that uptake of MoO_4^{2-} is low or non-existent which can be attributed to its large size in comparison to sulfate[66, 72]. Ettringite showed an anion preference in the order of $\text{B}(\text{OH})_4^- > \text{SeO}_4^{2-} > \text{CrO}_4^{2-} > \text{MoO}_4^{2-}$ [66]. Conclusively, two main factors, size and electronegativity difference of oxyanions compared to sulfate, are thought to be inversely proportional to the extent of solid solution [71].

1.3.2.4. On hydrogarnet, hydrotalcite, gypsum, and calcite.

Regarding other phases existing in hydrated cement paste, such as hydrogarnet, hydrotalcite, gypsum, and calcite, they exhibit lower sorption potential than other cement phases. Sorption on hydrogarnet ($3\text{CaO}\cdot\text{Al}_2\text{O}_3\cdot 6\text{H}_2\text{O}$) may occur through ion substitution, e.g., Cr(III) may substitute Al-sites [73]. Besides, hydrogarnet has been identified as a major phase in chromium ore processing residue and has a capacity to host Cr(VI)[74]. The maximum amount of chromate corresponds to a replacement of about one out of every eight hydroxyl tetrahedral per unit cell by a CrO_4^{2-} tetrahedron. Hydrotalcite ($\text{Mg}_6\text{Al}_2(\text{CO}_3)(\text{OH})_{16}\cdot 4(\text{H}_2\text{O})$) has a positively charged layer structure and can incorporate di- and trivalent cations. Previous reports also show hydrotalcite-like minerals' affinity for oxyanions, e.g., $\text{SeO}_3^{2-}/\text{SeO}_4^{2-}$ [75-77], MoO_4^{2-} [75, 78], and AsO_3^- , facilitated by the intercalation of guest anions in most cases. As(V) undergoes strong chemical binding with hydrotalcite-Fe(III) unlike Mo(VI) and Se(VI). In addition, As(V) has the strongest affinity for hydrotalcite varying in the order $\text{As}(\text{V}) > \text{Mo}(\text{VI}) > \text{Se}(\text{VI})$ and selenium oxyanions have heavier partial intercalation than As(V) and Mo(VI)[75]. Generally, an interlayer distance change can be observed once the intercalation occurs[78]. However, high concentrations of soluble carbonate prevent anion exchange and it has been predicted that hydrotalcite is quantitatively less important than ettringite and monosulfate in cement [79]. In hydrated OPC, gypsum and calcite phases are seldom considered as possible sinks for oxyanions in nuclear waste, although they are abundant in HCP. Calcite is highly crystalline and has a much smaller reactive surface area and a high symmetry structure. In the case of co-precipitation, Se(IV) substituting for

carbonate sites in the calcite structure is favored[80], leading to the formation of a $\text{Ca}(\text{SeO}_3)_x(\text{CO}_3)_{(1-x)}$ solid solution[81]. Conversely, Se(VI) does not incorporate, but catalyzes the step propagation rate of calcite without changing the growth pattern [82]. The co-precipitation can be viewed as a sequence of adsorption and entrapment events [81]. Oxyanions, like AsO_3^{3-} and SeO_3^{2-} , possessing a lone electron pair and a carbonate-like pyramidal trigonal (coordination number is three) shape, are more favored to be sorbed by calcite, than other oxyanions, such as SeO_4^{2-} and MoO_4^{2-} [71]. Conversely, SO_4^{2-} tetrahedron sites in gypsum prefer tetrahedral SeO_4^{2-} substitution, forming a range of $\text{Ca}(\text{SO}_4, \text{SeO}_4) \cdot 2\text{H}_2\text{O}$ solid solutions [83]. However, solid solution formation with gypsum will be limited for molybdate and antimonite[71].

1.3.2.5. On iron sulfides existing in cement, clays, and granites

The high pH pore solution conditions and its better resistance to sulfate attack[84] make CEM-V/A type cement preferred for the construction of nuclear waste repositories in France. It consists of 50% Portland cement, 25% blast furnace slag (which may contain 2-4 % sulfide of Cd, Cu, Fe and Fe^0), and 25 % fly ash (rich in silica and containing a small amount of Fe oxides).

Metal sulfides are widely present not only in CEM-V/A cement, but also in natural barriers of claystones and granitic rocks[85-87], as potential scavengers for RNs in nuclear waste repositories. So far, several hundred sulfide minerals have been known, and the five most abundant ones are pyrite (FeS_2), pyrrhotite (Fe_{1-x}S , $x \sim 0-0.125$), galena (PbS), sphalerite ($(\text{Zn}, \text{Fe})\text{S}$) and chalcopyrite (CuFeS_2), with iron sulfides (pyrite and pyrrhotite) dominant[88]. Besides, mackinawite (tetragonal FeS) and greigite (Fe_3S_4)[89] are also two important nanocrystalline iron sulfides, which play critical roles in serving as precursors to the formation of most stable iron sulfide phases (e.g., pyrite and pyrrhotite) [90]. Regarding metal sulfides, reductive precipitation on minerals surfaces is the main pathway to remove redox-sensitive RN anions, which has been the subject of numerous studies. For instance, Sb(V) can be completely reduced to Sb(III) at the mackinawite surface across a wide pH range and within 1 h. An amorphous or nanoparticulate SbS_3 -like solid is formed [91]. In coals, antimony may substitute for iron or sulfur in discrete pyrite grains, which occur as tiny dispersed sulfide particles in organic matter [92]. Investigation of U(VI) sorption on pyrite and galena have been reported numerously[93-99], and reduced hyperstoichiometric uranium species UO_{2+x} (e.g., U_3O_8 and U_4O_9) are often reported as end products, although uraninite

(UO_2) is the thermodynamically most stable form of uranium in pyrite-containing systems. Nevertheless, a recent study demonstrated that the reduction of aqueous U(VI) by pyrite was inhibited in most pH conditions, and partial reduction was only observed at pH 6.21-8.63 and 4.52-4.83 for synthetic and natural pyrite, respectively[98]. In contrast, aqueous U(VI) can be removed by mackinawite under anaerobic conditions to a large extent and almost fully reduced into UO_2 consistently[100-104]. In comparison to naturally occurring pyrite, the amorphous and very fine mackinawite and greigite particles possess large specific surface area and higher mineral solubility, capable of releasing more aqueous ferrous and sulfide ions. Thus, mackinawite and greigite possess stronger reactivity towards U(VI). Note that residual aqueous U(VI) after reaction can oxidize U(IV), resulting in intermediate U valences. Therefore, the critical effects of reaction kinetics on uranium end products is highlighted. Analogy is observed in the case of selenium oxyanions. Numerous studies have revealed the reduction of Se(IV)/Se(VI) by pyrite[105-109] and Se(0) seems to be the prevalent or only product in most of the laboratory experiments performed. Only few studies illustrate the formation of iron selenides (FeSe and Fe_7Se_8) on nano-particulate mackinawite[110, 111]. Furthermore, the thermodynamically predicted ferroselite, FeSe_2 , is only observed recently in the case of nanosized mackinawite and greigite [112-114]. Nano-sized FeS is also a potentially effective, transient scavenging agent for Mo in sulfidic environments, although FeS_2 and organic matter appear to be the ultimate hosts. Besides, the sorbed Mo can promote the recrystallization of amorphous FeS to more ordered products such as greigite[115]. In euxinic water, molybdate concentrations and FeS ion activity products are found to be linked and the existence of a new Fe-Mo-S phase, $\text{FeMo}_{0.6}\text{S}_{2.8}$, is postulated [116]. Sulfide anions will be released from the dissolution of sulfide minerals, especially of amorphous sulfide phases (e.g., mackinawite and greigite). Under anoxic and sulfidic conditions, the presence of dissolved sulfide reacts with molybdate (MoO_4^{2-}) to form thiomolybdate anions ($\text{MoO}_{4-x}\text{S}_x^{2-}$, $x = 1-4$)[117]. MoO_4^{2-} and MoS_4^{2-} adsorption onto iron sulfides is studied, suggesting that MoS_4^{2-} is generally more reactive than MoO_4^{2-} [115, 118, 119]. Furthermore, stable Mo-Fe-S cuboidal clusters can be formed between sorbed MoS_4^{2-} and pyrite [118-122]. However, a recent study concludes that pyrite is not the primary host in most euxinic shales, although pyrite should be viewed as a nontrivial sink for Mo. They speculate that Mo sequestered initially within pyrite can be released again during the strong recrystallization overprints [123].

It can be concluded that the reactivity of Fe sulfides is vital to the reaction processes and the end products. However, the influencing factors on pyrite reactivity remain unknown to date. It is generally accepted that the kinetics of reactions occurring at mineral-water interface are largely dependent on the surface reactivity [94, 124, 125], which is essentially controlled by reactive sites (e.g., Fe(II) and S(-II) sites) exposed on the surface, or solubility. More surface S(-II) and Fe(II) sites can be generated via the conchoidal-like {001} cleavage of pyrite. With each ruptured S-S bond, two mononuclear species (formally S(-I)) are produced, and this monomer is reduced to S(-II) during relaxation through oxidation of surface Fe(II) ions to Fe(III) [126]. Theoretically, both Fe^{3+} and S^{2-} can enhance pyrite reactivity. However, this hypothesis needs experimental data to be supported. Natural pyrite typically contains a host of minor and trace elements, such as As (9.6 wt.%), Co (2.2 wt.%), Sb (0.7 wt.%), Au (0.3 wt.%), and Ni (0.2 wt.%), often located within the lattice [127]. The variability in the chemical composition can result in variation of physico-chemical properties, e.g., the minor elements held in pyrite structure can enhance its reactivity. A previous study compared the oxidation kinetics between varying impurities-doped and undoped pyrites, with a conclusion that pyrite containing no impurities is least reactive and the one with As-dopant is more reactive than that with either Ni or Co [128]. Besides, pyrrhotite also shows stronger reactivity than pyrite due to its lattice-defect structure ($Fe_{1-x}S$) and thus its high sulfide solubility [129]. Regarding mackinawite and greigite, their small sizes decide the high solubility and reactivity. Nevertheless, sufficient experimental data is needed to support further conclusions.

1.3.3. On clays

In host rocks of nuclear waste repositories (e.g., clay and granitic minerals), apart from the metal sulfides discussed above, other effective phases, e.g., smectite in clays and annite in granites, have to be considered as potential sinks for RNs retention.

Clays are hydrous aluminosilicates, fine grained, such as smectite, illite, kaolinite, vermiculite, and chlorite. Numerous studies have been focused on aquatic environment remediation by smectite group clays, e.g., bentonite and montmorillonite, due to their considerably larger cation exchange capacity and specific surface area compared to other clay minerals [130]. Smectites have been considered for decades as effective adsorbents of trace heavy metal ions [131]. Their negatively charged surface and cationic interlayer define their strong affinity for cationic contaminants [132-136]. However, pristine smectites are relatively less attractive to anionic RNs, e.g., I⁻ [132, 137, 138], Cl⁻ [139], TcO_4^- [140, 141], and ReO_4^-

[142, 143]. In comparison, Se(IV) possesses a certain affinity towards smectites, resulting in larger distribution coefficient (K_d) values of 10^{-3} to $10^{-2} \text{ m}^3 \text{ kg}^{-1}$ [144, 145]. The Se(IV) sorption mechanisms on montmorillonite are still under debate on the formation of outer-sphere[146] and inner-sphere complexes[147]. Anions sorption on smectites decrease generally with increasing pH [140, 144, 145]. Besides, recent literature reports have described inorganically-modified (e.g., Fe- and Al- modified[148]) and organically-modified smectites (e.g., with cetylpyridinium[149], aluminum polyoxy and hexadecylpyridinium cations[150], and DDTMA and DDDDMA[151]) as excellent absorbents for various RN anions. The diffusion behavior of anionic RNs in smectites is widely investigated[142, 152-154], concluding that anions diffuse mainly through the free pore space and strong anion exclusion effects (Donnan exclusion) are exhibited in compacted smectites[155].

1.3.4. On granitic minerals

Granitic rocks are accepted as the preferred host rocks in potential repositories by China[156], Sweden[157], and Finland[158], benefiting from their satisfying properties of abundance, toughness, and low porosity. Sorption and diffusion of anionic RNs, e.g., $\text{SeO}_3^{2-}/\text{SeO}_4^{2-}$, I⁻, and TcO_4^{2-} , in intact and crushed granites are investigated, based on the effects of pH, oxygen conditions, ionic strength, and temperature [159-168]. K_d values and apparent diffusion (D_a) coefficients are obtained. As expected, pH is always an important factor for RNs sorption, as it changes RNs species and surface charge of granites. Results show that selenite sorption is closely controlled by oxygen concentrations [159, 165] and the sorption is largely enhanced under aerobic conditions. It is attributed to the sorption on Fe(III)-oxyhydroxides, formed from oxidation of Fe(II)-containing compounds, i.e., annite [159], although the oxides and oxyhydroxides of Al, Fe, Ca, and Mg in granites also show affinity for selenite at different pHs[169-171]. Besides, U(VI) sorption on granite is also studied, indicating that pH values and surface types mainly control the sorption capacity[172, 173]. Apart from the entire granite, retention ability of each mineral component of the granite is also an interesting area of research.

1.4. Objectives of the thesis

In my PhD thesis, I aim to determine the retention capacity and sorption affinity of each selected potential barriers in cementitious system towards various RNs, such as U(VI), Se(IV), Mo(VI), and Sb(V). Stable isotopes were always used as analogues of RNs. Through employing a combination of wet chemistry methods, thermodynamic modelling, and

synchrotron-based X-ray spectroscopic analysis, I attempt to better understand the determining factors (e.g., redox potentials in redox reactions) and the related retention mechanisms in the sorption processes. Specifically, the objectives are below:

i) To determine the different MoO_4^{2-} -sorption sites on AFm with increasing surface coverage: types of layer edge sites, interlayer exchange sites, and co-precipitation sites. This work allowed producing for the first time a model for the local geometry of different Mo active adsorption sites on AFm phases. **(Chapter 2)**

ii) To investigate the anion exchange process of Se(IV) and Mo(VI) oxyanions in AFm phases. By comparing with other anions, i.e., Cl^- , SO_4^{2-} , and MoO_4^{2-} , intercalated in AFm phases, I attempted to establish a relationship between inter-layer anions' structure and their basal spacing, further indicating the stability of these phases. This integrated approach allows a detailed account of anion exchange processes at work in CaAl LDHs based on kinetics and thermodynamics. **(Chapter 3)**

iii) To determine “in-situ” experimental Eh imposed by the steel (modeled here by NZVI) and its corrosion products couples, e.g., magnetite/hematite and magnetite/goethite, using redox-sensitive RNs, i.e., U, Se, Mo, and Sb, as the redox probes; To demonstrate for the first time a credible approach for an *ab initio* Eh determination in cement-based medium. **(Chapter 4)**

iv) To investigate sorption behavior of RNs, i.e., U, Se, Mo, and Sb, on pristine CEM-V/A hydrated cement paste (HCP), types of hydrated Fe-reinforced cement, and separated cement hydration products in cement pore water (pH ~13.5). We aim to determine potential active sorption sites for RNs and map the concentration distribution of each RN during its diffusion in Fe-reinforced CEM-V/A HCP. **(Chapter 5)**

v) To investigate the effects of minor element impurities, i.e., Pb-impurity, As-impurity, and Si-impurity, and the generated S(-II) due to pyrite crystal fracture on the reactivity of pyrite toward aqueous U(VI). **(Chapter 6)**

Chapter 2. Evidence of multiple sorption modes in AFm phases using Mo as structural probe

Abstract

Layered double hydroxides (LDHs) have been considered as effective phases for the remediation of aquatic environments, to remove anionic contaminants mainly through anion exchange mechanisms. Here, a combination of batch isotherm experiments and X-ray techniques was used to examine molybdate (MoO_4^{2-}) sorption mechanisms on CaAl LDHs with increasing loadings of molybdate. Advanced modelling of aqueous data shows that the sorption isotherm can be interpreted by three retention mechanisms, including two types of edge sites complexes, interlayer anion exchange, and CaMoO_4 precipitation. Meanwhile, Mo geometry evolves from tetrahedral to octahedral on the edge, and back to tetrahedral coordination at higher Mo loadings, indicated by Mo K-edge X-ray absorption spectra. Moreover, an anion exchange process on both CaAl LDHs was followed by in-situ time-resolved synchrotron-based X-ray diffraction, remarkably agreeing with the sorption isotherm. This detailed molecular view shows that different uptake mechanisms—edge sorption, interfacial dissolution-reprecipitation—are at play and control anion uptake under environmentally-relevant conditions, which is contrast to the classical view of anion exchange as the primary retention mechanism. This work puts all these mechanisms in perspective, offering a new insight into the complex interplay of anion uptake mechanisms by LDH phases, by using changes in Mo geometry as powerful molecular-scale probe.

2.1. Introduction

Layered double hydroxides (LDHs) are lamellar mixed hydroxides with a generic chemical formula $[M^{II}_{1-x}M^{III}_x(OH)_2]^{x+}(A^{n-})_{x/n} \cdot mH_2O$, where species under brackets form the hydroxide layer, those at the right form the interlayer, M^{II} and M^{III} represent divalent and trivalent cations, respectively, in the positively charged layers, and A^{n-} denotes interlayer anions[174]. Owing to LDH anion exchange capacity, abundant studies have investigated their uptake ability towards anionic contaminants (e.g., As, Se, Cr, B, halide species, etc.) from polluted water[175-178] without explicitly pointing out the field of LDH stability. Alumina ferric oxide monosulfate (so-called AFm) phases ($[Ca_4Al_2(OH)_{12}]^{2+} \cdot SO_4^{2-} \cdot mH_2O$), are minor but highly reactive phases present in hydrated cement, and belong to the CaAl LDHs family[38]. AFm-Cl₂ ($[Ca_4Al_2(OH)_{12}]^{2+} \cdot (Cl^-)_2 \cdot mH_2O$), of which Friedel's salt is one of the polytypes, is also an important cement hydration product [38] when concrete is subjected to Cl⁻ corrosion (e.g., when concrete is in contact with mixing water, sea water, or deicing salt, or when Cl-bearing aggregate and admixtures are used to produce it)[50, 51]. It is considered as an effective adsorbent for oxyanions due to their easy exchange for inter-layer Cl⁻, if compared to interlayer divalent oxyanions such as SO₄²⁻. AFm phases are therefore potential scavengers of toxic soluble anions[39, 58, 59, 61] via both surface adsorption and anion exchange processes.

Conversely, oxyanions present in LDHs which contain Ca as M^{II} and Al as M^{III} (CaAl LDHs) can be a threat to the environment and public health. Coal fly ash (CFA) and bottom ash are two of the main coal combustion products (CCPs), which are generated over 750 million tonnes per year on a global basis [57]. In contact with water, LDH types of minerals (e.g., CaAl LDHs[52, 53] and MgAl LDHs[179]) are widely detected or predicted to occur thermodynamically in bottom ash and Class C CFA[54-56]. Although extensively used as raw material or additive in the cement industry and in road embankments[180-182], coal ash is often considered as an environmental pollutant on a global scale due to its load of various potentially toxic trace elements[183], which include some oxyanionic species such as As, B, Cr, Mo, Sb, Se, V and W. According to recent investigations[184], many coal ash disposal sites are located close to residential areas, with a direct threat to local people. However, very little is known about the chemical stability, mobility and bioavailability of these oxyanions, which depend on the mechanism by which they are retained by the LDHs.

Molybdenum (Mo), considered a double-edged sword trace element for human's health, is present at high toxic concentrations in CFA particles and their leachates[55, 57], as well as in irrigation drainage[185] and industrial discharge waters[186]. Furthermore, ^{99}Mo is widely used as a precursor of the radiopharmaceutical $^{99\text{m}}\text{Tc}$ [187] and ^{93}Mo ($t_{1/2} = 4,000$ years) is an activation product of the spent nuclear fuel[188]. These radionuclides should be disposed in nuclear waste repositories, in which cementitious based materials are abundant[189]. Mo(VI) oxyanions (MoO_4^{2-}) are very mobile at the near-neutral to alkaline pH values, with their speciation dominated by tetrahedral molybdate. In highly acidic solutions, the speciation is dominated by distorted octahedral molybdate present in clusters (e.g., $[\text{Mo}_7\text{O}_{24}]^{6-}$, $[\text{Mo}_8\text{O}_{26}]^{4-}$, and $[\text{Mo}_{12}\text{O}_{37}]^{2-}$)[190]. Cementitious phases are expected to act as effective barriers retarding the mobility of anionic Mo species, and thus preventing their release in the environment.

By analogy with clay minerals, LDH should have different sorption sites (high and low energy edge sites, interlayer exchange sites – see [191]) whose affinity for trace elements should depend on pH and ionic strength. This study aimed at validating this analogy by using a combination of chemical and physical methods, including sorption experiments, laboratory and synchrotron X-ray diffraction, and Mo K-edge X-ray absorption spectroscopy (XAS). These methods allowed producing for the first time a model for the local geometry of different Mo active adsorption sites on CaAl LDH.

2.2. Materials and methods

2.2.1. Materials and Chemicals.

Degassed Milli-Q water ($18.2 \text{ M}\Omega\cdot\text{cm}$) was used for all solutions and all the chemicals, including $\text{Na}_2\text{MoO}_4\cdot 2\text{H}_2\text{O}$ (purity >99%), were purchased from Sigma Aldrich and were analytical grade. All experiments were carried in a N_2 -filled glove box ($\text{O}_2 < 2$ ppm, using NaOH as the CO_2 trap) to prevent possible CO_2 contamination.

Three types of CaAl LDHs, including monosulfoaluminate (AFm- SO_4), Friedel's salt (AFm- Cl_2), and monocarboaluminate (AFm- CO_3), were synthesized. AFm- SO_4 was synthesized by suspending a 0.7:1 molar mixture of $\text{CaSO}_4\cdot 2\text{H}_2\text{O}$ and tricalciumaluminate (C_3A), which was obtained by heating the stoichiometric mixture of CaCO_3 and Al_2O_3 for 72 h at 1300°C [61], at a liquid-to-solid (L/S in kg/kg) ratio of 10 and was subsequently aged at room temperature for 42 days with constant magnetic stirring. After aging, the slurry was vacuum filtered through a Millipore[®] 0.22- μm membrane filter and dried in the glove box. A slight deficit (30%) of sulfate with respect to the AFm- SO_4 stoichiometry was kept in order to avoid small

amounts of ettringite, which were present in previous work[36]. As a result, 22 at% katoite [$\text{Ca}_3\text{Al}_2\text{O}_6 \cdot 6\text{H}_2\text{O}$] was detected by XRD (Figure S1). AFm- Cl_2 and AFm- CO_3 were prepared by mixing stoichiometric amounts of C_3A with $\text{CaCl}_2 \cdot 6\text{H}_2\text{O}$ or CaCO_3 , respectively, at the same L/S ratio.

2.2.2. Adsorption Experiments.

Kinetic experiments were performed in order to determine the equilibrium time of CaAl LDHs' dissolution and molybdate sorption. After 6 h and 12 h, the concentration of dissolved ions from AFm- SO_4 and AFm- Cl_2 became maximum and stable, respectively. Molybdate sorption finished within a few hours. Based on these results, an equilibrium time of 48 h after the dissolution equilibrium was used for sorption experiments.

Batch experiments were performed at room temperature in the glove box as a function of initial molybdate concentration. This ranged from 0.001 to 20 mM at an L/S ratio of 500 at pH 12.4, which was reached by adding tiny 2 M NaOH solution and equal to the pH value of the CaAl LDHs synthesis suspension. Thus the molar ratio of added MoO_4^{2-} to inter-layer $\text{SO}_4^{2-}/(\text{Cl}^-)_2$ was between 0.0002 and 4. The low-end of molybdate concentrations (Reactor CIC and SC) was chosen to keep a molar Mo concentration comparable to the surface site density and also to avoid the formation of Ca-bearing precipitates, according to thermodynamic calculations. Besides, high MoO_4^{2-} concentrations were also chosen to be similar to the stoichiometric amounts of inter-layer anions (Reactor CIF and SF), to provide enough MoO_4^{2-} for anion exchange. Besides, even higher loadings were introduced to supersaturate the suspension by $\text{CaMoO}_4(\text{s})$. All suspensions were equilibrated on an end-over-end shaker. At each sampled time, three aliquots of 4 mL of suspension each were taken from each reactor at different times and filtered through Chromafil[®] 0.22- μm syringe filters. The first sample was taken after dissolution equilibrium to measure the initial Ca, Al, S, and Cl concentrations. The second sample was collected immediately once molybdate was added. The last one was taken after the slurry reached equilibrium, following kinetic experiments. The solution pH was measured with a combined glass pH electrode (Metrohm 6.0233.100) connected to an Orion (525A) pH meter, that was previously calibrated using four pH reference solutions. Total Ca, Al, S, and Mo concentrations in the filtrate were analysed by inductively coupled plasma optical emission spectrometry (ICP-OES) with a Varian 720-ES apparatus and the concentration of released Cl^- was determined by ion chromatography (IC, Metrohm 883).

Six solid samples for each CaAl LDH were selected to be studied by synchrotron based X-ray spectroscopic methods, which were denoted by *Cl_i* (*Cl* represents AFm-Cl₂) and *Si* (*S* represents AFm-SO₄), with *i* = A (0.001 mM), B (0.005 mM), C (0.02 mM), D (0.25 mM), E (0.5 mM), and F (5 mM), respectively.

2.2.3. Aqueous Data Modelling.

The PHREEQC code[192] and the latest ThermoChimie database[193] was used to model all the sorption stages of MoO₄²⁻ on CaAl LDHs, and to calculate the SI value of each possible formed mineral phase. Regarding the sorption sites on surfaces, parameters for MoO₄²⁻ surface complexation were fitted using a non-electrostatic model because of a lack of experimental constraints that would be necessary to build a more complex surface complexation model. Note that, the value of the specific surface area has no influence on the calculation results in the framework of a non-electrostatic model. As MoO₄²⁻ loading increasing, the uptake amount was well modelled by the precipitation of a new LDH phase (AFm-MoO₄) and of CaMoO₄ phase further.

2.2.4. In-situ X-ray Diffraction.

In situ X-ray Diffraction (XRD) experiments were performed by circulating a mineral suspension through a capillary cell, as a function of different [Mo]_{initial}. A multifunctional reactor was used to control the pH, oxygen concentration, stirring and pumping speed. First, the CaAl LDHs were equilibrated with water at pH 12.4 under constant stirring, and the circulation through the capillary cell was started. The slurry went through the connected kapton capillary, which was sealed with PEEK nuts and ferrule fittings (IDEX Health & Science). Then, the concentration of molybdate was increased in the reactor step by step to repeat the six selected concentrations used in batch experiments, until the ratio of Mo to Cl₂/SO₄ was over 1:1. For each step, the measurement lasted from one to two hours, to assure equilibrium was reached.

The in-situ experiments were performed at the CRISTAL beam line (SOLEIL synchrotron). Diffraction patterns were recorded on a MAR345 image plate detector with an exposure time of 5 s at the wavelength of 0.978 Å (~12.8 keV). The wavelength and detector-to-sample distances were calibrated using a NIST LaB₆ standard. With the addition detector's read-out time, the time resolution of data acquisition was 120 s. After converted into one-dimensional XRD patterns using the program Fit2D, background was subtracted.

2.2.5. Solid Phase Characterization.

The synthesized CaAl LDHs were identified with powder X-ray diffraction. The samples were introduced in a humidity chamber CHC plus+ from Anton Paar to control the hydration state at a RH of 5% (approximately equal to the relative humidity in the glove box) and room temperature. They were ground using an agate mortar and dispersed in ethanol. Oriented mounts were prepared by drying the resulting suspension onto glass slides in the glove box. XRD patterns were recorded on a Bruker D8 powder diffractometer equipped with a SolX Si(Li) solid state detector from Baltic Scientific Instruments using Cu K α radiation at 1.5406 Å.

The nitrolysis method was used to quantify the elemental composition of the fresh CaAl LDHs. 10 mg of solid phase were digested in 2% HNO₃ in triplicates and the ratios between Ca, Al, and Cl/S were estimated by measuring the elemental concentration using ICP-OES and IC. The katoite impurity content and the amounts of each of the inter-layer anions were deduced from the Ca/Al stoichiometry.

Morphological images of the freshly synthesized CaAl LDHs were collected using a scanning electron microscope (SEM, Hitachi S-4800). The specific surface area was measured by the Brunauer–Emmett–Teller (BET) N₂-adsorption method. TEM was performed using a Philips CM20 operated at 200 kV and having a line resolution of 1.4 Å. Prior to observations, the samples were crushed, dispersed using an antistatic gun, and then embedded in resin. After the resin was polymerized, it was cut in slices having a thickness of 80 nm which were deposited on copper grids.

TGA/DTG were performed with a Mettler Toledo TGA/DSC 2 apparatus to determine the structural water content. Nitrogen was used as the reactive gas at a rate of 50 mL min⁻¹. The weight loss was measured from 60 to 1000 °C with a heating rate of 10 °C min⁻¹, after preheating at 60 °C for 1 h to remove physically sorbed water.

Reacted solid phases from the six selected low-loading reactors were analysed by PDF methods with synchrotron based XRD to determine the phase structure after molybdate sorption. Diffraction experiments were performed using the 2circle diffractometer of CRISTAL beamline at SOLEIL the French Synchrotron Facility. Two setups were used during these experiments: i) For PDF measurements, a high energy beam (wavelength of 0.257Å) was selected and patterns recorded on a MAR345 Image plate detector with exposure time of 20 min. One-dimensional diagrams were obtained by integration of the images using

fit2D software [194]. PDF were generated using the PDFgetX3 code [195]; ii) For the other measurements, a step by step rotation of a two dimensional hybrid pixel detector (XPAD) was employed to obtain a better angular resolution and to cover a large Q range. ImageReducer, a local program, was used to perform azimuthal integration and to regroup data from multiple images into a one-dimensional diagram. A wavelength of 0.436 Å was selected to collect these data. For each configuration, beam energy and detectors orientations were calibrated using a LaB6 (NIST- SRM660) standard powder sealed in an Ø2mm capillary.

Molybdenum K-edge X-ray absorption spectroscopy (XAS) measurements were conducted at the Core Level Absorption & Emission Spectroscopy (CLÆSS, BL22) beam line with a source of multipole wiggler at the Spanish synchrotron ALBA-CELLS, Barcelona, Spain, and at the SpLine Spanish CRG Beamline (BM25A) at the ESRF, Grenoble, France. The double crystal monochromator (DCM) with a pair of Si(311) crystals was used and the energy was always calibrated with a Mo(0) foil in parallel with measurement. The BM25A beamline are equipped with a -70 °C ethanol cooled double Si(111) crystal, which gives an energy resolution of $\Delta E/E = 1.5 \times 10^{-4}$. All samples were sealed using Kapton tape mounted on a sample holder, and measured in fluorescence mode, except for the references and samples with high Mo concentration (E and F), which were prepared as pellets by diluting the solids in boron nitride and measured in transmission mode. Samples were always protected under N₂ atmosphere before being transferred into the vacuum experimental chamber, in which the temperature was lowered to 77 K within a liquid N₂ cryostat to minimize the effects of thermal disorder due to atomic vibrations, An Amptek Cadmium Telluride (CdTe) fluorescence detector (at the CLÆSS) and Sirius liquid nitrogen cooled Si(Li) 13-multi-element solid state X-Ray detector from e2v (at the BM25A) were used for data collection. The Demeter software package was used for the data integration and reduction of XANES (Athena), as well as the data fitting of the EXAFS (Artemis)[196]. Radial distribution functions were obtained by FT of k^3 -weighted EXAFS oscillations (k -range: 4.0-12.5 Å⁻¹) using a Kaiser-Bessel window. FEFF8.4[197] was used to calculate the theoretical backscattering paths to perform the fit in back-transformed reciprocal space (k), and it was also employed to obtain the calculated Mo K-edge XANES spectra. Several models of surface complexes were created using Materials Studio 4.0 (Accelrys Inc.) to generate scattering paths for the EXAFS fitting of the Mo-reacted CaAl LDHs.

2.3. Results and discussion

2.3.1. Wet Chemistry Experiments.

Morphology and elemental composition of the synthesized CaAl LDHs were characterized prior to wet chemistry experiments (Text S2.1). Sorption isotherms (on AFm-Cl₂ and AFm-SO₄ phases, where sorbed Mo has been measured as a function of [MoO₄²⁻]_{aq} at equilibrium) are shown in Figure 2.1.

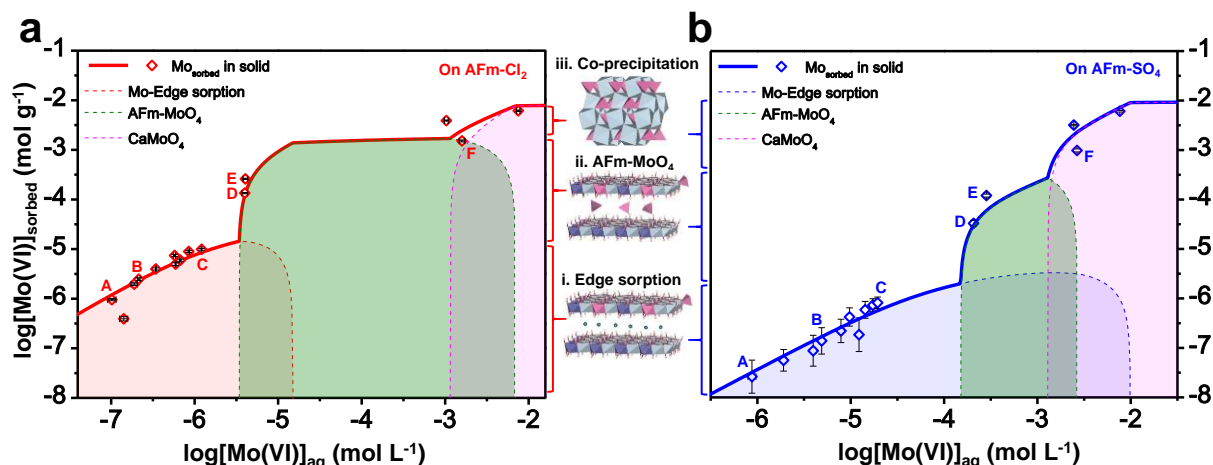


Figure 2.1. Sorption isotherm of molybdate after 48 h equilibration. (a) On AFm-Cl₂. From stage of edge sorption to that of Ca-precipitation, the capacities are 8×10^{-5} , 2×10^{-3} , and 8×10^{-3} mol g⁻¹, respectively. (b) On AFm-SO₄. The corresponding three types of sorption capacities are 8×10^{-6} , 2×10^{-3} , and 8×10^{-3} mol g⁻¹, respectively. Bold solid curves are the fitting results regarding the amount of sorbed Mo in solid. Each area under dash curve represents the dominated solid sorbent of each sorption stage. Selected adsorption products for X-ray spectroscopic techniques on each AFm phase are denoted by A to F (see Method section), as the increasing molybdate loading. Schematic representation of three retention mechanisms is shown in the middle panel.

Related aqueous data is shown in Table S2.1 to 2.4. A thermodynamic model, including surface adsorption, equilibrium with an AFm-MoO₄ phase, and precipitation of CaMoO₄, was implemented in PHREEQC code, adequately reproducing the aqueous chemistry data. Combining PHREEQC code geochemical modelling with the physical observation of solid phases, three different regimes are proposed: (i) At low Mo loading, layer *edge sorption* is the predominant retention mechanism, as confirmed by spectroscopy and scattering data. From geochemical modelling, the surface site density (mol sites/gram solid) obtained for AFm-Cl₂ (8.0×10^{-5}) was approximately tenfold over that of AFm-SO₄ (8.0×10^{-6}), in accordance with the roughly ten times difference in lateral surface area (S_l) between the two CaAl LDHs as deduced from SEM observations (Figure S2.2). It is intriguing that surface sorption capacity

is closely related to S_i , i.e., to edge sorption sites on CaAl LDHs[198]. In addition, AFm-Cl₂ ($\log K = 2.80$) has a larger equilibrium constant than AFm-SO₄ ($\log K = 1.05$), based on the equilibrium reactions (Table S2.5). For AFm-Cl₂, more than 95% molybdate was removed within 48 h in this sorption stage. Concomitantly, a proportional amount of inter-layer Cl⁻ was released (Figure S2.3), but with a proportionality constant five times higher than expected from a stoichiometric anion exchange. The presence of molybdate promotes the destabilization of CaAl LDHs and leads to the formation of katoite [Ca₃Al₂(OH)₁₂] solid (Text S2.2), which could explain the excess Cl⁻ release. Besides, aqueous Ca, Al, and Cl/SO₄ concentrations were also adequately described by the model (Figure S2.4), with 1.5 mM Cl⁻ impurity allowance (probably coming from AFm-Cl₂ solid synthesis) and a little adjustment (+0.3 log unit) of AFm-SO₄ solubility compared to the reference $\log K$ value of 73.07 in the databank. In terms of sorption and retardation factor, this mechanism leads to a much larger average R_d value of 9464 L kg⁻¹ obtained for AFm-Cl₂, as compared to that of 32 L kg⁻¹ for AFm-SO₄. Conclusively, in this stage, both types of CaAl LDHs are reactive towards the presence of molybdate, with AFm-Cl₂ having larger sorption capacity and higher affinity for Mo than AFm-SO₄. (ii) At medium loading, the second regime is observed which corresponds to *anion exchange* in the LDH interlayer, leading to the formation of AFm-MoO₄ (denoted by the area under olive-green dash curve in Figure 2.1). A good fit could be only obtained by the formation of AFm-MoO₄ ($\log K = 74.0$, fitted) concomitant to the disappearance of the AFm-Cl₂ phase. This indicates that, unexpectedly, random anion exchange process in the interlayer of CaAl LDHs is unlikely, and that interstratification or the formation of a solid solution[199] of pure AFm-Cl₂ and pure AFm-MoO₄ occurs, as observed in clay systems [200]. Solid speciation modeling shows that AFm-Cl₂ is replaced entirely by AFm-MoO₄ at Mo equilibrium concentration higher than $\sim 10^{-5}$ mol L⁻¹, which is in good agreement with in-situ XRD data where a transition between two phases is observed between CIE and CIF. In contrast, AFm-SO₄ cannot be replaced completely by AFm-MoO₄ as Mo loading increases. A minor AFm-MoO₄ phase is predicted to form, at most, 10% of AFm-SO₄ solid concentration, which is accordance with the presence of the minor diffraction signal (from SD to SF) derived from AFm-MoO₄ phase. Apart from the satisfactory reproduction of Mo uptake, the model also adequately described aqueous Ca, Al, and Cl/SO₄ concentrations (Figure S2.4). (iii) At higher Mo loading, a third regime, corresponding to final decomposition of CaAl LDHs and to the CaMoO₄ precipitation, is indicated by the area under pink dash curve (Figure 2.1). The CaMoO₄ solubility tabulated in the THERMOCHIMIE database was too low to reproduce the data. The solubility had to be increased by +1.6 log unit to reproduce our data. This change in

solubility is in qualitative agreement with the nano/amorphous nature of the phase precursor. Regarding the formation of this new solid phase, the transformation from an unstable precursor to a more stable bulk phase³⁸ may lead to a reversed decrease of $[\text{MoO}_4^{2-}]_{\text{aq}}$ (the one data point after sample F).

2.3.2. In-situ Time Resolved X-ray Diffraction.

In-situ time resolved XRD experiments were carried out to check for possible structural transitions, and for modifications of the interlayer space composition (through a change in the layer-to-layer distance) as the concentration of molybdate is increased.

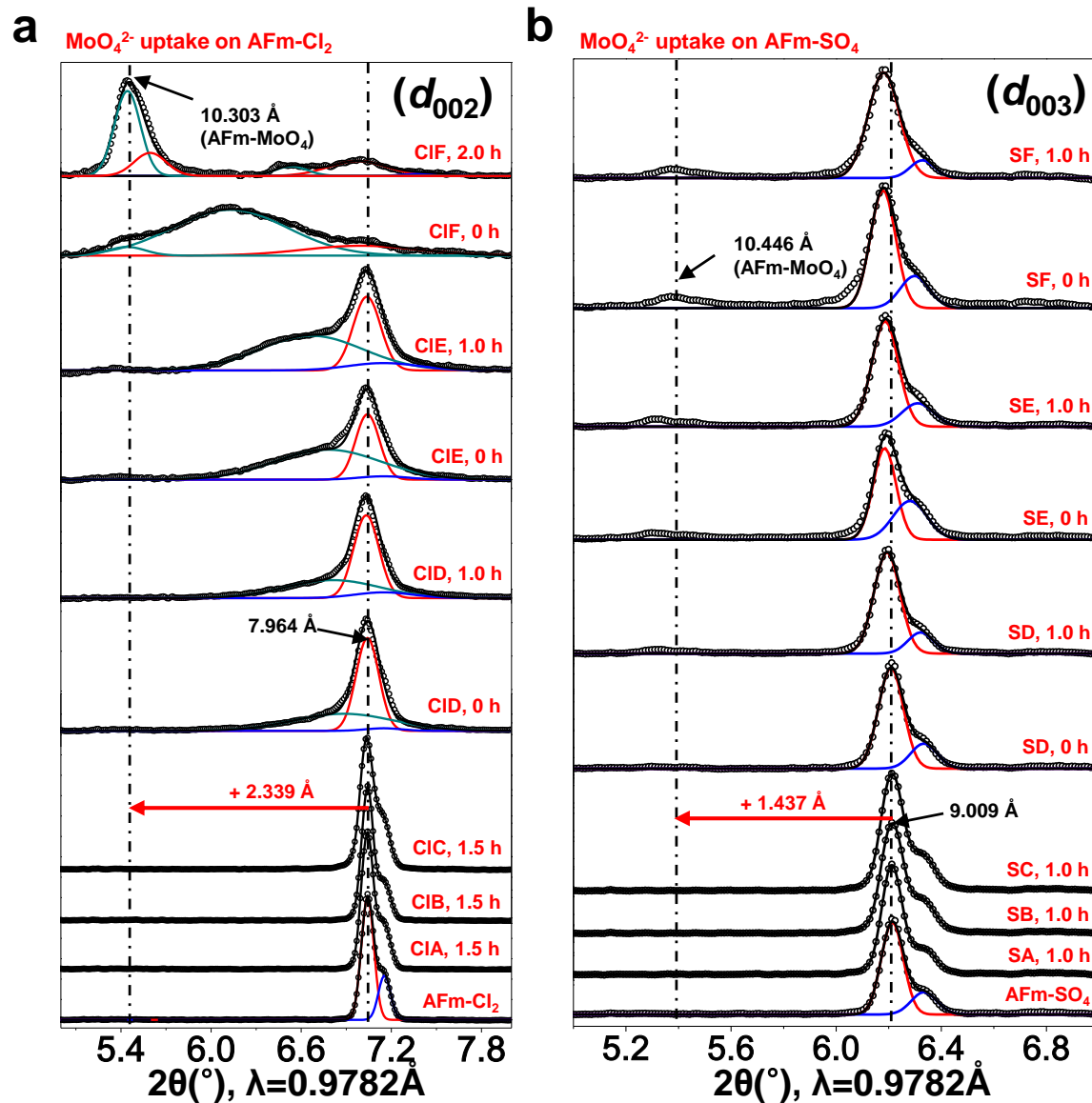


Figure 2.2. In-situ time resolved XRD patterns of inter-layer peak details. (a) XRD patterns collected for molybdate uptake on AFm-Cl_2 . (b) XRD patterns on AFm-SO_4 . The experimental data, plotted with black circles, are fitted with Gaussian function (indicated by curves in color). The black curves represent the total fitted curves. The equilibrium time for

each step is shown following the sample name. The small shoulders of inter-layer peaks at slightly higher 2θ values, displayed in blue colour, may be attributed to different swelling levels of the stacked crystalline layers or to non-stoichiometric intercalated anions (e.g., slightly structural substitution of OH⁻).

Intercalated anions in LDHs can be replaced by aqueous oxyanions, resulting in changes in the layer-to-layer distance, which can be followed through the study of basal reflections. In-situ experiments were performed on CaAl LDHs slurries, leading to an extremely hydrated initial state. Initial inter-layer distances of the fresh CaAl LDHs were larger than those of dry samples, with $d_{\text{interlayer}} = 9.01 \pm 0.02 \text{ \AA}$ for AFm-SO₄ and $d_{\text{interlayer}} = 7.96 \pm 0.01 \text{ \AA}$ for AFm-Cl₂ (Figure S2.5 and Figure S2.6). Mo was added in six steps (repeating Mo loadings in wet chemistry experiments from A to F, with a ratio of inter-layer Cl₂/SO₄ to added Mo ranging from 5000 to 1). At each concentration, the subscripts 0 and t represent the first acquisition once molybdate was added and the final one, after 1-2 h equilibration, respectively. A peak shift toward low angle region was observed in the angular range from 4° to 8° in 2θ ($\lambda = 0.9782 \text{ \AA}$), attributed to a layer-to-layer distance increase. An enlarged view of this diffraction peak is shown in Figure 2.2.

The small shoulders, appearing in inter-layer peaks (corresponding spaces are $\sim 7.84 \text{ \AA}$ and $\sim 8.87 \text{ \AA}$ for AFm-Cl₂ and AFm-SO₄, respectively) of fresh CaAl LDHs, may be attributed to different swelling levels of the stacked crystalline layers, rather than to OH⁻ exchange with intercalated anions (resulting in interlayer spaces between 5.35 \AA and 7.23 \AA [201]). For AFm-Cl₂, above the CIC concentration, the peak started to shift gradually towards low angles, suggesting that the layer-to-layer distance was increased due to MoO₄²⁻ exchange and intercalation. Eventually, an inter-layer distance of 10.3 \AA was observed. No obvious peak shift was observed for AFm-SO₄. Only a tiny peak at 5.37° , corresponding to an interlayer distance of 10.4 \AA , appeared as the SO₄/MoO₄ ratio increased above that of the SC sample. This value, close to the value obtained in the case of AFm-Cl₂, indicates that intercalated SO₄²⁻ can also exchange with MoO₄²⁻, but with a lower exchange capacity. Lastly, when initial Mo to inter-layer Cl₂/SO₄ ratio is beyond 0.004 (i.e., at surface coverage higher than that of sample C), anion exchange starts to occur on both CaAl LDHs, becoming the dominant molybdate retention mechanism. The lack of LDHs swelling at low concentrations confirms that other adsorption and incorporation mechanisms of Mo retention exist in naturally-occurring relevant conditions, reflecting a complex landscape of sorption modes in LDHs.

2.3.3. Local Geometry of Adsorbed Molybdate.

XANES allows discerning between tetrahedral (TC) and octahedral coordinated Mo atoms (OC), mainly through the level of intensity of the pre-peak feature, more intense for TC molybdate[190]. This peak results from dipole allowed electronic transitions from 1s to mixed 4d, 5s and 5p orbitals, and from quadrupolar 1s to 4d transitions. The intensity of this pre-peak is maximum for pure TC (e.g., Na₂MoO₄), a bit lower for distorted OC (p-d mixing allowed with dipole transition, e.g., polymerized molybdate), and has its lowest value in the case of pure OC (centro-symmetric molecule: *p-d* mixing forbidden and only quadrupolar transitions allowed; see calculated spectra in Figure S2.7). Mo K-edge X-ray absorption near edge spectroscopy (XANES) spectra of the reacted samples indicated in Figure 2.1 and of TC and OC standards are shown in Figure 2.3. Molybdate coordination in AFm-Cl₂ samples evolves with increasing surface coverage from TC (sample CIA) to distorted OC (samples CIB and CIC), and back to TC (sample CIF), suggesting a complex evolution of the mechanism of uptake when passing from [MoO₄²⁻]_{initial}/[(Cl)₂]_{intercalated} ratios of 2×10⁻⁴ (CIA) to 1 (CIF). AFm-SO₄ showed a similar behaviour, though samples with lowest Mo concentrations were too diluted to allow recording of XANES spectra. Sample SC showed octahedral Mo coordination, suggesting edge complexation. Samples SD to SF showed features consistent with a tetrahedral coordination.

It is worth noting here that aqueous speciation of molybdate depends strongly on molybdenum concentration and solution pH[190], with octahedral polymeric molybdate species being present at low pH values. However, under the high pH values controlled by CaAl LDHs phases (~12.4), the monomeric tetrahedral species is present in all the concentration range. Thus, the observed octahedral species cannot be explained by aqueous speciation. The change in molybdate coordination from TC to OC is observed prior to the observation of anion exchange, suggesting at least two different types of surface complexes at low loadings.

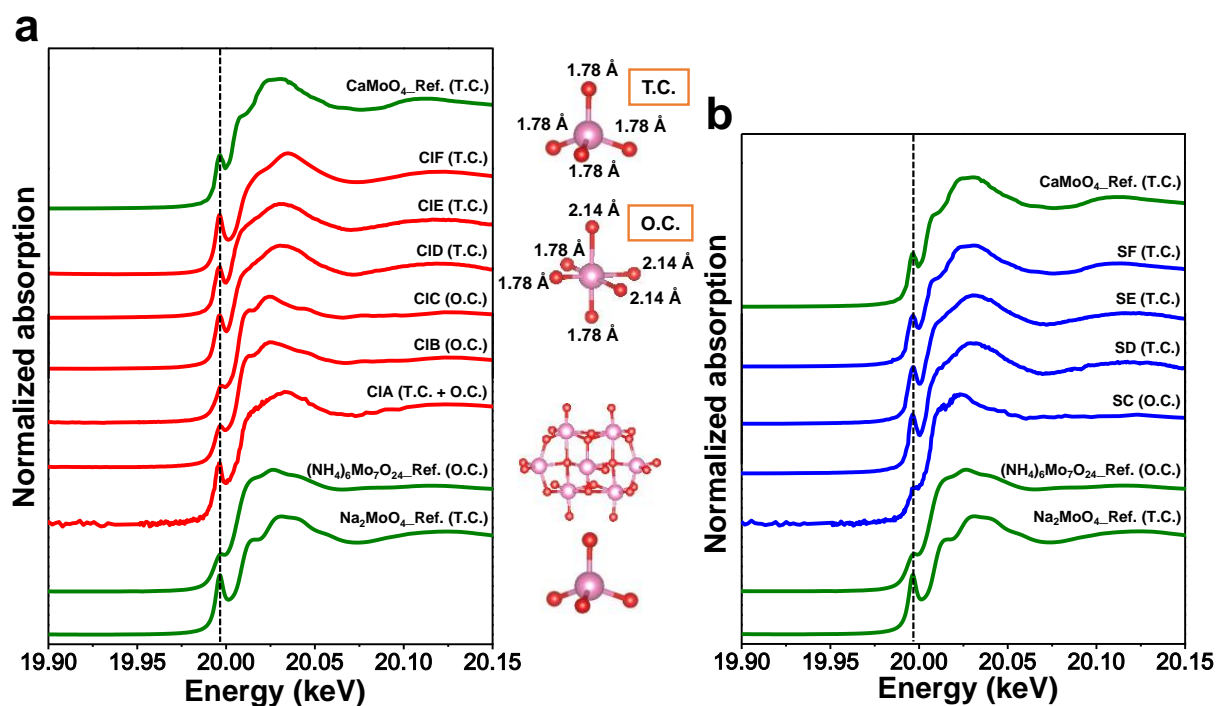


Figure 2.3. Experimental Mo K-edge XANES spectra of selected AFm-Cl₂ (a) and AFm-SO₄ (b) sorption products from batch sorption experiments and reference compounds (bottom). Geometry schematic representation of molybdenum in different coordination is shown in the middle panel.

2.3.4. Mo Distribution in Reacted LDHs Particles.

Mo-reacted LDHs samples CIC and CIF were characterized by transmission electron microscopy (TEM) to better understand the spatial distribution of adsorbed molybdate (Figure 2.4). The selected area electron diffraction (SAED) shows hexagonally arranged spots (inset in Figure 2.4a), indicating that the main phase of reacted AFm particles are still composed of crystalline Ca-Al-O layers. Averaged elemental concentrations obtained from Energy dispersive X-ray (EDX) spectroscopy analyses of the particle edges and of the observed nanoparticle precipitates are shown in Fig 4b. They show that high Mo concentrations were detected in some nanoparticles, which are located near the LDHs' edges. With a lower Ca/Al ratio (~1.33 at.%) than LDHs and much lower Cl content (~0.89 at.%), these newly formed amorphous nanoparticles (confirmed by SAED) have the katoite (Ca₃Al₂(OH)₁₂) stoichiometry, and could be precursors of katoite crystalline phase precipitation, as observed by XRD (Figure S2.8). Both the strong affinity of molybdate for Ca²⁺ and the comparable radius of Mo⁶⁺ to Al³⁺ could provide convenience to structural incorporation onto the layers' edge. The enrichment of molybdate on katoite can be interpreted as a process of AFm-Cl₂ edge de-stabilization, followed by co-precipitation of Mo-bearing katoite. Compared to the

bond length of Ca-O (~ 2.46 Å) and Al-O (~ 1.91 Å) in CaAl LDHs, the Mo-O bond-length (~ 1.78 Å) is shorter, which could potentially be a reason leading to the instability of Mo LDH edge complexation. Thus, most of the adsorbed molybdate and its local environment would dissolve and re-precipitate into Mo-bearing katoite. At higher Mo loading, Figure 2.4c,d show results from sample CIF, where anion exchange dominated the sorption process. Molybdate, accounting for 12.73 at.%, almost totally occupied the interlayer by replacing chloride (Figure S2.4). After reaction, the LDHs particle still conserved its hexagonal shape, indicating the preservation of the LDHs morphology.

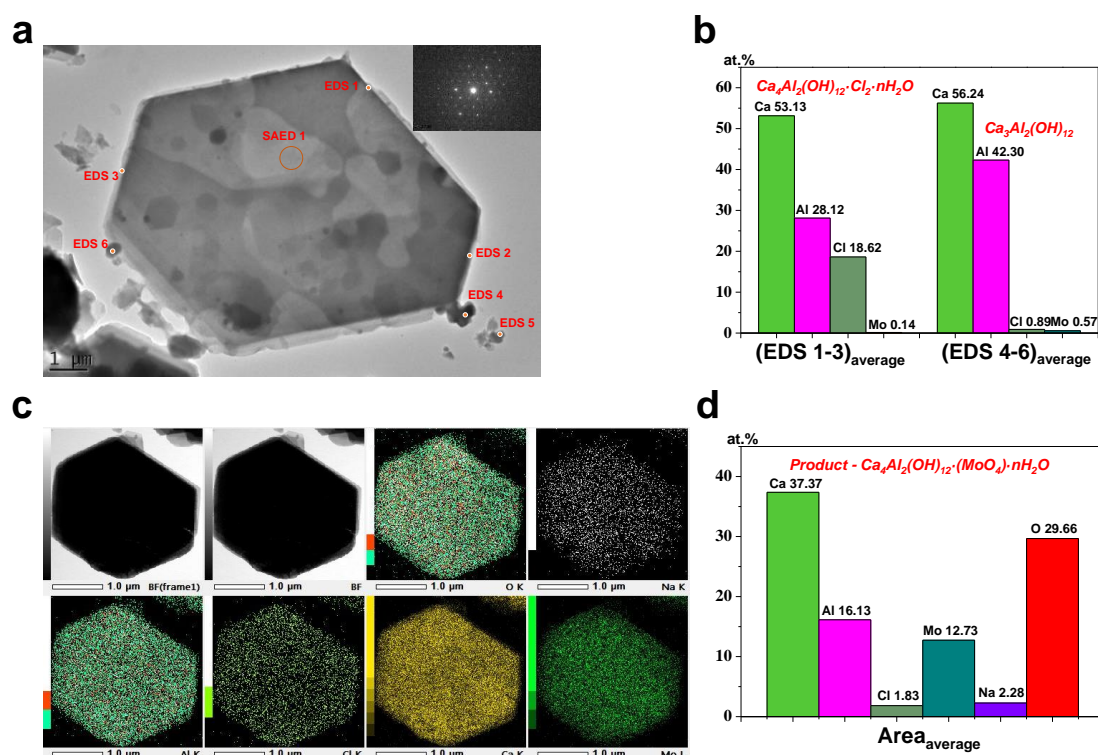


Figure 2.4. Characterization of Mo-reacted LDHs sheets. (a) TEM images of reacted AFm-Cl₂ particles in Sample CIC with six spots of EDS. Scale bar, 1 μm. Inset is the corresponding SAED pattern in agreement with katoite. (b) Elemental compositions obtained from the corresponding EDS spectra in (a). (c) Element mapping images of reacted AFm-Cl₂ particles in Sample CIF. Scale bar, 1 μm. (d) Elemental compositions obtained from the LDH hexagon area in (c).

Our combined wet chemistry, XRD, XANES, and TEM-EDX data depict a situation in which MoO₄²⁻ is retained at a first step forming a surface complex with tetrahedral geometry firstly (sample CIA). At higher concentrations (sample CIB and CIC), both the XANES and EXAFS data are consistent with an inner-sphere surface complex (ISC), in which Mo is in an octahedral coordination, i.e., with a face-sharing ISC. The observation of katoite nanoparticles concomitantly to the edge adsorption process, suggests that the decomposition of CaAl LDHs is promoted upon Mo edge surface complexation. At higher concentrations, the AFm-Cl₂

structure undergoes formation of AFm-MoO₄ and swelling, as identified by XRD and by the dominant tetrahedral coordination of Mo in these samples (CID, CIE, and CIF).

2.3.5. Complexation environment around adsorbed Mo.

EXAFS data representing the local environment of molybdate oxyanions in two references and in AFm-Cl₂ sorption products are shown in Figure 2.5a. The single oscillation frequency present in the spectrum of the Na₂MoO₄ reference is characteristic of a single coordination shell, which is also confirmed by the Fourier transform (FT) of the EXAFS data (Figure 2.5b). Only the characteristic peak corresponding to a Mo-O distance in MoO₄²⁻ was observed, with a characteristic distance of $d_{Mo-O} = 1.78 \text{ \AA}$. In contrast, the polymerization of Mo oxyanions in (NH₄)₆Mo₇O₂₄·4H₂O and their octahedral geometry resulted in various Mo-O bond lengths (Table 2.1) and a second shell, attributed to neighbouring Mo atoms at the distances of $d_{Mo-Mo} = 3.23$ and 3.40 \AA . The existence of polymerized Mo can be therefore excluded in the samples.

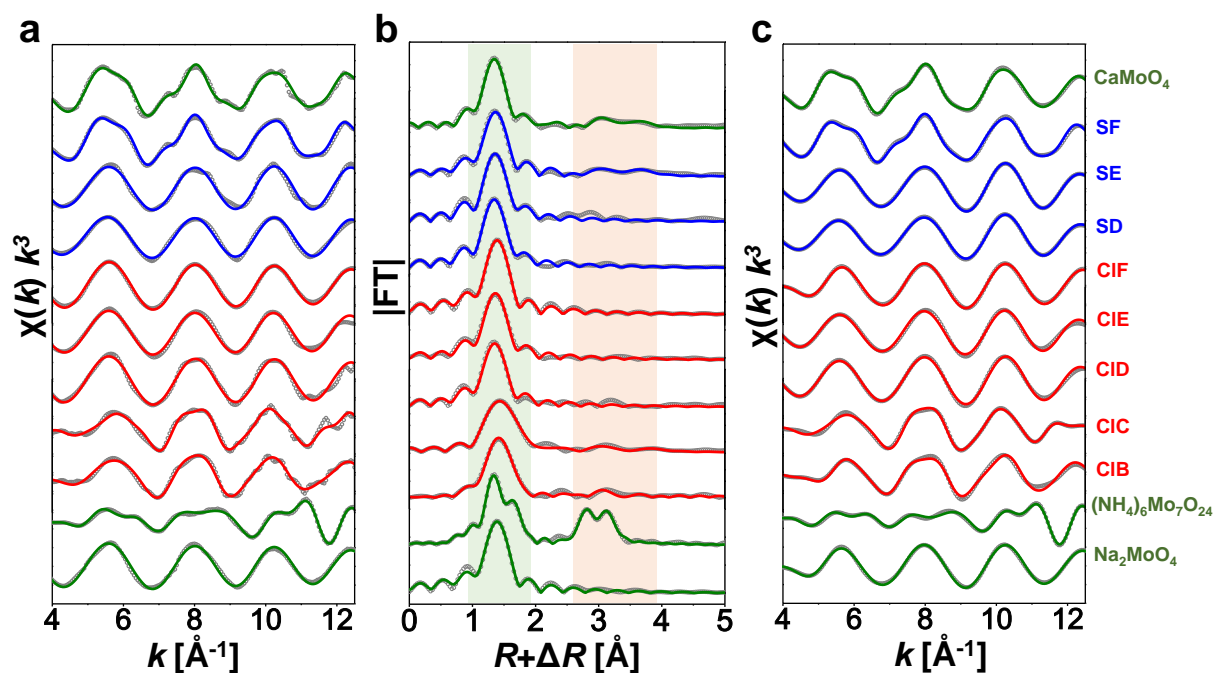


Figure 2.5. Experimental Mo K-edge EXAFS spectra of selected Mo-reacted LDHs samples from batch sorption experiment and reference compounds. (a) k^3 -weighted EXAFS oscillations. (b) Fourier transformed (not corrected for phase shift) EXAFS signals with the first shell highlighted in green and the further shell in champagne. (c) Back-Fourier transformed EXAFS signal (ranging from 1.00 to 4.20 \AA). For samples curves, the grey circles are the experimental data and the solid lines are fit results. Red, blue, and olive-green solid lines represent the fit results of AFm-Cl₂ samples, AFm-SO₄ samples, and references, respectively.

Table 2.1. Local structure of molybdate references and of selected batch sorption experiment samples obtained from EXAFS refinement at Mo K-edge^a.

ID	CN 1 st shell	<i>R</i> (Å)	σ^2 (Å ² ·10 ³)	CN 2 nd shell	<i>R</i> (Å)	σ^2 (Å ² ·10 ³)	ΔE^0 (eV)	<i>R</i> factor %
Na ₂ MoO ₄	4.0(2) O	1.78(4)	1.5(4)				0.6(9)	0.7
(NH ₄) ₆ Mo ₇ O ₂₄	2.2(2) O	1.72(1)	3.2(1)	1.1(1) Mo	3.23(1)	2.9(3)	-5.9(3)	1.6
	1.2(3) O	1.93(2)	8.6(1.7)	1.1(1) Mo	3.40(1)	3.7(4)		
	0.9(1) O	1.98(1)	1.6(1)					
	0.9(1) O	2.16(1)	0.3(6)					
	1.0(1) O	2.31(1)	2.5(1.0)					
CaMoO ₄	4.0(1) O	1.79(1)	1.6(1)	1.8(7) O	2.95(3)	9.7(6.8)	1.4(4)	1.7
				4.0(5) Ca	3.75(5)	5.1(1.1)		
				3.9(8) Mo	3.97(8)	7.6(1.4)		
CIB	3.1(1) O	1.78(1)	1.5(5)	0.9(8) Ca	3.63(3)	3.3(3.1)	-3.6(2.9)	2.1
	2.9(1) O	2.14(2)	4.2(1.8)	2.0(9) O	4.27(8)	4.5(3.2)		
CIC	2.6(1) O	1.78(1)	0.2(6)	0.9(4) Ca	3.61(4)	3.3(3.2)	-3.5(1.3)	3.1
	3.7(4) O	2.14(2)	6.0(1.7)	2.4(9) O	4.28(5)	0.6(9)		
CID	3.9(1) O	1.78(1)	1.2(8)				0.8(1.5)	0.7
CIE	3.9(4) O	1.79(1)	1.9(1.2)				2.4(3.6)	0.9
CIF	4.2(2) O	1.78(1)	1.6(3)				1.2(9)	0.6
SD	3.7(4) O	1.78(1)	0.6(1.5)				-1.8(1.4)	1.9
SE	3.5(2) O	1.78(1)	0.3(3)				1.2(8)	0.1
SF	3.9(2) O	1.79(1)	1.4(3)	1.1(5) O	2.93(2)	4.3(3.4)	1.3(6)	0.7
				2.5(3) Ca	3.74(1)	2.7(1.9)		
				2.4(9) Mo	3.97(2)	9.7(1.9)		

^a CN: coordination numbers; *R*: atomic distances; σ^2 : Debye-Waller factors; ΔE^0 : shift of the threshold energy; *R* factor: goodness of fit. S_0^2 , 0.9991 and 0.8718 for (NH₄)₆Mo₇O₂₄ and the rest samples, respectively, which were obtained from the experimental EXAFS fit of Na₂MoO₄ reference by fixing CN as the known crystallographic value. Uncertainties are given by the number in brackets on the last digit(s), i.e., 6.0(1.7) represents 6.0 ± 1.7, and 1.78(4) means 1.78 ± 0.04.

Mo-reacted AFm-Cl₂ samples CIB to CIF were studied using EXAFS. The spectra of samples CIB and CIC show similar features. Their first peak in the FT, which corresponds to O in the first shell, broadens and shifts to longer distances as compared to the FT peak of the Na₂MoO₄ reference. Fits of these data yield a first shell of ~6 O atoms that are separated in two different shells of three atoms each, at distances of $d_{Mo-O} = 1.78$ and 2.14 Å (Table 2.1). These results are consistent with an octahedrally coordinated Mo sorption complex sharing three oxygens with the Ca-Al-O structure, with $d_{Mo-O} = 2.14$ Å, and three others exposed to the solution, with $d_{Mo-O} = 1.78$ Å. This geometry is similar to that observed in heptamolybdate clusters, with the difference that Mo-Mo neighbours were not identified in our case. Indeed, a second shell at $d \sim 3.5$ Å can be fitted with Mo-Ca and Mo-O backscattering pairs from the Ca-Al-O structure. Provided that octahedrally coordinated molybdate could be incorporated inside the Ca-Al-O layer plane, the coordination number (CN) of Ca should be ~3. However, lower CNs (~ 1 Ca) are obtained, which may result from multiplicity of possible configurations or to interfacial ill-coordinated Mo. Both factors could induce slight changes in CN and bond lengths in the second shell. Besides, the lack of Mo-Mo backscattering pairs on samples CIB and CIC suggests the octahedral molybdate is still monomeric, not polymerized. The situation changes in samples CID, CIE and CIF, where anion exchange dominates the sorption process. The spectra of the dominant intercalated molybdate reveal a single oscillation with the identical frequency of Na₂MoO₄ reference, suggesting the coordination environment of the intercalated molybdate returns to that of unbonded tetrahedral MoO₄²⁻.

EXAFS data from Mo-reacted AFm-SO₄ samples are also shown in Figure 2.5a. Samples SD and SE showed a single shell fitted with a Mo-O distance at $d_{Mo-O} = 1.78$ Å. More distant neighbours were only found in sample SF, which was fitted with a model of powellite (CaMoO₄) (Table 2.1). EXAFS signal of samples with lower Mo concentration cannot satisfy a credible fit.

2.3.6. Estimation of edge sites density.

At low Mo loading, the change in molybdate coordination from TC to OC and the lack of LDHs swelling were observed, indicating at least two different types of surface complexation. In clay systems, the existence of high and low affinity sites on the clay edges has been highlighted in a variety of studies on divalent metal adsorption on montmorillonite[191]. With increasing pH conditions, cations sorption occurs successively through cation exchange and sorption on two types (high and low affinity) of edge sites, and finally by co-precipitation

[191]. The mechanisms observed for the intrinsically alkaline case of CaAl LDHs reflect a similar situation, showing the presence of two types of complexes prior to the precipitation of AFm-MoO₄. The structure of CaAl LDHs edge sites is unknown. However, comparison on the proportions between the number of moles of adsorbed molybdate and the number of sites can be made from experimentally determined edge perimeters and crystallographical considerations. Prior to the structural incorporation (cases of samples ClB and ClC), molybdate could be adsorbed by sharing one oxygen with the CaAl-LDH structure. Given the high affinity between molybdate and calcium [202], one could hypothesize that a >Ca-O-Mo-O₃ complex could be formed at an edge site, probably with some tilt towards the interlayer space, where the electrostatic potential is expected to be positive due to the net positively structural charge per formula unit of 0.33 e⁻ that is carried by the CaAl(OH)₂ structure. Assuming a conservative value of an active site density of ~1 site per nm edge, and using the measured values of layer edge perimeter and layer surface area (Table S2.6), this would make a total site density of 2.01×10⁻⁵ mol L⁻¹ for AFm-Cl₂ and 1.64×10⁻⁶ mol L⁻¹ for AFm-SO₄. As described in Table S2.7, the estimated edge sites concentration is comparable to the amount of adsorbed molybdate on both LDHs.

2.3.7. Environmental implications.

Sorption on the CaAl LDHs of oxyanions, such as molybdate, goes through three processes with increasing surface coverage: two types of edge surface sites complexation—tetrahedral and octahedral complexation on the edge, interlayer anion exchange leading to formation of AFm-MoO₄, and finally, decomposition of LDHs structures turning into CaMoO₄ precipitation. Under environmentally-relevant conditions (e.g., for nuclear waste disposal), removal of trace amounts of anionic contaminants should occur mainly by surface edge sorption mechanisms, rather than anion exchange. Therefore, LDHs behave not so much as anion exchangers, as often claimed, with relatively low affinity for the oxyanions, but rather at low adsorbate concentrations, as very efficient adsorbents where sorption induces structural modifications of the particle edges. This work gives a new insight into the complicated interplay of anions uptake mechanisms by LDH phases. The ability of Mo to change local geometry offers a spectroscopic probe to follow the different sites. These should possess distinct bonding strengths as a function of total Mo concentration. For instance, for trace contaminant concentrations, the strong binding strength provided by structural incorporation would lead to a low contaminant bioavailability. This work provides also a conceptual framework for improving toxic oxyanion leaching regulation for CaAl LDHs containing

materials, such as fly- and bottom-ashes. Whereas the calcium oxyanion precipitates and oxyanions present in anion exchange positions should be removed by leaching for the storage and reuse of such material in safe conditions, the amount of edge sorbed oxyanions could be tolerated, as they will be much harder to remove, becoming less bioavailable.

Supporting Information

Associated content

XRD patterns, FE-SEM micrographs, and TGA/DTG curves of fresh CaAl LDHs. PHREEQC modelling of aqueous results. In-situ time resolved XRD patterns in large 2θ range. Calculated Mo K-edge XANES spectra of different Mo coordination. Synchrotron based XRD/PDF patterns of sorption products. Tables for original aqueous data and for edge sites density estimations.

Text S2.1. Characterization of Synthesized CaAl LDHs.

Freshly synthesized Cl^- and SO_4^{2-} CaAl LDHs have well-crystallized hexagonal-shaped plate morphology (Figure S2.2) but different average sizes: around $\text{Ø}0.5 \mu\text{m}$ for AFm- Cl_2 and $\text{Ø}5 \mu\text{m}$ AFm- SO_4 , respectively. The specific surface areas and the average edge lengths thus differ (Table S2.6), with lateral surface (S_l) area concentrations equal for AFm- Cl_2 and AFm- SO_4 to 2.19×10^{18} and $2.29 \times 10^{17} \text{ nm}^2 \text{ g}^{-1}$, respectively, as obtained from[203]:

$$S_l = \frac{P}{S \times \rho} \quad (\text{S2.1})$$

where P , S , and ρ represent CaAl LDHs particle's perimeter (nm), basal plane surface area (nm^2), and density (g nm^{-3}), respectively.

X-ray diffraction (XRD) was used to determine the nature and amount of eventual impurities and the inter-layer distances of the synthesized CaAl LDHs (Figure S2.1), including AFm- SO_4 , AFm- Cl_2 , and AFm- CO_3 . Due to the sulfate-deficiency during the synthesis, no ettringite was formed in the fresh AFm- SO_4 , but katoite [$\text{Ca}_3\text{Al}_2(\text{OH})_{12}$] was observed as an impurity. AFm- SO_4 and AFm- Cl_2 powders were also characterized after 7 days in equilibrium with N_2 -saturated water at pH 12.4. The (003) inter-layer distance of AFm- SO_4 , was initially $8.128 \pm 0.006 \text{ \AA}$ at 5% relative humidity (RH) corresponding to 10.5 H_2O hydration state[201], and it changed to a shorter distance of $7.884 \pm 0.006 \text{ \AA}$ with time. The lack of SO_4^{2-} is compensated with OH^- in the inter-layer space, resulting in the formation of AFm-OH with 13 H_2O molecules. Besides, a tiny diffraction peak occurred at 11.65° after equilibration of AFm- SO_4 in water, which is probably derived from gypsum formed during sample drying. A strict N_2 protection gives us confidence to exclude formation of AFm- CO_3 (i.e., CO_2 contamination) in both reacted AFm- SO_4 and AFm- Cl_2 . No detectable impurity is observed with the AFm- Cl_2 phase, characterized by an inter-layer distance of $7.838 \pm 0.006 \text{ \AA}$.

Atomic ratios between each element in CaAl LDHs were estimated by digesting 100 mg CaAl LDHs solid phase in a certain amount of 1% HNO₃, and by measuring total aqueous Ca, Al, and S concentrations using inductively coupled plasma optical emission spectrometry (ICP-OES). This nitrolysis method was applied for each CaAl LDH in duplicate. Katoite impurity in AFm-SO₄ was inferred from the Ca/Al stoichiometry. Structural water content was determined by thermal gravimetric analysis (TGA) and derivative thermogravimetric analysis (DTG) curves (Figure S2.9) and dehydration and dehydroxylation were included in the total water loss till 700 °C[204], at which temperature the water loss is assumed to be completed. Based on the calculation, 78 at.% AFm-SO₄ and 22 at.% katoite composed the product for AFm-SO₄ synthesis. The experimental chemical formula of AFm-SO₄ and AFm-Cl₂ were Ca₄Al₂O₆(SO₄)_{0.92}(OH)_{0.08}·6.4H₂O and Ca₄Al₂O₆Cl_{1.64}(OH)_{0.36}·7.4H₂O, respectively.

Text S2.2. Instability of CaAl LDHs in presence of Mo.

The released Cl⁻ is more than the stoichiometric amount that may be derived from the corrosion of double-layer structure. This is confirmed by the newly appearance of a katoite diffraction peak for Mo-reacted samples in the synchrotron based XRD patterns since sample CIA (Figure S2.8), in agreement with saturation index (SI) computed from the aqueous phase composition after reaction of both CaAl LDHs with molybdate for 48 h (Figure S2.10). Molybdate could also affect heavily the metastability of AFm-SO₄ and result in ettringite formation (Figure S2.8). Compared to the dissolution products for 7 days (Figure S2.1), phases transformation seems to be promoted under the effect of molybdate. Indeed, the pair distribution function (PDF) analysis of high energy XRD data conducted on six selected sorption products, and compared to the calculated PDF patterns of katoite, ettringite, and powellite, shows almost no apparent phase transformation, except the formation of katoite and ettringite in Mo-reacted AFm-Cl₂ and AFm-SO₄, respectively (Figure S2.11 and Figure S2.12).

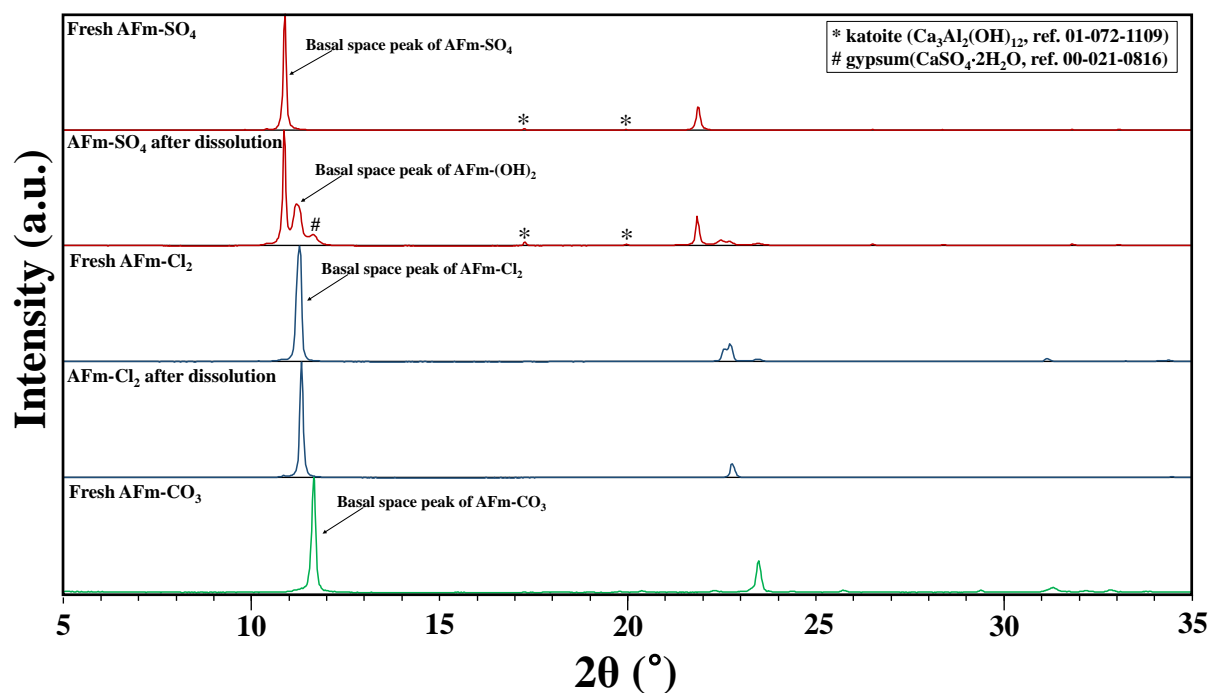


Figure S2.1. X-ray diffraction patterns of fresh CaAl LDHs and the phases after dissolution. The dissolution equilibrium was set at pH ~12.4 for 7 days and samples were mounted oriented at relative humidity of 5%. Cu K α radiation at 1.5406 Å is used.

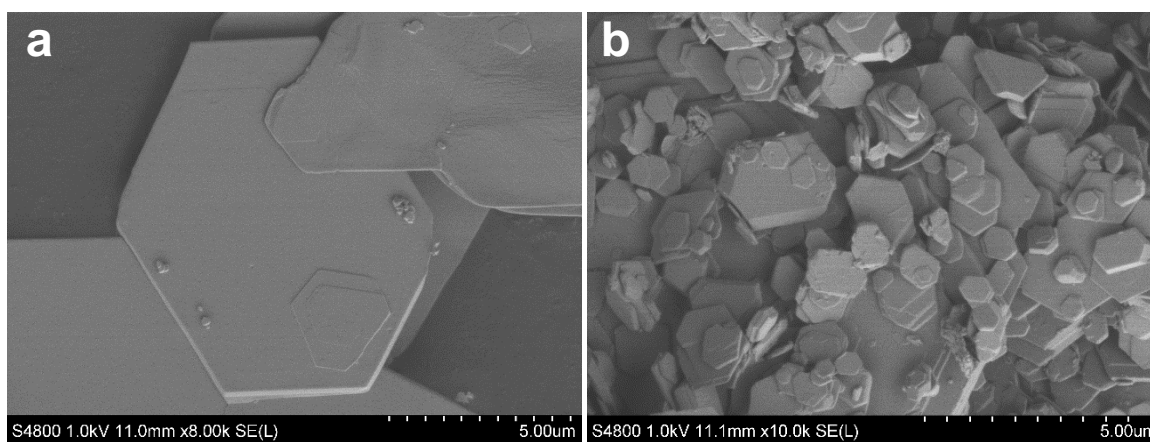


Figure S2.2. FE-SEM micrographs of the synthesized CaAl LDHs. Scale bar, 5 μm. (a) Pristine AFm-SO₄ particles. (b) Pristine AFm-Cl₂ particles.

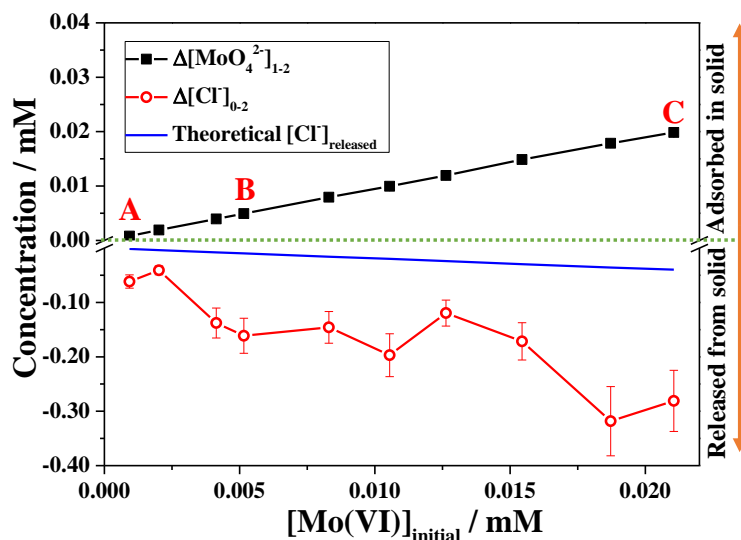


Figure S2.3. Concentration variation profile of aqueous MoO_4^{2-} and Cl^- as a function of molybdate loading on AFm- Cl_2 . The change in concentration of adsorbed MoO_4^{2-} is plotted by the black solid dots and the released Cl^- is represented by the red hollow dots. The theoretical $[\text{Cl}^-]_{\text{released}}$ is estimated by a stoichiometric anion exchange, shown as the blue curve. The selected three adsorption products are marked by A, B, and C.

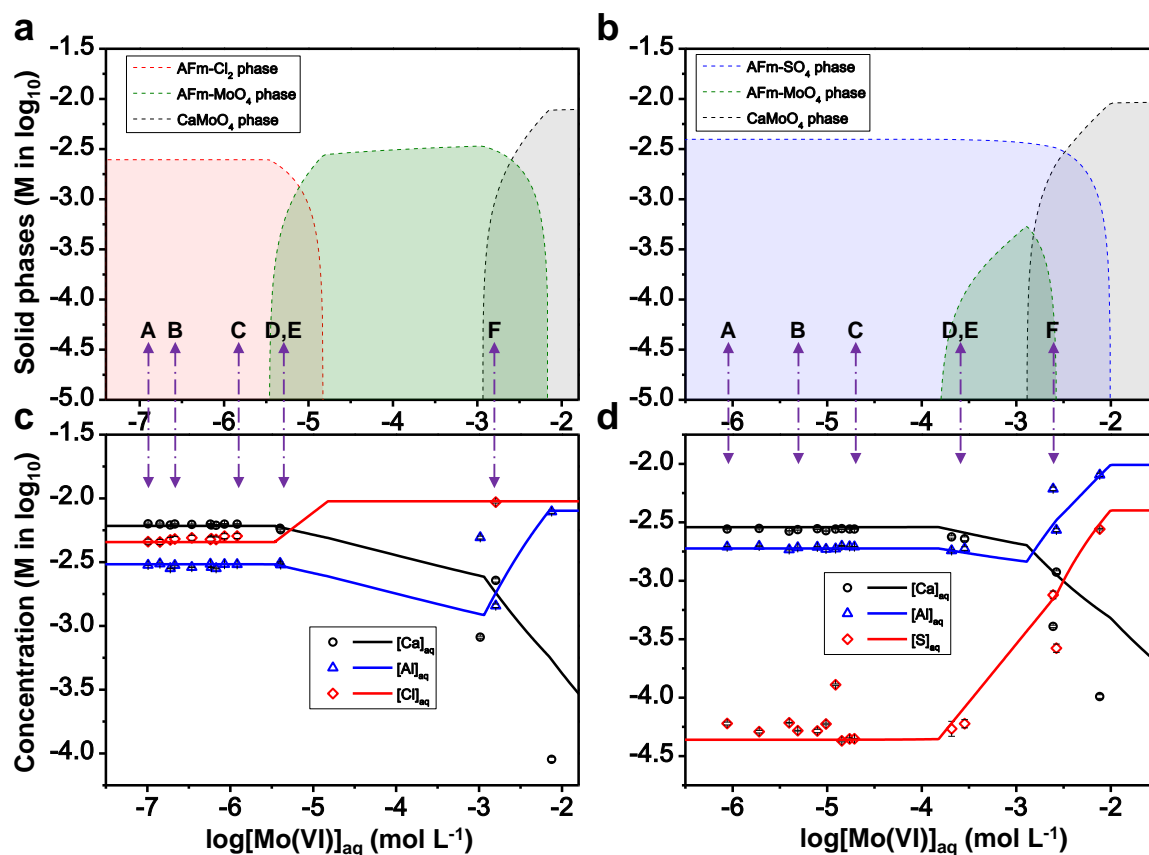


Figure S2.4. PHREEQC modelling results as a function of $[\text{Mo(VI)}]_{\text{aq}}$ in equilibrium. (a) Dominated solid speciation in AFm- Cl_2 reactors. (b) Dominated solid speciation in AFm- SO_4 reactors. (c) Modelling results of aqueous Ca, Al, and Cl concentrations in AFm- Cl_2 reactors. (d) Modelling results of aqueous Ca, Al, and S concentrations in AFm- SO_4 reactors. Reactors, marked by A to F, correspond to the same ones in Figure 2.1.

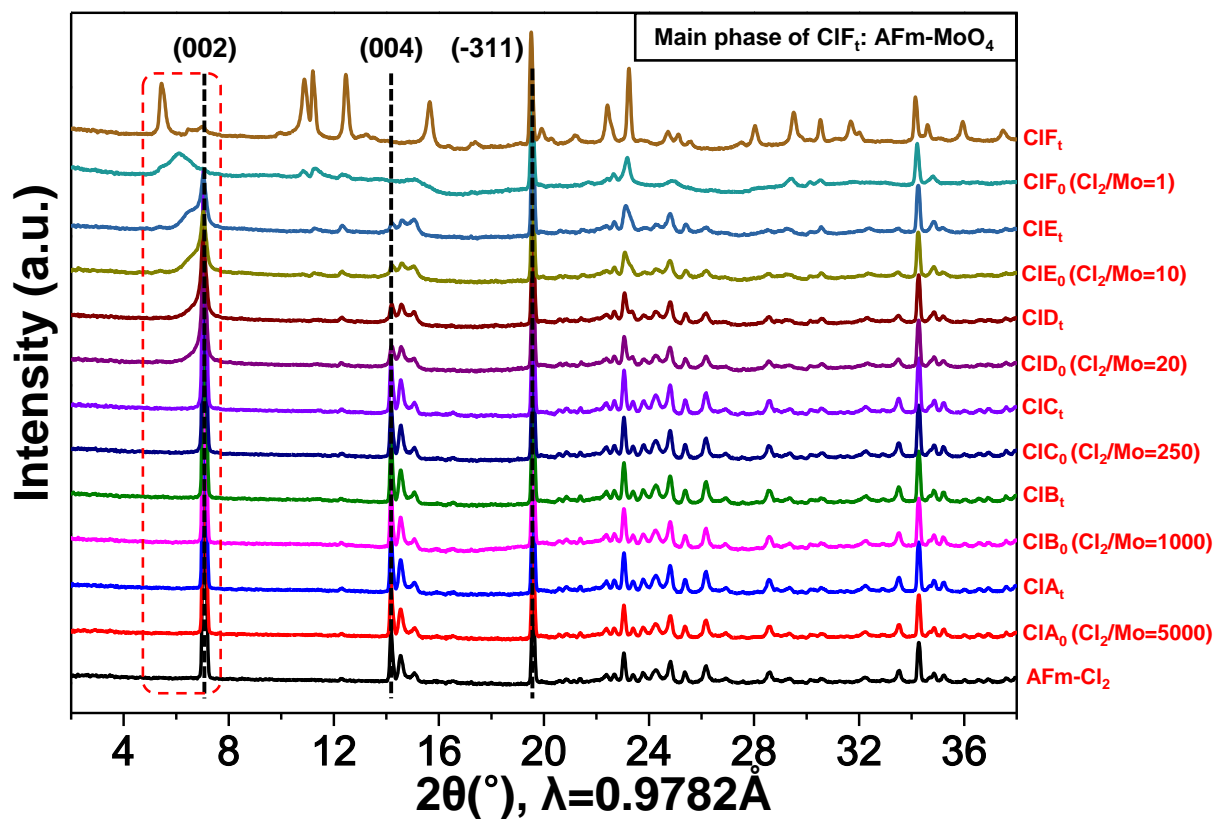


Figure S2.5. In-situ time resolved XRD patterns of reacted AFm-Cl_2 at each loading step. The diffraction peak range of layer-to-layer distance (d_{002}), circled by red dotted lines, is enlarged in the main text to provide more details. The Cl_2/MoO_4 ratio at each step is shown following the sample name. The main phase of ClF_i is AFm-MoO_4 , with no obvious signal of katoite and powellite observed.

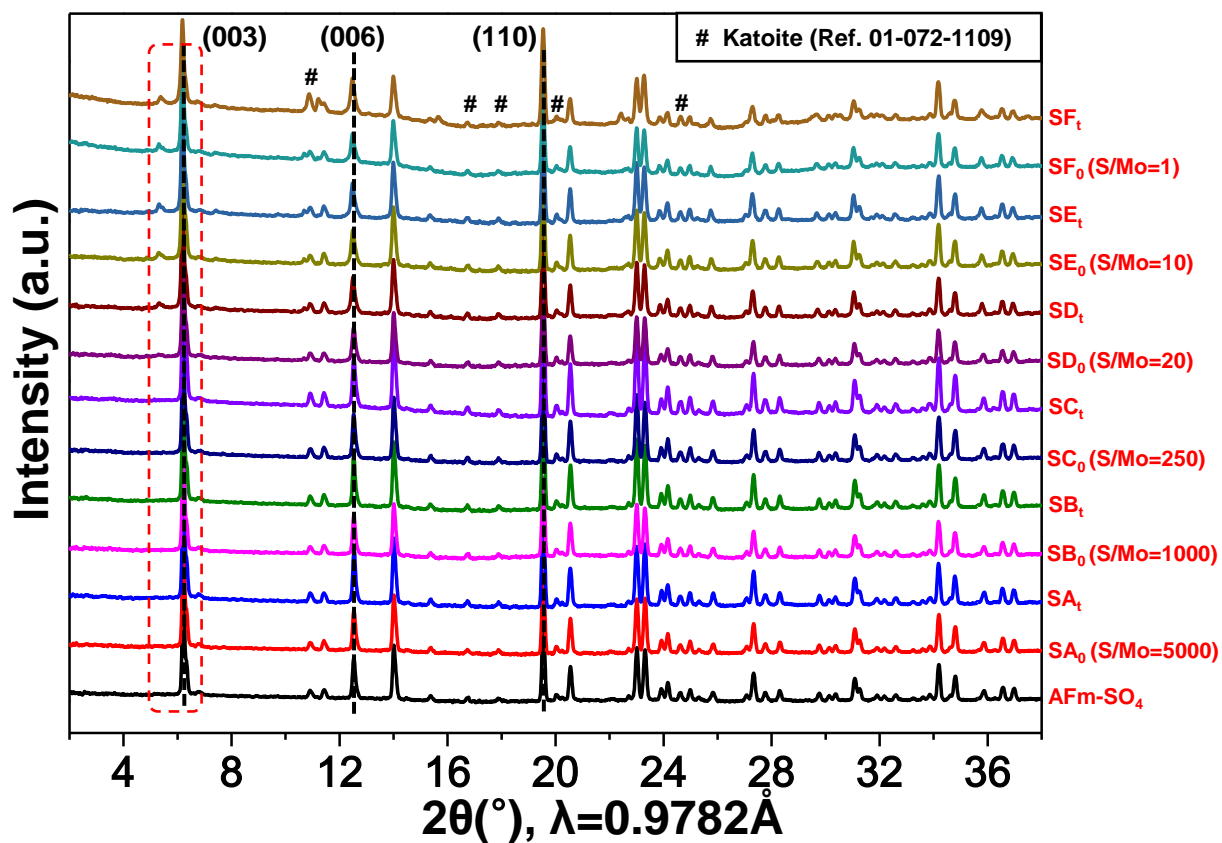


Figure S2.6. In-situ time resolved XRD patterns of reacted AFm-SO₄ at each loading step. The diffraction peak range of layer-to-layer distance (d_{003}), circled by red dotted lines, is enlarged in the main text to provide more details. The SO₄/MoO₄ ratio at each step is shown following the sample name.

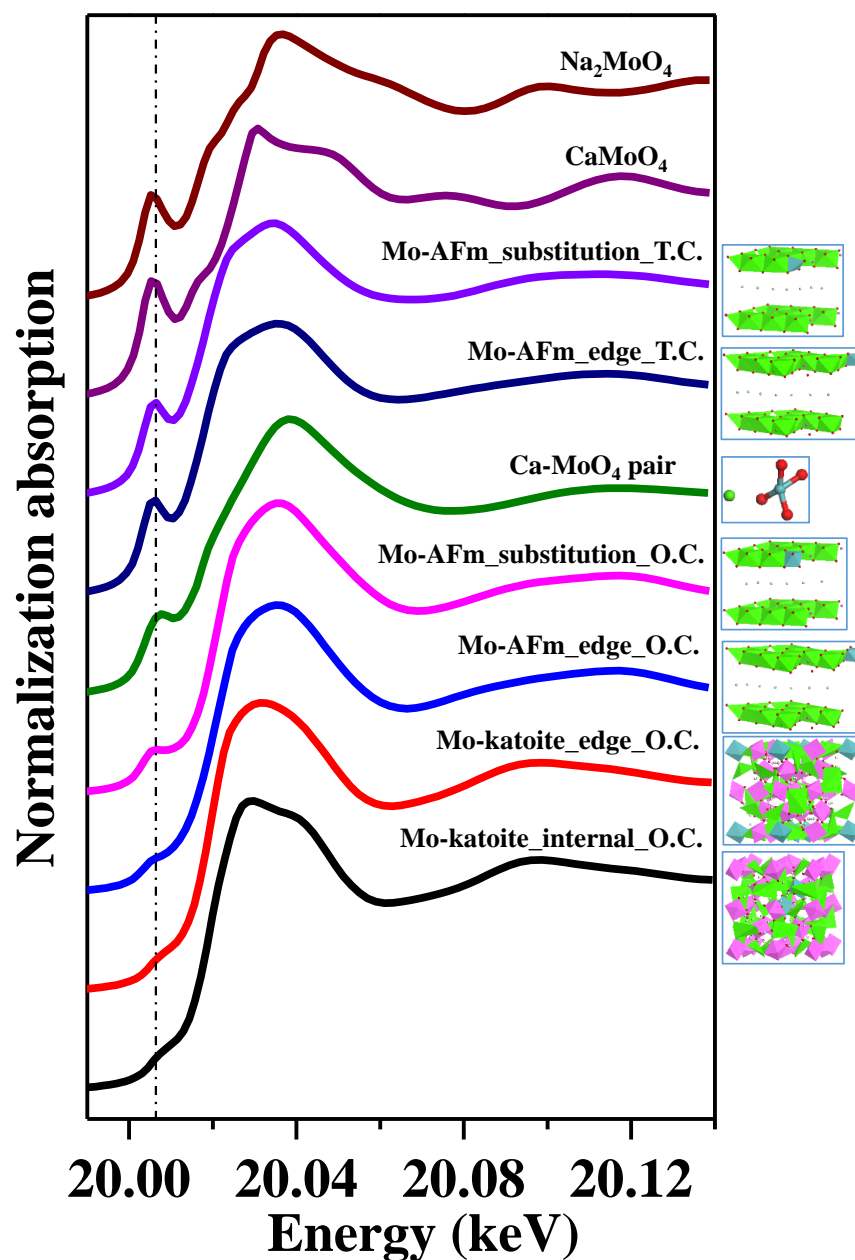


Figure S2.7. Calculated Mo K-edge XANES spectra of different Mo coordination. From the bottom up, the pre-edge intensity decreases steadily and the molybdate coordination environments are pure O.C. (octahedral Mo(VI)-katoite, both inner-incorporated and edge-incorporated), distorted O.C. (octahedral Mo(VI)-AFm phases, both the substitution and epitaxial growth), distorted T.C. (Ca-MoO₄ ion pair, both the substitution and epitaxial growth for tetrahedral Mo(VI)-AFm phases), and pure T.C. (CaMoO₄ and Na₂MoO₄). O.C and T.C. represent octahedral coordination and tetrahedral coordination, respectively.

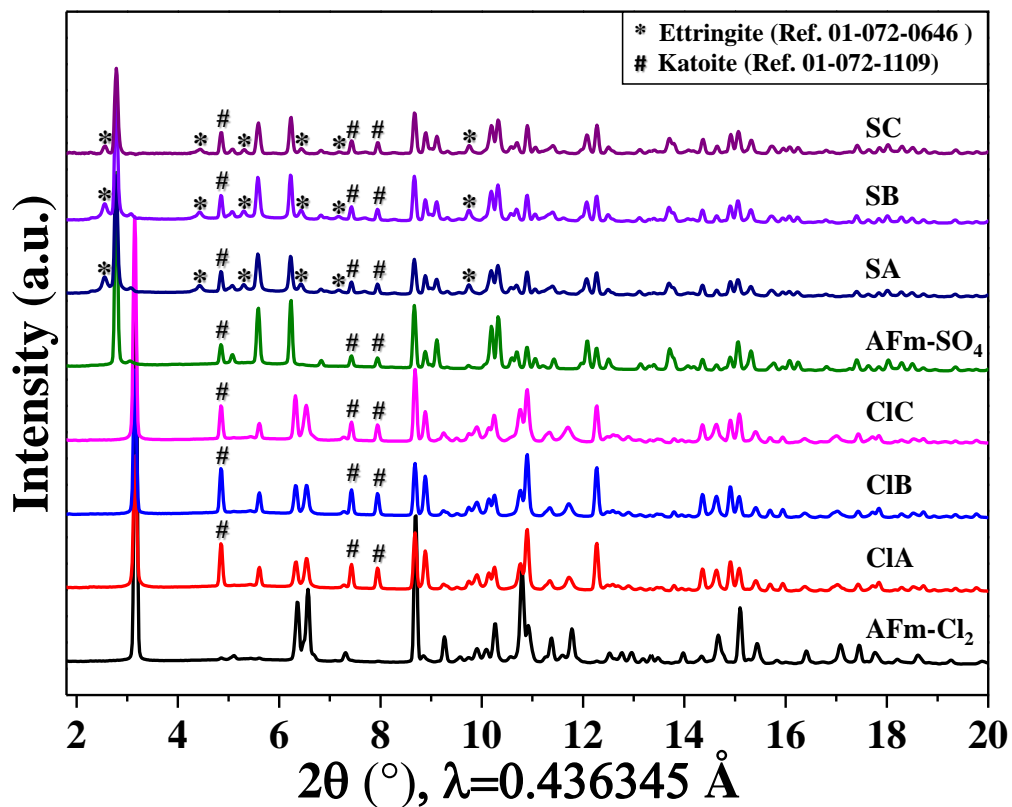


Figure S2.8. Synchrotron based X-ray diffraction patterns of the selected adsorption products for CaAl LDHs. Inter-layer peaks are located in the range of 2 - 4°.

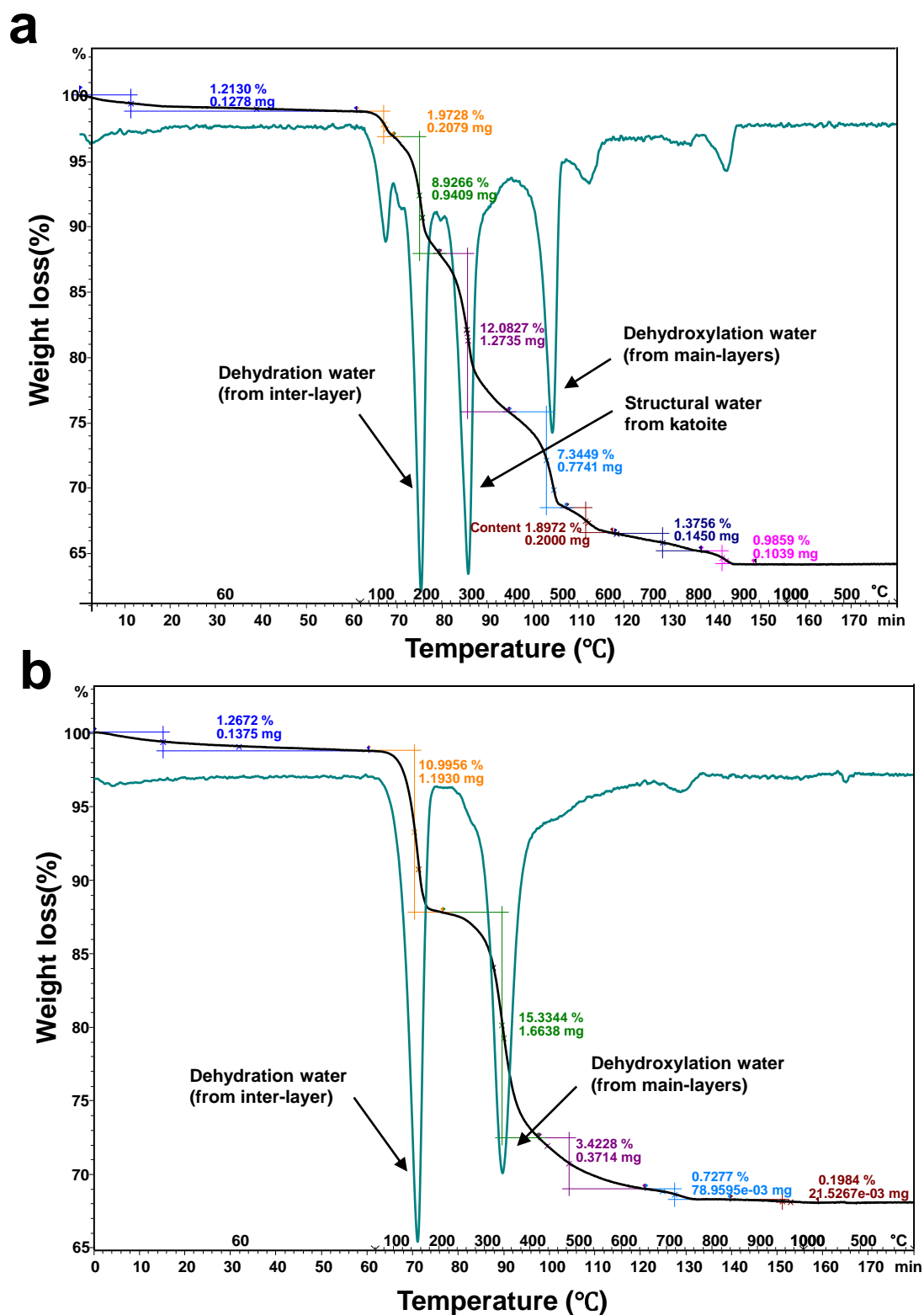


Figure S2.9. Thermogravimetric analyses of the synthesized CaAl LDHs. (a) AFm-SO₄ phase. (b) AFm-Cl₂ phase. TGA is represented as the black curves and DTG in olive-green curves.

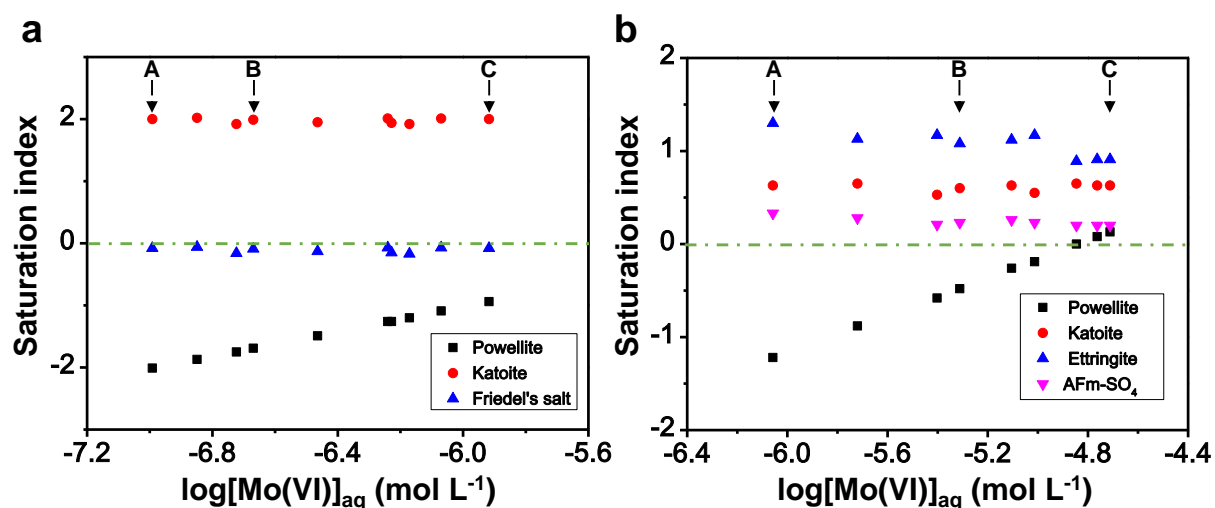


Figure S2.10. Saturation index of several possibly formed mineral phases as a function of $[\text{Mo(VI)}]_{\text{initial}}$. (a) For AFm-Cl₂ system. (b) For AFm-SO₄ system. Calculation is based on the aqueous data in batch sorption experiment on CaAl LDHs.

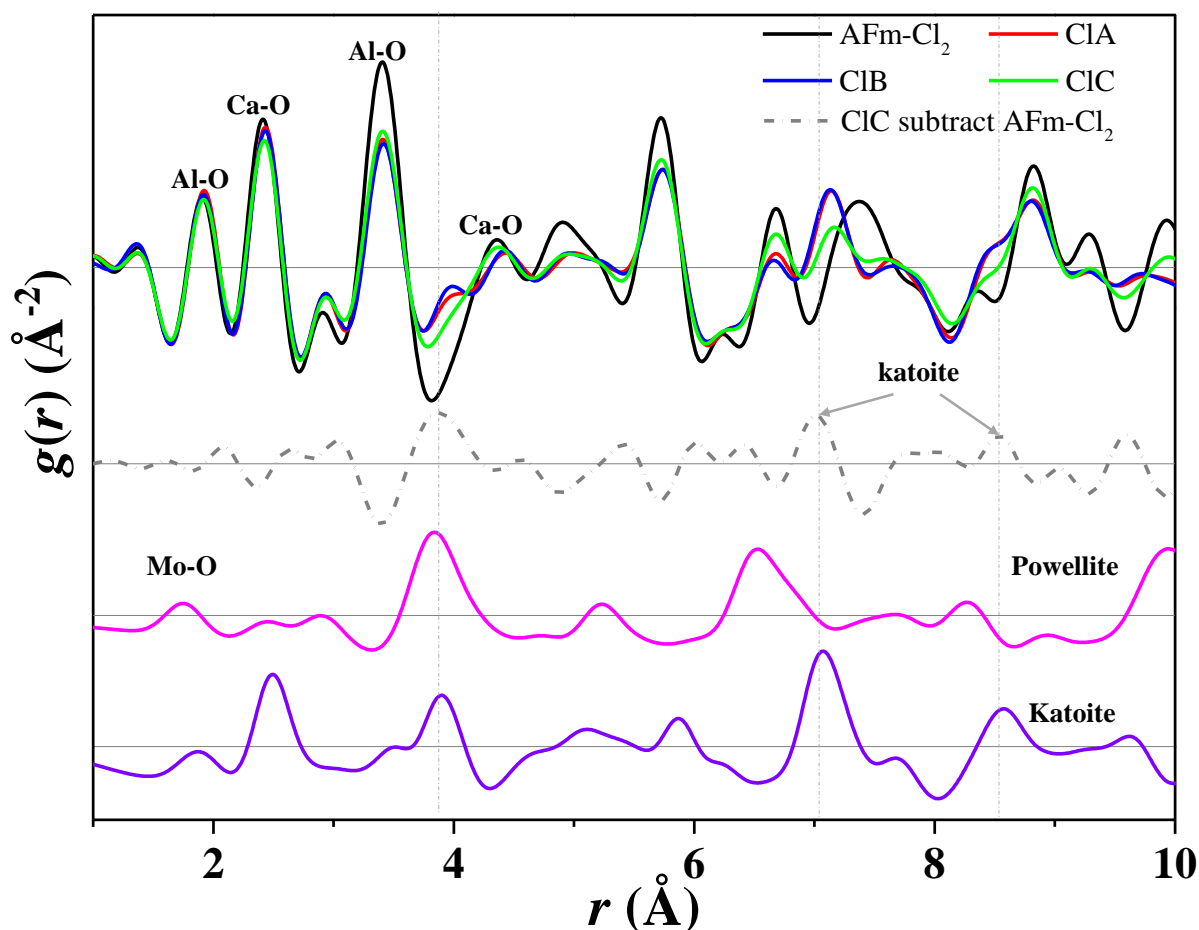


Figure S2.11. Comparison of calculated and experimental PDF of katoite, powellite, and AFm-Cl₂ samples in batch sorption experiment. The grey dotted line is the subtracted signal of CIC on fresh AFm-Cl₂.

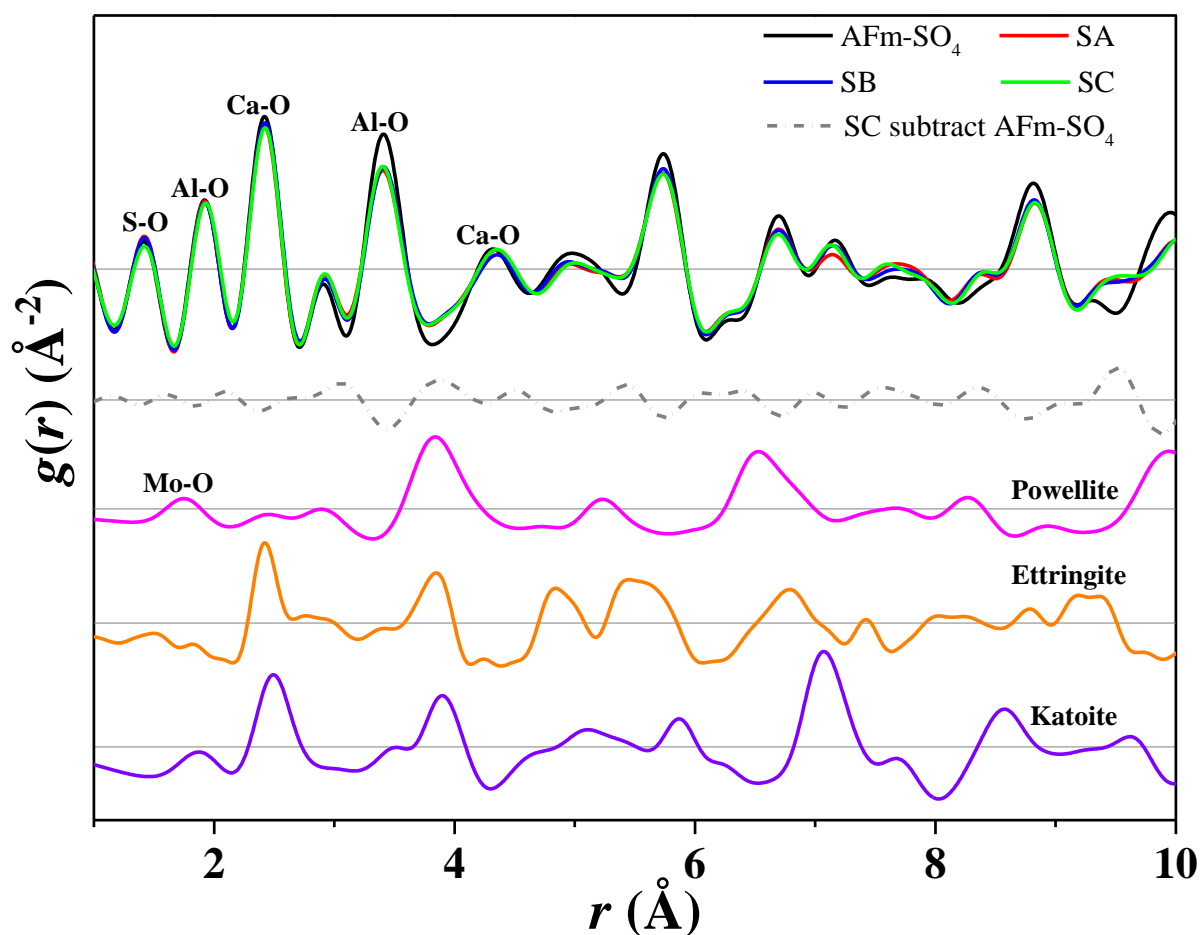


Figure S2.12. Comparison of calculated and experimental PDF of katoite, powellite, ettringite and AFm-SO₄ samples in batch sorption experiment. The grey dotted line is the subtracted signal of SC on fresh AFm-SO₄.

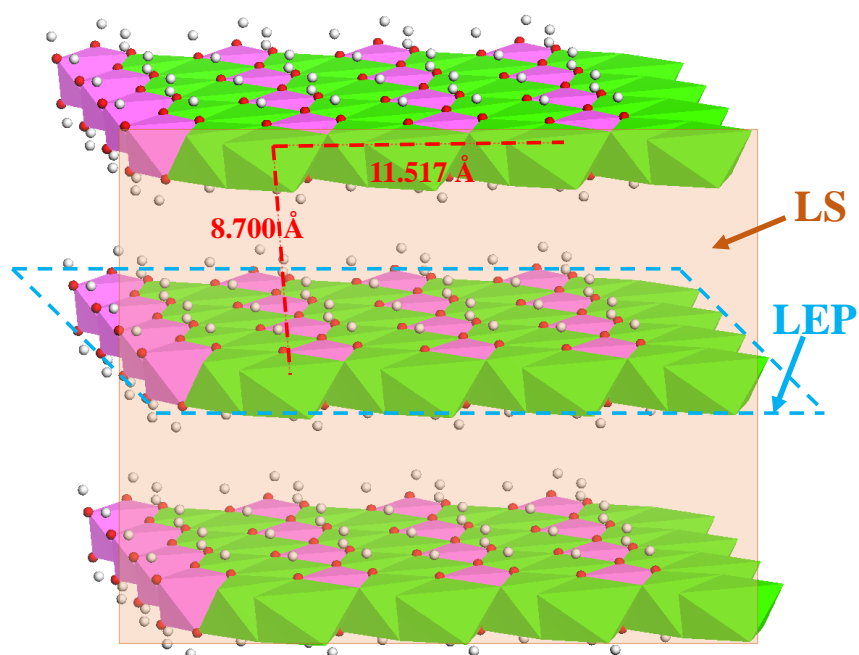


Figure S2.13. Schematic representation of the meaning of LS and LEP in LDHs. LS and LEP represent lateral surface and lateral edge perimeter, respectively.

Table S2.1. Solution content of selected elements for AFm-Cl₂ experiments before introducing MoO₄²⁻. Concentrations were determined after reaching dissolution equilibrium, which was confirmed by dissolution kinetics^a.

ID	pH	[Ca] _{aq} /mol L ⁻¹	[Al] _{aq} /mol L ⁻¹	[Cl] _{aq} /mol L ⁻¹
CIA	12.37	6.23(6)×10 ⁻³	3.25(1)×10 ⁻³	4.49(21)×10 ⁻³
	nd	6.31(7)×10 ⁻³	3.25(2)×10 ⁻³	4.54(21)×10 ⁻³
	nd	6.43(7)×10 ⁻³	3.25(2)×10 ⁻³	4.59(22)×10 ⁻³
CIB	nd	6.24(7)×10 ⁻³	3.26(2)×10 ⁻³	4.64(21)×10 ⁻³
	nd	6.36(8)×10 ⁻³	3.22(2)×10 ⁻³	4.76(23)×10 ⁻³
	nd	6.31(7)×10 ⁻³	3.29(3)×10 ⁻³	4.63(21)×10 ⁻³
	nd	6.35(6)×10 ⁻³	3.29(3)×10 ⁻³	4.64(23)×10 ⁻³
	nd	6.26(7)×10 ⁻³	3.24(1)×10 ⁻³	4.58(22)×10 ⁻³
	nd	6.28(6)×10 ⁻³	3.27(2)×10 ⁻³	4.74(21)×10 ⁻³
CIC	nd	6.28(6)×10 ⁻³	3.27(1)×10 ⁻³	4.79(23)×10 ⁻³

^a nd: not determined; Uncertainties from three times repeated analyses of identical samples are given by the number in brackets on the last digit(s).

Table S2.2. Solution content of selected elements for AFm-Cl₂ experiments after equilibrium with MoO₄²⁻ for 48 h^a.

ID	pH	[Mo] _{aq} /mol L ⁻¹	<i>q</i> /mol g ⁻¹	[Ca] _{aq} /mol L ⁻¹	[Al] _{aq} /mol L ⁻¹	[Cl] _{aq} /mol L ⁻¹
CIA	12.37	1.42(17)×10 ⁻⁷	3.93(42)×10 ⁻⁷	6.30(10)×10 ⁻³	3.07(4)×10 ⁻³	4.55(21)×10 ⁻³
	nd	1.02(12)×10 ⁻⁷	9.57(51)×10 ⁻⁷	6.32(8)×10 ⁻³	3.00(2)×10 ⁻³	4.58(21)×10 ⁻³
	nd	1.89(18)×10 ⁻⁷	1.97(13)×10 ⁻⁶	6.19(7)×10 ⁻³	2.82(2)×10 ⁻³	4.73(22)×10 ⁻³
CIB	12.37	2.14(8)×10 ⁻⁷	2.47(16)×10 ⁻⁶	6.29(8)×10 ⁻³	2.99(3)×10 ⁻³	4.80(22)×10 ⁻³
	nd	3.43(3)×10 ⁻⁷	3.98(21)×10 ⁻⁶	6.25(6)×10 ⁻³	2.88(1)×10 ⁻³	4.90(22)×10 ⁻³
	nd	5.91(7)×10 ⁻⁷	4.98(32)×10 ⁻⁶	6.18(6)×10 ⁻³	2.88(1)×10 ⁻³	4.83(22)×10 ⁻³
	nd	6.74(13)×10 ⁻⁷	5.98(30)×10 ⁻⁶	6.15(8)×10 ⁻³	2.82(2)×10 ⁻³	4.76(22)×10 ⁻³
	nd	5.75(16)×10 ⁻⁷	7.43(38)×10 ⁻⁶	6.28(6)×10 ⁻³	3.06(1)×10 ⁻³	4.76(22)×10 ⁻³
	nd	8.51(16)×10 ⁻⁷	8.93(40)×10 ⁻⁶	6.28(6)×10 ⁻³	3.04(1)×10 ⁻³	5.06(23)×10 ⁻³
CIC	12.37	1.21(1)×10 ⁻⁶	9.92(44)×10 ⁻⁶	6.28(6)×10 ⁻³	3.03(2)×10 ⁻³	5.07(23)×10 ⁻³
CID	12.38	3.98(32)×10 ⁻⁶	1.35(4)×10 ⁻⁴	5.83(15)×10 ⁻³	3.10(7)×10 ⁻³	nd
CIE	12.38	4.05(28)×10 ⁻⁶	2.60(7)×10 ⁻⁴	5.68(19)×10 ⁻³	3.02(5)×10 ⁻³	nd
CIF	12.37	1.59(13)×10 ⁻³	1.52(7)×10 ⁻³	2.27(7)×10 ⁻³	1.44(4)×10 ⁻³	9.35(16)×10 ⁻³
CIG	12.41	1.03(5)×10 ⁻³	3.90(9)×10 ⁻³	8.15(16)×10 ⁻⁴	4.93(12)×10 ⁻³	nd
CIH	12.42	7.50(35)×10 ⁻³	6.14(21)×10 ⁻³	8.97(36)×10 ⁻⁵	7.86(23)×10 ⁻³	nd

^a nd: not determined; Uncertainties from three times repeated analyses of identical samples are given by the number in brackets on the last digit(s).

Table S2.3. Solution content of selected elements for AFm-SO₄ experiments before introducing MoO₄²⁻. Concentrations were determined after reaching dissolution equilibrium, which was confirmed by dissolution kinetics^a.

ID	pH	[Ca] _{aq} /mol L ⁻¹	[Al] _{aq} /mol L ⁻¹	[S] _{aq} /mol L ⁻¹
SA	12.35	2.69(3)×10 ⁻³	1.97(2)×10 ⁻³	5.08(22)×10 ⁻⁵
	nd	2.74(4)×10 ⁻³	1.97(2)×10 ⁻³	5.32(17)×10 ⁻⁵
	nd	2.77(3)×10 ⁻³	1.96(1)×10 ⁻³	5.08(26)×10 ⁻⁵
SB	nd	2.70(3)×10 ⁻³	1.98(1)×10 ⁻³	5.13(14)×10 ⁻⁵
	nd	2.73(3)×10 ⁻³	1.97(2)×10 ⁻³	4.88(29)×10 ⁻⁵
	nd	2.74(3)×10 ⁻³	1.97(1)×10 ⁻³	4.98(24)×10 ⁻⁵
	nd	2.68(2)×10 ⁻³	1.89(1)×10 ⁻³	6.04(16)×10 ⁻⁵
	nd	2.71(3)×10 ⁻³	1.96(1)×10 ⁻³	5.00(5)×10 ⁻⁵
	nd	2.72(3)×10 ⁻³	1.95(2)×10 ⁻³	4.93(24)×10 ⁻⁵
	nd	2.74(3)×10 ⁻³	1.97(2)×10 ⁻³	5.02(44)×10 ⁻⁵

^a nd: not determined; Uncertainties from three times repeated analyses of identical samples are given by the number in brackets on the last digit(s).

Table S2.4. Solution content of selected elements for AFm-SO₄ experiments after equilibrium with MoO₄²⁻ for 48 h^a.

ID	pH	[Mo] _{aq} /mol L ⁻¹	<i>q</i> /mol g ⁻¹	[Ca] _{aq} /mol L ⁻¹	[Al] _{aq} /mol L ⁻¹	[S] _{aq} /mol L ⁻¹
SA	12.34	8.75(90)×10 ⁻⁷	2.62(3.04)×10 ⁻⁸	2.77(3)×10 ⁻³	1.95(2)×10 ⁻³	6.00(17)×10 ⁻⁵
	nd	1.90(11)×10 ⁻⁶	5.61(3.67)×10 ⁻⁸	2.80(3)×10 ⁻³	1.97(2)×10 ⁻³	5.11(13)×10 ⁻⁵
	nd	3.96(26)×10 ⁻⁶	8.76(9.20)×10 ⁻⁸	2.65(3)×10 ⁻³	1.85(1)×10 ⁻³	6.09(4)×10 ⁻⁵
SB	12.35	4.88(35)×10 ⁻⁶	1.39(1.18)×10 ⁻⁷	2.74(3)×10 ⁻³	1.92(1)×10 ⁻³	5.21(4)×10 ⁻⁵
	nd	7.86(49)×10 ⁻⁶	2.21(1.59)×10 ⁻⁷	2.78(4)×10 ⁻³	1.94(3)×10 ⁻³	5.19(17)×10 ⁻⁵
	nd	9.70(6)×10 ⁻⁶	4.22(2.25)×10 ⁻⁷	2.68(3)×10 ⁻³	1.86(1)×10 ⁻³	5.95(9)×10 ⁻⁵
	nd	1.23(8)×10 ⁻⁵	1.85(2.20)×10 ⁻⁷	2.77(4)×10 ⁻³	1.88(3)×10 ⁻³	1.29(2)×10 ⁻⁴
	nd	1.43(8)×10 ⁻⁵	5.89(2.84)×10 ⁻⁷	2.79(4)×10 ⁻³	1.98(2)×10 ⁻³	4.27(9)×10 ⁻⁵
	nd	1.73(6)×10 ⁻⁵	7.29(2.58)×10 ⁻⁷	2.77(4)×10 ⁻³	1.96(2)×10 ⁻³	4.44(9)×10 ⁻⁵
SC	12.34	1.94(5)×10 ⁻⁵	8.17(2.51)×10 ⁻⁷	2.77(3)×10 ⁻³	1.95(1)×10 ⁻³	4.45(3)×10 ⁻⁵
SD	12.35	2.07(12)×10 ⁻⁴	3.30(49)×10 ⁻⁵	2.37(6)×10 ⁻³	1.81(4)×10 ⁻³	5.41(86)×10 ⁻⁵
SE	12.36	2.84(17)×10 ⁻⁴	1.20(8)×10 ⁻⁴	2.28(8)×10 ⁻³	1.88(7)×10 ⁻³	5.98(50)×10 ⁻⁵
SF	12.41	2.66(13)×10 ⁻³	9.81(72)×10 ⁻⁴	1.18(3)×10 ⁻³	2.71(8)×10 ⁻³	2.65(22)×10 ⁻⁴
SG	12.40	2.45(15)×10 ⁻³	3.19(10)×10 ⁻³	4.07(9)×10 ⁻⁴	6.10(21)×10 ⁻³	7.56(60)×10 ⁻⁴
SH	12.42	7.63(42)×10 ⁻³	6.07(22)×10 ⁻³	1.02(4)×10 ⁻⁴	8.04(26)×10 ⁻³	2.77(4)×10 ⁻³

^a nd: not determined; Uncertainties from three times repeated analyses of identical samples are given by the number in brackets on the last digit(s).

Table S2.5. Equilibrium constants of selected phases^a and reactions occurred on CaAl LDHs at each sorption stage. *logK* values of AFm edge sites sorption and AFm-MoO₄ formation were adapted.

	Equation	<i>logK</i>
<i>Solubility equilibrium</i>		
AFm-Cl ₂	$\text{Ca}_4\text{Al}_2\text{Cl}_2(\text{OH})_{12} \cdot 4\text{H}_2\text{O} + 12\text{H}^+ \Leftrightarrow 4\text{Ca}^{2+} + 2\text{Al}^{3+} + 2\text{Cl}^- + 16\text{H}_2\text{O}$	74.93
AFm-SO ₄	$\text{Ca}_4\text{Al}_2(\text{SO}_4)(\text{OH})_{12} \cdot 6\text{H}_2\text{O} + 12\text{H}^+ \Leftrightarrow 4\text{Ca}^{2+} + 2\text{Al}^{3+} + \text{SO}_4^{2-} + 18\text{H}_2\text{O}$	73.07
AFm-MoO ₄	$\text{Ca}_4\text{Al}_2(\text{MoO}_4)(\text{OH})_{12} \cdot 4\text{H}_2\text{O} + 12\text{H}^+ \Leftrightarrow 4\text{Ca}^{2+} + 2\text{Al}^{3+} + \text{MoO}_4^{2-} + 16\text{H}_2\text{O}$	74.00
CaMoO ₄	$\text{CaMoO}_{4(s)} \Leftrightarrow \text{Ca}^{2+} + \text{MoO}_4^{2-}$	-7.90
Katoite(C ₃ AH ₆)	$\text{Ca}_3\text{Al}_2(\text{OH})_{12} + 12\text{H}^+ \Leftrightarrow 3\text{Ca}^{2+} + 2\text{Al}^{3+} + 12\text{H}_2\text{O}$	80.32
Ettringite	$\text{Ca}_6\text{Al}_2(\text{SO}_4)_3(\text{OH})_{12} \cdot 26\text{H}_2\text{O} + 12\text{H}^+ \Leftrightarrow 6\text{Ca}^{2+} + 2\text{Al}^{3+} + 3\text{SO}_4^{2-} + 38\text{H}_2\text{O}$	56.97
<i>Sorption stage</i>		
Edge sorption	$2\text{AFm_edge-OH} + \text{MoO}_4^{2-} \Leftrightarrow (\text{AFm_edge})_2\text{-MoO}_4 + 2\text{OH}^-$	2.80 ^b , 1.05 ^c
AFm-MoO ₄ formation	$4\text{Ca}^{2+} + 2\text{Al}^{3+} + \text{MoO}_4^{2-} + 16\text{H}_2\text{O} \Leftrightarrow \text{Ca}_4\text{Al}_2(\text{MoO}_4)(\text{OH})_{12} \cdot 4\text{H}_2\text{O} + 12\text{H}^+$	-74.00
CaMoO ₄ precipitation	$\text{Ca}^{2+} + \text{MoO}_4^{2-} \Leftrightarrow \text{CaMoO}_{4(s)}$	7.90

^a *logK* values of other phases refer to THERMOCHEMIE database.^b For edge sorption on AFm-Cl₂.^c For edge sorption on AFm-SO₄.**Table S2.6.** Physical parameters of AFm particles.

	SA ¹ (m ² g ⁻¹)	AEL ² (μm)	Density (g cm ⁻³)	Basal area (m ²)	LEP ³ (nm g ⁻¹)	LS ⁴ (nm ² g ⁻¹)
AFm-Cl ₂	3.5	0.5	2.11	6.50×10 ⁻¹³	2.23×10 ¹⁷	2.19×10 ¹⁸
AFm-SO ₄	1.9	5.0	2.02	6.50×10 ⁻¹¹	2.26×10 ¹⁶	2.29×10 ¹⁷

¹ SA represents specific surface area measured by N₂-sorption BET.² AEL represents average edge length of AFm particles measured by SEM.³ LEP represents lateral edge perimeter.⁴ LS represents lateral surface.

Table S2.7. Edge sites concentration and adsorbed anion amount.

	LEP length conc. (nm L ⁻¹)	LS area conc. (nm ² L ⁻¹)	LEP site conc. (mol L ⁻¹)	LS site conc. (mol L ⁻¹)	Sample	Adsorbed Mo amount (mol L ⁻¹)
					CIA	7.86×10 ⁻⁷
AFm-Cl ₂	4.45×10 ¹⁷	4.38×10 ¹⁸	7.39×10 ⁻⁷	1.94×10 ⁻⁵	CIB	4.94×10 ⁻⁶
					CIC	1.98×10 ⁻⁵
					SA	5.25×10 ⁻⁸
AFm-SO ₄	3.52×10 ¹⁶	3.57×10 ¹⁷	5.85×10 ⁻⁸	1.58×10 ⁻⁶	SB	2.78×10 ⁻⁷
					SC	1.63×10 ⁻⁶

* The L/S ratio of 500 kg/kg was used. Layers' edge and lateral adsorption site densities are estimated as 1.00 nm⁻¹ and 2.67 nm⁻² (2.67 Ca atoms are included per area of 8.700×11.517 Å², seeing Figure S2.13), respectively. LS and LEP represent lateral surface and lateral edge perimeter, respectively.

Chapter 3. Selenite uptake by AFm phases: a description of intercalated anion coordination geometries

Abstract

Layered double hydroxides (LDHs) are anion exchangers with a strong potential to scavenge anionic contaminants in aquatic environments. Here, the uptake of selenite (SeO_3^{2-}) by CaAl LDHs was investigated as a function of Se concentration. Thermodynamic modelling of batch sorption isotherms shows that the formation of AFm- SeO_3 is the dominant mechanism controlling the retention of Se at medium loadings. AFm- Cl_2 shows much stronger affinity and larger distribution ratio ($R_d \sim 17800 \text{ L kg}^{-1}$) towards SeO_3^{2-} than AFm- SO_4 ($R_d \sim 705 \text{ L kg}^{-1}$). At stoichiometric SeO_3^{2-} loading for anion exchange, the newly formed AFm- SeO_3 phase results in two inter-layer distances, i.e., $9.93 \pm 0.06 \text{ \AA}$ and $\sim 11.03 \pm 0.03 \text{ \AA}$. Extended X-ray absorption fine structure spectra indicate that the intercalated SeO_3^{2-} forms inner-sphere bidentate binuclear complexes with the Ca-Al-O layers. In situ X-ray diffraction (XRD) shows that layer-to-layer distances of CaAl LDHs have a remarkable linear relationship with the size of hydrated intercalated anions (i.e., Cl^- , SO_4^{2-} , MoO_4^{2-} , and SeO_3^{2-}). These analyses confirm the co-existence of free and bonded intercalated SeO_3^{2-} . Contrary to AFm- SeO_3 with bonded SeO_3^{2-} , the phase with free intercalated SeO_3^{2-} is kinetically favored but thermodynamically unstable. This work offers new insights about the determination of intercalated anion complexation environments via XRD analyses.

3.1. Introduction

Layered double hydroxides (LDHs) are lamellar mixed hydroxides with a generic chemical formula $[M^{II}_{6-x}M^{III}_xO_6]^{x+}(A^{n-})_{x/n} \cdot mH_2O$, where species under brackets form the layer that contain M cations and species on the right form the interlayer, with A being an anion. LDHs are not only potentially used in the areas of catalysis, photochemistry, electrochemistry, and pharmaceuticals[205], but also abundantly employed to remove anionic contaminants of aquatic environments[174]. As potential scavengers of toxic soluble oxyanions, LDHs are often considered as efficient anion exchangers [177, 178] due to their high anion exchange capacity (2-3 meq/g), and positive structural charge. CaAl LDHs, in which M^{II} and M^{III} are Ca^{II} and Al^{III} cations, are widespread artificial LDHs around the world, due to their presence in Portland cement. These phases can be detected or thermodynamically predicted to occur in bottom ash [52, 53] and Class C coal fly ash (CFA) [54-56], which are two of the main coal combustion products (CCPs) with a global production of over 750 million tons per year [57]. Belonging to Ca-Al LDHs family, alumina ferric oxide monosulfate (so-called AFm) phases ($[Ca_4Al_2O_6]^{2+} \cdot SO_4^{2-} \cdot mH_2O$), are minor but highly reactive phases present in hydrated cement[38]. When concrete is subjected to Cl^- corrosion (e.g., exposed to sea water, or deicing salt), or when Cl-rich water, aggregate or admixtures are used to produce it [50, 51, 206], AFm- Cl_2 ($[Ca_4Al_2O_6]^{2+} \cdot (Cl^-)_2 \cdot mH_2O$) can also be present in cement hydration products. Both CaAl LDHs have strong ability to remove toxic soluble anions [39, 58, 59, 61] via surface adsorption and anion exchange processes.

Selenium (Se), is considered as both an important micronutrient and a severe environmental hazard, and has attracted extensive attention because both deficient ($<40 \text{ mg d}^{-1}$) and excess ($>400 \text{ mg d}^{-1}$) intake can lead to disease or even death [22, 207]. Furthermore, the radioactive isotope ^{79}Se ($t_{1/2} = 3.77 \times 10^5 \text{ y}$) is considered one of the few radionuclides that can dominate the ultimate biosphere exposure over geological time scale according to a scenario analysis[9]. Thus, it is necessary to find out how the mobility of the soluble selenium species[208] (e.g., SeO_3^{2-}) could be influenced by interaction with mineral surfaces in geologic nuclear waste repositories, in which cementitious material will act as physical, but also a chemical barrier.

Se(IV) uptake by various LDHs has been reported previously and the local complexation environment of resulting intercalated selenium is still debated. For instance, adsorbed SeO_3^{2-} on AFm- SO_4 has been described as bound in a chemical environment via outer-sphere

complexation (OSC) [37, 60]. Inner-sphere complexation has been identified to be the leading mechanism for selenite removal on MgAl-CO₃ LDHs[176]. Other studies[209, 210] show changes in the basal spacing of LDHs (e.g., MgAl LDHs, ZnAl LDHs, and ZnFe LDHs) upon interactions with SeO₃²⁻. The correlation between intercalated anions and layer-to-layer distances of LDHs has attracted extensive attention. It was demonstrated that the interlayer distance varied with the nature of intercalated anions and the water content for hydrocalumite[211]. Miyata [212, 213] pointed out that the increase of interlayer distances agrees with that of the intercalated ionic radii for hydrotalcite-like minerals, being inversely proportional to the mineral equilibrium constants. Besides, hydration state, hydrogen-bonding network, and ionic charge in the inter-layer environments can largely contribute to the LDHs swelling behavior and dynamics [214-216]. However, a detailed discussion, based on molecular-level experiments about the structural configurations of intercalated anions in CaAl LDHs, is still not well-documented.

This study addresses the anion exchange process of Se(IV) oxyanions in CaAl LDHs, the widespread cementitious materials acting as effective barriers in nuclear waste repositories. Using a combination of sorption experiments, in-situ time resolved synchrotron XRD, and X-ray absorption spectroscopy (XAS), this work aimed at explaining the coordination environment of intercalated SeO₃²⁻ and the resulting basal spacing change. By comparing with other anions, i.e., Cl⁻, SO₄²⁻, and MoO₄²⁻, intercalated in CaAl LDHs, a relationship between inter-layer anion structure and their basal spacing was established, further indicating the stability of these phases. This integrated approach allows a detailed account of anion exchange processes at work in CaAl LDHs based on kinetics and thermodynamics.

3.2. Materials and methods

3.2.1. Materials and chemicals.

Two types of Ca-Al LDHs, monosulfoaluminate (AFm-SO₄) and Friedel's salt (AFm-Cl₂), were synthesized and reacted. Generally, the Ca-Al LDHs were prepared by mixing stoichiometric amounts of tricalciumaluminate (C₃A, [Ca₃Al₂O₆]) with the corresponding calcium salts [217]. Specific synthesis procedures and characterizations can refer to Section 2.2.1 [217, 218]. Freshly synthesized CaAl LDHs have well-crystallized hexagonal-shape plate morphology (Figure S2.2) but different average sizes: AFm-Cl₂ is smaller than AFm-SO₄. Eventually, the experimental chemical formula of AFm-SO₄ and AFm-Cl₂ were

determined as $\text{Ca}_4\text{Al}_2\text{O}_6(\text{SO}_4)_{0.92}(\text{OH})_{0.08} \cdot 6.4\text{H}_2\text{O}$ and $\text{Ca}_4\text{Al}_2\text{O}_6\text{Cl}_{1.64}(\text{OH})_{0.36} \cdot 7.4\text{H}_2\text{O}$ [217], respectively.

Deionized water (18.2 M Ω ·cm) was firstly degassed and then used for all solutions. All the chemicals, including $\text{Na}_2\text{SeO}_3 \cdot 5\text{H}_2\text{O}$ (purity > 99%), were purchased from Sigma Aldrich and were analytical grade. All experiments were carried in a N_2 -filled glove box ($\text{O}_2 < 2$ ppm), using NaOH as an extra CO_2 trap to prevent possible CO_2 contamination.

3.2.2. Adsorption experiments.

Kinetics of CaAl LDHs' dissolution and selenite sorption were investigated. An equilibrium time of 48 h was chosen, the dissolution equilibrium being reached in ~12 h, for sorption experiments. Batch sorption experiments were conducted in the glove box at ~25 °C as a function of initial selenite concentration. Selenite loadings ranged from 0.01 to 1 mM at a L/S (liquid to solid) ratio of 500. Thus, the resulting molar ratios of inter-layer $\text{SO}_4^{2-}/(\text{Cl}^-)_2$ to introduced SeO_3^{2-} varied from 500 to 5, approximately. The solution pH was maintained at 12.4 (the pH value of the CaAl LDHs synthesis suspension) using a 2 M NaOH solution. A combined glass pH electrode (Metrohm 6.0233.100) connected to an Orion (525A) pH meter was used for pH determination, straight after its calibration by pH buffer solutions with manual temperature compensation. All suspensions were reacted on an end-over-end shaker. Aliquots of 4 mL of suspension were taken from each reactor at two reaction times, once reached equilibrium (to determine initial Ca, Al, S, and Cl concentrations) and once reached selenite sorption equilibrium (to determine Ca, Al, S, Cl and Se concentrations in equilibrium). The suspension samples were filtered through Chromafil® 0.22- μm syringe filters and the filtrate was analyzed by inductively coupled plasma optical emission spectrometry (ICP-OES) with a Varian 720-ES apparatus. The released Cl^- concentration was determined by ion chromatography (IC, Metrohm 883). The distribution ratio (R_d) was then calculated (Text S3.1).

Three solid samples for each CaAl LDH were selected to be studied by synchrotron based X-ray spectroscopic methods, which were denoted by *Cl_i* (*Cl* represents AFm- Cl_2) and *Si* (*S* represents AFm- SO_4), with initial SeO_3^{2-} concentrations $i = \text{A}$ (0.05 mM), B (0.1 mM), and C (1.0 mM), respectively.

3.2.3 Aqueous data modelling.

The THERMOCHEMIE database[193] and the PHREEQC code[192] were employed to reproduce the sorption isotherms of SeO_3^{2-} on CaAl LDHs, and also to calculate the saturation index (SI) value of each potentially formed solid phase. A non-electrostatic model was used to describe SeO_3^{2-} surface complexation on Ca-Al LDHs.

3.2.4 In-situ time-resolved XRD.

The XRD experiments were performed at the CRISTAL beam line (SOLEIL synchrotron). The self-designed in-situ set-up includes a closed anaerobic tubing system, with Ca-Al LDHs suspension circulating inside and through the connected polyimide capillary intercepting the beam, all parts being sealed with PEEK nuts and ferrule fittings (IDEX Health & Science). First, the Ca-Al LDHs were equilibrated with water at pH 12.4 under constant stirring, and circulation. Then, certain portions of selenite were introduced step by step to reproduce the three selected concentrations in batch sorption experiments, until the ratio of Cl_2/SO_4 to Se was about 1:1. In the case of AFm- Cl_2 , a higher selenite loading, with a ratio equal to 1:2, was tested, in order to examine the LDH stability when exposed to an overload of anions. For each step, continuous XRD pattern acquisitions lasted for 1-2 hours so the conditions approached as much as possible to equilibrium. Diffraction patterns were recorded on a MAR345 image plate detector with an exposure time of 5 s at the wavelength of 0.978 Å (~12.8 keV). The wavelength and detector-to-sample distances were calibrated using a NIST LaB_6 standard. With the additional detector's read-out and refresh time, the time resolution of data acquisition was 150 s. The images were converted into a one-dimensional XRD pattern using the program Fit2D[219], after which the background was subtracted.

3.2.5 Solid phase characterization.

Three selected sorption products were characterized by synchrotron based high-energy X-ray diffraction (HEXD) and pair distribution function (PDF) analysis at the CRISTAL beamline at SOLEIL Synchrotron, in order to determine the structure of the phase after sorption. The same X-ray beam wavelengths, instrumental setup, and data treatment used in our previous work[217] were applied.

Selenium K-edge X-ray absorption spectroscopy (XAS) measurements were performed at the Core Level Absorption & Emission Spectroscopy (CLÆSS, BL22) beam line with a source of multipole wiggler at the Spanish ALBA-CELLS synchrotron facility, Barcelona, Spain. An

Amptek Cadmium Telluride (CdTe) fluorescence detector was used for data collection. Sulfur K-edge XAS experiments were conducted at the XAFS beamline of synchrotron Elettra, Basovizza, Trieste[220]. A Si(111) double-crystal monochromator was used with about 0.3 eV resolution at 2.5 keV. The fluorescence signal was recorded using a silicon drift detector (KETEK GmbH AXAS-M with an area of 80 mm²). All the samples for XAS were sealed using polyimide tape (double-faced sealing for selenium samples, but one-side pasting for sulfur samples), mounted on a sample holder, and measured in fluorescence mode, except of Na₂SeO₃·5H₂O reference, which was prepared as a pellet with boron nitride matrix and measured in transmission mode. Before being transferred into the vacuum experimental chamber, samples were stored under N₂ atmosphere. A liquid N₂ cryostat was used to lower the temperature to 77 K, in order to minimize the effects of thermal disorder due to atomic vibrations. Data integration and reduction of X-ray absorption near edge structure (XANES) spectra (Athena), as well as the data fitting of the EXAFS spectra (Artemis)[196], were performed using the Demeter software package. The k^3 -weighted EXAFS functions were Fourier transformed (FT) in a k range 4.0-12.5 Å⁻¹ using a Kaiser-Bessel window. Theoretical backscattering paths were calculated by FEFF8.4[197], to perform the fit in back-transformed reciprocal space (k).

3.3. Results and discussion

3.3.1 Batch sorption isotherm.

As shown in Figure 3.1, selenite sorption isotherms (sorbed Se *vs.* [SeO₃²⁻]_{aq} at equilibrium) on both CaAl LDHs can be described by the thermodynamic model developed previously for MoO₄²⁻[217], which includes surface adsorption, precipitation of a new LDH phase (AFm-SeO₃), and precipitation of CaSeO₃ with increasing Se loading. These sorption mechanisms in sequent are also in good agreement with the following spectroscopic results and any exclusion of the three mechanism would not reproduce the sorption isotherms well. Related aqueous data is shown in Table S3.1 to S3.4. The log*K* values of AFm-SeO₃ formation and CaSeO₃ precipitation were obtained from the sharp increase of sorbed Se in the case of AFm-Cl₂ and AFm-SO₄, respectively.

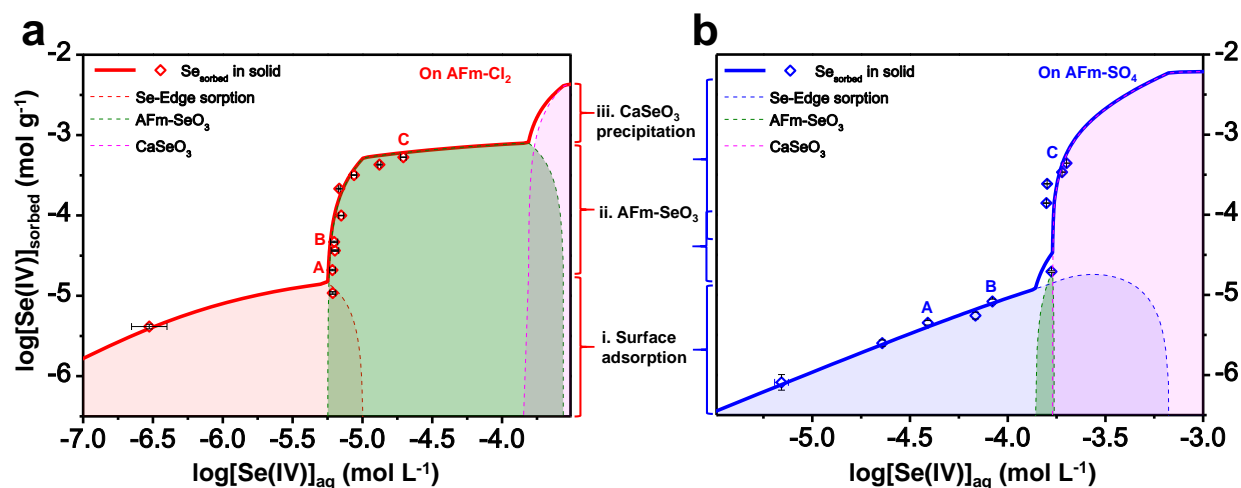


Figure 3.1. Sorption isotherm of selenite on AFm-Cl₂ (a) and AFm-SO₄ (b) at 48 h equilibration time. Bold solid curves are the fitting results regarding the amount of sorbed Se in solid. Each area under dash curve represents the dominated solid sorbate of each sorption stage. Selected adsorption products for X-ray spectroscopic techniques on each AFm phase are denoted by A, B, and C on these Figures (see Method section), and correspond to increasing selenite loading.

The surface site density (mol sites/gram solid) obtained for AFm-Cl₂ (2.0×10^{-4}) via PHREEQC modelling was closed to the one (3.2×10^{-4}) obtained for AFm-SO₄, based on the equilibrium reactions, listed in Table S3.5. Differing from the MoO₄²⁻ case[217], no relationship between surface edge area and surface site density can be established in the case of SeO₃²⁻ sorption, suggesting that SeO₃²⁻ adsorption is not only taking place on surface edge sites. However, a larger surface complexation equilibrium constant was obtained for AFm-Cl₂ ($\log K = 3.6$), than for AFm-SO₄ ($\log K = 0.5$). In Figure 3.1b, the steep increase of sorbed Se can only be reproduced adequately by adding $-0.89 \log$ units to the CaSeO₃·H₂O solubility, of which original $\log K$ value in the THERMOCHEMIE database is -6.4 . Besides, the complexation constant of Ca-SeO₃ ion pair from [221] was added in the input code as $10^{3.17}$. The $\log K$ value (-7.29) of CaSeO₃ obtained in this work is in very good agreement with the experimental value (-7.27) obtained by Baur et al[58]. An identical $\log K$ value for the formation of AFm-SeO₃ ($\log K = 73.7$, fitted) was applied in the sorption isotherm of AFm-SO₄, presenting a strong overlap with the formation of CaSeO₃. It is intriguing that precipitation of AFm-SeO₃ and CaSeO₃ almost occurred simultaneously in the case of AFm-SO₄. Thus, the obtained $\log K$ value of -7.29 should not only derive from CaSeO₃ precipitation alone, but more likely from the two mixed SeO₃²⁻-bearing phases, in which the structural configuration of SeO₃²⁻ could be diverse. Similarly to previous published work[58], no obvious structural changes can be observed in HEXD and PDF patterns (Figure S3.1 and

S3.3), exception made of small amounts of secondary mineral phases (e.g., katoite and ettringite). An explanation to the lack of evidence of structural changes could be the diverse structural configurations of sorbed Se on AFm-SO₄, which is also indicated by our sorption isotherms modeling. Regarding AFm-Cl₂, Se-O distance peak at 1.66 Å and possible inter-layer space enlarging were observed from differential PDF (d-PDF) (Figure S3.2). The inter-layer peak shift of sample ClC was also displayed in HEXD results (Figure S3.1, details explained in Text S3.2), compatible with a mechanism of anion exchange.

Se removal efficiency on CaAl LDHs is very high. For AFm-Cl₂, more than 94% selenite was removed within 48 h. Concomitantly, a proportional amount of inter-layer Cl⁻ was released. As a result, a much larger average R_d value of ~ 17800 L kg⁻¹ was obtained for AFm-Cl₂, in comparison to that of ~ 705 L kg⁻¹ for AFm-SO₄. Besides, aqueous Ca, Al, and Cl/SO₄ concentrations were also adequately described by the model (Figure S3.4), with 1.5 mM Cl⁻ impurity allowance and a little adjustment of CaAl LDHs solubility (+0.16 log unit on $\log K = 74.93$ for AFm-Cl₂, and +0.4 log unit on $\log K = 73.07$ for AFm-SO₄). Aqueous results indicate that AFm-Cl₂, as an anion exchanger, has larger sorption capacity and higher affinity for Se, probably due to its more easily exchanged inter-layer Cl⁻ than the divalent oxyanion SO₄²⁻.

3.3.2. In-situ time resolved XRD.

Changes in layer-to-layer distance ($d_{\text{interlayer}}$), caused by the intercalation of anions in Ca-Al LDHs, has been followed in *real-time* through an *in-situ* study of XRD reflections. *In-situ* time resolved XRD experiments were performed on CaAl LDHs suspension with $d_{\text{interlayer}} = 9.01 \pm 0.02$ Å for AFm-SO₄ and $d_{\text{interlayer}} = 7.96 \pm 0.01$ Å for AFm-Cl₂. The $d_{\text{interlayer}}$ value for AFm-SO₄ is in accordance with the value reported under 100% humidity condition[201]. Se was then added in four steps (reproducing the A to C, three Se loadings in sorption isotherm, with S/Cl₂:Se ratios ranging from 100 to 5), with a last step introduction of a stoichiometric amount (1:1) of Se. At each concentration, the subscripts 0 and t represent the first acquisition once selenite was added and the final one, after 1 to 1.5 h equilibration, respectively (Figure S3.5-S3.6). A peak shift towards low angles was observed in the 4° to 8° angular range in 2θ ($\lambda = 0.9782$ Å), attributed to a layer-to-layer distance increase. An enlarged view of this diffraction peak is shown in Figure 3.2. For AFm-Cl₂, above the ClB concentration, the d_{001} peak shift towards low angles can be observed, indicating that the layer-to-layer distance increased due to SeO₃²⁻ intercalation. For ClD₀, a large contribution to the multiple and broad

d_{001} peak could be compatible with randomly ordered interstratification (R0 interstratification)[222]. Although AFm- SeO_3 formation mechanism should also predominate in CIB sample based on batch sorption isotherms, no visible peak shift can be detected due to the low Se loading ($\text{S}/\text{Cl}_2:\text{Se}$ ratio = 50:1). Eventually, two inter-layer distances of 11.01 ± 0.01 Å and 9.99 ± 0.01 Å were obtained under the stoichiometric loading, which differed from that of AFm- MoO_4 , which had a single value of 10.37 ± 0.07 Å observed (Figure 2.2).

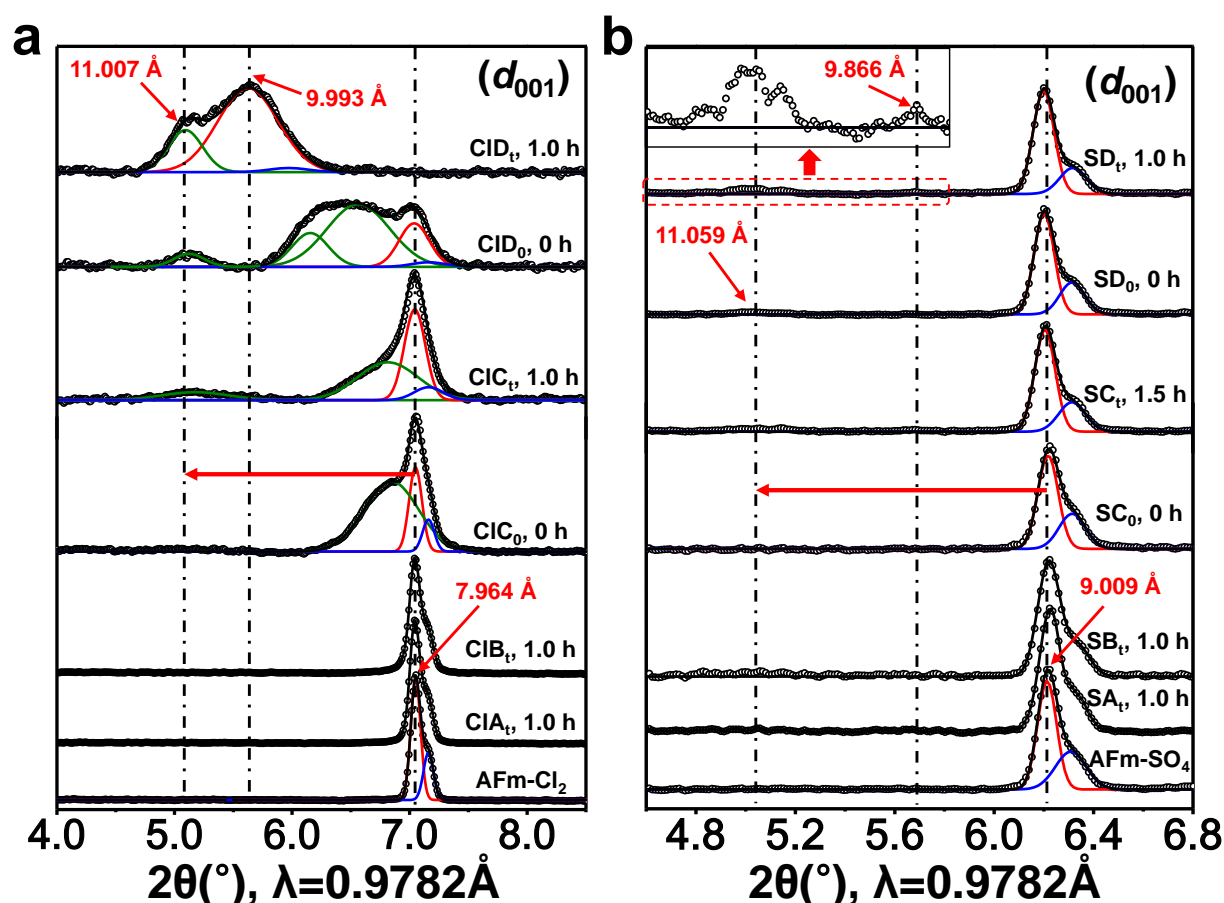


Figure 3.2. In-situ time resolved XRD patterns of inter-layer peak details. (a) XRD patterns collected for selenite uptake on AFm- Cl_2 . (b) XRD patterns on AFm- SO_4 . Inset is the partially enlarged patterns of SD_t , with the original signal marked with red dashed lines. The experimental data, plotted with black circles, are fitted with Gaussian function (indicated by curves in color). The black curves represent the total fitted curves. The equilibrium time for each step is shown following the sample name. The small shoulders of inter-layer peaks at slightly higher 2θ values, displayed in blue color, may be attributed to different swelling levels of the stacked crystalline layers.

These two distances may result from different complexation configurations of intercalated SeO_3^{2-} , rather than on other possible intercalated anions (e.g., OH^- , resulting in interlayer space of 5.35 Å and 7.23 Å at relative humidity of 0% and 97%, respectively [201]) or differing polytypes and space groups of CaAl LDHs. Indeed, many possible polytypes, e.g., 1R, 3R, 6R, 1H, 2H, 3H, and 6H, can exist in hydroxycalcite-like minerals[223]. Some of them

may further affect the true symmetry or space group, giving different intensity and positions of XRD peaks. However, the resulting layers spacing difference is much smaller than the difference of $\sim 1 \text{ \AA}$ observed here. For instance, the two space groups of AFm-Cl₂, C2/c at room temperature and $R\bar{3}$ (same with AFm-SO₄[224]) above 30 °C, only lead to an interlamellar distance difference of 0.06 Å [225]. Besides, it is intriguing that the spacing of 11.01 Å was almost immediately reached, while that of 9.99 Å was obtained through a relatively slow evolution of 1-2 hours, suggesting that the Se configuration in CIC for larger basal spacing was kinetically favored while that for smaller spacing may be the thermodynamic equilibrium state. The inter-layer swelling of AFm-SO₄ was less obvious than for AFm-Cl₂, indicating that intercalated SO₄²⁻, as divalent anion is more difficult to exchange, leading to a lower exchange capacity towards SeO₃²⁻ compared to Cl⁻. However, two swelling peaks also can be observed at $11.06 \pm 0.01 \text{ \AA}$ and $9.87 \pm 0.01 \text{ \AA}$, with similar distances to the case of AFm-Cl₂. The two coherent inter-layer peaks, probably representing two intercalated SeO₃²⁻ configurations, occurred in both SeO₃²⁻ sorption products of CaAl LDHs. The two possible coordination environments of intercalated SeO₃²⁻ were further investigated.

3.3.3. Sorbed Se coordination.

First, the +4 oxidation state of sorbed selenium was determined using Se K-edge XANES spectra (Figure S3.7). EXAFS data of the six sorption products and of a Na₂SeO₃ reference are shown in Figure 3. Na₂SeO₃ reference only reveals a single oscillation frequency in the k^3 -weighted EXAFS (Figure 3.3a), resulting from the first Se-O shell. After FT (Figure 3.3b), a characteristic distance of $d_{Se-O} = 1.70 \text{ \AA}$ was obtained. All Se-reacted AFm-SO₄ samples (SA, SB, and SC) show only one oscillation frequency and thus one neighbor shell in the FT, which corresponds to Se-O backscattering pair with 1.70 Å bond length. The lack of further neighbors in sample SA and SB indicates that the selenite ion is adsorbed on the surface of AFm-SO₄ as an outer-sphere complex (OSC), facilitated by the positive surface charge of the layer[226]. Regarding sample SC, simultaneous precipitation of AFm-SeO₃ and CaSeO₃ dominate the Se uptake process, based on the modelling hypothesis of sorption isotherms. The absence of a second Se neighbor shell, also observed in previous work[60], might be due to various structural configuration of SeO₃²⁻ and highly disorder structures of the newly precipitated Se-bearing phases. Regarding AFm-Cl₂ sorption products, sample CIA, still predominated by a surface adsorption mechanism, also shows a single Se-O shell peak at 1.70

Å in its R space, similar to samples SA and SB. In summary, SeO_3^{2-} adsorbed on the surface of CaAl LDHs form outer-sphere surface complexes. Furthermore, samples CIB and CIC show similar features. In addition of the Se-O peak at 1.70 Å, fits of these spectra yield a second shell at $d \sim 3.5$ Å, attributed to two Se-Ca backscattering pairs (Table S3.6). AFm- SeO_3 formation dominates the Se sorption in CIB and CIC. It can be concluded that an inner-sphere bidentate binuclear complex could be formed in Ca-Al-O layers, between selenite and two surface oxygen atoms that are bonded to two individual Ca atoms. A Se-Ca backscattering path ($R \sim 3.22$ Å) derived from CaSeO_3 phase was also checked for EXAFS fit, but did not match the spectra.

According to these EXAFS results, the intercalated SeO_3^{2-} is present as an inner-sphere complex for sample CIB and CIC. However, this conclusion still cannot explain the two observed inter-layer distances of AFm- SeO_3 , resulting from at least two possible selenite structural configurations. This leads us to conclude that both inner-sphere and outer-sphere complexes are present in the interlayer.

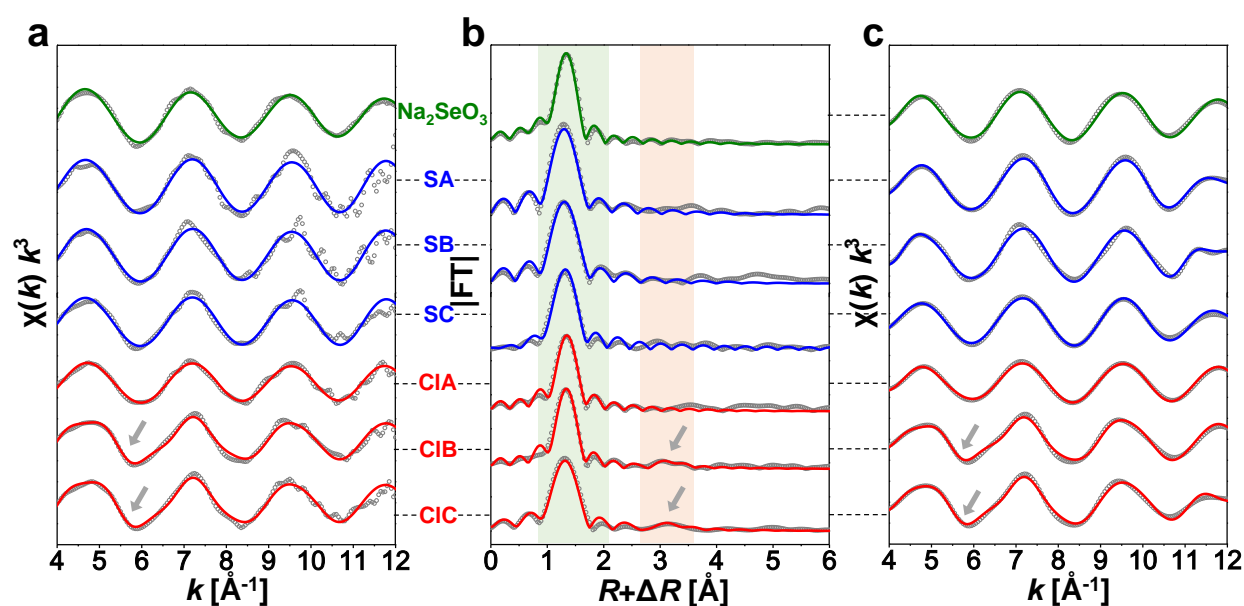


Figure 3.3. Experimental Se K-edge EXAFS spectra of the selected sorption products from batch sorption experiment and of a Na_2SeO_3 reference. (a) k^3 -weighted EXAFS oscillations. (b) Fourier transformed (FT) EXAFS signals (not corrected for phase shift) with the first shell highlighted in green and the further shell in champagne. (c) Back-Fourier transformed EXAFS signal (ranging from 1.00 to 4.00 Å). For samples curves, the gray circles are the experimental data and the solid lines are fit results. Red, blue, and olive-green solid lines represent the fit results of AFm- Cl_2 samples, AFm- SO_4 samples, and reference, respectively.

3.3.4. Sulfur K-edge EXAFS results.

In order to establish a relationship between intercalated anion identity and basal spacing of CaAl LDHs, the complexation environment of intercalated SO_4^{2-} and MoO_4^{2-} ions was examined by EXAFS. S K-edge XAS results for AFm- SO_4 , a complete anion exchange product of AFm- Cl_2 (named AFm- Cl_2 - SO_4), and a Na_2SO_4 reference are shown in Figure 3.4. Overall, the two samples show very similar features. Both intercalated sulfur species have +6 oxidation state (Figure 3.4a). The variations of feature peaks (i.e., A, B, C, and D regions in Figure 3.4a) from crystalline Na_2SO_4 reference can be assigned to the more unconstrained and hydrated SO_4^{2-} in AFm- SO_4 [227]. As shown in Figure 3.4b, only one oscillation frequency is observed in k^3 -weighted EXAFS spectra of AFm- SO_4 and AFm- Cl_2 - SO_4 . In comparison, more oscillation frequencies are present in the Na_2SO_4 reference. After FT (Figure 3.4c), fits of Na_2SO_4 data yield four S-O backscattering pairs at $d \sim 1.48$ Å and another neighbor shell for S-Na and S-O (Table S3.7). In contrast, the two samples have only one neighbor shell, attributed to the S-O pair at $d \sim 1.48$ Å. Conclusively, sulfur EXAFS data show intercalated SO_4^{2-} in both synthesized AFm- SO_4 and AFm- Cl_2 sulfate exchange product to form OSC. In addition, it could be predicted that intercalated Cl^- ions also prefer staying unconstrained due to their lower charge and higher exchangeability than SO_4^{2-} , and also the strong hydration shell observed in solution[228, 229]. Regarding intercalated MoO_4^{2-} in CaAl LDHs, only one oscillation frequency (fitted by four Mo-O pairs) exists in its k^3 -weighted EXAFS spectra[217], indicating alias an OSC formation.

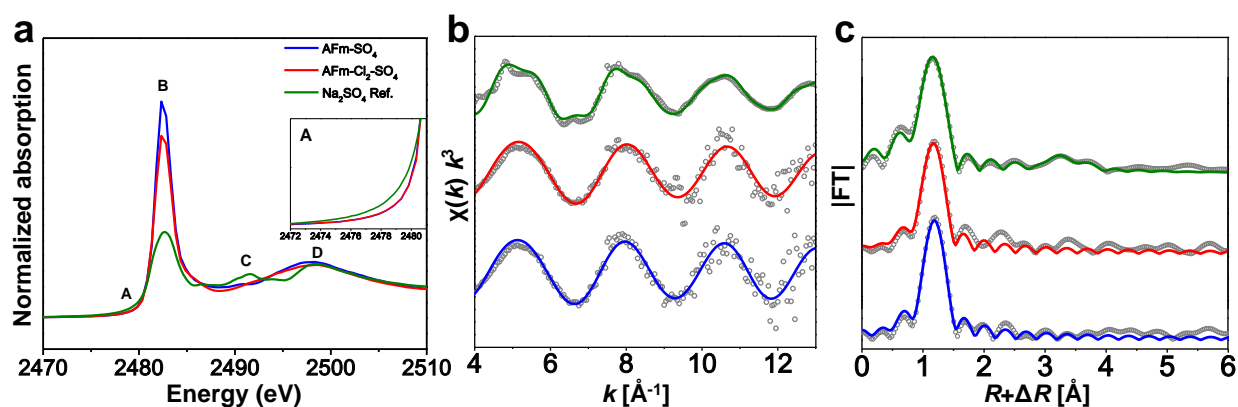


Figure 3.4. Experimental S K-edge XAS spectra of AFm- SO_4 , AFm- Cl_2 - SO_4 , and Na_2SO_4 reference. (a) XANES data (inset: their expanded section A). (b) k^3 -weighted EXAFS oscillations. (c) FT EXAFS signals (not corrected for phase shift). Gray circles are the experimental data and the solid lines are fit results.

3.3.5. Linear relationship between basal spacing and hydrated anions' radii.

Basal spacing of AFm-MoO₄ under extremely hydrated state was also obtained by *in-situ* XRD experiment, resulting in a mean distance value of 10.37 Å. Taking ions' hydration effect into account, Stokes radius (R_{stokes}) is considered as the sum of the ion's hard sphere radius and the thickness of its immobilized electrostatic first hydration layer. As shown in Table 3.1, according to the calculated R_{stokes} , AFm-MoO₄ should have a larger inter-layer spacing than AFm-SeO₃ due to its larger R_{stokes} . However, the existence of larger spacing value (11.03 Å) for AFm-SeO₃ indicates that the lone electron-pair of oxyanions with “-ite” postfix (e.g., selenite and sulfite) may contribute more to H-bonding with water molecules than the oxygen atoms bonded to the hydrated anion. However, the hydrated radii of oxyanions with lone pairs can be identified experimentally by large angle X-ray scattering (LAXS) technique (also called PDF) [230]. For hydrated anions in aqueous solution, it could be more reasonable to use distances between central atoms and the hydrogen-bonded water molecules, instead of R_{stokes} . By employing the value of 11.03 Å for AFm-SeO₃, the basal spacing of CaAl LDHs under 100 % humidity conditions (e.g., in aqueous solution) shows a good linear relationship with the hydrated anion diameter based on LAXS results (Figure 3.5). From the above discussion, intercalated Cl⁻, SO₄²⁻, and MoO₄²⁻ should stay as unbonded anions, indicating that the 11.03 Å spacing in Se sorption samples should also result from free hydrated sorbed SeO₃²⁻. The smaller spacing value of 9.93 Å deviates heavily from the linear relationship, and may originate from the inner-sphere SeO₃²⁻ complex that is confirmed by Se K-edge EXAFS data. The coordination number corresponding to the water shell decreases due to the inner-sphere complexation, leading to a decrease of the interlayer distance. This linear relationship will allow us to judge roughly whether intercalated anions have bonding contact (e.g., inner-sphere complexation) with the Ca-Al-O layers in CaAl LDHs.

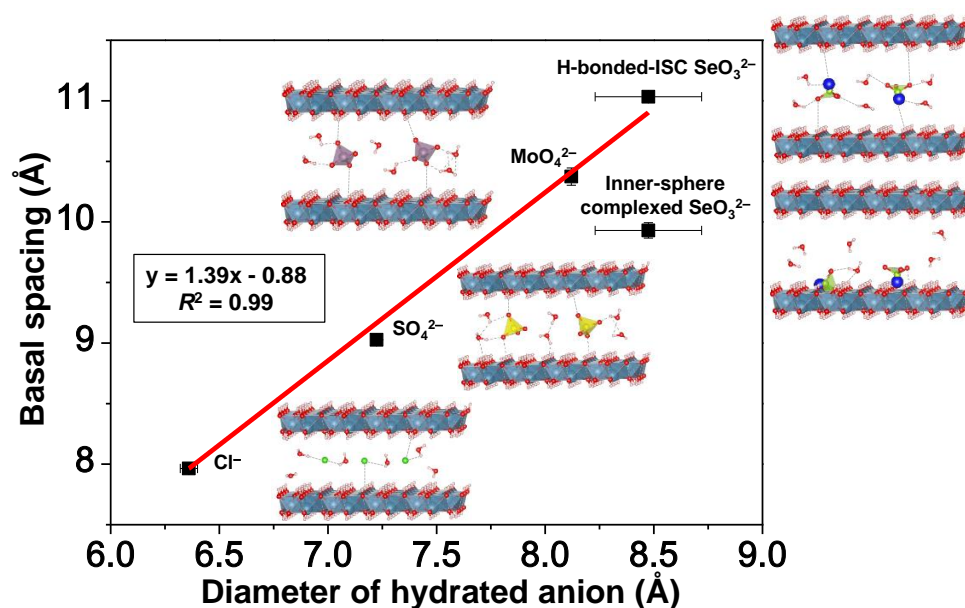


Figure 3.5. Linear relationship between basal spacing and hydrated anions' diameters. Schematic representation of CaAl LDH charged by each intercalated anion just adjoins the corresponding anion. The blue sphere attaching on selenite anion represents its lone electron-pair.

Table 3.1. Basal spacing of CaAl LDHs and hydrated anions' radii^a.

Anions	Basal spacing (Å)	Mean X...O _w (Å)	R _{stokes} (Å)
Cl ⁻	7.96(1)	3.16, 3.20[229, 231]	1.81+0.43[232]
SO ₄ ²⁻	9.03(2)	3.61[233]	2.32[234], 2.40+0.38[232]
MoO ₄ ²⁻	10.37(7)	4.06[235]	2.68+0.29[232]
SeO ₃ ²⁻	11.03(3)&9.93(6)	3.87(2)&4.36(8)[230]	2.49[236]

^a X...O_w: distance between central atom of anions and oxygen atom of hydrogen binding water molecules. For SeO₃²⁻, 3.87 and 4.36 Å are mean Se...O_w distances to the water molecules hydrogen binding to selenite oxygens and to those clustered outside the lone electron-pair, respectively. R_{stokes} represents Stokes radius, which is equal to the sum of ion radius and the hydration shell width. Uncertainties are given by the number in brackets on the last digit(s), i.e., 9.03(2) represents 9.03 ± 0.02.

3.3.6. Structural stability of AFm-SeO₃.

As shown in Figure 3.6, the structural stability of AFm-SeO₃ was examined by in-situ time-resolved XRD, after addition of twice as much selenite (Cl₂:Se ratio = 0.5) ions in CID sample (see Figure 3.2). Structural changes were followed by in-situ XRD every 150 s. From the left panel, an obvious change of layer-to-layer distance (*d*₀₀₁) peak was observed with time. Expanding the *d*₀₀₁ peak region into the right panel, two main peaks, at same position as in

CID_i can be obtained by Gaussian function fitting. Under excess selenite corrosion, the diffraction peak intensity at low 2θ value (in olive-green) decreased while the one at higher 2θ (in red) increased with contacting time. These two Gaussian peaks' areas and the area ratios are shown in Table S3.8. From the above discussion, the peak at lower 2θ originates from free intercalated SeO_3^{2-} ions and the corresponding LDH phase is kinetically favored. However, it is likely that more thermodynamically stable SFm- SeO_3 phase with inner-sphere complexed SeO_3^{2-} ion, as indicated by the Gaussian peak in red, will drive the reaction on the long term. It can be concluded that AFm- SeO_3 phase with free intercalated SeO_3^{2-} is kinetically favored but thermodynamically unstable, contrary to the phase with inner-sphere complexed SeO_3^{2-} .

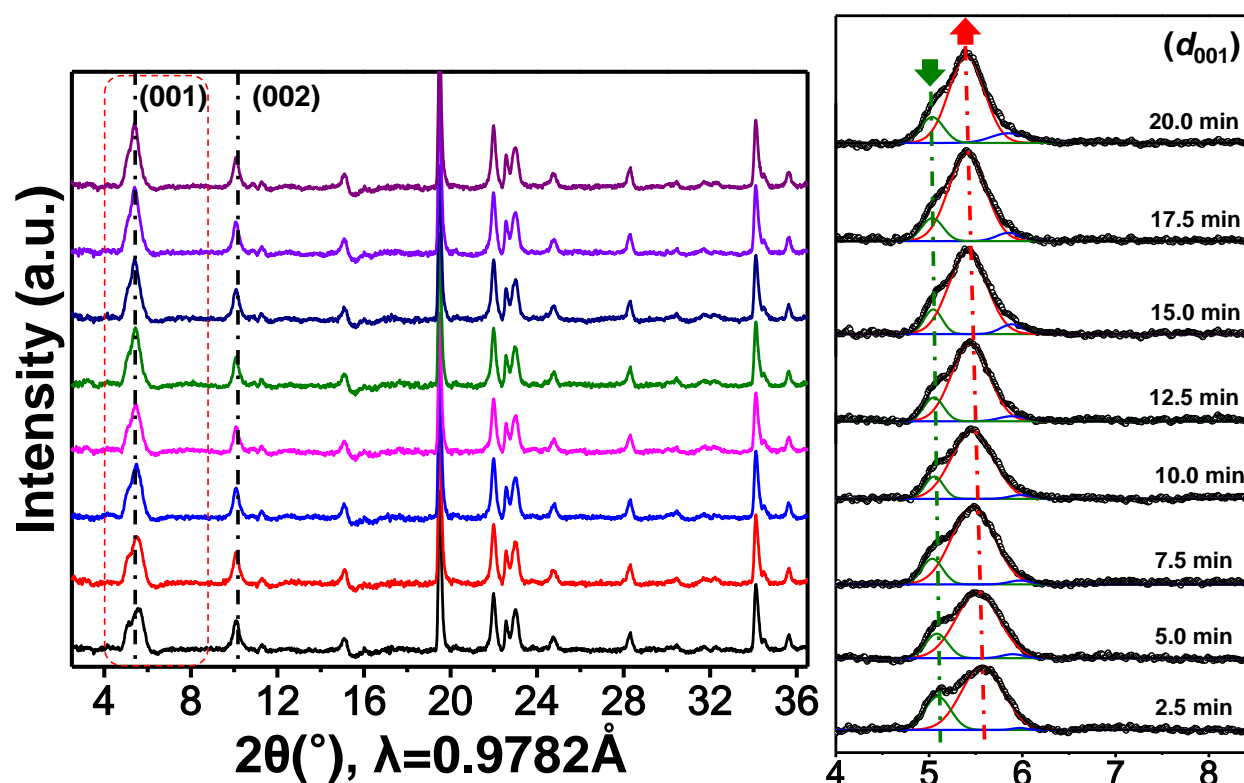


Figure 3.6. In-situ time resolved XRD patterns of Se(IV) reacted AFm- Cl_2 at the Cl_2/Se ratio of 1:2 (left panel) and the expanded basal spacing (d_{001}) peak region (right panel) with Gaussian function fits (indicated by curves in color). Time interval between each data collection is 150 s.

3.3.7. Environmental Implications.

CaAl LDHs can behave as anion exchangers under medium anion concentrations, and have potential for aquatic environment remediation but only at high pH values. In any case, anionic contaminants removal efficiency and the converted contaminant bioavailability largely depend on the complexation behavior of intercalated anions. By investigating the inter-layer distance and intercalated anion complexation environment in four CaAl LDHs (i.e., Cl^- , SO_4^{2-} ,

SeO₃²⁻, and MoO₄²⁻ saturated CaAl LDHs), this work established for the first time a linear relationship between hydrated anion radius and basal spacing of CaAl LDHs in solution. With this linear relationship, structural configurations of intercalated anions could be predicted preliminarily, as well as the structural stability of the corresponding phases. For instance, basal spacing values below the fitting line (Figure 3.5) would show more stable structures thus lower contaminant bioavailability, compared to the values on or above the line. This work provides also an insight into kinetic vs. thermodynamic control on preferred configurations of anions, potentially forming inner-sphere complexes (e.g., SeO₃²⁻, SO₃²⁻, and AsO₂⁻) when they are subject to the uptake by LDHs via anion exchange mechanisms. Finally, CaAl LDHs could act as efficient sink for SeO₃²⁻ via a variety of mechanisms depending on surface coverage, thus potentially retard ⁷⁹Se diffusion in a cement-based nuclear waste repository.

Supporting Information

Associated content

FE-SEM micrographs. Synchrotron based HEXD/PDF patterns of sorption products. PHREEQC modelling of aqueous results. In-situ time resolved XRD patterns. Se K-edge XANES spectra. Saturation index calculation. Tables for original aqueous data, equilibrium equations, and EXAFS refinement at Se and S K-edge.

Text S3.1. Calculation of distribution ratios.

The distribution ratio (R_d) was calculated by

$$R_d = \frac{C_0 - C_{aq}}{C_{aq}} \cdot \frac{V}{m} \quad (\text{L kg}^{-1}) \quad (\text{S3.1})$$

where C_0 and C_{aq} denote Se concentrations added initially and measured in solution at equilibrium (mol L^{-1}), respectively. V represents the volume of liquid phase (L) and m is the mass of the solid phase (kg).

Text S3.2. Characterization of CaAl LDHs sorption products by PDF/HEXD.

The selected each three sorption products of CaAl LDHs were studied by HEXD analysis and d-PDF method. As shown in Figure S3.1, no obvious phase structure change or possible inter-layer peak shift can be observed for AFm-SO₄ sorption products. Instead, small amounts of newly formed ettringite and originally contained katoite were detected, which was in agreement with saturation index (SI) computed from the aqueous phase composition after reaction of both CaAl LDHs with selenite for 48 h (Figure S3.8). AFm-SO₄ was supposed to be metastable with respect to katoite and ettringite[36]. The HEXD results indicated selenite could aggravate the metastability of AFm-SO₄ and promote the ettringite formation. Regarding AFm-Cl₂, inter-layer diffraction peak of sample ClC had an obvious shift towards small angles and no peak could be attributed to CaSeO₃ spectra.

Experimental PDF patterns of CaAl LDHs and their each three sorption products, calculated PDF patterns of katoite, ettringite, and CaSeO₃·H₂O, and also d-PDF patterns are shown in Figure S3.2 and Figure S3.3. In Figure S3.3, d-PDF peak at 3.86 Å could be the evidence of katoite and ettringite formation. Compared to fresh AFm-SO₄, Ca-O peak (at 2.42 Å) intensity of sample SC slightly decreased relative to that of Al-O (at 3.41 Å), which might suggest that Ca in Ca-Al-O layers was taken off due to the strong affinity of selenite. As shown in Figure S3.2, the experimental d-PDF yields a Se-O peak at 1.66 Å (attributed to

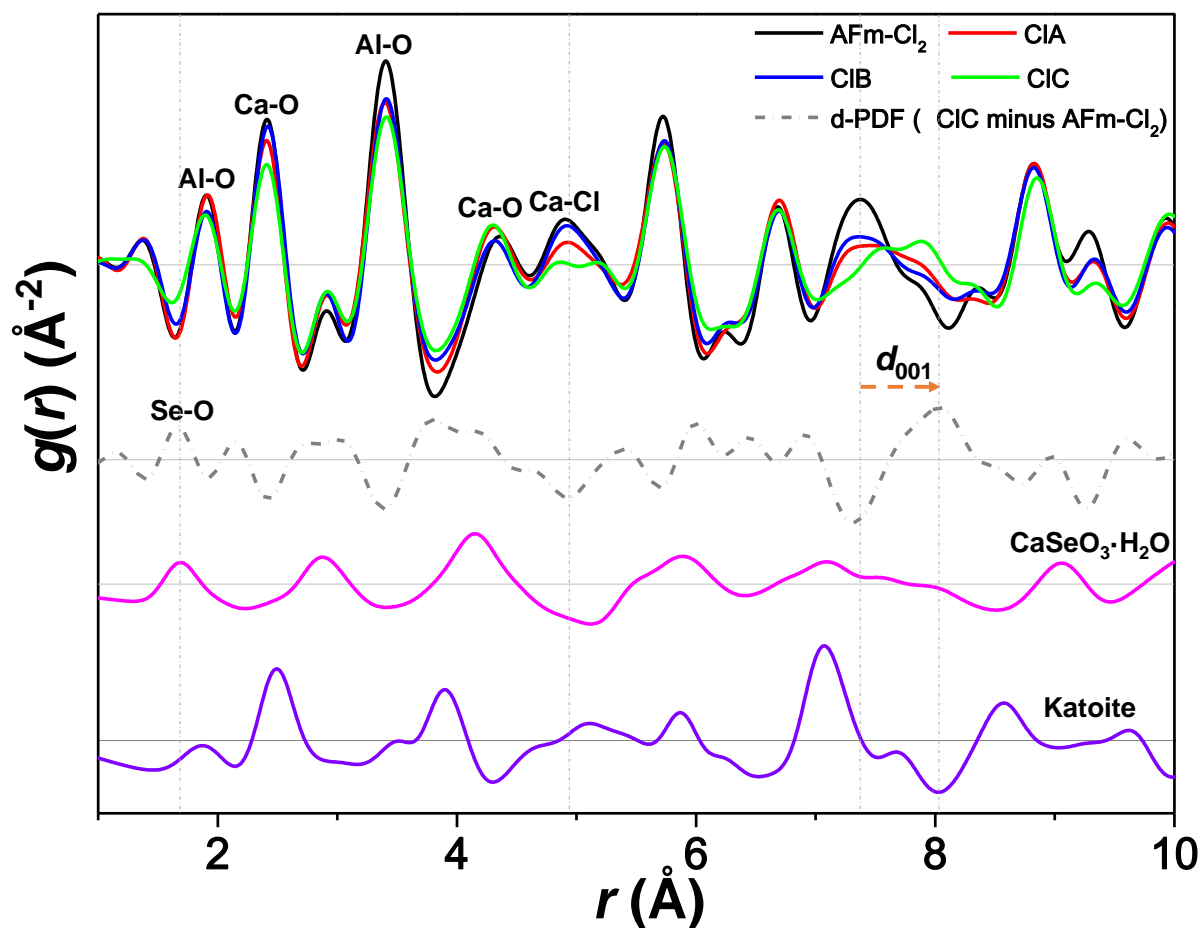


Figure S3.2. Top to bottom: experimental PDF of fresh AFm-Cl₂ and its selected three sorption products, d-PDF of sample CIC subtracting from fresh AFm-Cl₂, calculated PDF of CaSeO₃·H₂O and katoite.

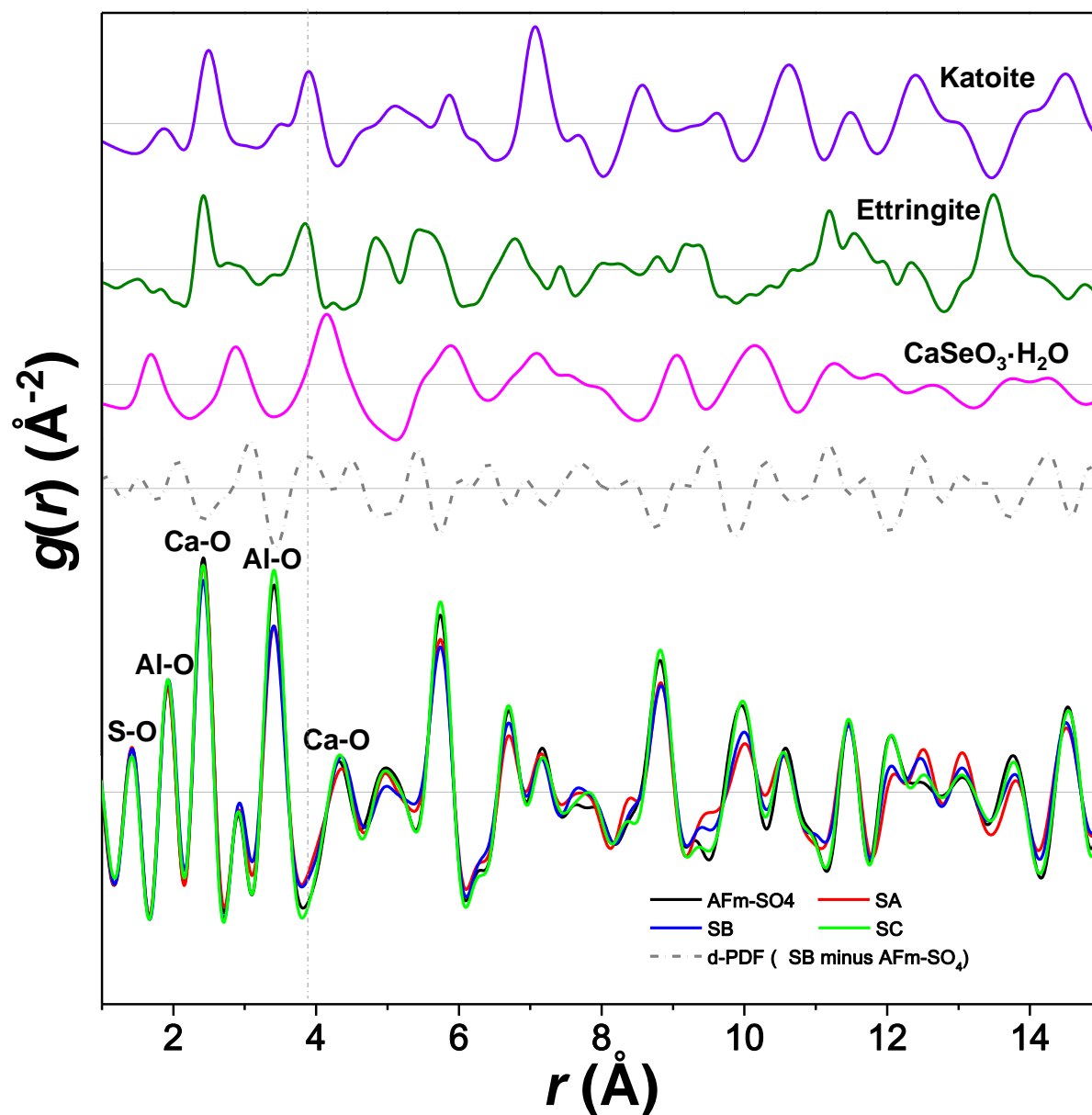


Figure S3.3. Top to bottom: calculated PDF of katoite, ettringite, and $\text{CaSeO}_3 \cdot \text{H}_2\text{O}$, d-PDF of sample SB subtracting from fresh AFm-SO₄, experimental PDF of fresh AFm-SO₄ and its selected three sorption products.

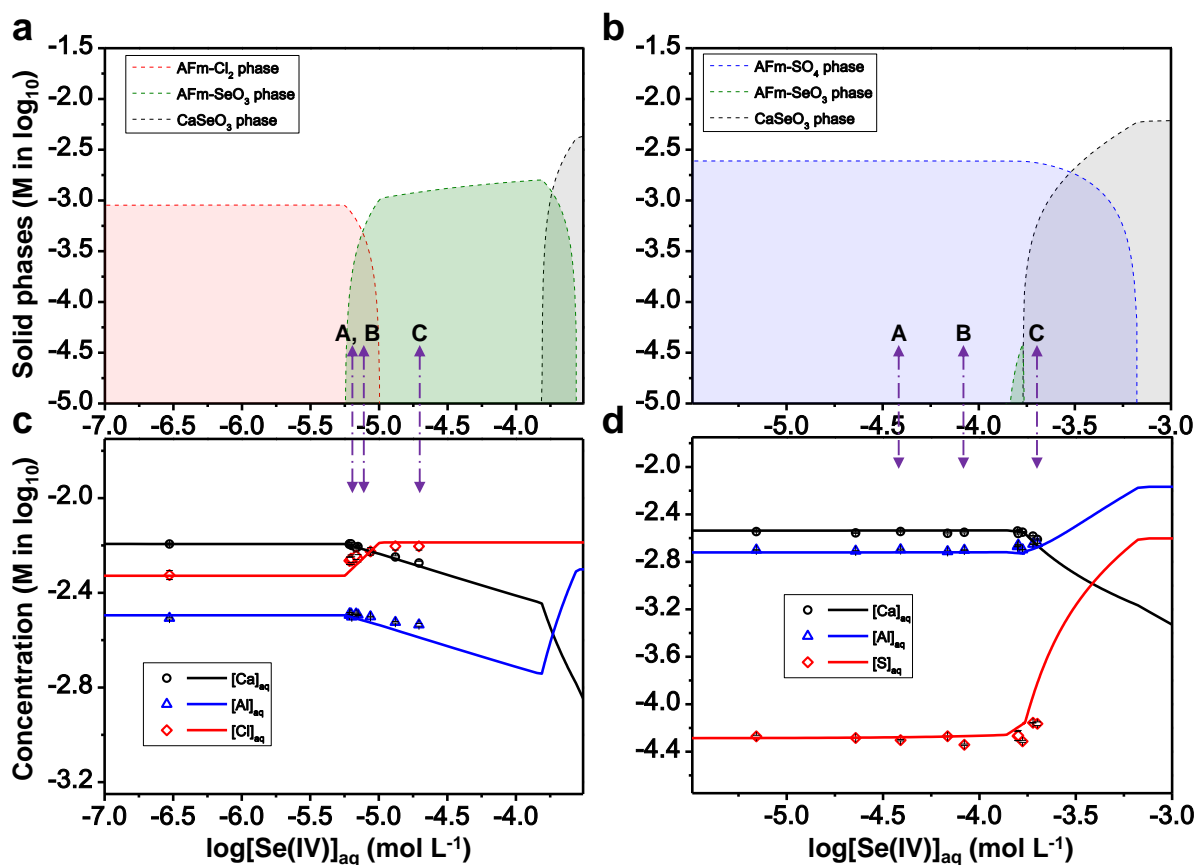


Figure S3.4. PHREEQC modelling results as a function of $[\text{Se(IV)}]_{\text{aq}}$ in equilibrium. (a) Dominated solid speciation in AFm-Cl₂ reactors. (b) Dominated solid speciation in AFm-SO₄ reactors. (c) Modelling results of aqueous Ca, Al, and Cl concentrations in AFm-Cl₂ reactors. (d) Modelling results of aqueous Ca, Al, and S concentrations in AFm-SO₄ reactors. Reactors, marked by A, B, and C, correspond to the same ones in Figure 3.1.

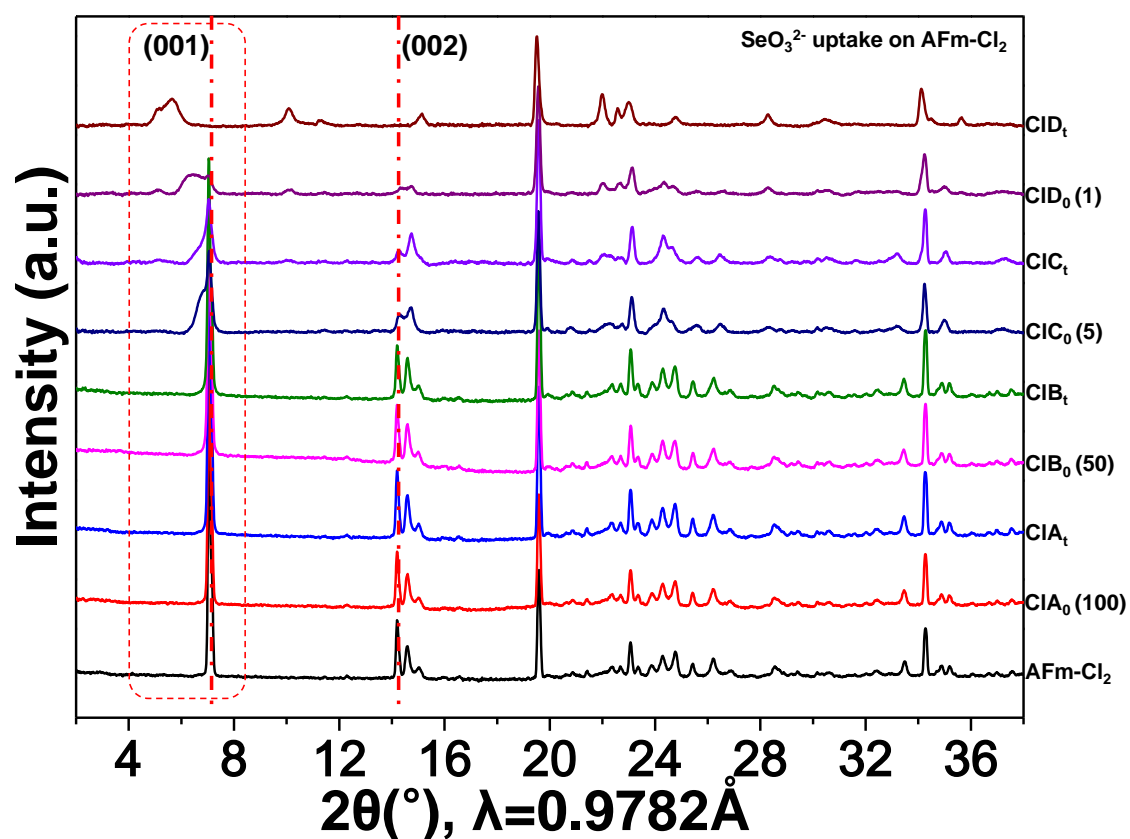


Figure S3.5. In-situ time resolved XRD patterns of reacted AFm-Cl₂ at each loading step. The diffraction peak range of layer-to-layer distance (d_{001}), circled by red dotted lines, is enlarged in the main text to provide more details. The Cl₂/SeO₃ ratio at each step is shown following the sample name. Main phase of CID_t can be AFm-SeO₃, with no obvious signal of katoite and powellite observed.

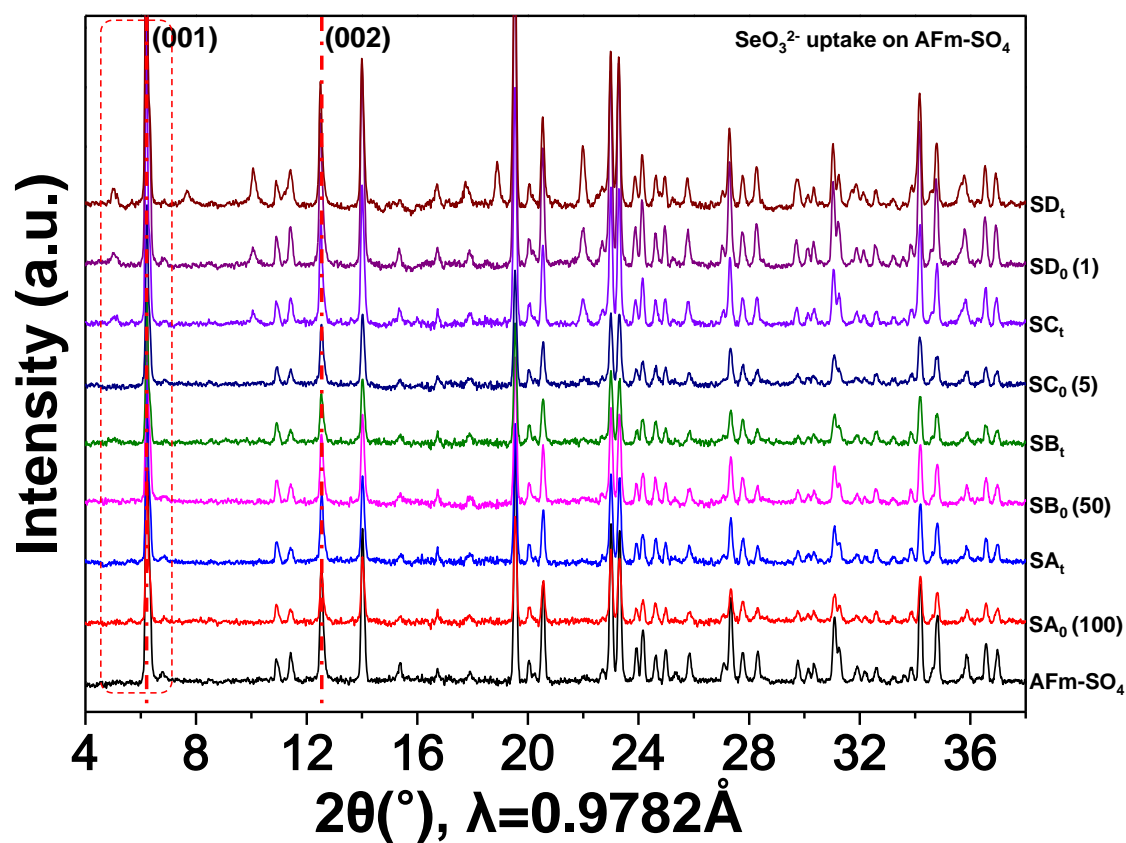


Figure S3.6. In-situ time resolved XRD patterns of reacted AFm-SO₄ at each loading step. The diffraction peak range of layer-to-layer distance (d_{001}), circled by red dotted lines, is enlarged in the main text to provide more details. The SO₄/SeO₃ ratio at each step is shown following the sample name.

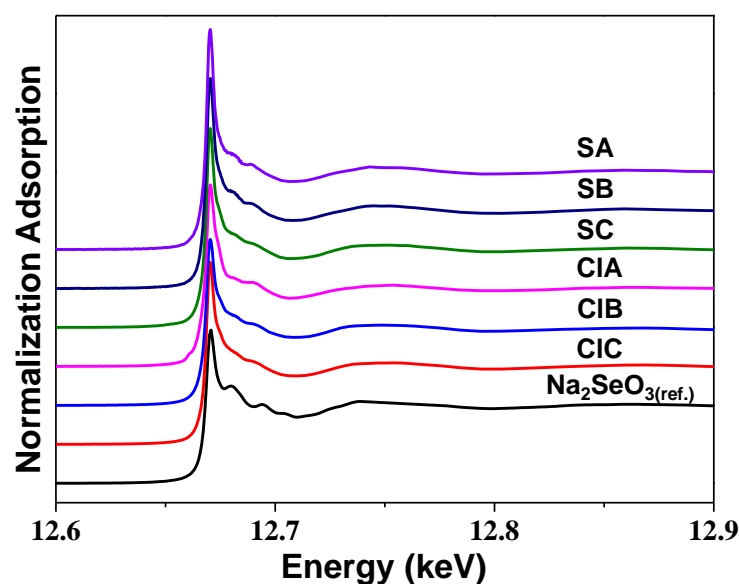


Figure S3.7. Se K-edge XANES spectra of Na_2SeO_3 reference and selected sorption samples from batch experiment.

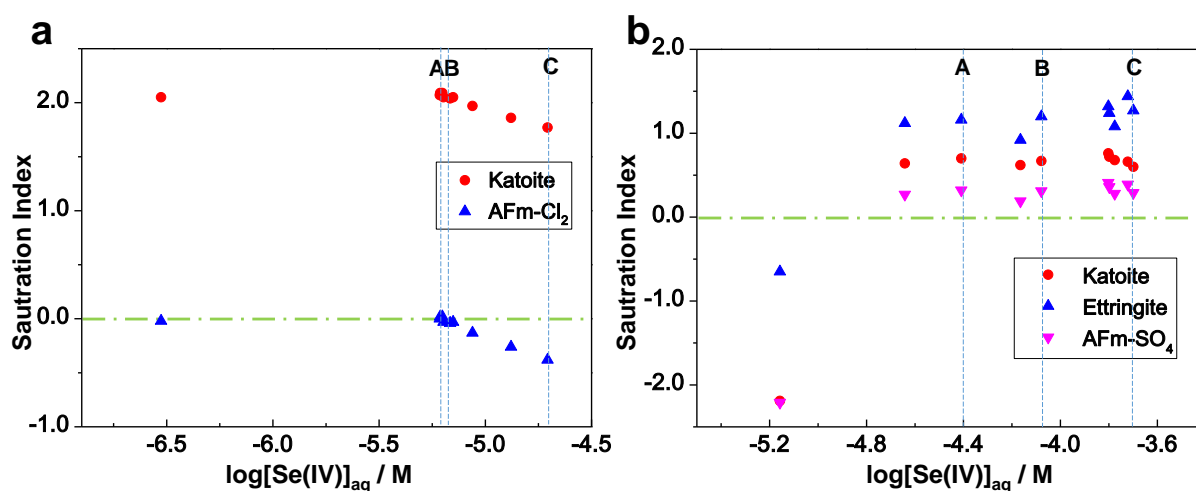


Figure S3.8. Saturation index (SI) of several possibly formed mineral phases as a function of $[\text{Se(IV)}]_{\text{aq}}$ in equilibrium. (a) For AFm- Cl_2 system. The negative SI values of AFm- Cl_2 after reactor A indicated that aqueous phase was saturated by other solid phases, rather than AFm- Cl_2 . (b) For AFm- SO_4 system. Katoite and ettringite phases were oversaturated for all the three reactors. Calculation is based on the aqueous data in batch sorption experiment on CaAl LDHs.

Table S3.1. Solution content of selected elements for AFm-Cl₂ experiments before introducing SeO₃²⁻. Concentrations were determined after reaching dissolution equilibrium, which was confirmed by dissolution kinetics^a.

ID	pH	[Ca] _{aq} /mol L ⁻¹	[Al] _{aq} /mol L ⁻¹	[Cl] _{aq} /mol L ⁻¹
CIA	12.37	6.32(7)×10 ⁻³	3.23(1)×10 ⁻³	4.20(2)×10 ⁻³
	Nd	6.29(8)×10 ⁻³	3.23(2)×10 ⁻³	4.14(2)×10 ⁻³
	Nd	6.40(6)×10 ⁻³	3.24(2)×10 ⁻³	4.07(2)×10 ⁻³
CIB	Nd	6.45(7)×10 ⁻³	3.20(2)×10 ⁻³	4.12(2)×10 ⁻³
	Nd	6.29(6)×10 ⁻³	3.24(2)×10 ⁻³	4.34(2)×10 ⁻³
	Nd	6.31(7)×10 ⁻³	3.25(3)×10 ⁻³	4.15(2)×10 ⁻³
	Nd	6.36(9)×10 ⁻³	3.28(5)×10 ⁻³	4.00(2)×10 ⁻³
	Nd	6.23(9)×10 ⁻³	3.26(4)×10 ⁻³	4.10(2)×10 ⁻³
	Nd	6.24(6)×10 ⁻³	3.22(2)×10 ⁻³	4.45(2)×10 ⁻³
	Nd	6.19(7)×10 ⁻³	3.22(3)×10 ⁻³	3.98(2)×10 ⁻³

^a nd: not determined; Uncertainties from three times repeated analyses of identical samples are given by the number in brackets on the last digit(s).

Table S3.2. Solution content of selected elements for AFm-Cl₂ experiments after equilibrium with SeO₃²⁻ for 48 h^a.

ID	pH	[Se] _{aq} /mol L ⁻¹	<i>q</i> /mol g ⁻¹	[Ca] _{aq} /mol L ⁻¹	[Al] _{aq} /mol L ⁻¹	[Cl] _{aq} /mol L ⁻¹
CIA	12.38	2.98(1.0)×10 ⁻⁷ ₇	4.14(29)×10 ⁻⁶	6.40(7)×10 ⁻³	3.11(3)×10 ⁻³	4.73(21)×10 ⁻³
	nd	6.13(31)×10 ⁻⁶	1.08(4)×10 ⁻⁵	6.41(8)×10 ⁻³	3.25(3)×10 ⁻³	5.43(20)×10 ⁻³
	nd	6.10(30)×10 ⁻⁶	2.09(4)×10 ⁻⁵	6.38(6)×10 ⁻³	3.20(1)×10 ⁻³	5.44(20)×10 ⁻³
CIB	12.38	6.35(41)×10 ⁻⁶	3.65(9)×10 ⁻⁵	6.30(6)×10 ⁻³	3.15(1)×10 ⁻³	5.44(20)×10 ⁻³
	nd	6.27(38)×10 ⁻⁶	4.69(11)×10 ⁻⁵	6.41(7)×10 ⁻³	3.24(3)×10 ⁻³	5.55(21)×10 ⁻³
	nd	7.05(29)×10 ⁻⁶	9.98(8)×10 ⁻⁵	6.24(7)×10 ⁻³	3.21(2)×10 ⁻³	5.57(21)×10 ⁻³
	nd	6.83(11)×10 ⁻⁶	2.15(2)×10 ⁻⁴	6.18(7)×10 ⁻³	3.24(2)×10 ⁻³	5.71(21)×10 ⁻³
	nd	8.70(37)×10 ⁻⁶	3.18(2)×10 ⁻⁴	5.93(6)×10 ⁻³	3.16(1)×10 ⁻³	5.96(22)×10 ⁻³
	nd	1.32(3)×10 ⁻⁵	4.29(5)×10 ⁻⁴	5.64(6)×10 ⁻³	2.99(2)×10 ⁻³	6.26(24)×10 ⁻³
	CIC	12.39	1.96(9)×10 ⁻⁵	5.31(3)×10 ⁻⁴	5.32(9)×10 ⁻³	2.92(4)×10 ⁻³

^a nd: not determined; Uncertainties from three times repeated analyses of identical samples are given by the number in brackets on the last digit(s).

Table S3.3. Solution content of selected elements for AFm-SO₄ experiments before introducing SeO₃²⁻. Concentrations were determined after reaching dissolution equilibrium, which was confirmed by dissolution kinetics^a.

ID	pH	[Ca] _{aq} /mol L ⁻¹	[Al] _{aq} /mol L ⁻¹	[S] _{aq} /mol L ⁻¹
SA	12.35	2.73(3)×10 ⁻³	1.96(2)×10 ⁻³	4.70(19)×10 ⁻⁵
	Nd	2.69(3)×10 ⁻³	1.95(1)×10 ⁻³	5.15(19)×10 ⁻⁵
	Nd	2.68(2)×10 ⁻³	1.92(1)×10 ⁻³	4.93(12)×10 ⁻⁵
SB	Nd	2.77(4)×10 ⁻³	1.95(3)×10 ⁻³	4.89(7)×10 ⁻⁵
	Nd	2.66(3)×10 ⁻³	1.95(1)×10 ⁻³	5.25(28)×10 ⁻⁵
	Nd	2.66(3)×10 ⁻³	1.96(2)×10 ⁻³	4.99(13)×10 ⁻⁵
	Nd	2.72(2)×10 ⁻³	1.96(6)×10 ⁻³	4.99(32)×10 ⁻⁵
	Nd	2.67(3)×10 ⁻³	1.95(2)×10 ⁻³	4.74(28)×10 ⁻⁵
	Nd	2.63(3)×10 ⁻³	1.93(1)×10 ⁻³	5.31(31)×10 ⁻⁵
	Nd	2.70(5)×10 ⁻³	1.96(3)×10 ⁻³	5.08(26)×10 ⁻⁵

^a nd: not determined; Uncertainties from three times repeated analyses of identical samples are given by the number in brackets on the last digit(s).

Table S3.4. Solution content of selected elements for AFm-SO₄ experiments after equilibrium with SeO₃²⁻ for 48 h^a.

ID	pH	[Se] _{aq} /mol L ⁻¹	<i>q</i> /mol g ⁻¹	[Ca] _{aq} /mol L ⁻¹	[Al] _{aq} /mol L ⁻¹	[S] _{aq} /mol L ⁻¹
SA	12.35	6.96(59)×10 ⁻⁶	8.11(2.0)×10 ⁻⁷	2.85(3)×10 ⁻³	2.00(1)×10 ⁻³	5.36(11)×10 ⁻⁵
	nd	2.28(5)×10 ⁻⁵	2.50(23)×10 ⁻⁶	2.78(3)×10 ⁻³	1.96(1)×10 ⁻³	5.19(6)×10 ⁻⁵
	nd	3.90(8)×10 ⁻⁵	4.48(30)×10 ⁻⁶	2.86(4)×10 ⁻³	2.01(2)×10 ⁻³	4.98(6)×10 ⁻⁵
SB	12.35	6.84(15)×10 ⁻⁵	5.52(56)×10 ⁻⁶	2.76(3)×10 ⁻³	1.94(2)×10 ⁻³	5.37(3)×10 ⁻⁵
	nd	8.35(8)×10 ⁻⁵	8.27(57)×10 ⁻⁶	2.81(3)×10 ⁻³	1.99(1)×10 ⁻³	4.55(6)×10 ⁻⁵
	nd	1.68(1)×10 ⁻⁴	1.96(5)×10 ⁻⁵	2.82(3)×10 ⁻³	2.01(1)×10 ⁻³	4.86(9)×10 ⁻⁵
	nd	1.58(2)×10 ⁻⁴	1.40(1)×10 ⁻⁴	2.88(3)×10 ⁻³	2.14(1)×10 ⁻³	5.39(49)×10 ⁻⁴
	nd	1.59(3)×10 ⁻⁴	2.43(1)×10 ⁻⁴	2.75(3)×10 ⁻³	2.20(2)×10 ⁻³	5.44(58)×10 ⁻⁵
	nd	1.90(4)×10 ⁻⁴	3.41(3)×10 ⁻⁴	2.61(3)×10 ⁻³	2.23(2)×10 ⁻³	6.97(4)×10 ⁻⁵
SC	12.36	2.00(3)×10 ⁻⁴	4.40(2)×10 ⁻⁴	2.45(3)×10 ⁻³	2.27(2)×10 ⁻³	6.85(24)×10 ⁻⁵

^a nd: not determined; Uncertainties from three times repeated analyses of identical samples are given by the number in brackets on the last digit(s).

Table S3.5. Equilibrium constants of selected phases^a and reactions occurred on CaAl LDHs at each sorption stage. *logK* values of AFm surface sites adsorption and AFm-SeO₃ formation were adapted.

	Equation	<i>logK</i>
<i>Solubility equilibrium</i>		
AFm-Cl ₂	$\text{Ca}_4\text{Al}_2\text{Cl}_2(\text{OH})_{12} \cdot 4\text{H}_2\text{O} + 12\text{H}^+ \Leftrightarrow 4\text{Ca}^{2+} + 2\text{Al}^{3+} + 2\text{Cl}^- + 16\text{H}_2\text{O}$	74.93
AFm-SO ₄	$\text{Ca}_4\text{Al}_2(\text{SO}_4)(\text{OH})_{12} \cdot 6\text{H}_2\text{O} + 12\text{H}^+ \Leftrightarrow 4\text{Ca}^{2+} + 2\text{Al}^{3+} + \text{SO}_4^{2-} + 18\text{H}_2\text{O}$	73.07
AFm-SeO ₃	$\text{Ca}_4\text{Al}_2(\text{SeO}_3)(\text{OH})_{12} \cdot 4\text{H}_2\text{O} + 12\text{H}^+ \Leftrightarrow 4\text{Ca}^{2+} + 2\text{Al}^{3+} + \text{SeO}_3^{2-} + 16\text{H}_2\text{O}$	73.70
CaSeO ₃ ·H ₂ O	$\text{CaSeO}_3 \cdot \text{H}_2\text{O}_{(s)} \Leftrightarrow \text{Ca}^{2+} + \text{SeO}_3^{2-} + \text{H}_2\text{O}$	-6.40
Katoite(C ₃ AH ₆)	$\text{Ca}_3\text{Al}_2(\text{OH})_{12} + 12\text{H}^+ \Leftrightarrow 3\text{Ca}^{2+} + 2\text{Al}^{3+} + 12\text{H}_2\text{O}$	80.32
Ettringite	$\text{Ca}_6\text{Al}_2(\text{SO}_4)_3(\text{OH})_{12} \cdot 26\text{H}_2\text{O} + 12\text{H}^+ \Leftrightarrow 6\text{Ca}^{2+} + 2\text{Al}^{3+} + 3\text{SO}_4^{2-} + 38\text{H}_2\text{O}$	56.97
<i>Sorption stage</i>		
Surface adsorption	$2\text{AFm_surface-OH} + \text{SeO}_3^{2-} \Leftrightarrow (\text{AFm_surface})_2\text{-SeO}_3 + 2\text{OH}^-$	3.60 ^b , 0.50 ^c
AFm-SeO ₃ formation	$4\text{Ca}^{2+} + 2\text{Al}^{3+} + \text{SeO}_3^{2-} + 16\text{H}_2\text{O} \Leftrightarrow \text{Ca}_4\text{Al}_2(\text{SeO}_3)(\text{OH})_{12} \cdot 4\text{H}_2\text{O} + 12\text{H}^+$	73.70
CaSeO ₃ precipitation	$\text{Ca}^{2+} + \text{SeO}_3^{2-} + \text{H}_2\text{O} \Leftrightarrow \text{CaSeO}_3 \cdot \text{H}_2\text{O}_{(s)}$	6.40

^a *logK* values of other phases refer to THERMOCHIMIE database.^b For surface adsorption on AFm-Cl₂.^c For surface adsorption on AFm-SO₄.

Table S3.6. Local structure of selenite reference and of selected batch sorption experiment samples obtained from EXAFS refinement at Se K-edge^a.

ID	Atomic pair	CN	R (Å)	σ^2 (Å ² ·10 ³)	ΔE^0 (eV)	R factor %
Na ₂ SeO ₃	Se-O	3.0(1)	1.70(1)	1.5(7)	9.7(7)	0.8
SA	Se-O	2.9(2)	1.70(1)	0.6(8)	7.8(9)	1.1
SB	Se-O	2.8(2)	1.70(1)	0.1(9)	9.0(1.6)	1.6
SC	Se-O	2.6(1)	1.70(1)	0.2(8)	8.8(2.1)	1.4
CLA	Se-O	2.5(2)	1.70(1)	0.7(6)	9.7(1.4)	1.0
CIB	Se-O	2.5(2)	1.70(1)	9.1(7)	8.8(6)	1.7
	Se-Ca	2.2(4)	3.52(2)			
CIC	Se-O	2.5(2)	1.70(1)	9.9(8)	9.9(7)	2.1
	Se-Ca	2.1(5)	3.54(2)			

^a CN: coordination numbers; R : atomic distances; σ^2 : Debye-Waller factors; ΔE^0 : shift of the threshold energy; R factor: goodness of fit. S_0^2 , 0.8718, was obtained from the experimental EXAFS fit of Na₂SeO₃ reference by fixing CN as the known crystallographic value and was fixed to all the samples. Uncertainties are given by the number in brackets on the last digit(s), i.e., 9.0(1.6) represents 9.0 ± 1.6 , and 3.52(2) means 3.52 ± 0.02 .

Table S3.7. Local structure of sulfate reference, fresh AFm-SO₄, and AFm-Cl₂-SO₄ obtained from EXAFS refinement at S K-edge^a.

Sample	Atomic pair	CN	R (Å)	σ^2 (Å ² ·10 ³)	ΔE^0 (eV)	R factor %
AFm-SO ₄	S-O	3.9(2)	1.48(1)	0.7(7)	8.0(1.2)	1.54
AFm-Cl ₂ -SO ₄	S-O	3.9(2)	1.47(2)	1.2(8)	6.5(1.4)	2.35
Na ₂ SO ₄ _ref.	S-O	4.0(1)	1.48(1)	2.3(8)	8.1(1.6)	0.80
	S-Na	7.7(2.0)	3.37(3)	15.7(9.2)		
	S-O	3.9(1.7)	3.60(4)	2.6(4.8)		
	S-O	4.2 (1.5)	4.06(4)	2.6(4.3)		

^a CN: coordination numbers; R : atomic distances; σ^2 : Debye-Waller factors; ΔE^0 : shift of the threshold energy; R factor: goodness of fit. S_0^2 , 0.9148 and 0.9518, for Na₂SO₄_ref. and samples, respectively. Uncertainties are given by the number in brackets on the last digit(s), i.e., 8.0(1.2) represents 8.0 ± 1.2 , and 1.48(1) means 1.48 ± 0.01 .

Table S3.8. The red and olive-green Gaussian peaks' areas and area ratios for excess selenite corroded AFm-Cl₂ (Cl₂:Se ratio = 0.5) as a function of reaction time.

Reaction time / min	Area of the olive-green peak	Area of the red peak	Area ratio of the red to the olive-green
2.5	25.48	79.16	3.11
5.0	16.12	83.37	5.17
7.5	15.86	98.07	6.18
10.0	12.23	84.15	6.88
12.5	14.68	86.48	5.89
15.0	13.12	91.90	7.01
17.5	14.54	95.88	6.60
20.0	14.53	96.08	6.61

Chapter 4. Determination of redox potentials imposed by steel corrosion products in cement-based media

Abstract

The redox potential (Eh) in a cementitious nuclear waste repository determines the retardation behaviors of redox-sensitive radionuclides (RNs). It is largely controlled by embedded steel corrosion but nearly impossible to measure directly. Here, we propose a new method to obtain this Eh value based on experimental results and on the Nernst equation. Oxidized RNs (U^{VI} , Se^{IV} , Mo^{VI} , and Sb^V) were employed as species probes in hyperalkaline cement pore water. Steel (Fe^0) and steel corrosion product couples (magnetite/hematite, and magnetite/goethite) and especially Fe^0 , showed a good affinity towards RNs, resulting in decreasing K_d order for $U > Sb > Se > Mo$ both under N_2 and H_2 atmospheres. Linear combination fit of X-ray absorption near-edge structure spectroscopy, was used to identify and quantify reduced species of sorbed U, Se, and Sb, present as UO_2 , U_4O_9 , $FeSe$, $FeSe_2$, Se^0 , Sb^0 , and Sb_2O_3 . The presence of H_2 did not obviously enhance the removal rate of aqueous RNs, but it promoted the formation of the most reduced species, e.g., $FeSe$ or Sb^0 . According to equilibrium computation, the solution total concentration was set equal to the concentration of the single most oxidized aqueous species, for any given RN. Experimental Eh values could then be obtained using the Nernst equation. They were remarkably closed together and centered around -450 mV at pH ~13.5 for both Fe^0 and Fe-oxyhydroxides couples, compared to -850.1 mV for $Fe^0/Fe(OH)_2$ half-reaction coupled to H_2O . This Eh value appears to be controlled by the nano-crystalline $Fe(OH)_2/Fe(OH)_3$ or $(Fe_{1-x},Ca_x)(OH)_2/Fe(OH)_3$ couple, which presence among corrosion product was confirmed by HE-XRD spectra analyzed by pair distribution function. This approach could pave the way for describing the Eh gradient in reinforced concrete or any other solid or biological materials where direct Eh measurements are not feasible.

4.1. Introduction

The redox potential (Eh) in a geological nuclear waste repository is of great importance to the migration behavior of redox-sensitive radionuclides (RNs) and thus its safety assessment[12]. In France, a cementitious-rich repository in Callovo-Oxfordian clay system is foreseen for radioactive waste disposal [9, 237]. Reinforced concrete structures (e.g., galleries or alveoles) will act as barriers that limit the mobilization of RNs, which must be isolated permanently from the biosphere. In such system, Eh will be mainly controlled by the corrosion of embedded steel, producing a thin (over a few microns) film based on the dynamic Fe^{II}-oxyhydroxides/magnetite/Fe^{III}-oxyhydroxides thin-film “sandwich” structure[13]. Less than five years after repository alveoli closure, the O₂ will be consumed, the system water saturated and the Eh will become reducing, which is imposed by the anoxic corrosion of steel and resulting hydrogen production[12]. A maximum H₂ pressure of 70 - 100 bars range [238] in the waste canister is expected and H₂ is potentially an electron donor for numerous oxidized RNs species (e.g., U^{VI}, Se^{IV}, Mo^{VI}, and Sb^V) present at the site[239]. However, H₂ is not a very soluble gas and not likely to be reactive enough without specific catalysis. Due to the complex corrosion interface and unclear H₂ contribution, the actual Eh which will prevail in the alveoli still remains undetermined.

Steel corrosion products, from inner to outer level, can be white rust (Fe(OH)₂), magnetite (Fe₃O₄), goethite (α-FeOOH), and more condensed hematite (α-Fe₂O₃) [240]. Under aerobic conditions, Fe₃O₄ is the intermediate oxidation product on the steel surface while Fe(OH)₂ is the intermediate product under anaerobic conditions[14]. Previous studies have reported that the oxidized RNs species can be immobilized by these Fe-oxyhydroxides via reductive precipitation and surface adsorption. For instance, U^{VI} can be reduced by ferrous iron on colloidal hematite[16], nanocrystalline magnetite[17, 18], and nanoscale zero-valent iron (NZVI)[15]. Besides, Fe^{III}-oxyhydroxides, e.g., goethite, can also remove aqueous U^{VI} by surface complexation[19]. Regarding aqueous Se^{IV}, reduced species, e.g., Se⁰, FeSe, and FeSe₂, could be also obtained on these Fe-oxyhydroxides[22], meanwhile surface adsorption occurred. Fe-oxyhydroxides[24] and Fe⁰[27] also show strong sorption affinity to Sb^V, resulting in reductive precipitates (e.g., Sb₂O₃ and Sb⁰) and structural incorporation[26, 28]. In contrast, molybdate is much more difficult to be reduced, even by NZVI[29], and non-redox sorption occurred prevalingly on Fe-oxyhydroxides systems[30, 31]. In a redox reaction, pH affects heavily the redox potential. However, in hyperalkaline cement pore water

(CPW), sorption behavior of RN anions on these Fe-oxyhydroxides are still not well-documented.

In reinforced concrete, pH value is almost fixed at pH ~13 by cement hydration products, thus Eh becomes more critical to any redox reaction. Both hyperalkaline and H₂ conditions would disable regular Pt-electrode direct measurement of steel corrosion product interfacial Eh. Profound disagreement among field measured Eh and computed Nernstian values was caused by lack of internal equilibrium[241] and analytical difficulties with Pt-electrodes[242]. The redox potentials of structural Fe in clay minerals (i.e., smectites) were attempted to determine under nearly neutral conditions by using organic one-electron-transfer mediating compounds, suggesting different redox-activities of structural Fe over the tested Eh range[243-246]. However, under hyperalkaline conditions, i.e., in cement environment, the speciation of organics may be different. In this study, a combination of wet chemistry methods and synchrotron-based X-ray spectroscopic analysis, including X-ray absorption near edge structure (XANES) and pair distribution function (PDF) spectroscopy, was employed to describe RNs sorption behaviors on NZVI and Fe-oxyhydroxides in CPW. We aim to determine “in-situ” experimental Eh imposed by the steel (modeled here by NZVI) and its corrosion products couples, e.g., magnetite/hematite (abbreviating into M/H) and magnetite/goethite (abbreviating into M/G), using redox-sensitive RNs, i.e., U, Se, Mo, and Sb, as the redox probes. This work demonstrated for the first time a credible approach for an *ab initio* Eh determination in cement-based medium.

4.2. Materials and methods

4.2.1. Materials and chemicals.

Boiled and argon-degassed Milli-Q water (18.2 MΩ·cm) was used for all solutions and suspensions. All chemicals used for synthesis and stock solutions, including Fe-salts (e.g., FeCl₂·4H₂O, FeCl₃·6H₂O, and Fe(NO₃)₃·9H₂O) and chemicals for nuclide anions (e.g., Na₂SeO₃·5H₂O, Na₂MoO₄·2H₂O, and KSb(OH)₆), were purchased from Sigma Aldrich, were analytical grade and their containers opened for the first time before use in the glove box. An acidic 1000 ppm UO₂Cl₂ stock solution was used. Synthetic CPW of CEM-V/A cement, was prepared according to the protocol from ANDRA[247] and used as background solution in all reactors. The procedure is first to saturate the mixed NaOH (72 mM), KOH (211 mM), Na₂SO₄ (1.5 mM), and NaCl (1 mM) solution with CaO powder, then filtering the suspension through a Millipore[®] 0.22-μm membrane filter. The pH of the clear resulting CPW is ~13.5

and its composition given in Table S4.1. All experiments were performed in a N₂-filled glove box (O₂<2 ppm, using NaOH as the CO₂ trap) to prevent oxidation and possible CO₂ contamination.

4.2.2. Synthesis and characterization of Fe-bearing phases.

NZVI, magnetite, hematite, and goethite were synthesized and washed according to the recipes (details shown in Text S4.1) described in previous reports[248-252]. Except for NZVI, all the Fe-bearing phases were stored as suspensions with certain solid to liquid (S/L) ratios in the glove box. After freeze-drying, potential impurities presence of all the Fe-bearing phases was checked by powder X-ray diffraction (XRD) analysis (CuK_α radiation), indicating no instinct impurity diffraction peak (Figure S4.1). Their specific surface areas (Table S4.2) were measured by the Brunauer-Emmett-Teller (BET) N₂-absorption method, in order to verify the surface sites concentration used in sorption experiments. Besides, the particle size and shape as characterized further by scanning electron microscope (SEM), shown in Figure S4.2. The fairly uniform nano-sized magnetite, hematite, and goethite, were present as spherical, rhombohedral, and needle-like shape particles, respectively.

4.2.3. Batch sorption experiments.

All sorption experiments were performed at an identical total surface-site concentration of 2×10^{-4} M, approximately. In order to provide enough surface sites for RNs sorption, the site density is assumed to be at least 1 nm^{-2} [253]. Thus, the corresponding S/L ratios in the reaction suspensions were calculated as 4.17 g L^{-1} (NZVI), 1.60 g L^{-1} (magnetite) plus 2.86 g L^{-1} (hematite), and 1.60 g L^{-1} (magnetite) plus 6.12 g L^{-1} (goethite). To avoid co-precipitation of RNs and aqueous Ca²⁺ in CPW, RNs concentrations were set equal to 5×10^{-5} M for U and 2×10^{-4} M for the other three RNs (i.e., Se, Mo, and Sb). Thus, S/L ratios for U reactors were 4 times less than for the other RNs reactors. Prior to introducing RNs, iron solid phases were equilibrated with CPW for 24 h, to reach an equilibrium of their surface chemistry (Figure S4.3). In addition, sorption kinetics of the four RNs (i.e., U, Se, Mo, and Sb) on NZVI and M/H were investigated to determine the sorption equilibrium time, suggesting that the sorption reach equilibrium after ~21 d on an end-over-end shaker (Figure S4.4). Therefore, the equilibrium time of batch sorption reactors was extended to more than 21 d, to reach full thermodynamically equilibrium.

Individual sorption experiments of the various RN on each coupled steel products (i.e., NZVI, M/H, and M/G) were conducted at 25 °C under constant shaking in the glove box. After an

equilibrium time of ~100 d, 4 mL of suspension were sampled from each reactor and filtered through 0.22- μm syringe filters. Parallel sorption experiments were conducted at 25 °C in H_2 atmosphere ($P_{\text{H}_2} = 8.0$ bar) in stainless steel (T316) high pressure-high temperature reactors (PARR, USA)[254]. Without any stirring, the equilibrium time should be longer than the reactors in glove box. Two reaction times, 21 d and 70 d, were investigated to better know the reaction process and the speciation and concentration evolution, for various aqueous species and solid phases.

After reaction, the solution pH was measured by a combined glass Micro-pH electrode (Metrohm 6.0234.100, having a full pH measuring range from 0 to 14) straight after its calibration. An alkaline-resistant (working pH range from 0 to 14) combined Pt-ring ORP electrode (Metrohm 6.0451.100) was used for Eh measurement, after being calibrated with Zobell's solution (200 mV at 25 °C). Readings from the Eh meter was corrected, +207 mV at 25 °C, based on the standard hydrogen electrode (SHE) reference. Due to the extremely high pH conditions (pH ~ 13.5), the Eh meter had difficulties to reach stable readings and the measurement standard deviation was estimated to be ± 100 mV approximately based on repeated measurements. Eh values' stability criterion was a drift of less than 1.0 mV over 10 min, or a maximum equilibration time of 1 h, whichever occurred first. Total aqueous Ca, S, Fe, U, Se, Mo, and Sb concentrations were analyzed by inductively coupled plasma optical emission spectrometry (ICP-OES) with a Varian 720-ES apparatus. The possible presence of aqueous reduced S (e.g., S^{2-}) and Sb (e.g., $\text{Sb}(\text{OH})_4^-$) species was checked by the methylene blue method[255] and high-performance liquid chromatography-mass spectrometry (HPLC-MS), respectively. However, no reduced S and Sb can be detected in solution (Figure S4.5). The distribution coefficient (K_d) was calculated according to a standard definition (Text S4.2). Sorption products in each reactor were collected by vacuum filtration through 0.22- μm nitrocellulose membrane, stored in glove box, and extreme care was taken to prevent any possible sample oxidation during subsequent solid characterizations.

4.2.4. XANES spectroscopy.

XANES spectroscopy measurements at selenium K-edge (12658 eV), uranium L_3 -edge (17166 eV), molybdenum K-edge (20000 eV), and antimony K-edge (30491 eV), were conducted at the SpLine Spanish CRG Beamline (BM25A) at the European Synchrotron Radiation Facility (ESRF), Grenoble, France. For each element, energy calibration was done in parallel using the corresponding elemental foil, except of uranium. U L_3 -edge energy was

calibrated by the K-edge excitation energy of an yttrium (17038 eV) metallic foil. The collected sorption products in batch sorption experiments were sealed double-side using Kapton tape in glove box, then transferred in an anaerobic chamber to the synchrotron facility. All samples were measured in fluorescence mode, except for the references which were prepared as pellets by diluting the solids in cellulose and measured in transmission mode. A Sirius liquid nitrogen cooled Si(Li) 13-multi-element solid state X-Ray detector from e2v were used for data collection. During the measurement, samples were always under N₂ atmosphere protection. The Demeter software package was used for the data integration and reduction of XANES (Athena)[196]. A linear combination fit (LCF) was applied to the XANES spectra to identify and quantify the element species.

4.2.5. PDF spectroscopy.

Equilibrium products of NZVI with CPW at different contacting time were characterized by PDF method. The high-energy X-ray scattering experiments were performed in beamline ID31 at the ESRF, using energy of 78.3 keV and a Perkin Elmer XRD 1621 flat detector. To avoid any oxidation, the reacted NZVI fine powder was packed in Ø1 mm Kapton capillaries, and sealed in capillaries by epoxy glue inside the glove box. These loaded capillaries were stored in anaerobic conditions till put on the sample racks. NIST certified CeO₂ powder sample was used for instrumental calibration and empty capillary with the same specification for background subtraction. With collection time of 5 min, the obtained images were integrated to one-dimensional diagrams using Fit2D software[219]. PdfGetX3 code[195] was employed to transform the data into PDF patterns and calculated PDF patterns were obtained by PDFGui software[256]. After PDF data normalization by the incident photon flux, differential PDF (d-PDF) were obtained by subtracting the PDF pattern of pristine NZVI from those of NZVI samples contacted with CPW.

4.3. Results and discussion

4.3.1. Aqueous phase results.

Firstly, equilibrium kinetics of NZVI and M/H with CPW were conducted and results are shown in Figure S4.3. Total aqueous concentrations of Ca and S, mostly prevalent as bivalent Ca²⁺ and SO₄²⁻ ions, were followed with reaction time. As shown, the total aqueous S concentration in both reactors is almost constant, indicating that nearly no SO₄²⁻ can be adsorbed or reductively precipitated on NZVI or M/H. In contrast, most Ca²⁺ in CPW can be

removed instantly. Especially for M/H, equilibrium was reached within 2 h, suggesting that this fast Ca^{2+} removal is more likely occurring via a surface adsorption mechanism. The pH value (~ 13.5) in extremely alkaline CPW is always above the points of zero charge of iron oxides, which are in the range of 6.3 (for magnetite) to 9.5 (for hematite and goethite)[252]. The resulting highly negative surface leads to adsorption of cations. Furthermore, Ca^{2+} sorption on NZVI was relatively slow, and underwent two stages, with a first one lasting ~ 6 h and a second going till 24 h. After 24 h, even more Ca^{2+} was removed, compared to the M/H case. Bare NZVI has strong reducing ability towards water, due to its non-stabilized surface and high specific surface area[257]. The formed Fe^{II} -hydroxide phases may remove Ca not only by surface adsorption but probably also by co-precipitation. Structure of NZVI in equilibrium will be discussed in Section 4.4.

After equilibrating iron products with CPW for 24 h, the four RNs were introduced and the sorption kinetics studied. As shown in Figure S4.4, U, Se, and Sb had always a much stronger affinity for NZVI than for Fe-oxides couples (i.e., M/H). RNs sorption can reach equilibrium within 50 h, while aqueous Ca^{2+} was continuously removed from solution till reaching a minimum platform. In contrast, RNs sorption on M/H was relatively weak and sorption equilibrium reached after 200 h for U, Mo, and Sb. For Se, removal proceeded continuously till 540 h. MoO_4^{2-} had the least affinity for the various Fe phases, as expected for negatively charged Fe oxyhydroxides surface. After introducing RNs in M/H reactors, aqueous Ca^{2+} concentration nearly kept constant.

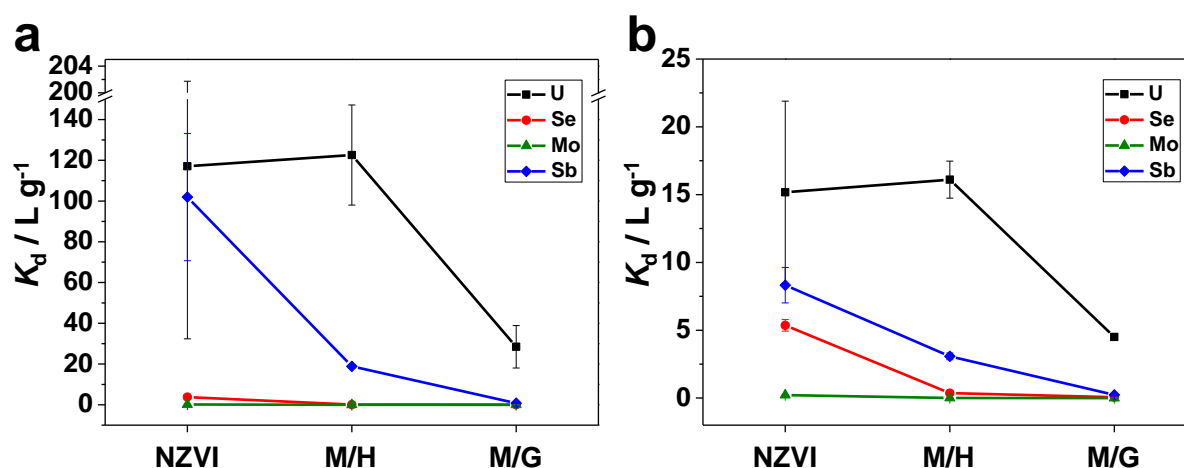


Figure 4.1. K_d values derived from batch sorption experiments, including the sorption of four RN anions (i.e., U^{VI} , Se^{IV} , Mo^{VI} , and Sb^{V}) on NZVI, M/H, and M/G. (a) In N_2 atmosphere, under continuous shaking, reacting 100 d. (b) Under 8.0 bar H_2 atmosphere, after 70 d reaction without shaking.

Aqueous results, including ion concentrations, pH, Eh (measured by ORP Pt-electrode), and K_d values, of batch sorption experiments are listed in Table S4.3-S4.5. Under N_2 atmosphere, Eh values for NZVI reactors changed with reaction time, from -740 mV at the beginning to -530 mV at equilibrium, approximately. The bottom Eh line of water stability domain, i.e. the H_2O/H_2 stability border calculated for $P_{H_2} = 1$ bar at pH ~ 13.5 , is -798.7 mV. Thus, the lowest Eh values recorded in the NZVI reactors could be controlled by H_2O decomposition by NZVI (-850.1 mV for $Fe^0/Fe(OH)_2$). After reacting with H_2O , the NZVI surface was covered by the Fe^{II} -hydroxide reaction products and the imposed Eh values increased. In M/H and M/G reactors, the Eh values were close to about -440 mV. Regarding reactors in H_2 atmosphere ($P_{H_2} = 8.0$ bar), the Eh values should be dictated by the dissolved H_2/H_2O couple equilibrium, resulting in a value of ~ -740 mV. Throughout sorption experiments, pH values in all the reactors were always constant and equal to ~ 13.5 .

K_d values derived from reactions under both N_2 and H_2 atmosphere are shown in Figure 4.1. Hydrogen atmosphere does not lead to any obvious RN removal enhancement from aqueous phase. The effect of H_2 on solid species will be discussed in following sections. The obtained K_d values indicate an affinity of these Fe corrosion products for RNs in the order of $U > Sb > Se > Mo$. Aqueous U^{VI} concentration in equilibrium with hyperalkaline cement leachate, i.e., alkali/alkaline-earth uranates (e.g., $Na(UO_2)O(OH) \cdot (H_2O)_{0-1}$ and $CaUO_4$), can be present at very low concentration ($\sim 10^{-9}$ M) [258]. However, the filtrate of U^{VI} -CPW blank sample through 0.22- μm membrane filter can still have a $\sim 4 \times 10^{-5}$ M U^{VI} total “dissolved” concentration (Table S4.3), suggesting the presence of nano-sized uranate colloids dispersed in solution. These U^{VI} nano-colloids are expected to be stable for years [259], but can be removed rapidly from aqueous phase by the iron corrosion products. For antimony, the strong complexation affinity of Ca^{2+} for antimonite may also greatly contribute to the large K_d values for this element [260]. Among all the iron products, NZVI was the phase leading to the strongest sorption among all RNs. M/H couple showed a little stronger sorption affinity to RNs than the M/G couple. RNs sorption results in H_2 atmosphere with 21 d and 70 d reaction time, are shown in Table S4.4 and S4.5. After 21 d reaction, sorption of U and Sb reached equilibrium while the removal of Se and Mo still proceeded further. Species evolution in solid phase will be discussed in following sections.

4.3.2. Surface Se and Sb species.

Sorption products of batch experiments under N_2 and H_2 atmosphere were characterized by XANES. Based on reference compounds, LCF analysis of XANES was conducted to identify and quantify solid species of sorbed RNs. Experimental Se K-edge XANES spectra are shown in Figure 4.2a and the LCF results listed in Table S4.6. In our system, sorbed selenium could be present as $FeSe$, $FeSe_2$, and Se^0 reduced species, or as Se^{IV} (surface) complexes with Ca and Fe, e.g., $CaSeO_3$ and $FeSeO_3$. In presence of NZVI, selenite can be reduced into $FeSe$ and $FeSe_2$, while Fe-oxyhydroxides couples can only reduce selenite into Se^0 . The effective reductant in the iron couples should be magnetite, which can reduce selenite into Se^0 and even Fe selenides under slightly acid conditions [110, 261].

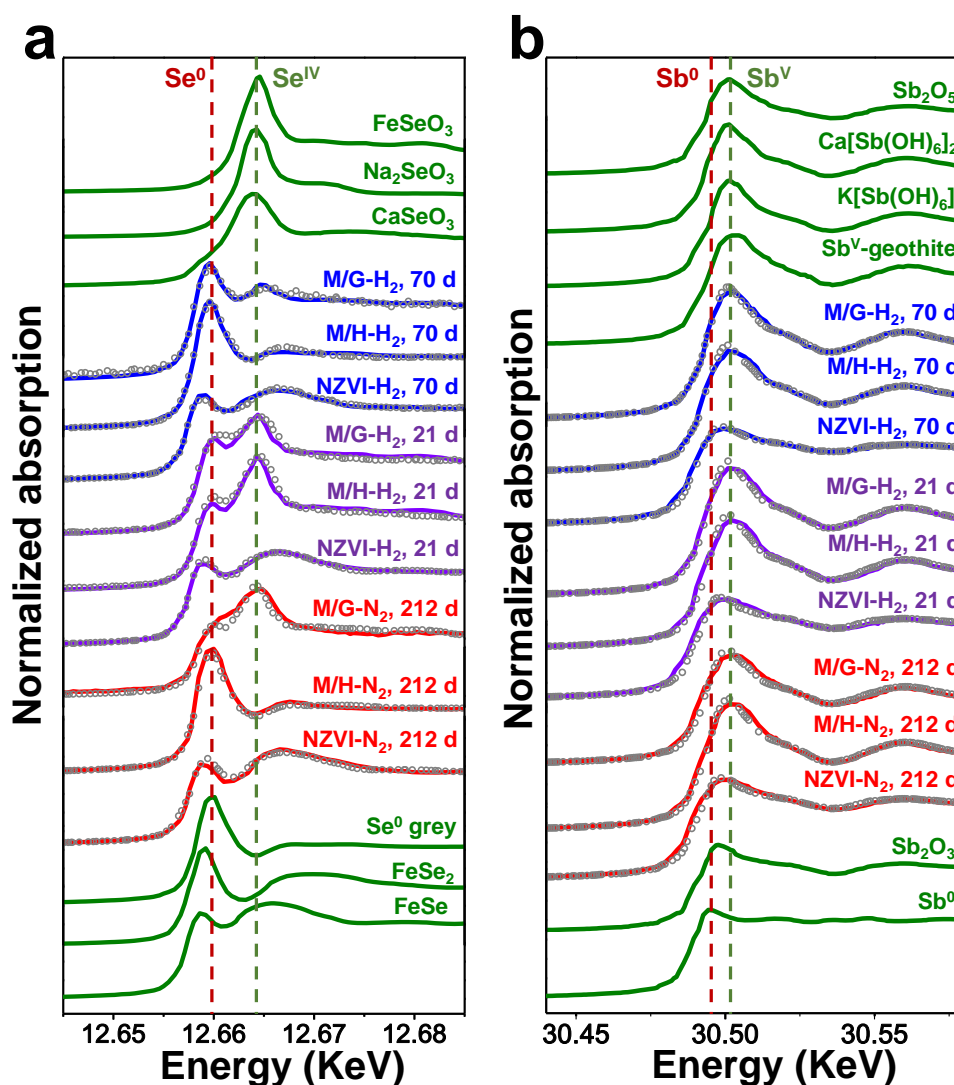


Figure 4.2. Experimental XANES spectra of reference compounds and RNs sorption products on NZVI, M/H, and M/G in N_2 and H_2 atmosphere. (a) Se K-edge XANES spectra of selenium sorption products. (b) Sb K-edge XANES spectra of antimony sorption products.

The grey dots represent the experimental data and the solid curves are the linear combination fit (LCF) results.

Previous reports illustrate that selenite can be reduced into FeSe by Fe/FeC₃ ultrasmall particles[23]. Besides, Se^{-II} can be immobilized by pyrite via strong surface redox reaction, producing FeS and Se⁰[262]. Here, in extremely alkaline solution (pH ~13.5), NZVI is also able to act as a powerful reductant towards selenite. According to LCF results of NZVI samples, more FeSe was formed and the generated amount of reduced species was larger in presence of H₂, compared to the N₂ case. Presence of dissolved H₂ may inhibit NZVI oxidation by water, thus other oxidation pathway, i.e., NZVI oxidation by selenite, would be benefited. However, it can be clearly observed that the formation of low oxidation state Se species was proceeding with time in H₂ reactors. In addition, adsorbed Se^{IV} was more likely to complex with Ca than to remain present as free ion.

For antimony, the introduced antimonate could be strongly associated with Ca²⁺[260], i.e., form Ca[Sb(OH)₆]₂⁰ soluble complex and co-precipitates, while forming with Fe^{III} hydroxides[26] octahedral inner-sphere surface complexes. In reducing environment, lower oxidation state Sb species, e.g., Sb^{III} and Sb⁰, can be formed. For instance, magnetite can reduce Sb^V into Sb^{III} and the reduction increases with pH values [24]. Sb^{III} was also found present at the surface of Fe-bearing rims [25]. In addition, Sb⁰ was detected in soil samples from Swiss shooting ranges, probably derived from reduction by Pb⁰ present in PbSb alloy-containing unweathered bullet fragments[26]. Thus, Fe⁰, with lower standard reduction potential than Pb⁰, can also generate Sb⁰ [27]. Experimental Sb K-edge XANES spectra and the LCF results were shown in Figure 4.2b and Table S4.7. Sb₂O₃ was detected prevalently in all sorption products, while Sb⁰ was only identified in the NZVI reactors. Although all H₂ reactors had very low redox potentials (Table S4.4 and S4.5), closed to values recorded in NZVI reactors, no Sb⁰ was observed in Fe oxide-couples reactors probably due to a lack of enough water-mineral interface. From the LCF results for NZVI reactors, introducing H₂ resulted in larger molar fractions of formed Sb⁰. Sb^V-sorbed goethite was prepared from K[Sb(OH)₆] in CPW, to have a XANES reference of Sb^V-Fe^{III} hydroxide complex. As shown in Table S4.7, Sb^V-goethite surface complex and Ca[Sb(OH)₆]₂(s) precipitate contribute a lot to total sorbed Sb^V species signal observed on Fe-oxyhydroxides couples, rather than the originally introduced K[Sb(OH)₆].

4.3.3. Surface U and Mo species.

As discussed above, uranium total trace aqueous concentration in equilibrium with CPW should be extremely low ($\sim 10^{-9}$ M), as U^{VI} prefers to form mobile metal (e.g., Ca, Na, and K) uranate(VI) nano-colloids, as demonstrated by Bots et al[259]. The XANES reference of uranate(VI) was prepared by mixing Ca^{2+} , Na^+ , and UO_2^{2+} at pH ~ 13 . Experimental U L3-edge XANES spectra were shown in Figure 4.3a and the LCF analysis results presented in Table S4.8. Through fitting the spectra with a large amount of references, including $UO_3 \cdot 2H_2O$, uranate(VI), $UO_2(NO_3)_2 \cdot 6H_2O$ [263], $NaUO_3$, U_4O_9 , U_3O_8 [264], and UO_2 [265], three potential components, i.e., uranate(VI), U_4O_9 and UO_2 , of U sorption products were chosen. LCF results showed that all the adsorbed U^{VI} was uranate(VI), in accordance with results from Bots et al[259]. Once uranyl was introduced into the CPW suspension of iron particles, uranate ion would complex with alkali or alkali-earth cations and transform into metal uranates(VI) colloids or complex, immediately, which could thereafter aggregate or be sorbed on iron surface to allow further redox reactions to occur. Regarding potential reductive reactions, only NZVI was able to reduce U^{VI} into pure U^{IV} , with more UO_2 generated in H_2 reactors than in N_2 reactors, while, U reduced species in reactors of Fe-oxyhydroxides couples were always U_4O_9 , a +4 and +6 mixed valence solid compound. Previous work also indicated that UO_2 should be the reduction product of U^{VI} on the surface of magnetite and the reaction to be facilitated by electron transfer between the Fe and U[18]. Indeed, regarding the U L3-edge XANES spectra of UO_2 and U_4O_9 , their similar shapes and close white-line positions (< 1 eV difference) increase the difficulty to distinguish the two species very clearly[263]. However, it is certain that reduced U species with oxidation states between +4 and +4.5 were present.

Regarding molybdenum, the XANES spectra and LCF results are shown in Figure 4.3b and Table S4.9, respectively. Spectra of adsorbed Mo on Fe-oxyhydroxides couples were too noisy to perform LCF analysis, thus they are not posted here. For sorbed Mo on NZVI, no reduction can be observed from XANES spectra. However, removal of aqueous Mo by NZVI is not negligible. As shown in Figure 4.3b, Mo^{VI} pre-edge peak intensity of sorption products are quite weak, and similar to $FeMoO_4$ pre-edge peak. Thus, based on LCF analysis, considerable amount of $FeMoO_4$ existed in the sorption products. Pre-edge peak of Mo^{VI} can give us the information of Mo geometry and also its coordination environment[217]. The decreased pre-edge intensity suggests that the tetrahedral MoO_4^{2-} was distorted and octahedral

Mo may probably form inner-sphere structural coordination with iron during the Fe^0 oxidation and further $\text{Fe}(\text{OH})_2$ formation.

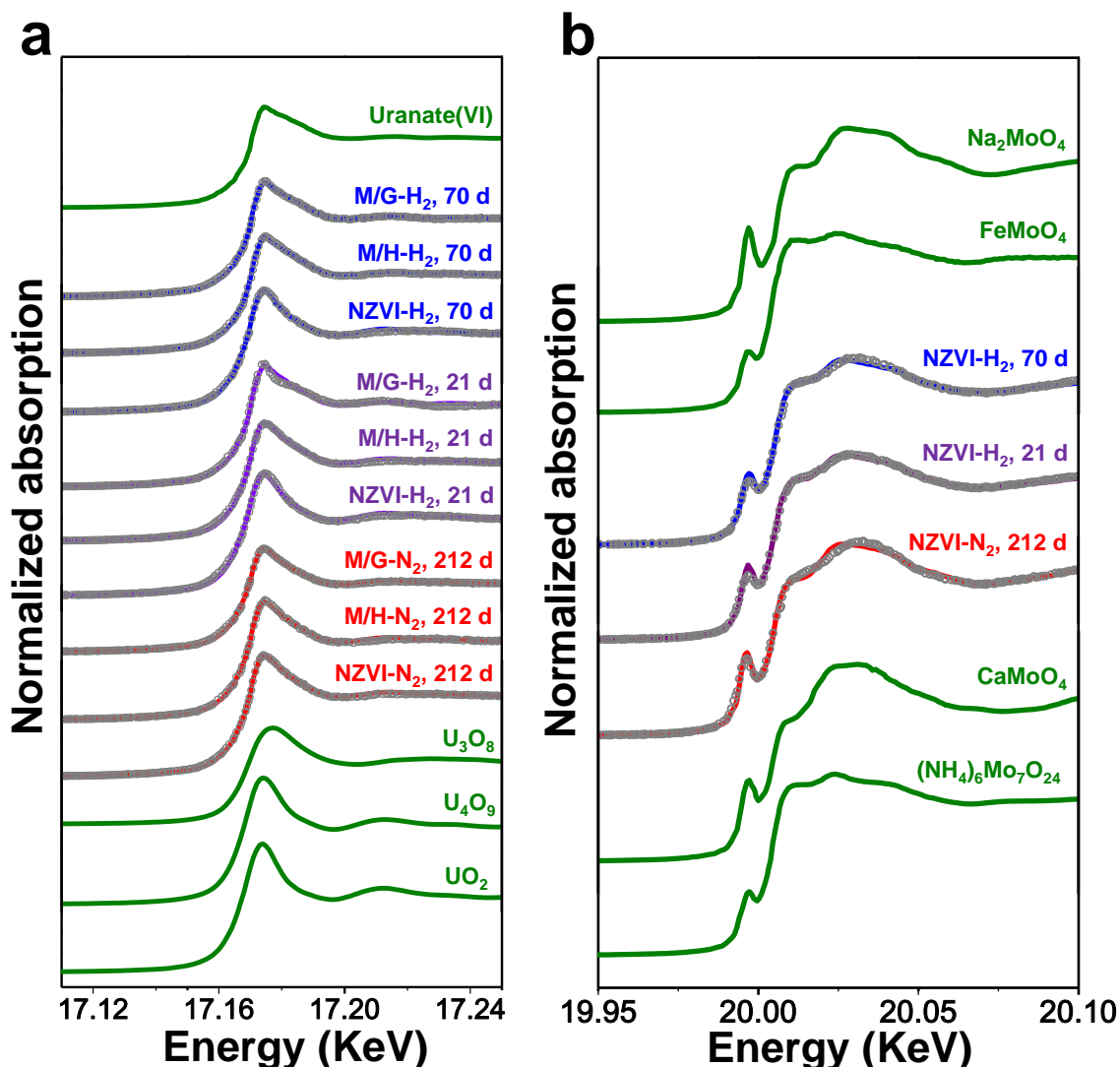


Figure 4.3. Experimental XANES spectra of reference compounds and RNs sorption products on NZVI, M/H, and M/G in N_2 and H_2 atmosphere. (a) U L3-edge XANES spectra of uranium sorption products. (b) Mo K-edge XANES spectra of molybdenum sorption products. The grey dots represent the experimental data and the solid curves are the linear combination fit (LCF) results.

4.3.4. PDF analysis of reacted NZVI.

Once suspended in CPW, the negatively surface charged NZVI passivation coatings could adsorb Ca^{2+} and meanwhile react with water molecules. It is then intriguing to better understand the possible role of Ca in promotion “in-situ” NZVI corrosion process. Here, synchrotron-based PDF technique was employed to describe NZVI phase transformation in CPW. NZVI, suspended in CPW for various time were characterized by PDF. The d-PDF patterns obtained after subtracting the PDF of pristine NZVI from NZVI reacted with CPW

for 10 min, 23 h, 72 h, 168 h, and 264 h, are shown in Figure 4.4a. By subtracting the NZVI signal, several negative differential reflections can be observed, in accordance with Fe-Fe reflections of pristine NZVI (e.g., at 2.52 Å, 4.10 Å, 4.84 Å, and 6.38 Å), suggesting that Fe-Fe bond lengths decreased during NZVI reaction with CPW. Positive differential reflections, at 2.13 Å, 3.33 Å, and 3.63 Å, were also observed. Compared to reference patterns of $\text{Fe(OH)}_{2(\text{cr})}$ and Ca(OH)_2 , these three reflections can be attributed to Fe-O, Fe-Fe, and Ca-Ca scattering pairs, respectively. The continuously increased positive differential signals of Fe-O and Fe-Fe indicate that NZVI was oxidized by water into Fe(OH)_2 gradually. In addition, the positive Ca-Ca signal can be derived from Ca^{2+} surface adsorption and possible Ca(OH)_2 solid phase formation. The $d_{\text{Fe-O}}$ at 2.13 Å was easily identified as it is nearly the distance observed within $\text{Fe(OH)}_{2(\text{cr})}$ reference. In contrast, distances of 3.33 Å and 3.63 Å in d-PDF were correspondingly ~ 0.07 Å longer than Fe-Fe distance (3.26 Å) in $\text{Fe(OH)}_{2(\text{cr})}$ and Ca-Ca distance (3.57 Å) in Ca(OH)_2 . Instrumental calibration could be responsible for these atomic distance shifts. However, these shifts to longer distances could probably also indicate that Fe^{II} and Ca^{II} hydroxides formed very amorphous solid phases within 72 h. Note that Ca-Ca reflection at 3.63 Å kept increasing within 72 h and clearly separated from Fe-Fe at 3.33 Å. Later on the Ca-Ca peak decreased steeply and tended to merge with Fe-Fe into a broad peak after 264 h. Meanwhile, aqueous Ca^{2+} concentration curves indicated no Ca^{2+} desorption according to sorption kinetic experiments. Thus, two reaction processes are occurring concomitantly on NZVI particle surface: i) Ca^{2+} adsorption and Ca(OH)_2 precipitation, ii) Fe^0 oxidation into Fe(OH)_2 . The first process is faster, forming amorphous Ca(OH)_2 phase. The pH value (~ 13.5) imposed by hyperalkaline CPW is higher than precipitation pH edge of both Ca and Fe, which should provide favorable conditions to co-precipitation of Ca^{2+} , Fe^{2+} , and OH^- . Thus, small amounts of $(\text{Fe}_{1-x}, \text{Ca}_x)(\text{OH})_2$ phase might have formed. The surface of reacted NZVI at 264 h reaction time was also studied by X-ray photoelectron spectroscopy (XPS) analysis (Figure S4.6). Fe 2p_{3/2} region yielded three contributions of Fe^0 metal, Fe(II)-O, and Fe(III)-O, of which the Fe(III)-O contribution may result from oxygen oxidation during sample preparation and transfer to the XPS facility. Besides, the strong Ca(II)-O peak in the Ca 2p region indicates that Ca^{II} is incorporated into the surface of reacted NZVI during Fe^{II} hydroxides formation. In addition, previous report also showed that a rather thick (50 - 200 μm) and porous layer of iron oxides interspersed with Ca(OH)_2 can be observed with time [266]. The adsorbed/co-precipitated $(\text{Fe}_{1-x}, \text{Ca}_x)(\text{OH})_2$ may act as a corrosion passivation layer, increasing Fe^{II} hydroxide solubility and further shifting the interfacial Eh values to lower values.

Within 45 days reaction time, NZVI totally transformed into $\text{Fe}(\text{OH})_2$, as shown in Figure 4.4b. The broadened reflection peaks indicate the formation of quite amorphous precipitates, compared to crystalline $\text{Fe}(\text{OH})_2$. A 0.2 mM SeO_3^{2-} solution was added to react with $\text{Fe}(\text{OH})_2$ on the surface. Although Se^{IV} can thermodynamically oxidize $\text{Fe}(\text{OH})_2$ into Fe^{III} -hydroxides, no new Fe^{III} phase, like goethite or magnetite, could be observed in PDF data probably due to the low Se loading.

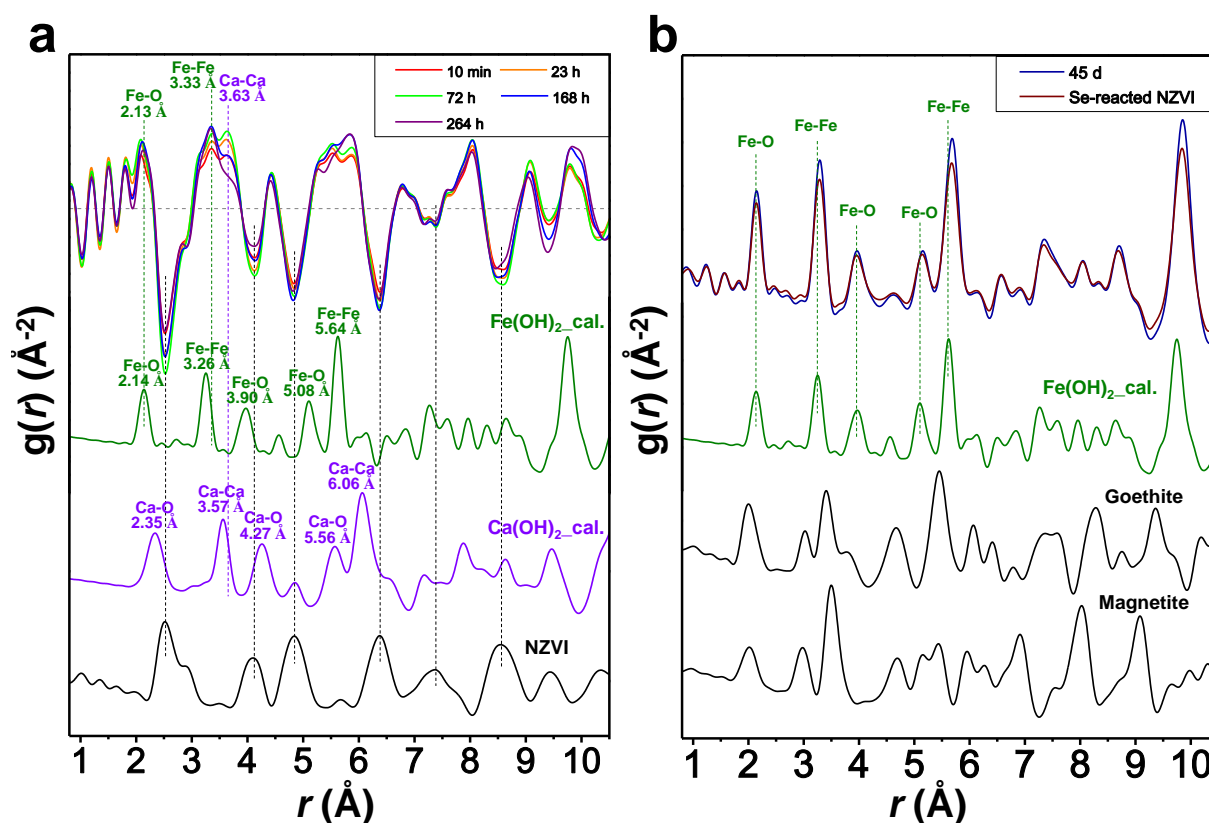


Figure 4.4. Differential PDF (d-PDF) and PDF patterns of reacted NZVI with CPW at different reaction time. (a) Experimental PDF of pristine NZVI and d-PDF of reacted NZVI; Calculated PDF references of $\text{Fe}(\text{OH})_{2(\text{cr})}$ and $\text{Ca}(\text{OH})_2$. (b) PDF references are derived from calculated $\text{Fe}(\text{OH})_{2(\text{cr})}$, synthesized goethite and magnetite. Experimental PDF of reacted NZVI with CPW at 45 d and Se^{IV} -reacted NZVI is shown on the top.

4.3.5. “In-situ” experimental Eh values.

An experimental “in-situ” Eh value can be computed in the following way. The LCF analysis of XANES spectra allows reduced species for each RN to be identified and their fraction ratio to be quantified within the solid phases. As shown from the above kinetic experiments, we assumed these species to be at chemical equilibrium. The Eh-pH diagrams can then be drawn using PhreePlot code[267] and ANDRA Thermochemie database[193], under conditions prevailing in our experiments (Figure S4.7). For each RN, various solid reduced species were

considered and allowed to precipitate according to thermodynamics. Regarding aqueous RNs species, MoO_4^{2-} predominates for Mo and $\text{UO}_2(\text{OH})_4^{2-}$ for U. For Se and Sb, besides SeO_3^{2-} and $\text{Sb}(\text{OH})_6^-$ which predominate in oxic environments, HSe^- and $\text{Sb}(\text{OH})_4^-$ aqueous species may also exist at equilibrium in reducing environments. However, as they are controlled by the precipitation of very insoluble FeSe and valentinite, HSe^- and $\text{Sb}(\text{OH})_4^-$ aqueous concentrations can be assumed to be extremely low. Indeed, no HPLC retention peak was observed for $\text{Sb}(\text{OH})_4^-$. Thus the total aqueous concentration can be in all cases considered to be equal to the concentration of the dominant oxidized species. After identifying and quantifying all reduced, solid RNs species, a set of redox reactions susceptible to occur between RN couples and the considered iron product couples were identified and are listed in Table 4.1. The Eh values of the corresponding half-reactions could then be calculated according to the Nernst equation:

$$E_h = -\frac{\Delta_r G^0}{nF} - \frac{RT}{nF} \ln \frac{a_{\text{Red}}}{a_{\text{Ox}}} \quad (4.1)$$

Where R and F are the universal gas constant and Faraday constant, respectively, n is the moles number of electrons transferred, a is the chemical activity for the relevant species, and $\Delta_r G^0$ is the standard Gibbs free energy of reaction.

All the RNs species standard Gibbs free energies of formation ($\Delta_f G^0$) were taken from ANDRA ThermoChimie database[193], and are listed in Table S4.10. All solid activities were set equal to 1.0 as first approximation, although this may not fully be true due to the nanosize of reductively precipitated solid phases. “In-situ” experimental Eh values were then calculated according to equation (1) and are found to fall in the stability domain of water, whose lower limit is -798.7 mV at pH 13.5 (Figure 4.5). The Fe(0)/Fe(OH)₂ couple should impose an Eh value of -850.1 mV, lying outside the water stability domain, and this may account for the observed formation of Sb⁰ according to the Sb(III)/Sb(0) limit depicted in Figure S4.8. For all other RNs species, experimental Eh values of all NZVI systems are all centered in the narrow range of -446.4±78.0 mV (Figure 4.5). For reactors with the M/H redox couple, the obtained Eh values lay between ~-346.2 mV and ~-509.4 mV, with an average value of ~-430 mV and a large standard deviation. The Eh values in M/G reactors were slightly higher, correspondingly, probably due to a higher Eh (average value is -576.0 mV) imposed by M/G, compared to M/H couple (-649.4 mV).

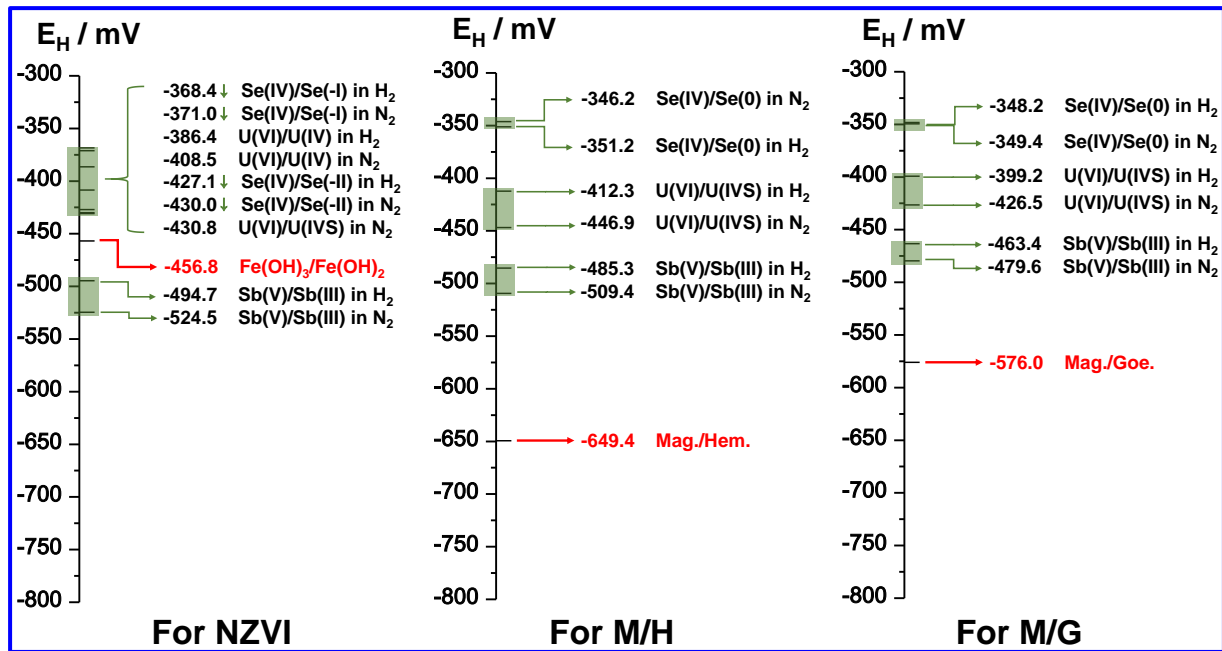


Figure 4.5. “In-situ” experimental Eh values for all the RNs systems and Eh values imposed by Fe-oxyhydroxides couples in stability domain of water. Down arrows put on Se(IV)/Se(-II) and Se(IV)/Se(-I) indicates even lower Eh values due to possibly more diluted Fe(OH)₃⁻.

Using the $\Delta_f G^0$ values listed in Table S4.10, the Eh values imposed by the various couples were computed, to try to match the experimental Eh values derived from individual RN half-cell redox reactions. In the case of NZVI, at least two Fe-oxyhydroxides couples, i.e., two interfacial Eh values, should be considered due to the fast oxidation of NZVI by water: the Fe(0)/Fe(OH)₂ couple and Fe(OH)₂/Fe(OH)₃ couple. $\Delta_f G^0$ values are critical to Eh calculation. According to PDF results, amorphous Fe(OH)₂ phase or its impurity-doped lattice, like (Fe_{1-x},Ca_x)(OH)₂ structure, are present and will be characterized by larger solubility product (K_{sp}), thus larger $\Delta_f G^0$ than corresponding crystalline phases. Using $\Delta_f G^0$ values of amorphous Fe(OH)₂[252] and Fe(OH)₃[268], the theoretical Eh imposed by Fe(OH)₂/Fe(OH)₃ couple was calculated to be equal to -456.8 mV, a value very closed to the experimental Eh values computed for the NZVI reactors. Theoretical Eh values from M/H (-649.4 mV) and M/G (-576.0 mV) couples were significantly lower than the experimental single RN half-reaction Eh values. Note that the two computed Eh values were derived from bulk Fe-oxyhydroxides and have not counted contributions of surface energy[269] and surface hydration effect[253] caused by nano-sized reaction particles, which could increase $\Delta_f G^0$. With the method described by Silvester et al[253], $\Delta_f G^0$ (+) factors of Fe-oxyhydroxides was calculated and shown in Table S4.11. After applying the surface energy adjustments, -666.8 mV and -523.8 mV were obtained for M/H and M/G couples, respectively, which still not perfectly match the experimental Eh values. In addition,

structural water on the surface of nano-particles can also lead to a higher $\Delta_f G^0$. For instance, $\sim +30 \text{ kJ mol}^{-1}$ $\Delta_f G^0$ adjustment can be estimated for nano-hematite (with an A_s of $109 \text{ m}^2 \text{ g}^{-1}$), compared to the inner bulk hematite[253].

Table 4.1. Half-cell reactions used for the computation of Eh values ^a.

System	Half-cell reaction equation
Se(IV)/Se(0)	$\text{SeO}_3^{2-}(\text{aq}) + 4\text{e}^- + 6\text{H}^+ \Leftrightarrow \text{Se}^0(\text{s}) + 3\text{H}_2\text{O}$
Se(IV)/Se(-I)	$2\text{SeO}_3^{2-}(\text{aq}) + \text{Fe}(\text{OH})_3^- + 10\text{e}^- + 15\text{H}^+ \Leftrightarrow \text{FeSe}_2 + 9\text{H}_2\text{O}$
Se(IV)/Se(-II)	$\text{SeO}_3^{2-}(\text{aq}) + \text{Fe}(\text{OH})_3^- + 6\text{e}^- + 9\text{H}^+ \Leftrightarrow \text{FeSe} + 6\text{H}_2\text{O}$
Sb(V)/Sb(III)	$2\text{Sb}(\text{OH})_6^- + 4\text{e}^- + 6\text{H}^+ \Leftrightarrow \text{Sb}_2\text{O}_3 + 9\text{H}_2\text{O}$
Sb(III)/Sb(0)	$\text{Sb}(\text{OH})_4^- + 3\text{e}^- + 4\text{H}^+ \Leftrightarrow \text{Sb}^0 + 4\text{H}_2\text{O}$
U(VI)/U(IVS)	$4\text{UO}_2(\text{OH})_4^{2-} + 6\text{e}^- + 14\text{H}^+ \Leftrightarrow \text{U}_4\text{O}_9(\text{s}) + 15\text{H}_2\text{O}$
U(VI)/U(IV)	$\text{UO}_2(\text{OH})_4^{2-} + 2\text{e}^- + 4\text{H}^+ \Leftrightarrow \text{UO}_2(\text{s}) + 4\text{H}_2\text{O}$
Fe(0)/Fe(OH) ₂ couple	$\text{Fe}(\text{OH})_2 + 2\text{e}^- + 2\text{H}^+ \Leftrightarrow \text{Fe}^0 + 2\text{H}_2\text{O}$
Fe(OH) ₂ /Fe(OH) ₃ couple	$\text{Fe}(\text{OH})_3 + \text{e}^- + \text{H}^+ \Leftrightarrow \text{Fe}(\text{OH})_2 + \text{H}_2\text{O}$
M/H couple	$3\text{Fe}_2\text{O}_3 \text{ (hematite)} + 2\text{e}^- + 2\text{H}^+ \Leftrightarrow 2(\text{Fe}^{\text{II}}\text{Fe}^{\text{III}})_2\text{O}_4 + \text{H}_2\text{O}$
M/G couple	$6\text{FeOOH} \text{ (goethite)} + 2\text{e}^- + 2\text{H}^+ \Leftrightarrow 2(\text{Fe}^{\text{II}}\text{Fe}^{\text{III}})_2\text{O}_4 + 4\text{H}_2\text{O}$

^a Experimental $[\text{Fe}]_{\text{total}}$ was under the ICP-OES detection limit (~ 10 ppb). Here, $\text{Fe}(\text{OH})_3^-$ concentration is estimated at ~ 5 ppb (i.e., 10^{-7} M).

Thus, the nano-sized Fe-oxyhydroxides couples may lead to values close to the experimental Eh values, accordantly. However, another acceptable way to explain experimental Eh distribution in M/H and M/G reactors can be a control by formed amorphous $\text{Fe}(\text{OH})_2/\text{Fe}(\text{OH})_3$ couple on the surface. In extremely alkaline CPW, most dissolved Fe^{2+} and Fe^{3+} present on the surface of Fe-oxyhydroxides could precipitate instantaneously into amorphous $\text{Fe}(\text{OH})_2$ and $\text{Fe}(\text{OH})_3$ phases, and then participate in the following redox reactions, listed in Table 4.1. Finally, the presence of an 8.0 bar H_2 at room temperature did not have large effects on the experimental “in-situ” Eh values.

4.3.6. Environmental implications.

In geological repositories, the iron corrosion interface in reinforced concrete are complex, resulting in an expected strong Eh gradient from the steel surface outwards in the concrete bulk. In our CPW-systems, all the experimental redox potentials derived from RNs half-

reactions pointed out to a unique central value of ~ -450 mV. This value is probably imposed by the amorphous $\text{Fe}(\text{OH})_2/\text{Fe}(\text{OH})_3$ or $(\text{Fe}_{1-x},\text{Ca}_x)(\text{OH})_2/\text{Fe}(\text{OH})_3$ couple, rather than by the originally added Fe-oxyhydroxides.

In literature[241], disagreements are frequently observed between computed Nernstian Eh and electrode-measured Eh values and often attributed to analytical defects at Pt-electrode-water interface (which is worse in the case of Pt-electrode in hyperalkaline cement leachate). In contrast, the approach described here shows a good internal consistency among all individual RN half-reaction Eh value and thus appear to be a reliable new method to compute Eh in concrete, but also in other (e.g., biological) systems where local Eh direct measurement is not feasible.

In this study, a combination of synchrotron-based spectroscopic techniques and wet chemistry methods under anaerobic conditions was employed to “*in-situ*” identify and quantify solid and aqueous RNs species, which allows us to get *ab initio* reliable Eh values experimentally using Nernst equation. Regarding the severe hyperalkaline cement environment prevailing in geological repositories, $\text{H}_2(\text{g})$ is also expected to occur, which would further totally disable the measuring with Pt-electrodes. This study will facilitate the estimation of the “experimental” redox potential in reinforced cement matrix and thus allow a better evaluation of RNs redox behavior. Therefore, our approach here could pave the way for RNs speciation mapping in real reinforced concrete blocks and further description of the Eh gradient (spatial resolutions depend on the sizes of X-ray beam scanning pixels: $\sim\mu\text{m}$ level). Besides, this method could also be applied for the corrosion assessment of the bridge (e.g., cast iron bridges) bases, high power electric transmission towers foundations, and high-speed rail foot in corrosive coastline environments.

Supporting Information

Associated content

XRD patterns, FE-SEM micrographs, and specific surface area of synthesized NZVI and Fe-(hydr)oxides. Fe-(hydr)oxides equilibrium and RNs sorption kinetics. HPLC analysis of aqueous Sb. XPS spectra of equilibrated NZVI. Eh-pH diagrams of RNs systems. Eh values out of water stability domain. CPW content. Aqueous results of reactors in N₂ and H₂ atmosphere. LCF results of XANES. List of $\Delta_f G^0$ values used. Surface energy contributions to $\Delta_f G^0$ values.

Text S4.1. Synthesis of NZVI, magnetite, hematite, and goethite.

The initial NZVI suspension was obtained initially by dropwise addition of 80 ml of 1.6 M NaBH₄ solution into 40 ml of 1 M FeCl₃·6H₂O solution under continuously magnetic stirring in the glove box[248]. Through 0.22- μ m membrane filtration, the NZVI cake was quickly washed by alternate degassed water and acetone six times. Finally, NZVI particles were re-dispersed in acetone, and freeze-dried. Magnetite was synthesized by slowly adding 50 ml of a mixed ferrous/ferric chloride solution ($Fe^{II}/Fe^{III} = 0.5$ and $[Fe]_{total} = 1.2$ M) into 400 ml of 0.9 M NH₃ solution under constantly magnetic stirring and inert atmosphere. The suspension was washed by replacing the supernatant with degassed water six times [249]. Hematite was prepared by hydrolysis of ferric solutions[250, 251]. Under vigorous stirring, 0.02 M Fe(NO₃)₃·9H₂O was introduced into preheated 2 L of 0.002 M HCl at 98 °C. Incubation lasted 7 days at 98 °C in a forced convection oven to complete sol formation. After incubation and cooling, a compact and bright red precipitate was formed. With centrifugation, the particles were washed four times by Milli-Q water. Goethite was obtained by transformation of ferrihydrite under alkaline conditions [252]. Firstly, ferrihydrite was precipitated by adding 180 ml of 5 M NaOH solution into 100 ml of 1 M Fe(NO₃)₃·9H₂O. Then, dilute the suspension into 2 L with Milli-Q water and place it in a 70 °C oven for 60 h. Transformation from the redbrown ferrihydrite to a compact yellow goethite precipitate can be seen. Washing four times by centrifuging, the goethite suspension was transferred in glove box and fixed into a suitable S/L ratio.

Text S4.2. Calculation of distribution coefficient.

The distribution coefficient (K_d) was calculated by

$$K_d = \frac{C_0 - C_{aq}}{C_{aq}} \cdot \frac{V}{m} \quad (\text{L g}^{-1}) \quad (\text{S4.1})$$

where C_0 and C_{aq} denote Se concentrations added initially and measured in solution at equilibrium (mol L^{-1}), respectively. V represents the volume of liquid phase (L) and m is the mass of the solid phase (g).

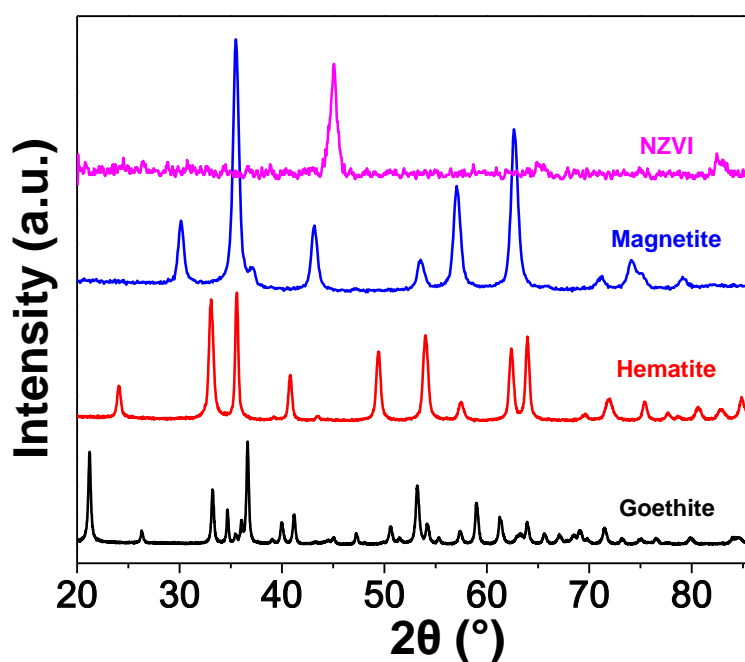


Figure S4.1. X-ray diffraction patterns of synthesized iron products. Cu $K\alpha$ radiation at 1.5406 \AA is used.

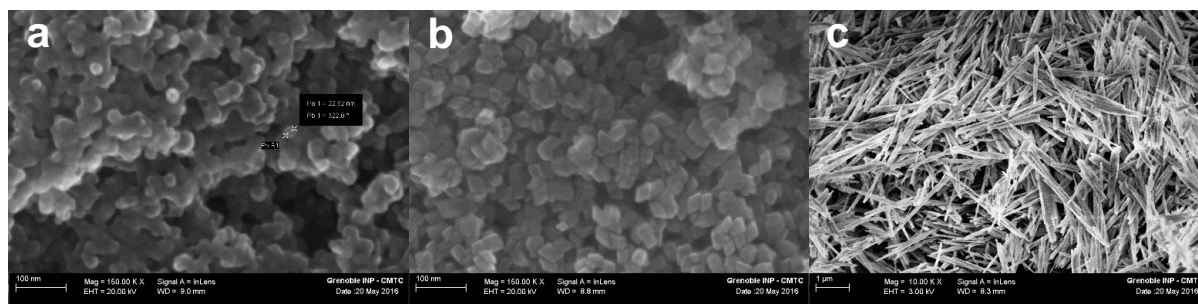


Figure S4.2. FE-SEM micrographs of the synthesized iron products. (a) Magnetite particles, scale bar, 100 nm. (b) Hematite particles, scale bar, 100 nm. (c) Goethite particles, scale bar, 1 μm .

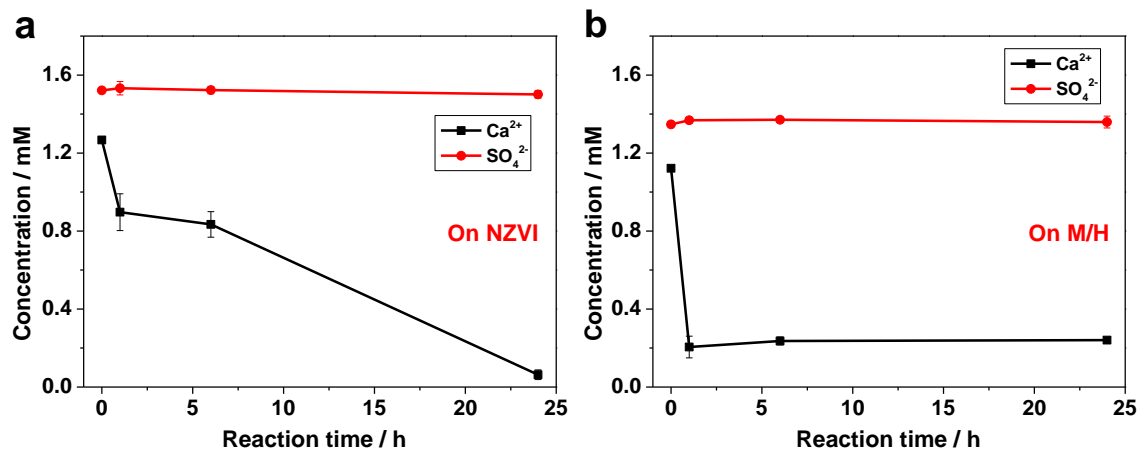


Figure S4.3. Concentration profiles of aqueous Ca^{2+} and SO_4^{2-} of CPW with reaction time. (a) On NZVI, S/L ratio is 4.94 g L^{-1} ; (b) On M/H, S/L ratio is $1.34 + 6.03$ (Magnetite + Hematite) g L^{-1} .

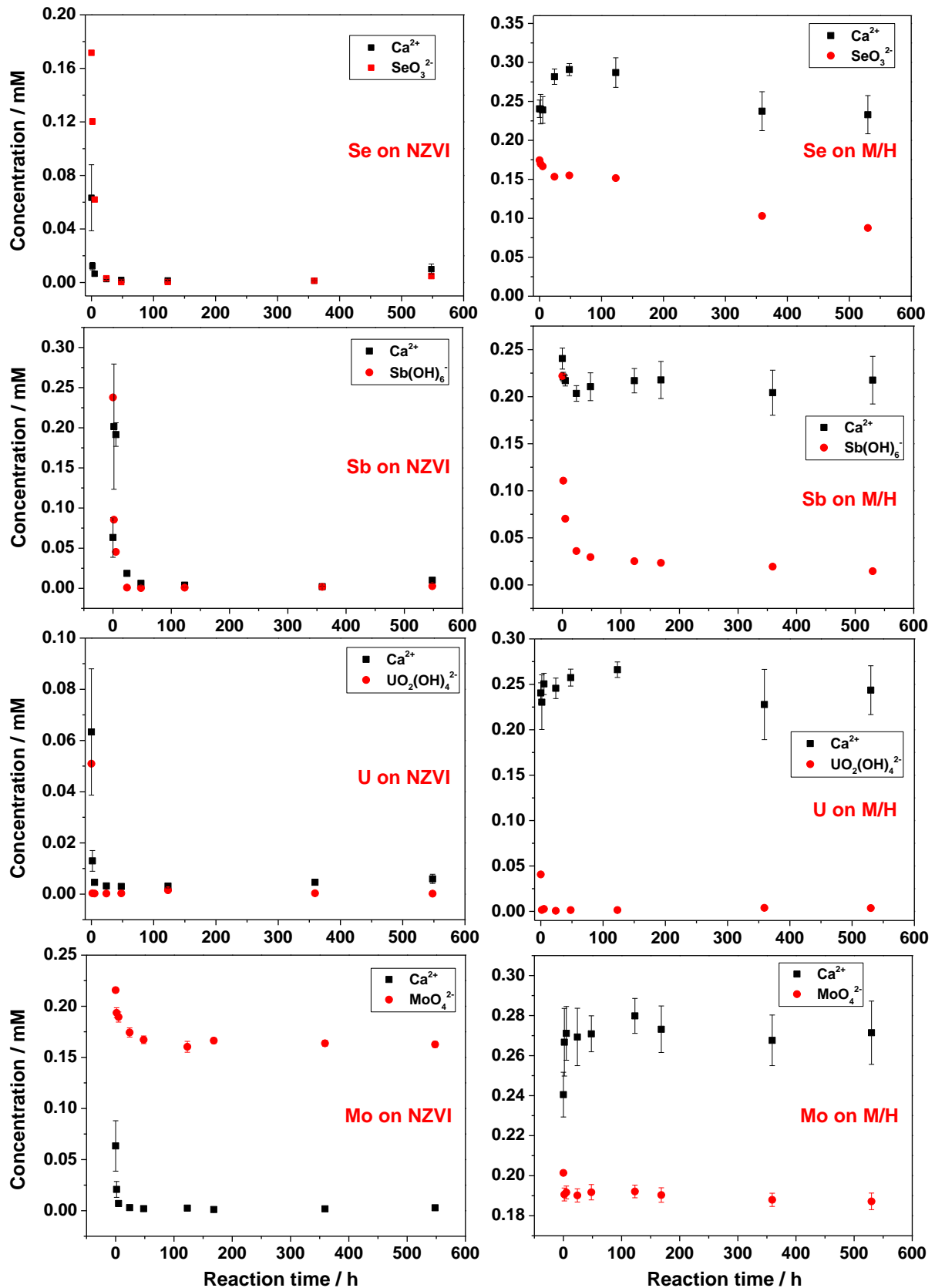


Figure S4.4. Sorption kinetics of Se, Sb, U, and Mo (from top to bottom) on NZVI (left panel) and M/H (right panel). Same S/L ratios were used with their equilibrium kinetics with CPW in Figure S4.3.

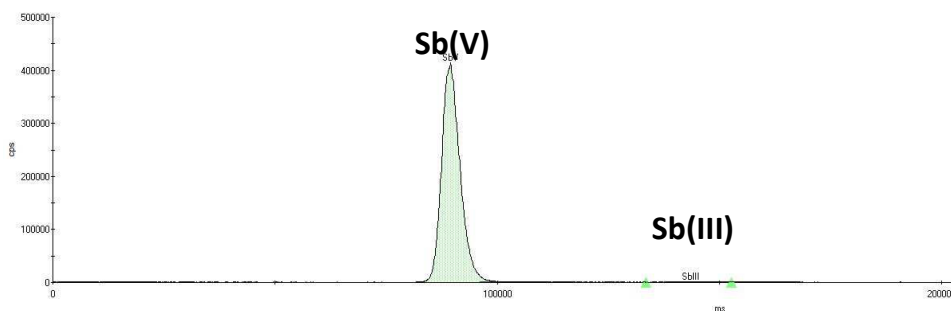


Figure S4.5. HPLC analysis results of aqueous sample Sb-NZVI-H₂-70d (Sb(OH)₆⁻ reacting with NZVI for 70 d under H₂ atmosphere). The tiny peak at longer retention time belongs to Sb(III), suggesting that almost no aqueous Sb(III) existed.

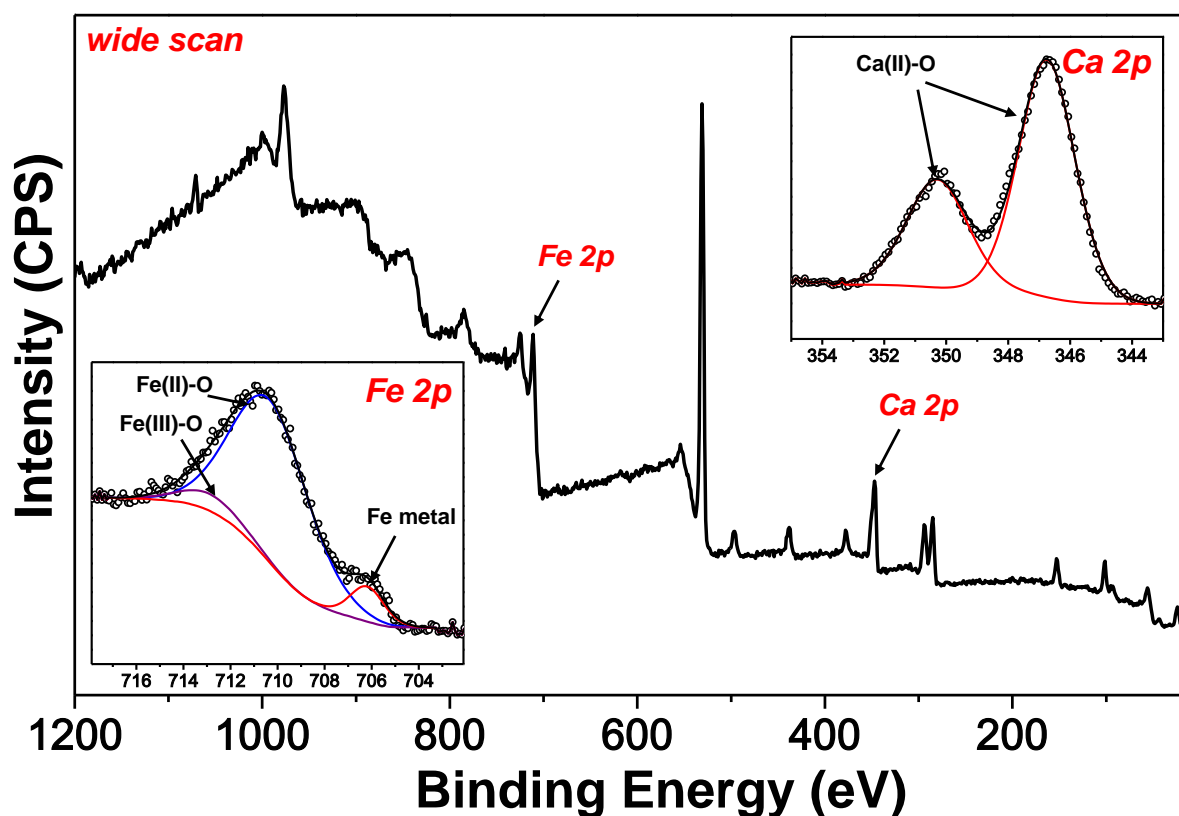


Figure S4.6. Fitted Fe 2p and Ca 2p regions (insets) and wide scan XPS spectra of equilibrated NZVI with 264 h. The solid line and black dots represent the fit curve of each contribution and the experimental data, respectively. Scans were done with monochromated Al K α X-rays and electrostatic lens are used.

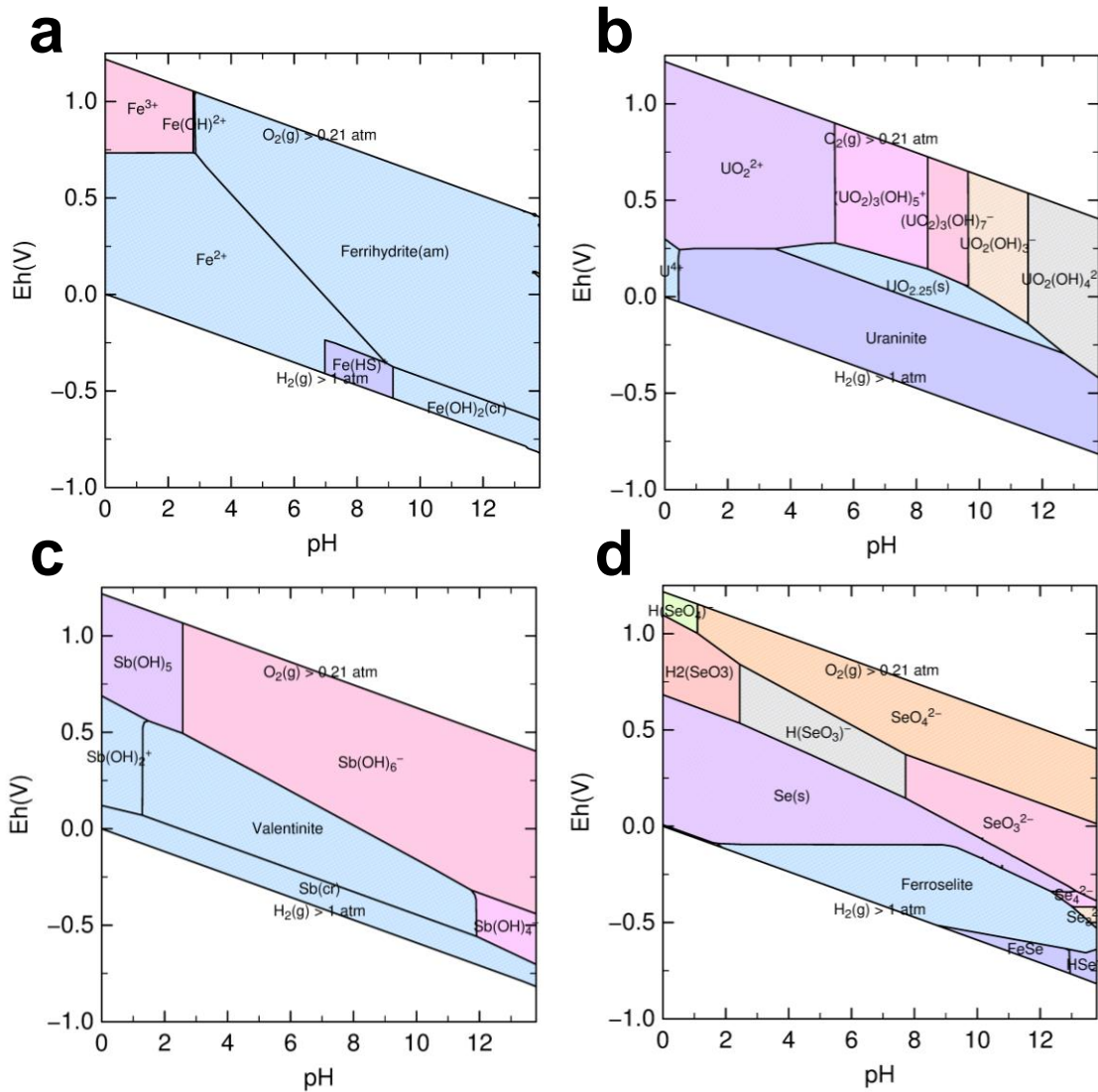


Figure S4.7. Eh-pH diagrams of (a) Fe system (Σ Fe = 5 ppm), (b) U system (Σ U = 10 ppm) (c) Sb system (Σ Sb = 20 ppm), and (d) Se system (Σ Se = 14 ppm), 298.15 K, 10^5 Pa. Experimental content of CPW was input as the background matrix. Selected equilibrium phases, which were identified by XANES analysis, are set saturated for each RN. The lower limit is traditionally set up for $P_{H_2} = 1$, although P_{H_2} was initially imposed at 8 bar in H_2 reactors.

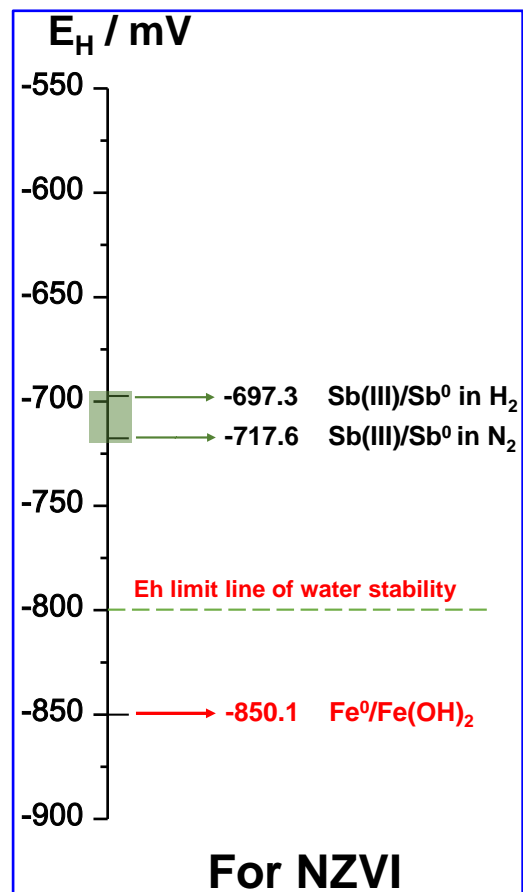


Figure S4.8. “In-situ” experimental Eh values for Sb(III)/Sb(0) system and the Eh value, out of water stability domain, imposed by Fe(0)/Fe(OH)₂ couple. NZVI was the only possible Fe phase in our reactors to reduce Sb(III) into Sb(0), thus Fe(0)/Fe(OH)₂ couple is responsible for Eh values of Sb(III)/Sb(0) system.

Table S4.1. Experimental concentrations (measured by ICP-OES) of main ion species in CPW.

Ion species	Content / mol L ⁻¹
K ⁺	2.11×10 ⁻¹
Na ⁺	7.60×10 ⁻²
Ca ²⁺	1.26×10 ⁻³
Cl ⁻	1.00×10 ⁻³
SO ₄ ²⁻	1.50×10 ⁻³

Table S4.2. The specific surface area (SSA) of each iron product and solid to liquid ratio applied in experiments.

	SSA m ² g ⁻¹	Site density nm ⁻²	Selected density nm ⁻²	Surface site mol L ⁻¹	[RN] ^a mM	S/L g L ⁻¹
Goethite	19.7	1.18[270]				6.12
Hematite	42.1	2.07[16]	1	2.00×10 ⁻⁴	0.20	2.86
Magnetite	75.4	1-20[271]				1.60
NZVI	28.9	-				4.17

^a U concentration added was 0.05 mM.

Table S4.3. Aqueous results of reactors in N₂ atmosphere. Reaction time was approximately 100 days, which was totally enough to reach sorption equilibrium. Total Fe concentration is below the ICP-OES detection limit (~ 10 ppb). The two Eh values for each NZVI sample were the Eh at the beginning and the end of the sorption^a.

RN	Fe phases	pH	Eh /mV	[Ca] _{tot} /mM	[S] _{tot} /mM	[RN] _{tot} /mM	K _d / L g ⁻¹
	-	13.470	-157.9	1.240(51)	1.510(4)	0.0407(3)	-
U ^{VI}	NZVI	13.468	-732.2, -533.6	0.655(17)	1.526(15)	0.0007(5)	117.1(84.7)
	M/H	13.448	-403.8	0.687(13)	1.537(13)	0.0003(1)	122.6(24.6)
	M/G	13.456	-459.3	0.786(10)	1.495(16)	0.0008(3)	28.5(10.4)
	-	13.521	-161.4	1.229(26)	1.526(19)	0.1644(18)	-
Se ^{IV}	NZVI	13.454	-732.7, -539.3	0.061(8)	1.415(15)	0.0099(6)	3.77(29)
	M/H	13.442	-416.7	0.035(5)	1.308(17)	0.1239(12)	0.07(1)
	M/G	13.472	-444.4	0.566(13)	1.386(28)	0.1186(15)	0.05(1)
	-	13.515	-164.9	1.277(23)	1.518(10)	0.2011(30)	-
Mo ^{VI}	NZVI	13.464	-754.6, -530.1	0.017(1)	1.404(4)	0.1229(20)	0.15(1)
	M/H	13.458	-437.2	0.029(5)	1.318(1)	0.2081(27)	0
	M/G	13.470	-441.4	0.582(12)	1.372(1)	0.2055(26)	0
	-	13.519	-159.0	1.278(18)	1.533(17)	0.2220(45)	-
Sb ^V	NZVI	13.445	-744.7, -532.6	0.045(9)	1.415(10)	0.0006(2)	102.0(31.2)
	M/H	13.456	-433.7	0.022(3)	1.318(27)	0.0026(1)	18.9(0.9)
	M/G	13.463	-442.3	0.515(11)	1.367(13)	0.0305(6)	0.81(4)

^a Eh values are relative to standard hydrogen electrode reference; Uncertainties are given by the number in brackets on the last digit(s).

Table S4.4. Aqueous results of reactors in the atmosphere of 7 bar H₂ and 1 bar N₂. Reaction time was approximately 21 days. Total Fe concentration is below the ICP-OES detection limit (~ 10 ppb). The stability criterion of Eh measurement was a drift of less than 1.0 mV over 10 min, or a maximum equilibration time of 1 h, whichever occurred firstly^a.

RN	Fe phases	pH	Eh /mV	[Ca] _{tot} /mM	[S] _{tot} /mM	[RN] _{tot} /mM	K _d / L g ⁻¹
U ^{VIb}	-	13.450	-730.9	1.241(329)	1.523(33)	0.0172(2)	-
	NZVI	13.467	-741.3	0.548(294)	1.552(23)	0.0003(2)	78.8(50.4)
	M/H	13.477	-739.7	1.104(121)	1.455(42)	0.0005(1)	34.6(8.6)
	M/G	13.480	-735.0	0.278(70)	1.470(18)	0.0035(1)	2.00(9)
Se ^{IV}	-	13.492	-733.1	1.451(131)	1.507(19)	0.1711(28)	-
	NZVI	13.452	-731.9	0.402(71)	1.487(20)	0.0480(5)	0.62(2)
	M/H	13.469	-743.8	0.439(54)	1.355(34)	0.1438(18)	0.04(1)
	M/G	13.465	-734.5	0.349(65)	1.345(25)	0.1270(25)	0.05(1)
Mo ^{VI}	-	13.459	-738.6	1.481(44)	1.511(25)	0.2016(115)	-
	NZVI	13.462	-743.9	0.404(48)	1.512(14)	0.1663(94)	0.05(3)
	M/H	13.469	-754.0	0.428(56)	1.349(18)	0.2052(117)	0
	M/G	13.479	-744.5	0.377(54)	1.350(13)	0.2062(118)	0
Sb ^V	-	13.474	-739.7	1.459(99)	1.518(20)	0.2207(153)	-
	NZVI	13.471	-744.0	0.034(7)	1.598(41)	0.0065(3)	8.00(92)
	M/H	13.482	-740.9	0.123(32)	1.391(47)	0.0137(7)	3.40(45)
	M/G	13.495	-736.1	0.149(24)	1.374(81)	0.0748(44)	0.26(5)

^a Eh values are relative to standard hydrogen electrode reference; Uncertainties are given by the number in brackets on the last digit(s).

^b Small amount of yellow U precipitate was observed in the reactors.

Table S4.5. Aqueous results of reactors in the atmosphere of 7 bar H₂ and 1 bar N₂. Reaction time was approximately 70 days. Total Fe concentration is below the ICP-OES detection limit (~ 10 ppb). The stability criterion of Eh measurement was a drift of less than 1.0 mV over 10 min, or a maximum equilibration time of 1 h, whichever occurred firstly^a.

RN	Fe phases	pH	Eh /mV	[Ca] _{tot} /mM	[S] _{tot} /mM	[RN] _{tot} /mM	K _d / L g ⁻¹
U ^{VI}	-	13.432	-734.3	0.925(309)	1.515(25)	0.0361(9)	-
	NZVI	13.440	-731.5	0.352(223)	1.476(28)	0.0026(10)	15.2(6.7)
	M/H	13.477	-730.3	0.594(224)	1.484(29)	0.0019(1)	16.1(1.4)
	M/G	13.465	-730.9	0.676(73)	1.478(18)	0.0037(1)	4.5(2)
Se ^{IV}	-	13.407	-743.3	1.119(49)	1.506(24)	0.1696(40)	-
	NZVI	13.405	-738.0	0.162(26)	1.370(15)	0.0073(4)	5.36(43)
	M/H	13.451	-725.6	0.203(19)	1.332(22)	0.0650(8)	0.36(2)
	M/G	13.458	-729.9	0.085(15)	1.329(17)	0.1147(13)	0.06(1)
Mo ^{VI}	-	13.472	-749.7	1.130(82)	1.527(24)	0.1983(112)	-
	NZVI	13.405	-738.7	0.140(87)	1.377(22)	0.1054(61)	0.21(5)
	M/H	13.447	-729.6	0.190(14)	1.344(14)	0.1940(112)	0.01(3)
	M/G	13.446	-724.4	0.080(6)	1.355(23)	0.2002(115)	0
Sb ^V	-	13.498	-726.9	0.885(378)	1.535(31)	0.2442(94)	-
	NZVI	13.423	-751.1	0.015(15)	1.406(17)	0.0070(8)	8.32(1.31)
	M/H	13.442	-725.7	0.013(13)	1.345(23)	0.0166(6)	3.07(25)
	M/G	13.435	-727.7	0.003(3)	1.379(21)	0.0872(25)	0.23(2)

^a Eh values are relative to standard hydrogen electrode reference; Uncertainties are given by the number in brackets on the last digit(s).

Table S4.6. Quantification of selenium species (molar fraction) by LCF of XANES. Also reported is the concentration sum (Σ), which is not constrained to 100% for samples, and the value of the reduced χ square (χ_v^2), both indicating good matches to the experimental spectra. Uncertainties are given by the number in brackets on the last digit(s), i.e., 77.6(1) represents 77.6 ± 0.1 , and 53.1(1.2) represents 53.1 ± 1.2 .

ID	FeSe (%)	FeSe ₂ (%)	Se ⁰ (%)	CaSeO ₃ (%)	Na ₂ SeO ₃ (%)	FeSeO ₃ (%)	Σ (%)	χ_v^2 $\times 10^{-3}$
NZVI-N ₂ -212d	77.6(1)	22.8(1)	-	-	-	-	100.4	0.9
M/H-N ₂ -212d	-	-	100.0(1)	-	2.1(1)	-	102.1	1.3
M/G-N ₂ -212d	-	-	53.1(1.2)	53.4(1.1)	-	-	106.5	3.1
NZVI-H ₂ -21d	93.9(1.0)	6.6(1.1)	-	-	-	-	100.5	0.2
M/H-H ₂ -21d	-	-	53.0(1.1)	50.7(1.0)	-	-	103.7	2.4
M/G-H ₂ -21d	-	-	61.0(1.1)	41.7(1.0)	-	-	102.7	2.1
NZVI-H ₂ -70d	87.3(1.4)	11.8(1.4)	-	-	-	-	99.1	0.4
M/H-H ₂ -70d	-	-	92.9(7)	8.1(5)	-	-	101.0	0.8
M/G-H ₂ -70d	-	-	81.9(9)	22.1(8)	-	-	104.0	1.6

Table S4.7. Quantification of antimony species (molar fraction) by LCF of XANES. Also reported is the concentration sum (Σ), which is not constrained to 100% for samples, and the value of the reduced χ square (χ_v^2), both indicating good matches to the experimental spectra. Uncertainties are given by the number in brackets on the last digit(s), i.e., 68.5(8.2) represents 68.5 ± 8.2 .

ID	Sb ⁰ (%)	Sb ₂ O ₃ (%)	K[Sb(OH) ₆] (%)	Ca[Sb(OH) ₆] ₂ (%)	Sb ^V - Goe. (%)	Sb ₂ O ₅ (%)	Σ (%)	χ_v^2 $\times 10^{-3}$
NZVI-N ₂ - 212d	68.5(8.2)	20.2(10.9)	11.7(11.0)	-	9.7(10.0)	-	110.2	1.8
M/H-N ₂ - 212d	-	14.0(2.4)	-	22.2(4.5)	75.4(4.7)	-	111.6	1.3
M/G-N ₂ - 212d	-	37.7(3.2)	-	19.3(6.4)	56.8(6.3)	-	113.9	2.4
NZVI-H ₂ - 21d	76.6(9.5)	12.7(12.4)	16.1(12.5)	-	5.4(10.7)	-	110.8	2.6
M/H-H ₂ - 21d	-	13.2(3.2)	-	26.9(6.3)	72.1(6.5)	-	112.3	2.3
M/G-H ₂ - 21d	-	9.6(2.5)	-	49.0(5.1)	50.6(5.2)	-	109.2	1.4
NZVI-H ₂ - 70d	76.3(6.8)	5.3(9.0)	16.1(10.1)	-	8.2(8.4)	-	105.9	1.1
M/H-H ₂ - 70d	-	18.6(2.5)	-	29.7(4.7)	58.7(5.2)	-	107.0	1.4
M/G-H ₂ - 70d	-	17.4(1.6)	-	68.9(3.0)	18.4(3.4)	-	104.7	0.8

Table S4.8. Quantification of uranium species (molar fraction) by LCF of XANES. Also reported is the concentration sum (Σ), which is not constrained to 100% for samples, and the value of the reduced χ square (χ_v^2), both indicating good matches to the experimental spectra. Uncertainties are given by the number in brackets on the last digit(s), i.e., 13.2(4.7) represents 13.2 ± 4.7 .

ID	UO ₂ (%)	Uranate(VI) (%)	U ₄ O ₉ (%)	Σ (%)	χ_v^2 $\times 10^{-3}$
NZVI-N ₂ -212d	13.2(4.7)	67.9(1.2)	19.5(5.7)	100.6	0.1
M/H-N ₂ -212d	-	70.8(1.5)	29.8(7.1)	100.6	0.2
M/G-N ₂ -212d	-	60.8(1.1)	39.4(1.0)	100.2	0.2
NZVI-H ₂ -21d	21.5(9.5)	34.8(2.4)	45.1(11.6)	101.5	0.6
M/H-H ₂ -21d	-	63.9(1.8)	37.0(8.7)	100.9	0.3
M/G-H ₂ -21d	-	82.2(2.1)	17.8(2.0)	100.0	0.7
NZVI-H ₂ -70d	46.2(6.5)	54.6(1.6)	-	100.8	0.3
M/H-H ₂ -70d	-	88.8(1.9)	12.2(9.3)	101.0	0.4
M/G-H ₂ -70d	-	92.3(1.2)	7.8(1.2)	100.0	0.2

Table S4.9. Quantification of molybdenum species (molar fraction) by LCF of XANES. Also reported is the concentration sum (Σ), which is not constrained to 100% for samples, and the value of the reduced χ square (χ_v^2), both indicating good matches to the experimental spectra. Uncertainties are given by the number in brackets on the last digit(s), i.e., 19.1(2.3) represents 19.1 ± 2.3 .

ID	FeMoO ₄ (%)	CaMoO ₄ (%)	Na ₂ MoO ₄ (%)	(NH ₄) ₆ Mo ₇ O ₂₄ (%)	Σ (%)	χ_v^2 $\times 10^{-3}$
NZVI-N ₂ -212d	19.1(2.3)	44.1(3.2)	35.7(3.3)	-	99.0	0.4
NZVI-H ₂ -21d	49.9(1.3)	12.9(1.8)	36.5(1.7)	-	99.4	0.1
NZVI-H ₂ -70d	49.8(1.6)	23.0(2.2)	26.2(2.2)	-	99.0	0.2

Table S4.10. Standard Gibbs free energies of formation ($\Delta_f G^0$, kJ mol⁻¹) used for performing thermodynamic calculations. All the data is from ANDRA Thermo-Chimie database[193], except of $\Delta_f G^0$ values of α -Fe₂O₃, amorphous Fe(OH)₃ and Fe(OH)₂.

Reactant	$\Delta_f G^0$ / kJ mol ⁻¹	STD error	Reactant	$\Delta_f G^0$ / kJ mol ⁻¹	STD error
H ⁺	0	-	FeSe ₂	-101.3	15
H ₂ O(l)	-237.14	-	HSe ⁻	43.5	2.0
Fe(OH) ₃ ⁻	-619.865	-	Se ₂ ²⁻	112.628	6.772
α -Fe ₂ O ₃	-744.249[272]	-	Sb ⁰	0	-
Fe(OH) ₃	-688.352[268]	-	Sb ₂ O ₃	-626.649	2.983
Fe ₃ O ₄	-1012.206	-	Sb(OH) ₄ ⁻	-814.504	1.698
FeOOH	-488.334	-	Sb(OH) ₆ ⁻	-1216.635	2.232
Fe(OH) ₂	-484.2[252]	-	UO ₂ (cr)	-1031.8	1
Se ⁰	0	-	UO _{2.25} (cr)	-1069.125	1.702
SeO ₃ ²⁻	-362.39	-	UO ₂ ²⁺	-952.551	1.747
β -FeSe	-70.1	4.0	UO ₂ (OH) ₄ ²⁻	-1716.172	4.260

Table S4.11. Contributions of surface energy to $\Delta_f G^0$ values of Fe-(hydr)oxides ^a.

Fe-(hydr)oxides	MW / g mol ⁻¹	A _s / m ² g ⁻¹	γ_s / J m ⁻²	$\Delta_f G^0$ (+) factor / kJ mol ⁻¹
Magnetite (Fe ₃ O ₄)	231.53	75.4	0.0489[273]	0.57
Hematite (Fe ₂ O ₃)	159.69	42.1	0.95[274]	4.26
Goethite (FeOOH)	88.85	19.7	1.6[275]	1.87
NZVI (Fe ⁰)	55.85	28.9	3[276]	3.23

^a MW represents the molecular weight; A_s is the specific surface area; γ_s is the mean surface free energy. $\Delta_f G^0$ (+) factor is equal to $\frac{2}{3} \cdot \gamma_s \cdot A_s \cdot MW$.

Chapter 5. RNs (i.e., U, Se, Mo, and Sb) sorption behavior on hydrated Fe-bearing CEM-V/A cement

Abstract

Reinforced cementitious structures in geologic nuclear waste repositories will act as barriers that limit the mobility of radionuclides (RNs) in case of eventual leakage. RN sorption can be coupled to the corrosion of steel reinforcements after intrusion of groundwater, via mechanisms which are critical to safety assessment. Here, we combine wet chemistry methods and synchrotron-based X-ray techniques to study the sorption behaviours of RNs (i.e., U, Se, Mo, Sb) on hydrated CEM-V/A cement and its types containing Fe-phases (i.e., NZVI, magnetite, hematite, goethite, magnetite/hematite, and magnetite/goethite). Hydrated NZVI-bearing cement possessed the highest RNs removal efficiency and the pristine hydrated cement had a better uptake performance than Fe-(hydr)oxides-bearing cement. All the types of cement showed a strong affinity towards Sb(V) and U(VI), resulting in decreasing R_d order of $Sb > U > Se > Mo$. Clarkeite-type colloidal nanoparticles formation and after adsorption on cement could be the predominated U(VI) sorption mechanisms, while co-precipitation with Ca-sites could be the most effective uptake path for Sb(V). S K-edge X-ray absorption near-edge structure (XANES) analysis uncovered the existence of reducing S species, e.g., sulfide and possible FeS_2 , which may act as reductants for RNs. Linear combination fit (LCF) of Se K-edge XANES spectroscopy revealed that Se(IV) uptake was attributed to complexation with Ca-sites and reductive precipitation by NZVI and sulfide, revealing that even the blank hydrated CEM-V/A cement was a good reductant towards Se(IV). Besides, pair distribution function (PDF) analyses of HE-XRD spectra showed that after SeO_3^{2-} corrosion, NZVI would completely transformed into $Fe(OH)_2$ and tetrahedron-octahedron iron bridging of magnetite would collapse due to the oxidation by Se(IV). No reduction of molybdate can be detected. Mo K-edge XAS analysis uncovered that AFm- SO_4 and Fe^0 were the two most effective phases for MoO_4^{2-} removal in reinforced cement. According to the microprobe mapping, U concentrated on the surface of Ca-rich phases while Mo had strong correlation with Fe phases. Fe^0 always showed strong affinity to all RNs, while hydrated cement phases had a certain selectivity (e.g., RNs' complexation ability with Ca). Evaluation of RNs sorption behaviours on hydrated CEM-V/A cement is significant and the obtained experimental results in

simulated reinforced concrete environment is expected to provide fundamental data to reach this goal.

5.1. Introduction

Deep geological storage in clay rich host rocks is foreseen in France and Switzerland for low- and intermediate-level radioactive waste (L/ILW)[277, 278]. In the repositories, reinforced cementitious materials are used for tunnel support and backfill, waste containers and waste matrixes, which are considered as barriers that inhibit the mobility of RNs in case of eventual leakage. Possessing advantages of longer internal high pH conditions and better resistance to sulfate attack[84], CEM-V/A type of cement is preferred in France, consisting of 50% Portland cement, 25% blast furnace slag (which may contain 2-4 % sulfide of Cd, Cu, Fe and Fe⁰), and 25 % fly ash (rich in silica and containing a small amount of Fe oxides).

In reinforced CEM-V/A cement system, cement hydration products and the corrosion products of embedded steel are potential to remove RNs (e.g., U, Se, Mo, Sb). Phases in hydrated CEM-V/A cement could include calcium silicate hydrate phases (CSH, the major component in hydrated cement)[35], two types of minor phases - ettringite[36, 37] and AFm phases[38, 39], portlandite, gypsum, metal sulfides from blast furnace slags, and possible pyrite. On the other hand, corrosion of steel could result in white rust (Fe(OH)₂), magnetite (Fe₃O₄), goethite (α -FeOOH), and hematite (α -Fe₂O₃) [240] from inner to outer level. Numerous studies have reported RNs sorption behavior on cement hydration products[49]. Previous reports show that AFm phases are potential candidates for the retention of I⁻[39], SeO₃²⁻/SeO₄²⁻[58-60], and MoO₄²⁻[217]. Besides, ettringite and CSH phase also show a good affinity to SeO₃²⁻ [58, 60] and UO₂²⁺[48]. Sorption of MoO₄²⁻ [73] and UO₂²⁺ [48] on hardened cement paste (HCP) has been also studied, showing that Mo-substitution in AFm phase and precipitation of calcium-uranate predominated, respectively. In addition, reduced S species (e.g., mackinawite and pyrite) originally from the slags can also immobilize SeO₃²⁻ [110, 261], Sb(OH)₆⁻[24], and UO₂²⁺[98, 99] via reductive precipitation under nearly neutral conditions. In addition, Fe⁰ and its corrosion products can also immobilize RNs (e.g., U^{VI}[15-19], Se^{IV}[22], Sb^V[24, 27] , and Mo^{VI}[29-31]) through reductive precipitation and surface adsorption. However, in a simulated hydrated cement environment under hyperalkaline conditions (pH ~13.5), sorption behaviors of RNs anions on these CEM-V/A cement hydration products and Fe⁰-reinforced CEM-V/A cement are still not well-documented.

In this project, we combined wet chemistry methods and synchrotron-based X-ray spectroscopic analysis to study RNs sorption behaviors on pristine CEM-V/A HCP, types of hydrated Fe-reinforced cement, and separated cement hydration products in cement pore water (pH ~13.5). We aim to determine potential active sorption sites for RNs and map the concentration distribution of each RN during its diffusion in Fe-reinforced CEM-V/A HCP.

5.2. Materials and methods

5.2.1. Materials and chemicals.

Boiled and Argon-degassed Milli-Q water (18.2 M Ω ·cm) was used for all the reactors. Chemicals used here, including Fe-salts and RNs-bearing chemicals, are the same with those described in Chapter 4. CEM-V/A type cement powder (Calcia), serving for French geological nuclear waste repositories, was received from French Alternative Energies and Atomic Energy Commission (CEA). Its corresponding cement pore water (CPW) and all the Fe products, including NZVI, magnetite, hematite, and goethite, were synthesized as described in Chapter 4. All experiments were performed in a N₂-filled glove box (O₂<2 ppm, using NaOH as the CO₂ trap) to prevent oxidation and possible CO₂ contamination.

5.2.2. Preparation of powder samples of hydrated Fe-bearing cement products.

Seven types of hydrated Fe-bearing cement samples in form of powder, also including the blank hydrated CEM-V/A cement (named HCEM-V), were prepared by grinding the corresponding hydrated cement cores, for RNs batch sorption experiments. Three types among them, including NZVI-bearing cement (named C-NZVI), magnetite-hematite coupling cement (named C-M/H), and magnetite-goethite coupling cement (named C-M/G) were produced, aiming for simulating the corroded steel phases in hydrated cement. The mass ratio of CEM-V/A cement powder to total Fe element content was used as 4:1, with the Fe-(hydr)oxides couples added equally. Another three types were set as control samples for C-M/H and C-M/G, corresponding to hydrated cement phases with the three Fe-(hydr)oxides (i.e., magnetite, hematite, and goethite) introduced individually, named by C-Mag, C-Hem, and C-Goe, respectively. Water to cement (W/C) ratio was 0.4 and all the components were mixed sufficiently. After 2 days cement setting, the cement paste was covered by degassed ultrapure water for 28 days. After, the cement cores were extracted, grinded into powder with the agate mortar, and then stored in glove box, for following sorption experiments. All the preparation was performed under N₂ protection.

5.2.3. Synthesis of each separated CEM-V/A cement hydration product.

All syntheses were performed in a CO₂-free glove box. C-S-H suspension was obtained by mixing Ca(OH)₂ and amorphous SiO₂ (Aerosil 200) in water for 1 d, with a target Ca/Si ratio of 0.8[279]. After, the suspension was filtered, freeze-dried and left in closed containers in the glove box. Ettringite was prepared from a suspension of a 1:3 molar of C₃A and CaSO₄ mixture with an S/L ratio of 50 g L⁻¹ under N₂ atmosphere. After magnetic stirring for 14 days, the suspension was membrane-filtered and the filter cake was dried in the glove box[280]. AFm-SO₄ was synthesized using the same protocol described in Chapter 2. Mackinawite (FeS) and pyrite (FeS₂) could be the sources of S²⁻ leachate in CEM-V/A type cement, which are originally contained in the slags during cement manufacture. The mackinawite suspension ([Fe]_{tot} = 0.3 M) was prepared in the glove box by introducing equivalent stoichiometric Fe^{II} solution (Fe(NH₄)₂(SO₄)₂·4H₂O) into the S^{-II} solution (Na₂S). Black precipitate occurred instantly and aged for 1 day. After, the suspension was centrifuged in N₂ atmosphere and then freeze-dried[261]. Natural pyrite used is a commercial product from Alfa Aesar and always stored in the glove box. The portlandite and gypsum for reactions were purchased from Sigma Aldrich.

5.2.4. Kinetics experiments.

HCEM-V equilibrium kinetics with CPW and sorption kinetics of RNs (i.e., UO₂²⁺, SeO₃²⁻, MoO₄²⁻, and Sb(OH)₆⁻) on the equilibrated HCEM-V particles were investigated. The S/L ratio was fixed as 10 g L⁻¹, identically. Initial RNs concentrations of 5×10⁻⁵ M and 2×10⁻⁴ M were applied for U and other three RNs (i.e., Se, Mo, and Sb), respectively. At each defined interval time during the constant end-over-end shaking of reactors, a 2 mL aliquot of suspension was sampled by filtration through a 0.22 μm pore size membrane filters. The sampled filtrate was analyzed by ICP-OES to determine the aqueous total concentrations of U, Se, Mo, Sb, S, Ca and Fe. Aqueous sulfide species concentration from HCEM-V equilibrium and Se sorption kinetics experiments were analyzed by the methylene blue method [255].

5.2.5. Batch sorption experiments.

Batch sorption experiments of RNs (i.e., UO₂²⁺, SeO₃²⁻, MoO₄²⁻, and Sb(OH)₆⁻) on all the seven types of hydrated Fe-bearing cement products particles were conducted at 25 °C in N₂-filled glove box, in order to study the sorption capacity and affinity of varying cement particles towards RNs. After equilibrating the hydrated cement with CPW for 2 d, 5×10⁻⁵ M

of U or 2×10^{-4} M of each other RNs (i.e., Se, Mo, and Sb) was introduced into the reactors, separately. The S/L ratio of 10 g L^{-1} was kept identical to the kinetics experiments. All the reactors equilibrated for 30 d on an end-over-end shaker.

Batch sorption experiments of MoO_4^{2-} on HCEM-V and C-NZVI particles in CPW were also studied as a function of MoO_4^{2-} loadings, attempting for detecting active sorption sites existing in reinforced hydrated cement phases. Initial MoO_4^{2-} concentrations of 0.005, 0.01, 0.05, and 0.2 mM, were introduced into the cement suspension, with an S/L ratio of 10 g L^{-1} . A sorption equilibrium time of 45 d under constant end-over-end shaking was applied for all the reactors, after cement equilibrating with CPW firstly.

Sorption of MoO_4^{2-} on each separated component of reinforced hydrated cement, including CSH, portlandite, gypsum, ettringite, AFm- SO_4 , mackinawite, pyrite, and NZVI, was investigated. Initial Mo loading was 0.2 mM, identically. Besides, the S/L ratios of these components were set as 2, 10, 10, 5, 5, 1, 10, and 2 g L^{-1} , according to the particles' sizes and the estimation of active sites density. Firstly, these particles were dispersed in CPW for 2 days, in order to reach equilibrium. After, MoO_4^{2-} was introduced and reacted for 13 d under constant shaking.

After reaction, the aqueous and solid phases in all the batch sorption reactors were collected by the membrane ($0.22 \text{ }\mu\text{m}$ pore size) filtration. After dilution with degassed ultrapure water, the filtrate was measured by ICP-OES for the total concentrations of U, Se, Mo, Sb, S, Ca and Fe, and aqueous sulfide concentration from Se sorption reactors was determined by the methylene blue method. Sorption products, the filter cakes, in all the reactors were stored in glove box for following solid characterizations.

5.2.6. Preparation of RNs-containing Fe^0 -bearing cement cores.

RNs-containing (i.e., U, Se, Mo, and Sb) cement cores in the presence or absence of Fe^0 phases were prepared in 2 ml centrifuge tube under highly pure N_2 environment. The mass ratio of water to cement is 0.4 and the mass concentration of each RN reached 300 ppm. For cement cores without iron phases, CEM-V/A powder, degassed Milli-Q water, and certain portions of RNs stock solution were introduced into the tubes and then mixed sufficiently. Regarding the Fe-bearing cement cores, two types, i.e., NZVI-bearing (Type I) and steel coupon-bearing (Type II), were made. For Type I Fe-bearing cement cores, the mixing order of CEM-V/A powder, water, NZVI, and RNs are vital to the RNs sorption behavior. Therefore, three mixing orders were applied: i) NZVI-1: First to mix cement and RNs, then

introduce NZVI quickly, i.e., RNs contacting cement firstly; ii) NZVI-2: First to mix RNs and NZVI, then introduce cement quickly, i.e., RNs contacting NZVI firstly; ii) NZVI-3: First to mix cement and NZVI, then introduce RNs quickly, i.e., RNs contacting cement and NZVI at the same time. After mixing, sealing the 2 ml centrifuge tube tightly and curing for 3 months. For Type II, hydrated cement cores with 2 mm-thick Ø6 mm steel coupons were prepared. Firstly, the steel was cut into 2 mm-thick Ø6 mm steel coupons by diamond saw and then polished by different sizes of diamond pastes in order (the smallest size is 1 µm), to give a flat and more reactive Fe⁰ surface. After polishing, the steel coupons were washed by 0.1 M HCl quickly three times and then by acetone three times, temperately stored in glove box prior to using. After sufficiently mixing CEM-V/A powder, water, and RNs, a piece of steel coupons was immersed in the paste. After sealing the tube cap, the pastes were cured for 3 months till analysing.

5.2.7. Polishing of RNs-containing cement cores and Micro-probe analysis.

RNs-containing cement cores, and Type I and Type II Fe-bearing cement cores were studied by electron probe micro-analyser (EPMA). Firstly, the hardened cement cores were extracted from the 2-ml tubes. After, they were inserted in a Plexiglas container and embedded with epoxy resin under vacuum. Several minutes were required to let the epoxy resin to fill in cement pores, in order to consolidate the cement structure. Next, the bottom surface of the sample was polished in an N₂-filled glove bag, first by silicon carbide abrasive papers, and then by different sizes of diamond pastes, going through 15 µm, 9 µm, 6 µm, 3 µm, 1 µm, and 0.25 µm under ADS lubricant in sequence. The side face of the cement cylinder was the polished face. After cleaning with acetone, the sample surface was coated with 10 nm carbon film by Q150TE turbo-pumped carbon coater (Quorum technologies). The surface of the sample must be electrically conductive to avoid charging effect under electron beam. Therefore, samples are carbon coated in vacuum by passing electric current through high purity graphite rods (electrodes). Polished cement cores with coated surfaces were mounted on the sample holders of microprobe and shown in Figure S2. Finally, they were characterized by microprobe under vacuum, to look at corrosion products of NZVI/steel and RNs distribution among hydrated cement and corrosion products.

Electron-probe microanalysis was performed on the JEOL JXA-8230 electron microprobe at ISTerre, which is a powerful analytical tool that provides non-destructive, in-situ and complete quantitative chemical analysis of a flat solid surface. JEOL JX-8230 is equipped

with five wavelength dispersive spectrometers (WDS) providing quantitative analysis of elements from ${}^5\text{B}$ to ${}^{92}\text{U}$. The combination of WDS and energy dispersive spectrometers (EDS) can be used to obtain X-ray maps showing elemental distributions, which can deliver precision down to 300 ppm, for the various RNs under study. X-rays maps of U, Se, Sb, Mo and Fe were analyzed simultaneously by wave-length spectrometer (WDS) and major elements (Si, Ca...) using a silicon drift detector energy-dispersive spectrometer (SDD, EDS). Analytical conditions for mapping were 15keV accelerating voltage, 50nA beam current with a focused beam, a dwell time of 500ms and a step size of $1\mu\text{m}$.

5.2.8. Sulfur K-edge, Selenium K-edge, and Molybdenum K-edge XANES-EXAFS spectroscopy.

Sulfur K-edge (2474 eV) and Selenium K-edge (12658 eV) XAS experiments were conducted at the XAFS beamline of synchrotron Elettra, Basovizza, Trieste[220]. A Si(111) double-crystal monochromator was used with about 0.3 eV resolution at 2.5 keV. A silicon drift detector (KETEK GmbH AXAS-M with an area of 80 mm^2) was employed for collecting the fluorescence signal. For selenium, elemental Se foil was used for energy calibration in parallel. Due to the strong absorption of X-ray photon at low energy, sulfur energy calibration in parallel cannot be realizable. Instead, elemental sulfur standard was measured and then calibrated at the beginning and the end of S K-edge experiments. All the samples for XAS were sealed using polyimide tape (double-faced sealing for selenium samples, but one-side pasting for sulfur samples), mounted on a sample holder, and measured in fluorescence mode, except of the references for Se, which were prepared as pellets with cellulose matrix and measured in transmission mode. Before being transferred into the vacuum experimental chamber, samples were stored under N_2 atmosphere. For EXAFS signal collection, a liquid N_2 cryostat was used to lower the temperature to 77 K, in order to minimize the effects of thermal disorder due to atomic vibrations.

Molybdenum K-edge (20000 eV) XAS experiments were performed at the French absorption spectroscopy CRG-FAME beamline (BM30B) at the ESRF, Grenoble, France[281]. A Si(220) crystal monochromator was used with the beam size of $100\times 300\mu\text{m}^2$. Energy calibration was done in parallel using elemental Mo foil. A liquid helium cryostat was used to decrease the measurement temperature to 4 K, to minimize the effects of thermal disorder due to atomic vibrations and improve the measurements. All the samples were sealed double-faced using polyimide tape and stored under N_2 protection prior to measurements. The Mo

references were prepared as pellets with cellulose and measured in transmission mode, while Mo sorption products were measured in fluorescence mode. A highly sensitive fluorescence detection system was employed, which was achieved with a 30-element Canberra Ge solid state detector.

Data integration and reduction of XANES spectra (Athena), as well as the data fitting of the EXAFS spectra (Artemis)[196], were performed using the Demeter software package. A linear combination fit (LCF) was applied to the Se XANES spectra to identify and quantify the selenium species. The k^3 -weighted EXAFS functions of Se and Mo samples and the k^2 -weighted ones of S samples were Fourier transformed (FT) in a k range 3.0-13.0 \AA^{-1} using a Kaiser-Bessel window. Theoretical backscattering paths were calculated by FEFF8.4[197], to perform the fit in back-transformed reciprocal space (k).

5.2.9. PDF analysis.

Se(IV)-reacted Fe^0 and Fe-(hydr)oxides particles were investigated by PDF analysis of X-ray scattering. The high-energy X-ray scattering experiments were performed in beamline ID31 at the ESRF, using energy of 70.0 keV and a Perkin Elmer XRD 1621 flat detector. To avoid any oxidation, the reacted NZVI and Fe-(hydr)oxides powder samples were packed in $\text{\O}1$ mm polyimide capillaries, and sealed inside capillaries by epoxy glue in glove box. These loaded capillaries were stored in anaerobic conditions until they were put on the sample racks. NIST certified CeO_2 powder sample was used for instrumental calibration and empty capillary with the same specification for background subtraction. With collection time of 180 s, the obtained images were integrated to one-dimensional diagrams using Fit2D software[219]. PdfGetX3 code[195] was employed to transform the data into PDF patterns and calculated PDF patterns were obtained by PDFGui software[256].

5.3. Results and discussion

5.3.1. XRD characterization and dissolution kinetics of Fe-bearing hydrated cement.

The high purity of synthesized Fe products, including NZVI, magnetite, hematite, and goethite, was certified by the XRD patterns (Figure 5.1). By comparison with PDF cards, the visible peaks in XRD patterns of HCEM-V were attributed to contributions of portlandite, ettringite, gypsum, and AFm- SO_4 . In cement hydration products, nanocrystalline CSH phase is the main component[35] and can only result in weak diffraction signal. Regarding the

hydrated Fe-bearing CEM-V/A cement, in addition to the diffraction peaks of hydrated cement itself, the presence of corresponding iron phases can also result in obvious signals.

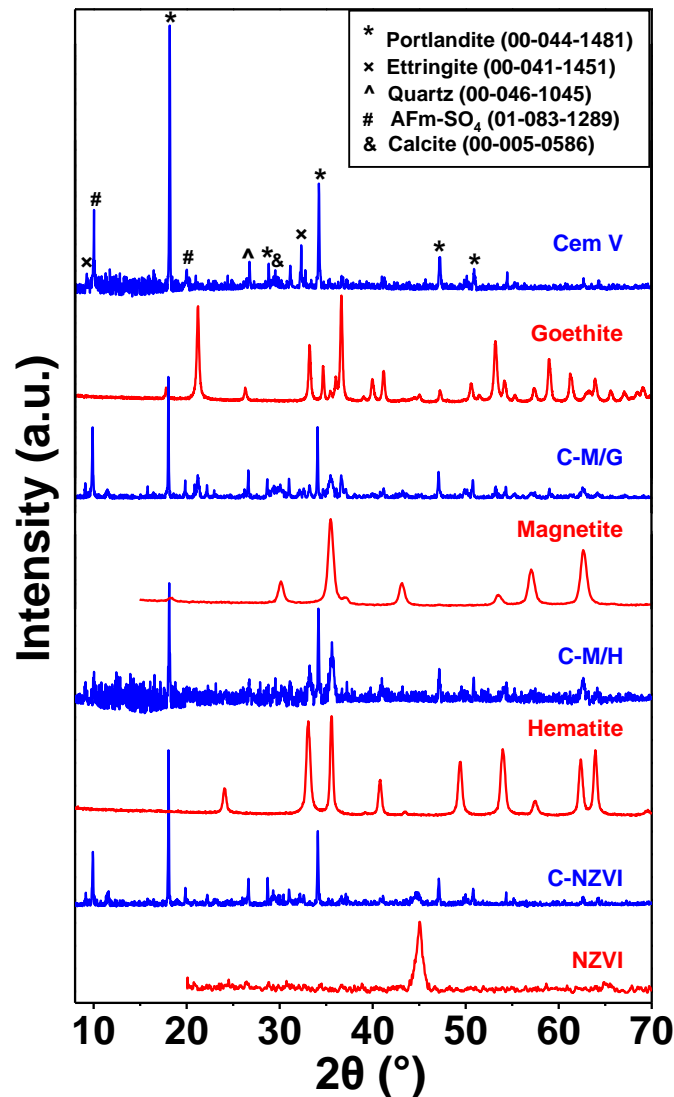


Figure 5.1. Laboratory-based X-ray diffraction patterns of synthetic Fe products, hydrated CEM-V/A cement, and Fe-bearing hydrated cement. Cu K α radiation at 1.5406 Å is used.

Dissolution kinetics of HCEM-V in CPW was studied, to know the equilibrium time (Figure 5.2). After grinded at a cement setting time of ~30 d, the HCEM-V powder was disposed in the glove box for 200 d till being used in dissolution kinetics experiments. Aqueous Ca and S, as the main contents of CPW together with Na and K, could play key role retarding RNs via co-precipitation, anion exchange, or reductive precipitation. Total concentrations of Ca and S were determined using ICP-OES, indicating that dissolution equilibrium could be reached just after 48 h. After contacting with hydrated cement, ~0.4 mM more S was leached into the aqueous phase, but ~30% of Ca²⁺ was adsorbed by HCEM-V, based on the concentrations in the synthetic CPW. In CPW, large amounts of Na⁺ and K⁺ exist, with their concentrations

reaching 0.076 and 0.211 M, respectively. The large ionic strength could be responsible for the large STD errors of $[\text{Ca}]_{\text{tot}}$ from the ICP-OES results. Besides, CEM-V/A cement consists of 25% blast furnace slag, which may contain 2-4 % sulfide of Cu, Cd and Fe^0 . Thus, the equilibrated suspension may also contain reduced S species. Employing the methylene blue method [282], total S(-II) species (e.g., S^{2-} , S_n^{2-} , and H_2S), here called as methylene-blue-detectable sulfur (MBS), was identified. As can be seen in Figure 5.2, considerable sulfide leached from HCEM-V, which could originate from the slags. Dissolving MBS concentration reached the maximum value of 0.15 mM at 144 h. After, [MBS] decreased till 0.13 mM when reaction time was 160 h. Aqueous sulfide could be generated from slag dissolution, while it might be also consumed by the oxidants existing in HCEM-V, like Fe(III)-oxides. This could be one factor leading to the decrease of sulfide when [MBS] becomes high. Sulfide is strong reductant, even in extremely alkaline conditions (pH \sim 13.5 in CPW), thus be able to promote reductive precipitations of RNs on CEM-V/A.

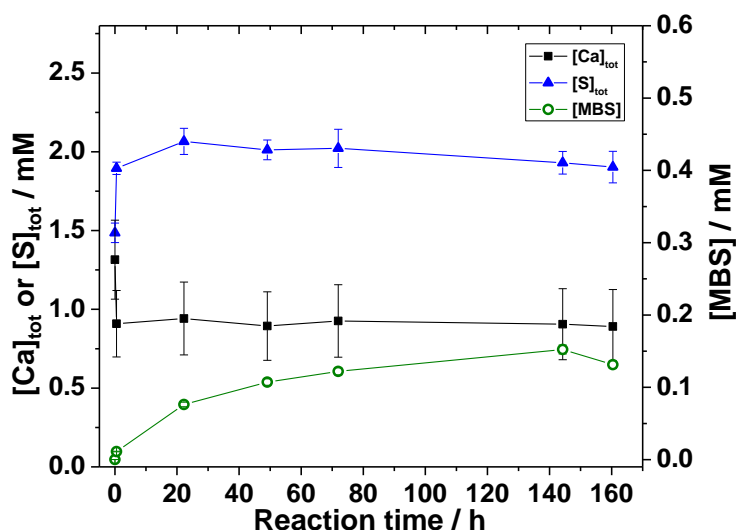


Figure 5.2. Kinetics of HCEM-V equilibrium with CPW. MBS represents methylene-blue-detectable sulfur.

5.3.2. U(VI) sorption on hydrated CEM-V/A cement particles.

As shown in Figure 5.3, kinetics of U(VI) sorption on HCEM-V were studied after the pre-equilibrium of HCEM-V. During the sorption process, almost no obvious concentrations change for aqueous Ca and S can be observed. For aqueous U, its concentration dropped sharply within 48 h and then gradually decreased and reach the bottom platform till reacting for 248 h. In our experiments, initial U(VI) concentration was 34.6 μM . Thermodynamic modeling predicts that U(VI) will form alkali and alkaline-earth uranates solid phases in hyperalkaline CPW, resulting a very low U(VI) solubility of 0.07 μM [259]. Once U(VI) is

introduced into CPW, clarkeite-type $((\text{Na,K,Ca})\text{UO}_2\text{O}(\text{OH})\cdot(\text{H}_2\text{O})_{0-1})$ colloidal nanoparticles can be formed instantly, which was predicted to be stable for years. In our case, most added aqueous U(VI) could also be incorporated into the nano-sized colloids. However, these colloids could not maintain their stability when co-existing with hydrated cement particles, leading to the significant removal efficiency from aqueous phase.

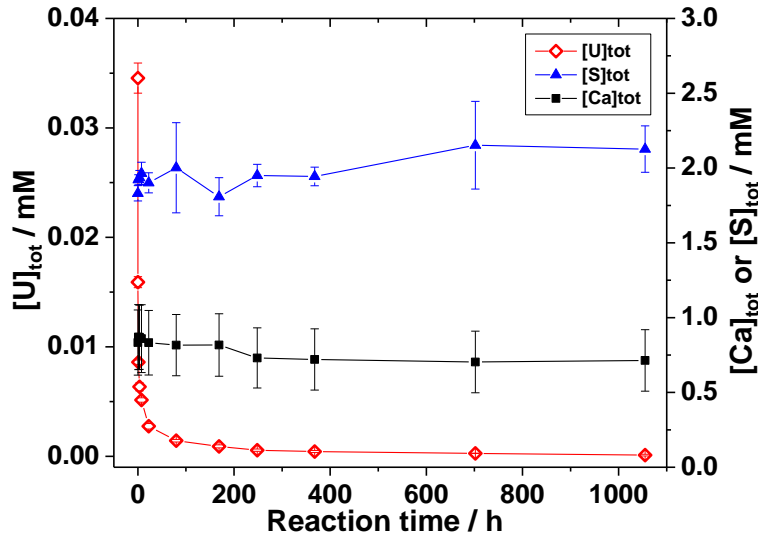


Figure 5.3. Kinetics of U(VI) sorption on HCEM-V. U(VI) was introduced after HCEM-V equilibrium with CPW for 160 h.

U(VI) sorption experiments on varying types of hydrated Fe-bearing cement were performed. After sorption equilibrium, the R_d value in each reactor was calculated. As shown in Table 5.1, HCEM-V and C-NZVI cement result in the largest R_d values, revealing that the pristine and NZVI-modified hydrated cement have the strongest affinity towards U(VI). Pristine hydrated cement could be the best supplier of Ca-bearing phases and NZVI in C-NZVI is the most reactive Fe phase among all the Fe products. Both co-precipitation with Ca^{2+} and reductive precipitation by NZVI can contribute a lot to the removal of aqueous U(VI). Similar to the observation in kinetics experiments of HCEM-V equilibrium, decrease of $[\text{Ca}]_{\text{tot}}$ and increase of $[\text{S}]_{\text{tot}}$ were discovered after CPW contacting with hydrated cement. As indicated from the above discussion, the formation of clarkeite-type colloidal nanoparticles could be the first step of U(VI) removal.

Table 5.1. Concentrations of selected aqueous ions and the retardation factors (R_d) in U(VI) reactors with an equilibrium time of 30 days, approximately. Prior to introducing U(VI), each type of hydrated cement equilibrated with CPW for ~ 48 h. Standard errors are given by the number in brackets on the last digit(s).

Cement type	Matrix	[Ca] _{tot} /mM	[S] _{tot} /mM	[U] _{tot} /mM	R_d / L g ⁻¹
-		1.150(231)	1.520(24)	0.0346(7)	-
HCEM-V		0.696(193)	2.220(46)	0.0002(1)	20.07(6.57)
C-Mag		0.756(208)	1.970(20)	0.0007(1)	4.63(12)
C-Hem		0.698(202)	2.160(49)	0.0005(1)	7.41(98)
C-Goe	CPW	0.547(185)	1.990(46)	0.0003(1)	10.49(3.34)
C-NZVI		0.595(180)	1.880(18)	0.0002(1)	21.32(12.16)
C-M/H		0.721(195)	2.270(42)	0.0013(1)	2.65(7)
C-M/G		0.720(200)	2.060(11)	0.0007(1)	4.54(40)

5.3.3. Se(IV) sorption on hydrated CEM-V/A cement particles.

Sorption of SeO_3^{2-} on hydrated CEM-V/A cement particles were investigated by kinetics and batch sorption experiments. After grinded at the cement setting time of ~30 d, the HCEM-V powder was disposed in the glove box for 200 d till being used in Se kinetics experiments. As shown in Figure 5.4, concentration profiles of kinetics experiments indicates that total Ca and S concentrations almost kept constant as reaction time. Besides, total Se concentration dropped rapidly from ~0.18 mM to ~0.14 mM within 24 h and then continued to decrease slowly till 700 h. For [MBS], a sharp decrease from ~0.13 mM to ~0.04 mM was observed once introducing Se. However, the decrease amount of MBS was not compatible to the decrease of total Se, i.e., to the 2:1 ratio of S to Se deriving from the possible redox reaction (i.e., S^{II} to S^0 and Se^{IV} to Se^0). Thus, the initially dramatically decrease of MBS should not originate from its oxidative precipitation. Among hydrated cement phases, AFm phase and ettringite are widely considered as potential phases to remove anionic contaminants via anion exchange and they possess large anion removal capacity. Once introducing SeO_3^{2-} , it would insert into the inter-layer of AFm phase and enlarge the layer-to-layer space, which may promote the co-sorption of S^{2-} anion, immediately. Then, [MBS] increased gradually and

reached the top at ~400 h, attributed to the dissolution of the metal (e.g., Cu, Cd, and Fe) sulfides existing in CEM-V/A cement powder. After reacting 400 h, a slightly [MBS] decrease was observed, probably due to redox reactions with Se(IV) or other oxidants, like Fe(III)-(hydr)oxides. Sulfide could be considered as a strong reductant in the hyperalkaline CPW towards Se(IV), with reaction products S^0 and Se^0 . The sorbed selenium speciation needs to be further identified.

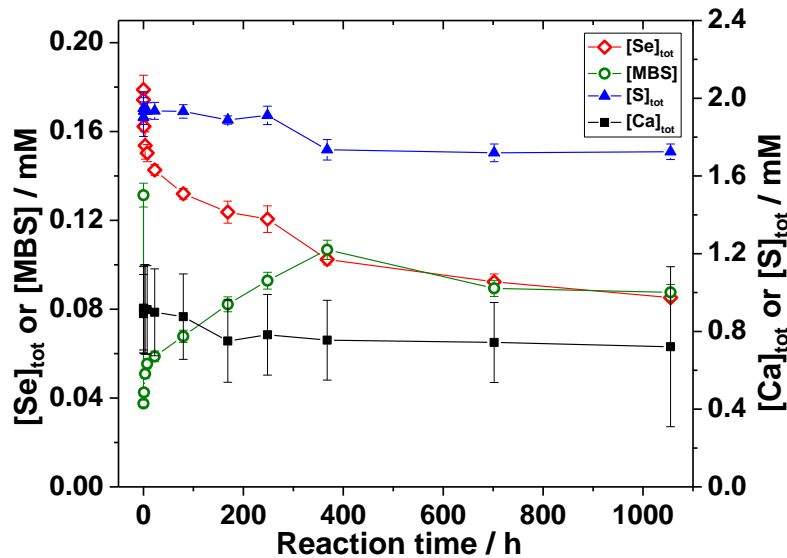


Figure 5.4. Kinetics of Se(IV) sorption on HCEM-V. Se(IV) was introduced after HCEM-V equilibrium with CPW for 160 h.

Batch sorption experiments of Se(IV) on varying types of hydrated Fe-bearing cement were conducted. After grinded at the cement setting time of ~30 d, all the types of cement powder were disposed in the glove box for 140 d till being used in Se kinetics experiments. As shown in Table 5.2, after reaction, $[Ca]_{tot}$ and $[S]_{tot}$ in all the reactors stayed around 0.8 mM and 1.5 mM, respectively. Besides, all the types of hydrated cement showed good affinity to selenite, resulting in a range of R_d values from 0.038 $L g^{-1}$ to 4.034 $L g^{-1}$. The hydrated cement containing NZVI, C-NZVI, showed the strongest affinity and the largest sorption capacity towards selenite, giving the largest R_d value of 4.034 $L g^{-1}$. It can be explained by the presence of NZVI, a strong absorbent via reductive precipitation. Besides, [MBS] in the C-NZVI reactor resulted in the highest value, 0.0472 mM, among all the reactors, suggesting that the strong reducibility of NZVI could protect sulfide from being oxidized into solid S^0 . However, sulfate cannot be reduced into sulfide by NZVI in the cement system (See Chapter 4), thus the process could not be one reason for the [MBS] increase. For other reactors with extra introduction of Fe(III)-(hydr)oxides, [MBS] could only reach ~0.03 mM in general, with

the concentration a little lower than that of HCEM-V. It indicated that Fe(III)-(hydr)oxides could be partially responsible for oxidizing sulfide species thus decreasing [MBS]. S(-II) is potential to reduce SeO_3^{2-} into Se^0 and thus to promote the sorption of SeO_3^{2-} . As a result, the R_d value on HCEM-V, 0.0676 L g^{-1} , was larger than other cases with extra Fe(III)-(hydr)oxides. It can be concluded that introducing Fe(III)-(hydr)oxides or magnetite in hydrated cement system would not enhance the decontamination performance of hydrated cement towards selenite, or even weaken a little its sorption ability. Thus, under hyperalkaline conditions, Fe(III)-(hydr)oxides and magnetite phases may have even weaker affinity to selenite than the hydration phases (e.g., AFm phase, ettringite, and sulfide species) of cement.

Table 5.2. Concentrations of selected aqueous ions and the retardation factors in Se(IV) reactors with an equilibrium time of 30 days, approximately. Prior to introducing Se(IV), each type of hydrated cement equilibrated with CPW for ~ 48 h. Standard errors are given by the number in brackets on the last digit(s).

Cement type	Matrix	[Ca] _{tot} /mM	[S] _{tot} /mM	[Se] _{tot} /mM	[MBS] /mM	R_d / L g^{-1}
-		1.230(263)	1.510(14)	0.1789(32)	0.0002(1)	-
HCEM-V		0.787(208)	1.470(11)	0.1067(11)	0.0355(8)	0.0676(33)
C-Mag	CPW	0.789(201)	1.530(43)	0.1259(18)	0.0291(6)	0.0420(30)
C-Hem		0.747(206)	1.540(16)	0.1192(27)	0.0322(9)	0.0501(37)
C-Goe		0.804(222)	1.450(22)	0.1174(18)	0.0271(6)	0.0524(32)
C-NZVI		0.658(198)	1.620(35)	0.0043(1)	0.0472(9)	4.0346(912)
C-M/H		0.768(213)	1.560(29)	0.1247(19)	0.0335(7)	0.0435(31)
C-M/G		0.781(211)	1.700(9)	0.1296(29)	0.0333(9)	0.0380(35)

Regarding the [MBS] in batch sorption experiments, the value of ~0.0355 mM on HCEM-V was quite less than the value of ~0.0893 mM in the kinetics experiment (Figure 5.4) at the same reaction time of ~700 h. The main difference between the HCEM-V used in kinetics and batch sorption experiments was the cement setting durations of ~200 d and ~140 d, respectively. The chemical properties of hydrated cement should not reach equilibrium after 28 d or even longer time. In our case, the aqueous results with ~200 d and ~140 d cement setting time showed the same total Ca and S leaching concentrations, but a higher [MBS] with longer curing time. It is satisfying that concrete structures could release more sulfide and thus

facilitate the reductive precipitation process of RNs under the large time-scale in nuclear waste repositories.

In order to figure out the source of MBS leachate, solid sulfur species in hydrated CEM-V/A cement (HCEM-V) and NZVI-bearing cement (C-NZVI) were characterized by S K-edge XANES-EXAFS spectra (Figure 5.5).

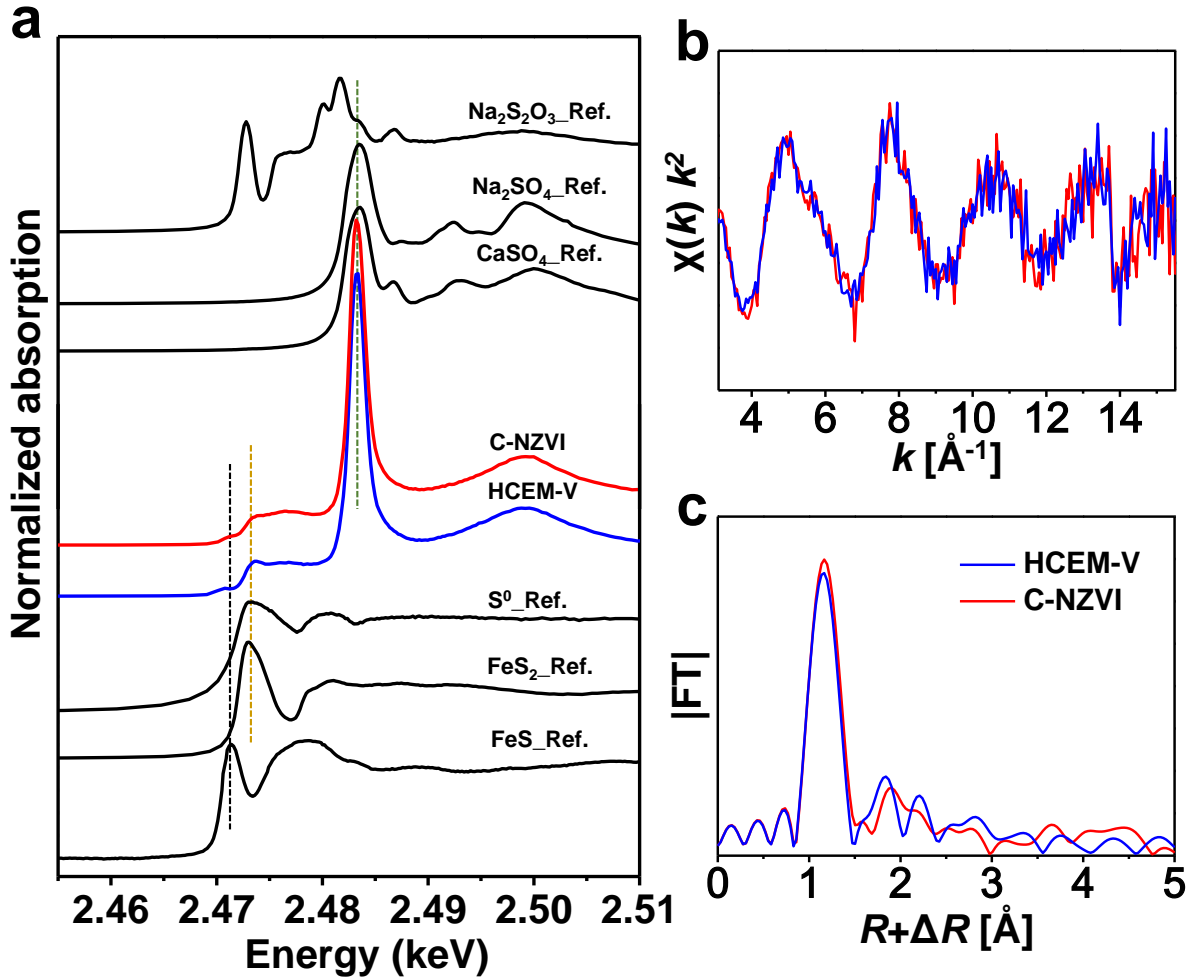


Figure 5.5. S K-edge XAS spectra. (a) Normalized XANES spectra of HCEM-V, C-NZVI, and related S references. (b) k^2 -weighted EXAFS oscillations of HCEM-V and C-NZVI. (c) Fourier transformed (not corrected for phase shift) EXAFS signals.

As shown in Figure 5.5a, the normalized XANES spectra of HCEM-V and C-NZVI were quite similar, possessing a main absorption peak at the energy position of sulfate white-line peak. In CEM-V/A cement, most sulfur species have +6 oxidation state, such as S(VI) in gypsum, AFm phase, and ettringite. Besides, in the spectra of cement samples, at least two small absorption peaks can be observed at lower energies, close to the energy of feature peaks of FeS, FeS₂, and S⁰. Absorption peak at ~2.471 keV of cement samples can be the strong evidence for the existence of sulfide minerals. However, due to the small amount thus weak

signal and different crystallization, it is hard to assure sulfide in CEM-V/A cement is the form of Fe-sulfide, or other metal (e.g., Cu and Cd) sulfides. In addition, the very close white-line peak positions of FeS₂ and S⁰ raised the difficulty to confirm the S species attributions at the absorption peak of ~2.473 keV. Both S(-I) and S(0) species have chance to exist in the hydrated CEM-V/A cement.

The k^2 -weighted EXAFS oscillations and Fourier transformed EXAFS signals of HCEM-V and C-NZVI were shown in Figure 5.5b and Figure 5.5c. The introduction of NZVI did not bring obvious difference to the hydrated CEM-V/A cement. The signal oscillation frequency in k space and the signal neighbor shell at $R+\Delta R \sim 1.17 \text{ \AA}$ were attributed to the four S-O backscattering pairs ($d \sim 1.48 \text{ \AA}$) from SO₄²⁻. However, signal contributions of other minor S species were not visible enough in the EXAFS spectra.

Sorption products on varying types of hydrated cement were analyzed by the LCF of Se K-edge XANES spectra (Figure 5.6a), to identify and quantify the sorbed Se species. From the LCF results listed in Table 5.3, reduction of Se(IV) only occurred, to a large extent, on C-NZVI, resulting in 68.1% FeSe and 6.9% Se⁰. Besides, 20.5% CaSeO₃ contribution was quantified by LCF, probably attributed to the co-precipitation of CaSeO₃ or inner-sphere complexes between Ca and SeO₃²⁻. As can be seen in Figure 5.6a, the spectrum of C-NZVI cannot be reproduced perfect by the three references, indicating that Se(IV) could be adsorbed by hydrated cement products or reduced by secondary phases generated from NZVI. For Se-sorbed on HCEM-V, Se species were mainly composed of CaSeO₃ and Na₂SeO₃, suggesting that sorbed SeO₃²⁻ may form inner-sphere complexes (like CaSeO₃) and outer-sphere complexes (i.e., more unconstrained SeO₃²⁻ as Na₂SeO₃). For instance, sorbed SeO₃²⁻ on AFm phase may form outer-sphere complexes, having similar XANES features to Na₂SeO₃. Besides, introduction of tiny amount (~0.7 %) of Se⁰ can decrease the reduced χ square value. After, the HCEM-V spectrum was used as a reference to perform the following LCF analysis of other cement samples. For the hydrated cement containing Fe-(hydr)oxides, in addition of the largest contribution of HCEM-V reference, small percentages of FeSeO₃ can be added to improve the fitting satisfaction, indicating that selenite may complex with the added Fe-(hydr)oxides. Besides, 3.0% Se⁰ was detected in C-M/G.

In the hydrated cement samples, the tiny amount of Se⁰ detected by LCF analysis was inconclusive, but their XANES spectra changes at the energy position of Se⁰ white-line peak were more apparent and convinced.

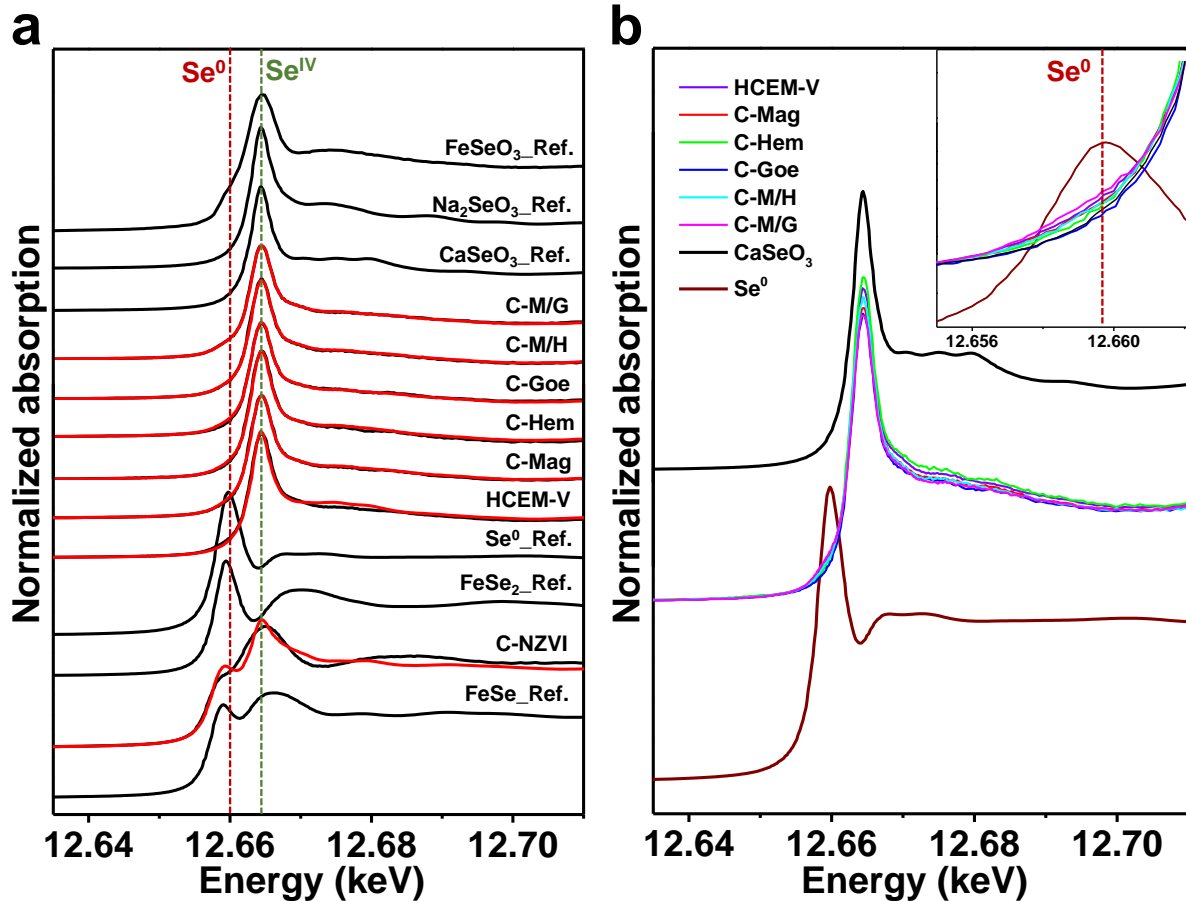


Figure 5.6. Se K-edge normalized XANES spectra. (a) Spectra of Se(IV) sorbed on hydrated cement with LCF results and the related Se references. (b) Normalized XANES spectra comparison of Se(IV)-sorption products and references of Se⁰ and CaSeO₃, showing reduction of Se(IV) to Se(0). Inset is the extended XANES spectra of cement samples at the energy position of Se⁰ white-line peak.

As shown in the inset of Figure 5.6b, signal raises of the samples spectra can be observed at the white-line peak position of Se⁰, indicating the formation of Se⁰. Note that the hydrated CEM-V/A cement (i.e., HCEM-V) without any Fe products introductions, showed an even larger signal raise than the samples with addition of magnetite, e.g., C-Mag and C-M/H. In hydrated CEM-V/A cement, the reductants responsible for the Se(IV) reduction should be sulfide phases, mentioned and confirmed in the aqueous results. Although the reactivity of sulfide phases towards selenite under extremely alkaline conditions is not significant, they can be considered as retention tanks potentially providing the reductive precipitation path of Se removal. Besides, spectra of C-Goe and C-Hem were the two ones with the least signal raises, suggesting that introductions of Fe(III)-(hydr)oxides could inhibit selenite reduction via decreasing or possibly oxidizing the sulfide released.

Table 5.3. LCF results of Se K-edge XANES of Se(IV)-reacted hydrated cement samples. Also reported is the concentration sum (Σ), which is not constrained to 100% for samples, and the value of the reduced χ square (χ_v^2), both indicating good matches to the experimental spectra. Uncertainties are given by the number in brackets on the last digit(s), i.e., 0.7(1.7) represents 0.7 ± 1.7 .

ID	FeSe (%)	FeSe ₂ (%)	Se ⁰ (%)	CaSeO ₃ (%)	Na ₂ SeO ₃ (%)	FeSeO ₃ (%)	HCEM-V (%)	Σ (%)	χ_v^2 $\times 10^{-3}$
HCEM-V	-	-	0.7(1.7)	56.6(7.0)	49.3(8.4)	-	-	106.6	3.0
C-Mag	-	-	-	5.8(3.2)	0.9(3.6)	13.2(2.5)	78.6(3.0)	98.5	0.4
C-Hem	-	-	-	22.0(4.8)	15.7(5.4)	3.5(3.7)	65.1(4.3)	106.3	1.0
C-Goe	-	-	-	2.0(3.0)	0.5(3.4)	3.2(2.4)	87.8(2.8)	93.5	0.4
C-NZVI	68.1(4.5)	-	6.9(3.1)	20.5(1.5)	-	-	-	95.4	3.6
C-M/H	-	-	-	3.1(3.5)	1.3(3.9)	3.8(2.7)	89.2(3.2)	97.4	0.5
C-M/G	-	-	3.0(0.4)	1.5(1.8)	-	3.2(1.4)	87.5(1.6)	95.1	0.1

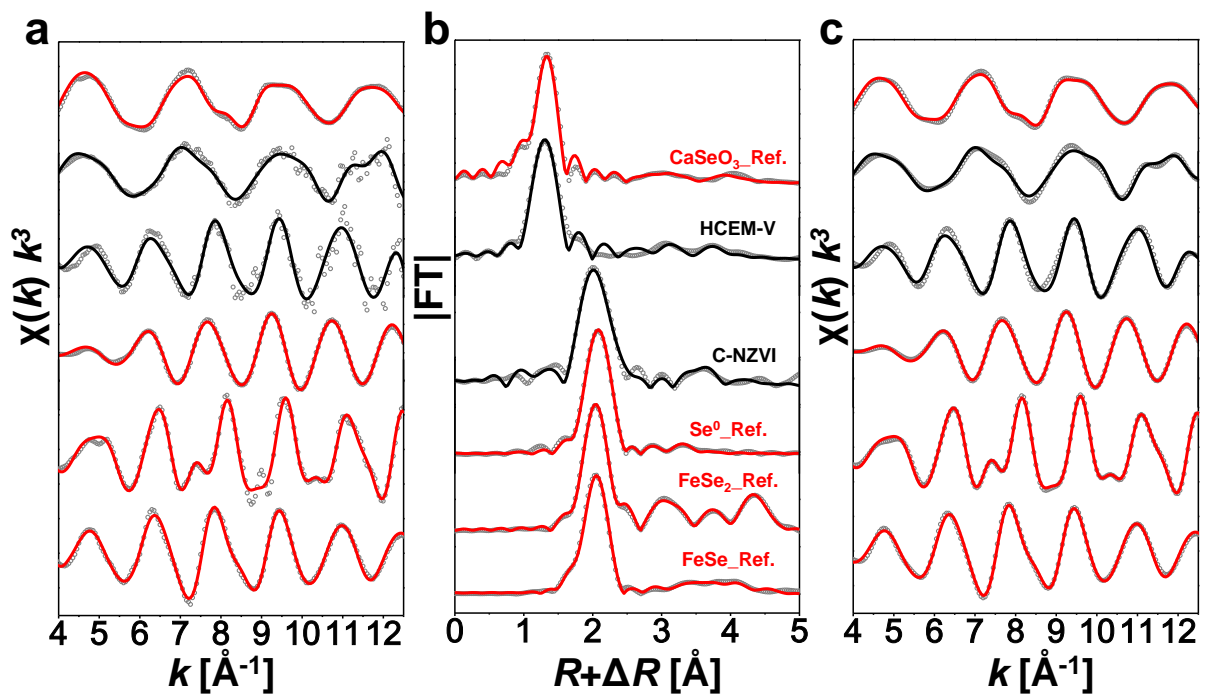


Figure 5.7. Experimental Se K-edge EXAFS spectra of HCEM-V and C-NZVI samples and reference compounds. (a) k^3 -weighted EXAFS oscillations. (b) Fourier transformed (not corrected for phase shift) EXAFS signals. (c) Back-Fourier transformed EXAFS signal. The grey circles are the experimental data and the solid lines are fit results.

Table 5.4. Local structure obtained from EXAFS refinement at Se K-edge^a.

Sample	Atomic pair	CN	R (Å)	σ^2 (Å ² ·10 ³)	ΔE^0 (eV)	R factor %
CaSeO ₃ _Ref.	Se-O	2.9(1)	1.70(1)	1.8(3)	9.7(1.1)	4.1
	Se-Ca	1.0(5)	3.24(4)	7.8(4.6)		
	Se-Ca	1.0(5)	3.57(4)	6.7(4.8)		
FeSe_Ref.	Se-Fe	4.0(1)	2.40(1)	4.6(4)	8.6(7)	3.5
	Se-Se	7.8(2.5)	3.72(2)	9.2(5.6)		
	Se-Se	4.8(1.1)	3.94(2)	9.8(1.5)		
FeSe ₂ _Ref.	Se-Fe	3.0(1)	2.37(2)	4.4(2)	8.1(3)	1.1
	Se-Se	1.0(1)	2.56(1)	4.4(6)		
	Se-Se	4.6(8)	3.23(4)	14.1(4.4)		
	Se-Se	2.1(5)	3.35(1)	9.1(1.2)		
Se ⁰ _Ref.	Se-Se	2.0(1)	2.37(1)	4.0(1)	6.1(8)	0.66
	Se-Se	4.3(9)	3.39(3)	14.4(2.3)		
	Se-Se	2.1(5)	3.70(3)	13.9(2.1)		
HCEM-V	Se-O	3.1(2)	1.69(2)	1.9(8)	5.4(3.4)	7.6
	Se-Ca	0.9(6)	3.29(6)	1.3(6)		
	Se-Ca	0.9(7)	3.53(6)	1.1(9)		
C-NZVI	Se-Se	1.0(3)	2.37(2)	3.3(2.5)	4.4(1.2)	8.5
	Se-Fe	1.4(3)	2.39(2)	5.1(3.1)		
	Se-Se	3.9(1.4)	3.74(1)	12.3(5.2)		
	Se-Se	2.7(1.3)	3.92(3)	5.6(2.6)		

^a CN: coordination numbers; R : atomic distances; σ^2 : Debye-Waller factors; ΔE^0 : shift of the threshold energy; R factor: goodness of fit. S_0^2 , 0.8950, was obtained from the experimental EXAFS fit of CaSeO₃ reference by fixing CN of first-shell Se-O at 3 and was applied for all the samples. Uncertainties are given by the number in brackets on the last digit(s), i.e., 7.8(4.6) represents 7.8 ± 4.6 , and 2.9(1) means 2.9 ± 0.1 .

EXAFS signal of sample HCEM-V and C-NZVI was also collected, together with the related references, in order to check the coordination environments of sorbed selenium. The k^3 -weighted EXAFS oscillations were shown in Figure 5.7a. As can be seen, sorbed Se in the two samples resulted in totally different oscillation frequencies. After FT, radial distribution functions (Figure 5.7b) were obtained and both samples had multiple neighbor shells. The first neighbor shell of HCEM-V are fitted with three Se-O backscattering pairs at $R = 1.69$ Å and the further shells can be reproduced by each one Se-Ca at $R = 3.29$ Å and 3.53 Å (Table 5.4), respectively. The Se complexation environment was similar to that of CaSeO₃ reference, suggesting that most sorbed SeO₃²⁻ on HCEM-V may co-precipitate with Ca or structurally

coordinate with Ca-sites of hydrated cement products. In contrast, most Se on C-NZVI were reducing species, with its first shell fitted by CN \sim 1.0 Se-Se pair at $R = 2.37 \text{ \AA}$ and CN \sim 1.4 Se-Fe pair at $R = 2.39 \text{ \AA}$. Besides, fitting of its further neighbor shells can be improved by adding the Se-Se backscattering pairs generated from FeSe structure. Thus, the Se coordination environment in C-NZVI can be described by that of Se^0 and FeSe. EXAFS results also confirmed the Se species distributions concluded from the LCF of XANES. It can be predicted that Se removal would go through co-precipitation/incorporation with calcium sites or reductive precipitation process, respectively, when in the bare hydrated cement phases or close to the embedded steel.

The above study on HCEM-V showed that aqueous selenite can be immobilized by the Ca sites and sulfide components in hydrated CEM-V/A cement. Regarding Fe-reinforced hydrated cement, the Fe-reinforcement could be another potential selenite scavenger. Here, selenite sorption by NZVI, M/H, and M/G in CPW was studied. Aqueous results were shown in Table 5.5. Aqueous selenite was removed to a great extent by NZVI, resulting in a large R_d value of 3.77 L g^{-1} . In contrast, the retention ability of M/H and M/G was much weaker than that of NZVI. According to the LCF analysis of Se K-edge XANES, selenite was reduced into Se^0 by magnetite and into more reducing species of FeSe and FeSe₂ by NZVI (See Chapter 4). The Fe phases before and after reaction with selenite were analyzed by the PDF of synchrotron-based high-energy X-ray scattering. As shown in Figure 5.8a, synthesized NZVI was characterized firstly and the broad reflection peaks compared to ones of calculated crystal Fe^0 indicated it was nano-sized and amorphous. PDF patterns of CPW-equilibrated NZVI and Se(IV) reacted NZVI were compared, showing that NZVI transformed into $\text{Fe}(\text{OH})_2$ completely due to the oxidation of Se(IV) and H_2O . For M/H, the experimental PDF of magnetite and hematite were shown in Figure 5.8b, with scattering pairs and their bonds lengths marked. By the comparison of reacted and unreacted M/H, the reflection signal at $\sim 3.50 \text{ \AA}$ decreased obviously after Se(IV) reaction, which could be attributed to the decreasing contribution of Fe-Fe scattering pair from magnetite. The crystal structure of magnetite was illustrated in Figure 5.9, in which the bond length of $\sim 3.50 \text{ \AA}$ is the distance between neighbored tetrahedron and octahedron. In the inverse spinel structure of magnetite, all tetrahedral sites are occupied by Fe(III) and octahedral sites are occupied by both Fe(III) and Fe(II). Selenite reduction on magnetite can lead to the collapse of tetrahedron-octahedron bridging, although tetrahedral sites have only Fe(III) instead of Fe(II). Similar phenomenon was observed in the case of M/G, shown in Figure 5.8c. After reaction, the signal intensity at

~3.50 Å decreased obviously, resulted from the oxidation of magnetite by selenite. It can be concluded that Fe-reinforcement in hydrated cement is also a considerable retardation factor towards selenite immobilization.

Table 5.5. Aqueous results of Se^{IV} sorption on Fe phases in N₂ atmosphere. Reaction time was approximately 100 days, which was totally enough to reach sorption equilibrium. Total Fe concentration is below the ICP-OES detection limit (~ 10 ppb).

RN	Fe phases	pH	[Ca] _{tot} /mM	[S] _{tot} /mM	[Se] _{tot} /mM	R _d / L g ⁻¹
	-	13.521	1.229(26)	1.526(9)	0.1644(9)	-
Se ^{IV}	NZVI	13.454	0.061(8)	1.415(8)	0.0099(3)	3.77(29)
	M/H	13.442	0.035(5)	1.308(9)	0.1239(6)	0.07(1)
	M/G	13.472	0.566(13)	1.386(14)	0.1186(8)	0.05(1)

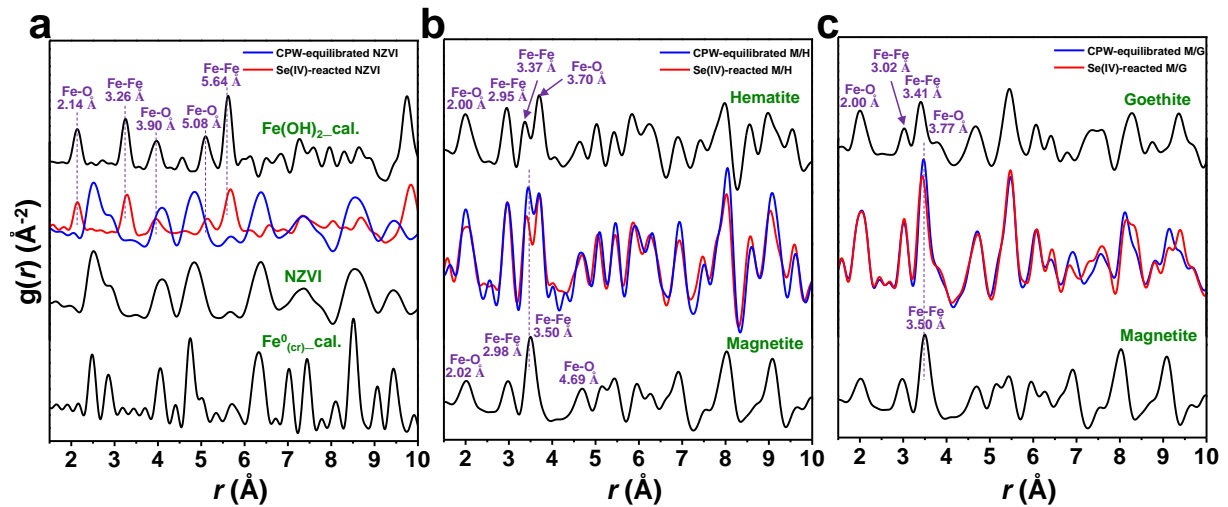


Figure 5.8. Experimental PDF patterns of Se(IV)-sorption products on Fe products (i.e., NZVI, M/H, and M/G) and calculated PDF patterns of the related Fe products. (a) Experimental PDF of pristine NZVI and Se(IV)-reacted NZVI; Calculated PDF references of Fe⁰(cr) and Fe(OH)₂. (b) Experimental PDF of magnetite, hematite, M/H couple, and Se(IV)-reacted M/H. (c) Experimental PDF of magnetite, goethite, M/G couple, and Se(IV)-reacted M/G.

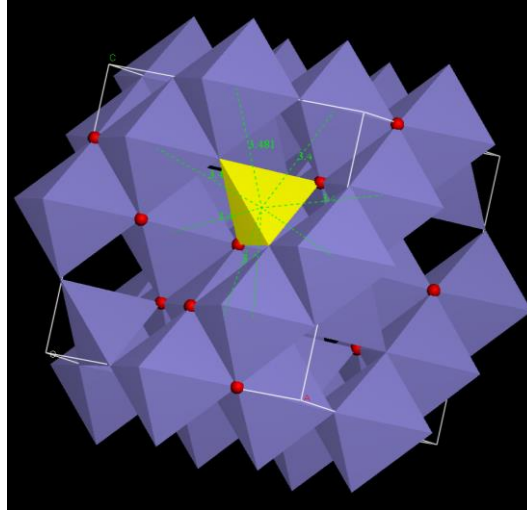


Figure 5.9. Crystal structure of magnetite. All tetrahedral sites are occupied by Fe^{3+} and octahedral sites are occupied by both Fe^{3+} and Fe^{2+} . Distances between neighbored tetrahedron and octahedron are 3.481 Å.

5.3.4. Mo(VI) sorption on hydrated CEM-V/A cement particles.

As shown in Figure 5.10, kinetics of MoO_4^{2-} sorption on HCEM-V were studied after a pre-equilibrium of HCEM-V. During the sorption process, almost no obvious concentrations change for aqueous Ca and S can be observed. Besides, MoO_4^{2-} showed no substantial decrease within 1000 hours, except of a little decrease at the very beginning of sorption. MoO_4^{2-} is quite soluble and hard to be adsorbed under extremely alkaline conditions. The fast but little decrease of aqueous Mo(VI) could be resulted from the sorption by minor active cement hydration products, such as the AFm phase.

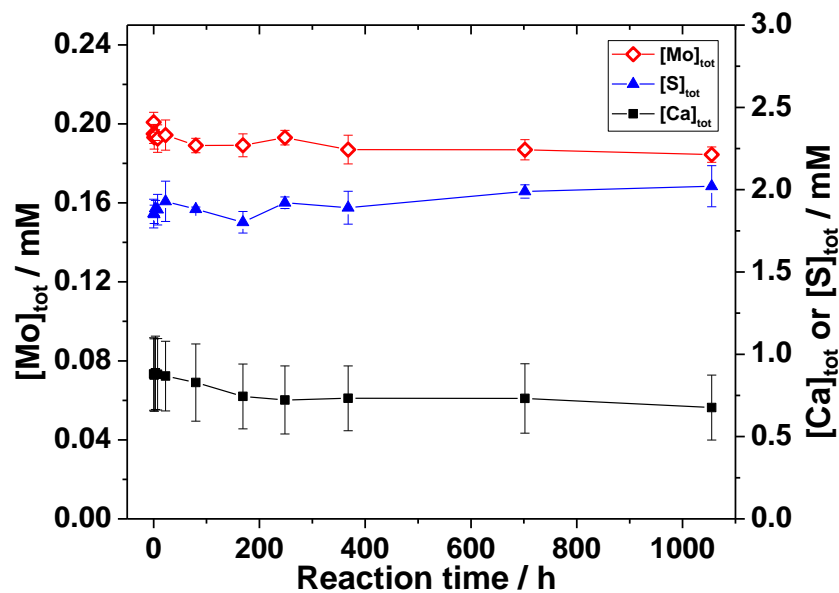


Figure 5.10. Kinetics of Mo(VI) sorption on HCEM-V. Mo(VI) was introduced after HCEM-V equilibrium with CPW for 160 h.

Table 5.6. Concentrations of selected aqueous ions and the retardation factors in Mo(VI) reactors. Sorption on hydrated cement and each separated hydrated cement phase was equilibrated for ~30 days and ~13 days. The solution matrix used was CPW. Prior to introducing Mo(VI), each solid absorbent was equilibrated with CPW for ~ 48 h. Standard errors are given by the number in brackets on the last digit(s).

Reactor	Absorbent	[Ca] _{tot-eq.} /mM	[S] _{tot-eq.} /mM	[Mo] _{tot-ini.} /mM	[Mo] _{tot-eq.} /mM	R _d / L g ⁻¹
MoC1	HCEM-V	0.741(211)	1.958(17)	0.0056(4)	0.0054(2)	0.0035(71)
MoC2	HCEM-V	0.764(212)	1.994(78)	0.0102(1)	0.0100(1)	0.0020(2)
MoC3	HCEM-V	0.762(211)	1.973(16)	0.0515(16)	0.0501(13)	0.0028(1)
MoC4	HCEM-V	0.753(205)	1.977(13)	0.2008(26)	0.1929(14)	0.0041(1)
MoFeC1	C-NZVI	0.615(200)	1.895(37)	0.0056(4)	0.0054(5)	0.0022(103)
MoFeC2	C-NZVI	0.605(184)	1.916(30)	0.0102(1)	0.0098(1)	0.0045(4)
MoFeC3	C-NZVI	0.616(190)	1.884(22)	0.0515(16)	0.0497(16)	0.0036(2)
MoFeC4	C-NZVI	0.597(183)	1.932(23)	0.2008(25)	0.1901(12)	0.0057(1)
MoFeS	mackinawite	0.206(96)	4.253(131)	0.2008(25)	0.2085(15)	0
MoFeS ₂	pyrite	1.114(262)	2.131(31)	0.2008(25)	0.2108(16)	0
MoAFt	ettringite	1.085(267)	3.562(34)	0.2008(25)	0.2042(15)	0
MoAFm	AFm-SO ₄	1.207(269)	0.044(4)	0.2008(25)	0.1149(22)	0.1496(41)
MoCSH	C-S-H	0.077(36)	1.610(11)	0.2008(25)	0.2053(13)	0
MoPot	potlandite	1.350(254)	1.584(6)	0.2008(25)	0.2015(12)	0
MoGyp	gypsum	4.742(290)	61.39(34)	0.2008(25)	0.2174(15)	0
MoNZVI	NZVI	0.018(2)	1.492(4)	0.2008(25)	0.1332(10)	0.2538(30)

Mo(VI) sorption on HCEM-V, C-NZVI and each separated CEM-V/A cement hydration product at different initial loadings of ~0.005, ~0.01, ~0.05, and ~0.2 mM, was studied by batch sorption experiments and Mo K-edge XAS spectra. Aqueous results were shown in Table 5.6. Regarding the sorption on HCEM-V and C-NZVI, both types of cement showed quite weak affinity to MoO₄²⁻ at all the loadings, resulting in an R_d value range from 0.0020 to 0.0057 L g⁻¹. Besides, R_d values from the C-NZVI case were generally a little larger than the

values from the HCEM-V, probably due to the extra NZVI introduction. For Mo(VI) sorption on separated hydration phases, an initial loading of ~ 0.2 mM was investigated and only two hydration products, i.e., AFm phase and NZVI, showed good affinity to Mo(VI). For other separated phases, almost no sorption can be detected.

Sorption products from cement reactors at higher initial loadings (i.e., ~ 0.05 and ~ 0.2 mM) and from MoAFm and MoNZVI reactors, together with Mo(VI) chemicals references, were measured by Mo K-edge XAS spectra (Figure 5.11). The LCF of normalized XANES spectra was shown in Figure 5.11a and the fitting results were listed in Table 5.7. As can be seen, no reducing Mo phase can be detected from LCF. Besides, Mo(VI) sorbed on AFm-SO₄ always predominated the solid Mo(VI) species in cement reactors. In addition, MoNZVI contribution to NZVI-bearing cement samples (i.e., MoFeC3 and MoFeC4) was obviously larger than that to pristine cement samples (i.e., MoC3 and MoC4), indicating that Mo(VI) sorbed and coordinated with NZVI introduced. Regarding cement samples (i.e., MoC4 and MoFeC4) at the highest Mo loadings, Na₂MoO₄ molar fraction was higher than those at relatively low loadings. The coordination environment of Na₂MoO₄ could be considered as less constrained MoO₄²⁻. At high Mo loading, AFm phase, as a minor phase in hydrated cement, would be subject to high Mo exposure. Thus, MoO₄²⁻ would prefer to insert into the interlayer of AFm phase and stay as outer-sphere complexed MoO₄²⁻ tetrahedron, similar to Na₂MoO₄ complexation environment (See Chapter 2). This could be one reason to explain the higher Na₂MoO₄ percentages at high Mo loadings. Besides, tiny amount of CaMoO₄ could be detected in the LCF. Furthermore, EXAFS spectra of MoC4, MoFeC3, and MoFeC4 were also collected and the k^3 -weighted EXAFS oscillations were shown in Figure 5.11b. Due to the much diluted solid Mo concentrations, the oscillation noise was still quite strong at high k range, although 30-element Ge solid state detector and very low measuring temperature (~ 4 K) was used. It can be concluded that mainly one oscillation frequency can be observed, especially for MoC4. Further neighbor shells may also exist in NZVI-bearing cement samples (Figure 5.11c). However, multiplicity of possible configurations or interfacial ill-coordinated Mo could weaken the EXAFS signal of further shells. Further EXAFS analysis will be performed.

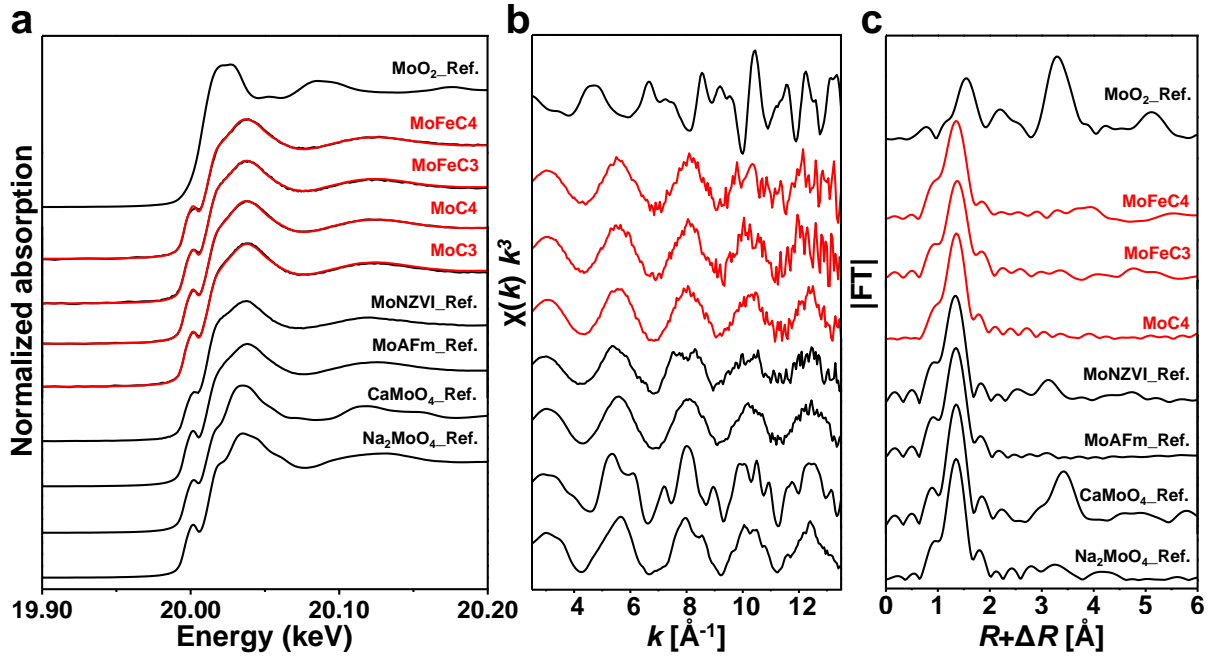


Figure 5.11. Mo K-edge XAS spectra of Mo-sorbed cement samples and the related references. (a) Normalized XANES spectra and the LCF results. (b) k^3 -weighted EXAFS oscillations. (c) Fourier transformed (not corrected for phase shift) EXAFS signals.

Table 5.7. LCF results of Mo K-edge XANES for identifying and quantifying Mo species (molar fraction) of reacted HCEM-V and C-NZVI samples. Also reported is the concentration sum (Σ), which is not constrained to 100% for samples, and the value of the reduced χ square (χ_v^2), both indicating good matches to the experimental spectra. Uncertainties are given by the number in brackets on the last digit(s), i.e., 4.3(3.0) represents 4.3 ± 3.0 .

ID	MoAFm	MoNZVI	Na ₂ MoO ₄	CaMoO ₄	Σ	χ_v^2
	(%)	(%)	(%)	(%)		
MoC3	86.1(5.2)	4.3(3.0)	5.5(3.9)	4.2(2.8)	100.2	0.06
MoC4	66.2(4.2)	8.2(2.4)	24.8(3.3)	1.0(2.4)	100.1	0.04
MoFeC3	62.6(4.6)	22.1(2.7)	15.9(3.6)	-	100.5	0.04
MoFeC4	54.1(6.0)	16.6(3.5)	25.4(4.7)	1.9(3.4)	98.0	0.08

Table 5.8. Concentrations of selected aqueous ions and the retardation factors in Mo(VI) reactors with an equilibrium time of 30 days, approximately. Prior to introducing Mo(VI), each type of hydrated cement equilibrated with CPW for ~ 48 h. Standard errors are given by the number in brackets on the last digit(s).

Cement type	Matrix	[Ca] _{tot} /mM	[S] _{tot} /mM	[Mo] _{tot} /mM	R _d / L g ⁻¹
-		1.290(260)	1.490(18)	0.2008(26)	-
HCEM-V		0.770(205)	1.990(9)	0.1895(15)	0.0060(16)
C_Mag		0.684(194)	1.900(15)	0.1934(15)	0.0038(15)
C-Hem	CPW	0.813(207)	1.800(69)	0.1901(14)	0.0056(15)
C-Goe		0.824(218)	1.720(17)	0.1948(20)	0.0031(16)
C-NZVI		0.622(195)	1.450(20)	0.1896(18)	0.0059(16)
C-M/H		0.803(209)	1.820(30)	0.1959(14)	0.0025(15)
C-M/G		0.780(211)	1.920(35)	0.1996(13)	0.0006(14)

The affinity of varying types of hydrated cement towards MoO₄²⁻ was checked by batch sorption experiments and the aqueous results were tabulated into Table 5.8. All the types of hydrated cement showed weak affinity and little sorption capacity to MoO₄²⁻, leading to an average R_d value of 0.0039 L g⁻¹. Note that the two largest R_d values (~0.0060 L g⁻¹) were obtained in the case of HCEM-V and C-NZVI, the two types of cement possessing the most AFm phase and Fe⁰ phase, respectively. The results confirmed again that AFm phase and Fe⁰ phase are the two most active sorption sites in reinforced cement.

5.3.5. Sb(V) sorption on hydrated CEM-V/A cement particles.

To start with, kinetics of Sb(V) sorption on HCEM-V were studied, shown in Figure 5.12. Total aqueous Ca and S concentrations almost kept constant. However, aqueous [Sb]_{tot} had a sharp decrease within several hours, reaching a bottom platform. Similar to sorption behavior of U(VI), antimonate could also be strongly associated with Ca[260] and form Ca[Sb(OH)₆]₂ precipitate. Thus, all the types of hydrated cement showed a strong affinity to Sb(OH)₆⁻ (Table 5.9), resulting in R_d values more than 20 L g⁻¹. Sb(OH)₆⁻ can be sorbed by Fe(III) hydroxides[26] forming octahedral inner-sphere complexes, which could explain the a little larger R_d values for hydrated Fe(III)-(hydr)oxides-bearing cement. In reducing environment,

such as in presence of Fe⁰ or Fe(II)-minerals, Sb species at lower oxidation states, e.g., Sb(III) and Sb(0), can be formed. This factor could lead to more Sb(OH)₆⁻ sorbed in C-NZVI reactor.

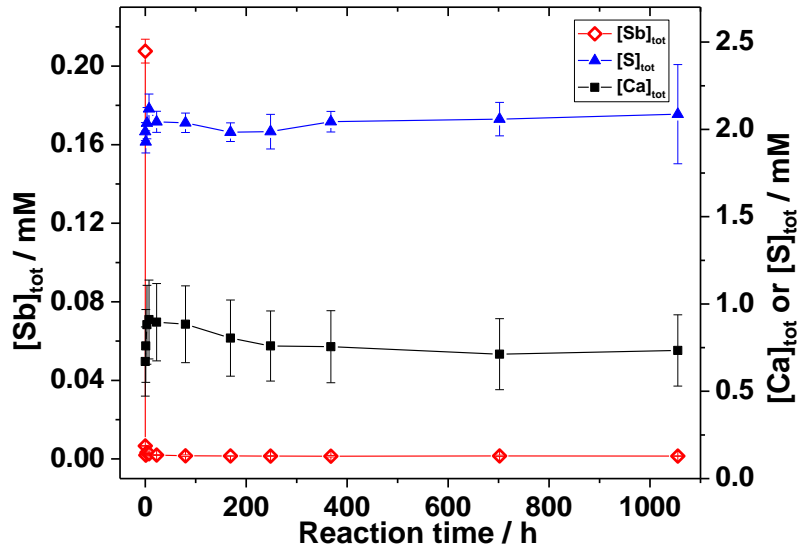


Figure 5.12. Kinetics of Sb(V) sorption on HCEM-V. Sb(V) was introduced after HCEM-V equilibrium with CPW for 160 h.

Table 5.9. Concentrations of selected aqueous ions and the retardation factors in Sb(V) reactors with an equilibrium time of 30 days, approximately. Prior to introducing Sb(V), each type of hydrated cement equilibrated with CPW for ~ 48 h.

Cement type	Matrix	[Ca] _{tot} /mM	[S] _{tot} /mM	[Sb] _{tot} /mM	R _d / L g ⁻¹
-		1.270(252)	1.550(2)	0.2076(30)	-
HCEM-V		0.857(203)	1.830(76)	0.0010(2)	21.56(3.01)
C_Mag		0.823(210)	1.700(16)	0.0008(1)	24.55(0.84)
C-Hem	CPW	0.820(210)	1.790(26)	0.0006(1)	33.58(4.43)
C-Goe		0.855(213)	1.770(33)	0.0008(1)	24.78(2.25)
C-NZVI		0.710(189)	1.720(20)	0.0007(2)	30.30(5.65)
C-M/H		0.846(220)	1.770(46)	0.0008(3)	25.18(7.40)
C-M/G		0.818(205)	1.720(18)	0.0009(1)	23.09(2.99)

5.3.6. Microprobe mapping on Fe⁰/cement interface in presence of RNs.

Secondary electron image (SEI), backscattered electron (BSE) image, and elements' mapping of selected sections for NZVI-1 samples are shown in Figure 5.13 and Figure 5.14. The

surface roughness can be observed in SEI and BSE can give us a general idea on the distribution of elements with different atomic numbers. Elements with larger atomic numbers, e.g., U, Fe, Mo, etc, will give more white spots. Regarding NZVI-1 samples, RNs firstly contact with cement, then NZVI. Mapping results show that the four RNs have different sorption sites preference. U distribution strongly overlapped with Ca-rich sites. Besides, U preferred to adsorb on the Ca-phases' surface, instead of co-precipitating with cement solid phases.

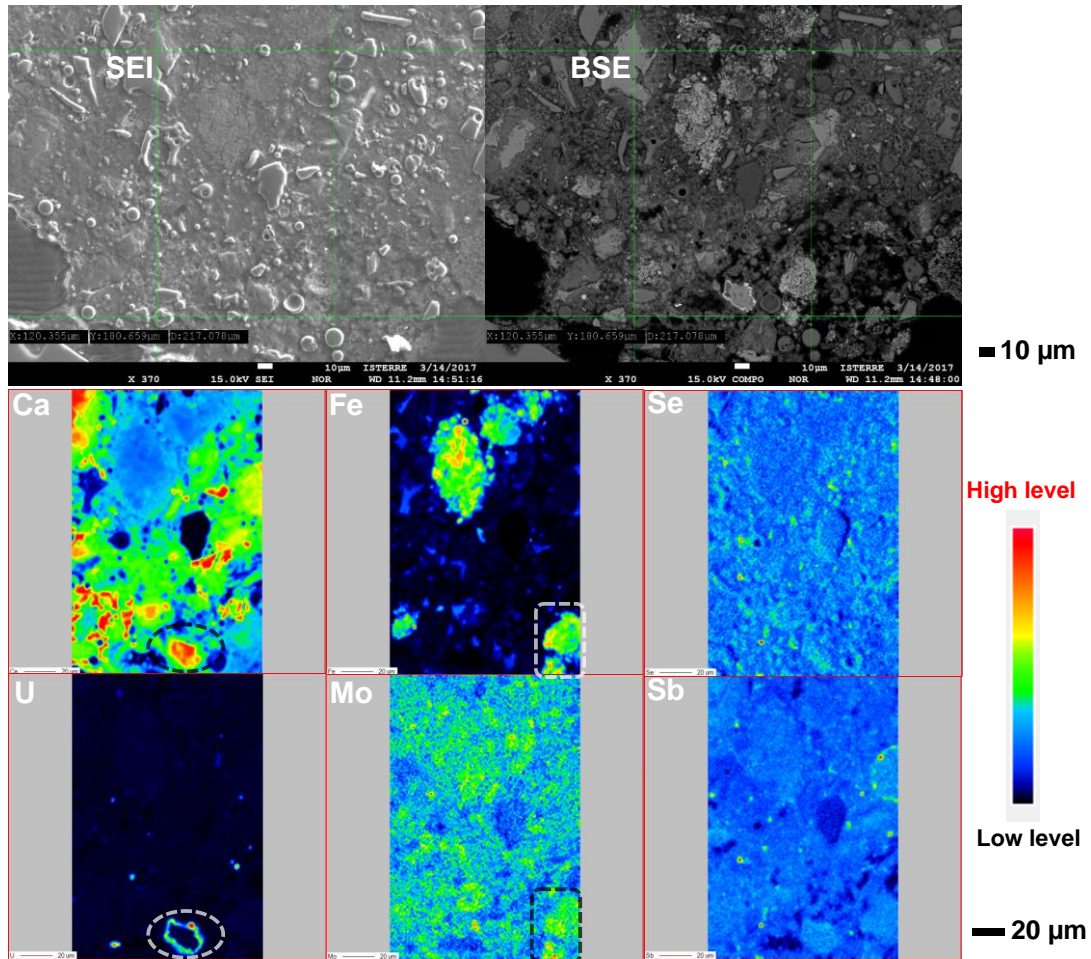


Figure 5.13. Secondary electron image (SEI), backscattered electron (BSE) image, and elements' mapping of selected section for NZVI-1 sample. The scale bar for SEI and BSE is 10 µm, the one for mapping is 20 µm. From the black to red colour, the element concentration level increases in mapping images.

Previous reports indicated that aqueous U(VI) concentration in equilibrium with, i.e., alkali/alkaline-earth uranates (e.g., $\text{Na}(\text{UO}_2)\text{O}(\text{OH}) \cdot (\text{H}_2\text{O})_{0-1}$ and CaUO_4) will be very low ($\sim 10^{-9}$ M) in hyperalkaline cement leachate[258]. Other research also concluded that the U(VI) colloids formed are nano-sized and could remain stable for several years, which would enhance potentially the mobility of U(VI)[259]. However, in our case, even if nano-sized

calcium uranate colloids were formed, they stayed on site in the cement paste. Therefore, the extremely low solubility of calcium uranate predominated the sorption process of U(VI) in Fe-cement. Besides, U(VI) should just precipitate on the surface of Ca-containing phases in hydrated cement and prefer to stay inert even the very reactive NZVI was introduced after.

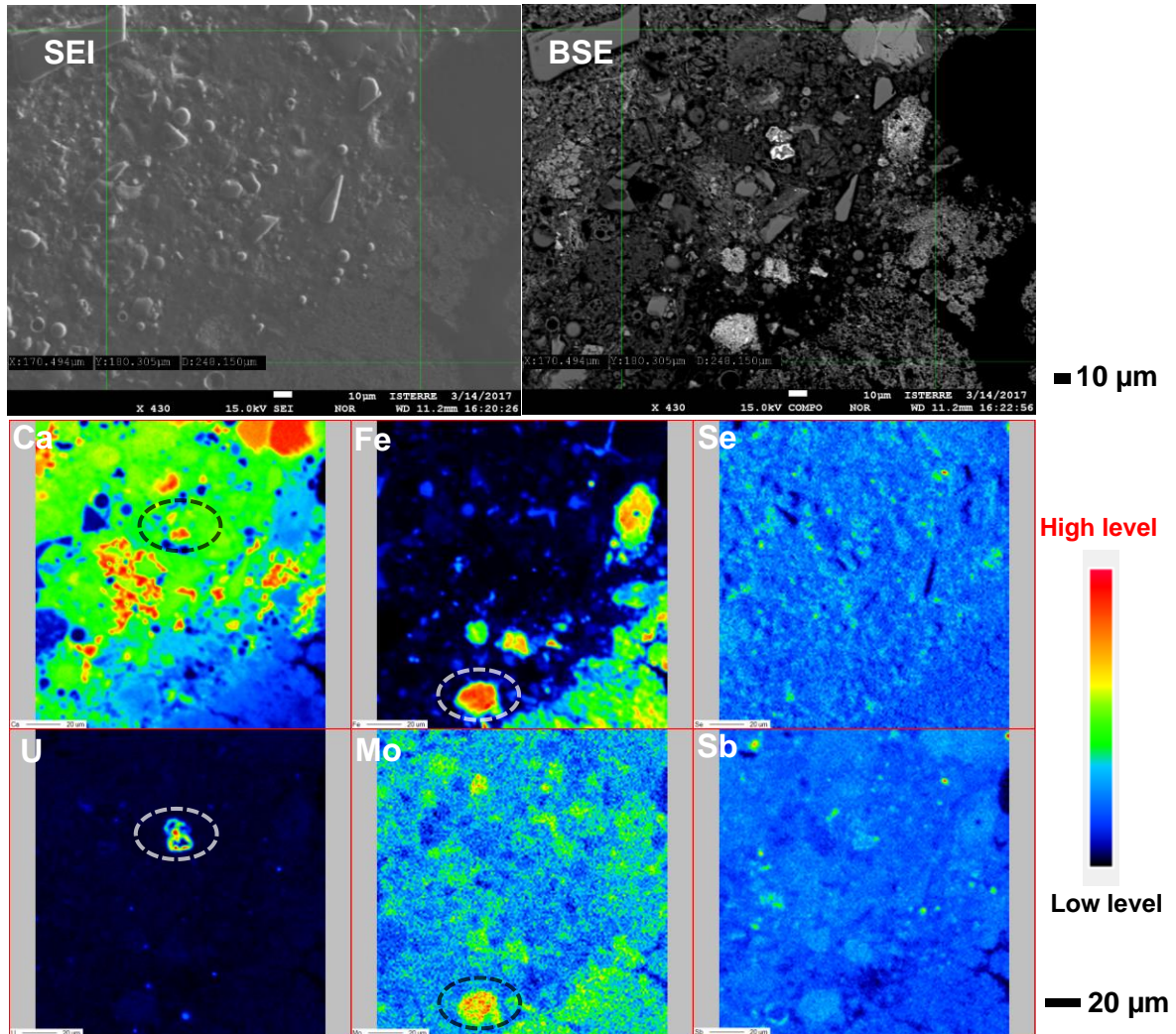


Figure 5.14. Secondary electron image (SEI), backscattered electron (BSE) image, and elements' mapping of selected section for NZVI-1 sample. The scale bar for SEI and BSE is 10 µm, the one for mapping is 20 µm. From the black to red colour, the element concentration level increases in mapping images.

In opposite, Mo(VI) had strong correlation with Fe, rather than Ca, as shown in Figure 5.13 and 5.14. This may result from the higher mobility of Mo(VI) in cement paste and/or less colloid formation with Ca ions, than U(VI). Ions in cement pore water cannot immobilize Mo(VI) sufficiently, which leave the removal chance to the following introduced NZVI. From mapping results, Mo(VI) was sorbed inside the bulk Fe-aggregates, suggesting that Mo(VI) may structurally complex with Fe-bearing phases (e.g., FeMoO_4 , Fe oxides, and green rust). From Chapter 4, it is known that NZVI has considerable retention ability ($K_d \sim 0.2 \text{ L g}^{-1}$) to

Mo(VI). Mo(VI) sorption in reinforced cement phases will be further discussed in the following sections. Regarding Sb and Se, no concentrated RN spots can be observed, i.e., the two RNs were adsorbed on hydrated cement and Fe phases equally. This could be explained by their comparable affinity to both cement and Fe phases.

Mapping results of NZVI-2 samples are shown in Figure 5.15. In this case, RNs firstly interacted with NZVI. As can be seen, once RNs were contacted with and sorbed by NZVI, they can be constrained strongly and desorption was difficult to occur, even though large amount of cement was introduced quickly. As a result, both U and Mo correlated obviously with Fe phases. For Se and Sb, they also preferred to be sorbed by Fe phases, although their signal was quite weak.

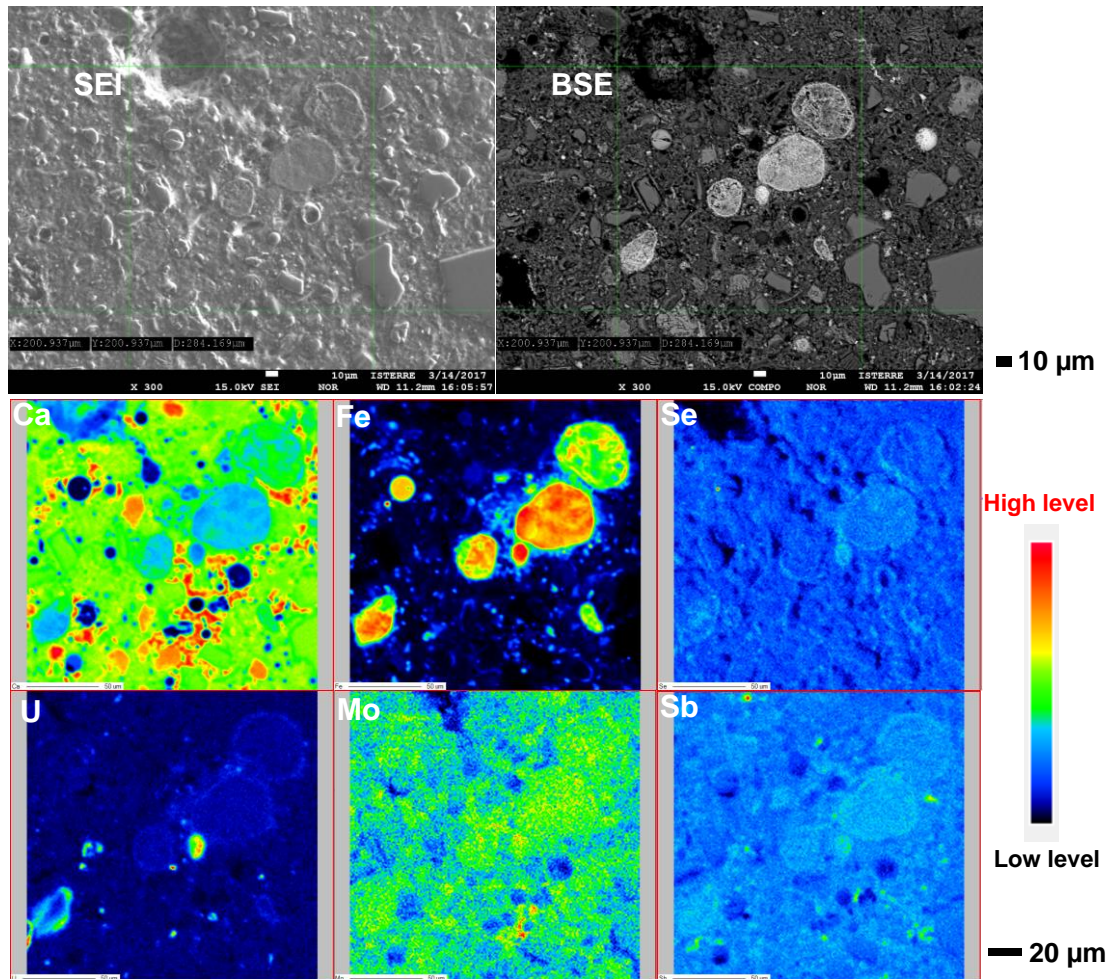


Figure 5.15. Secondary electron image (SEI), backscattered electron (BSE) image, and elements' mapping of selected section for NZVI-2 sample. The scale bar for SEI and BSE is 10 µm, the one for mapping is 20 µm. From the black to red colour, the element concentration level increases in mapping images.

Regarding NZVI-3 sample (Figure 5.16), CEM-V/A cement powder and NZVI were mixed sufficiently under dry state, then the RNs were introduced together with the certain portion of

water. With this preparation, it can be considered that RNs have almost equal opportunity to contact with NZVI and cement at the beginning. As shown, U preferred to concentrate on cement hydration phases, consisting of Ca, Al, and Si hydrates. Similar habitation behaviour of Sb were found. Regarding Se, it is likely to be adsorbed strongly by both Ca-rich and Fe-rich phases. While for Mo, it only correlated with Fe-rich phases. After hydration and reaction during cement hardening, NZVI has aggregated, oxidized into Fe-oxyhydroxides, and incorporated with cement hydrated phases.

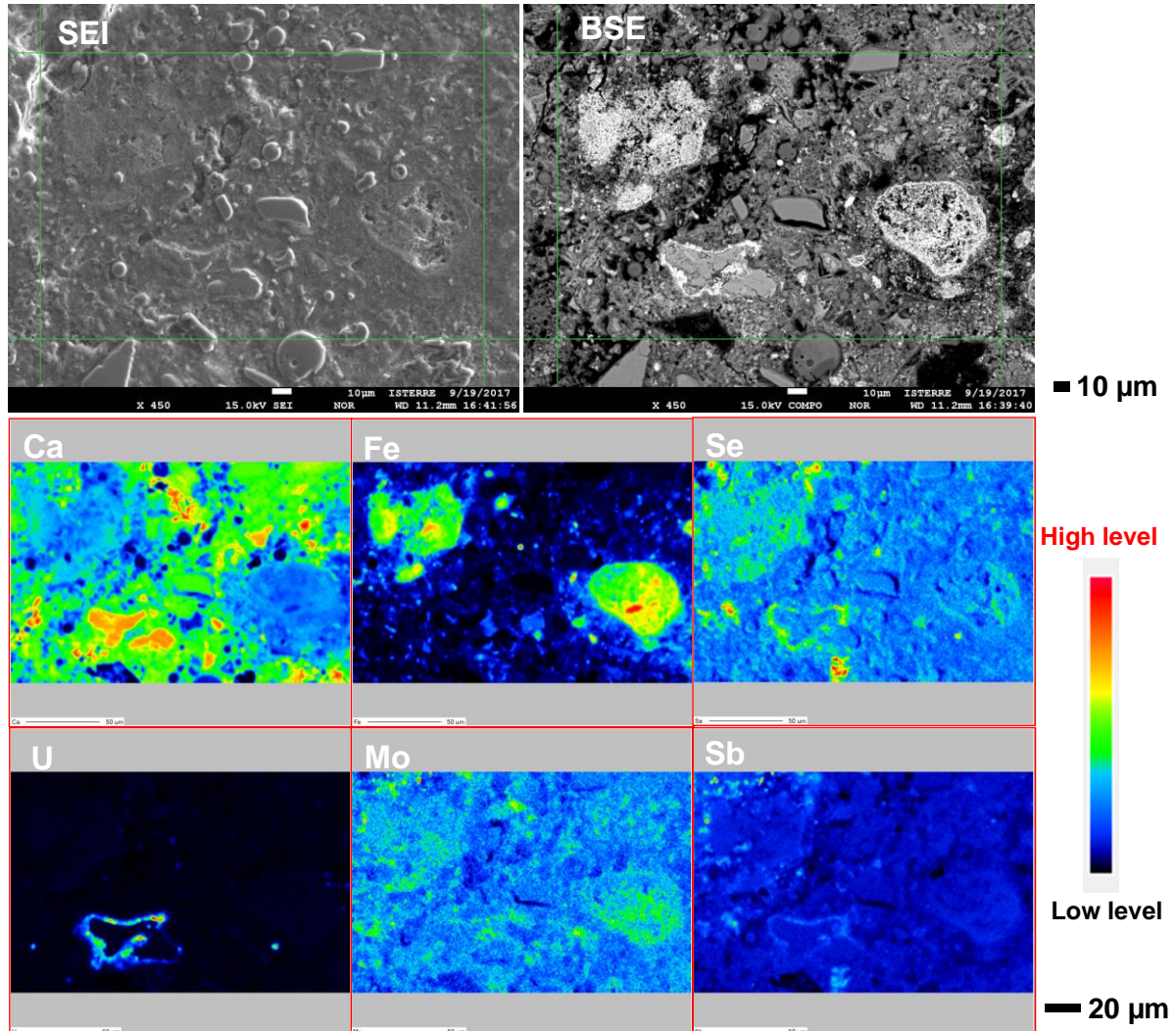


Figure 5.16. Secondary electron image (SEI), backscattered electron (BSE) image, and elements' mapping of selected section for NZVI-3 sample. The scale bar for SEI and BSE is 10 µm, the one for mapping is 20 µm. From the black to red colour, the element concentration level increases in mapping images.

By comparison of NZVI-1, NZVI-2, and NZVI-3 results, it can be concluded that the interaction order of Fe-cement phases with RNs and the solubility of RNs to Ca co-precipitates are critical to RNs sorption behaviours. Fe⁰ always shows very strong affinity to

all RNs, while cement phases have a certain selectivity. When RNs diffuse in the real reinforced concrete in geologic nuclear waste repositories, U can always be retarded by cement or steel, while some RNs, e.g., Mo(VI), will only be immobilized effectively when they encounter steel. This may give some hints to the structure design of reinforced concrete in repositories, e.g., embedding steels more outer.

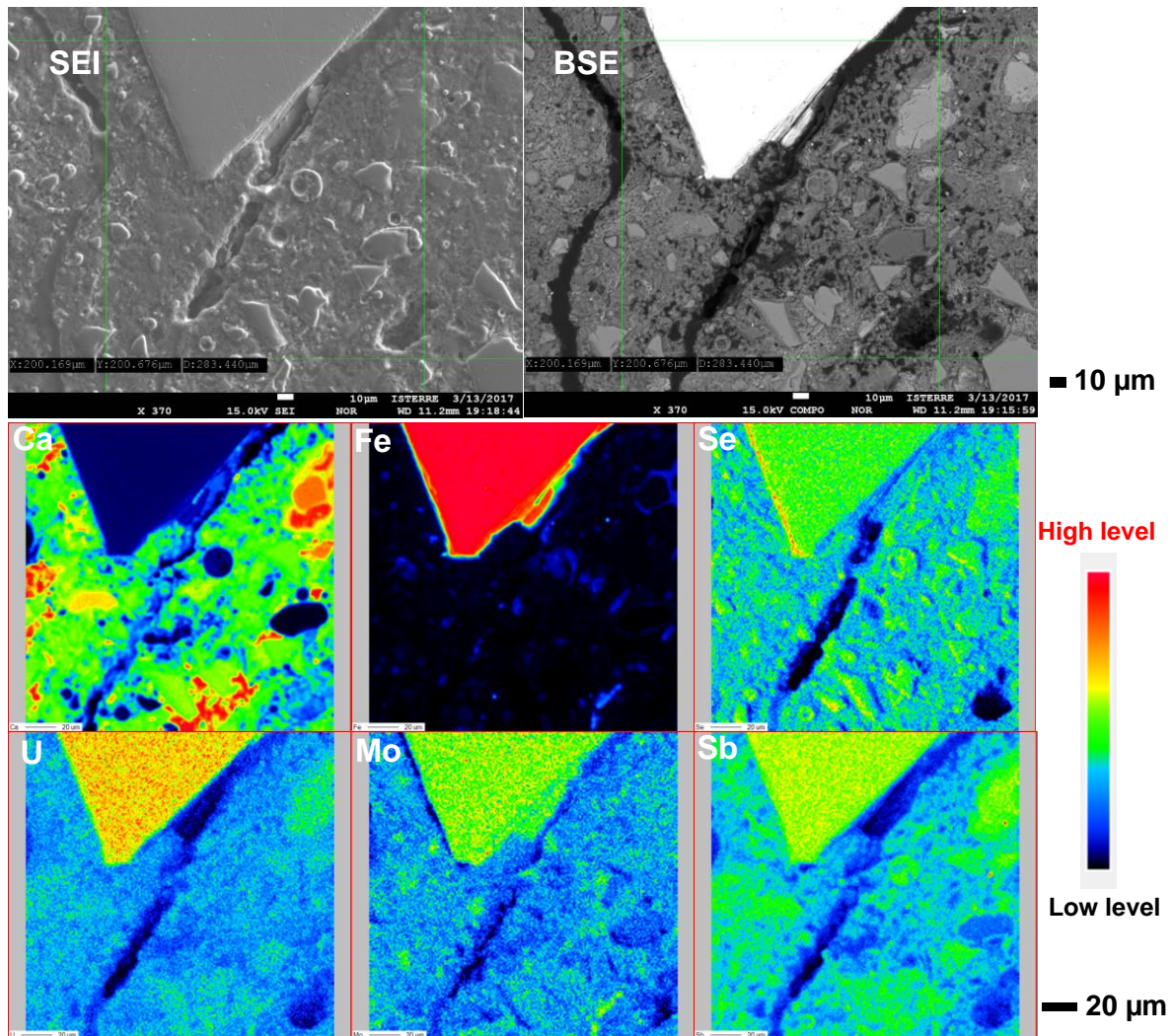


Figure 5.17. Secondary electron image (SEI), backscattered electron (BSE) image, and elements' mapping of selected section for Type II sample. The scale bar for SEI and BSE is 10 μm, the one for mapping is 20 μm. From the black to red colour, the element concentration level increases in mapping images.

Elements mapping results of Type II samples are shown in Figure 5.17. The triangle cross section in the steel coupon is shown on the upper part of the Figures. Two kinds of steel surfaces were contacted with cement phases, the left face polished previously and the right face unpolished. Shown in SEI and BSE images, the platform of steel is a little higher than that of hydrated cement, which should be resulted from the big hardness difference between hydrated cement and the steel. When polishing by hand, it can hardly be avoided to generate

different surface height levels and border effects. Besides, friction created cracks along the surface of steel coupon. From the mapping images, it can be found that the stronger signal was always from the higher-level platform of steel coupon. Higher-level face will result in stronger signal in microprobe measurement. Thus, the observed signal difference on steel coupon should originate from the uneven polished surface, instead of real elements concentrations effect. It has been attempted to observe more details on the thin corrosion layer on steel. However, due to the border effect and very slow corrosion rate ($\sim 1 \mu\text{m}$ per year), no convincing data could be obtained. Longer cement curing time (at least one year) and improved polishing skills are needed for the following experiment.

5.4. Conclusions

Sorption of RNs (i.e., U, Se, Mo, Sb) on hydrated CEM-V/A cement and its types containing Fe-phases (i.e., NZVI, magnetite, hematite, goethite, M/H couple, and M/G couple) was studied by wet chemistry methods and synchrotron-based X-ray techniques. All the types of cement showed a strong affinity towards U(VI), especially pristine and NZVI-bearing hydrated cement, revealing that co-precipitation with Ca and reductive precipitation by NZVI are the most effective uptake mechanisms. Besides, formation of clarkeite-type colloidal nanoparticles could be the first step of U(VI) removal. Similar to U(VI) sorption behavior, Sb(V) was also removed efficiently, with the uptake processes predominated by co-precipitation of $\text{Ca}[\text{Sb}(\text{OH})_6]_2$ and reductive precipitation. The LCF of Se K-edge XANES spectra and EXAFS refinement showed that SeO_3^{2-} can be reduced into FeSe by C-NZVI, thus leading to a high R_d value, and into Se^0 by even the blank hydrated CEM-V/A cement. Besides, Ca-sites in hydrated cement were also potential to adsorb SeO_3^{2-} based on the considerable CaSeO_3 XANES signal contributions. PDF analysis showed that after SeO_3^{2-} corrosion, NZVI would completely transformed into $\text{Fe}(\text{OH})_2$ and tetrahedron-octahedron iron bridging of magnetite would collapse due to the oxidation by Se(IV). MoO_4^{2-} was the most hard to be sorbed by cement. A combination of batch sorption experiments and Mo K-edge XAS analysis uncovered that AFm- SO_4 and Fe^0 were the two most active sorption phases for MoO_4^{2-} in reinforced cement. No Mo(VI) reduction can be detected on all the types of cement. Microprobe mapping results showed that U concentrated on the surface of Ca-rich phases while Mo had strong correlation with Fe phases. Fe^0 always showed strong affinity to all RNs, while hydrated cement phases had a certain selectivity (e.g., RNs' complexation ability with Ca). This may give some hints to the structure design of reinforced concrete in nuclear waste repositories, e.g., embedding steels more outer.

Chapter 6. The influence of surface impurities on the reactivity of pyrite toward aqueous U(VI)

Abstract

Pyrite, the Earth's most widespread and abundant sulfide mineral, may play a significant role in governing mobility of redox sensitive RNs, among which uranium, via redox process. In this study the influence of aqueous U(VI) reduction by pyrite of various factors were investigated. Natural Pb-, As- and Si-containing pyrite from different place were used. The results demonstrated that As-containing pyrite generally is more reactive than Pb-containing pyrite, but the coexisting SiO₂ can improve the reactivity of Pb-containing pyrite. Furthermore, fresh crushed pyrite showed much higher reactivity toward aqueous U(VI) in the case of Pb- and As-containing pyrite, while the redox reaction was inhibited at most pH conditions when these crushed pyrite were previously acid washed. Before the addition of aqueous U(VI), solution analyses showed the presence in the suspension of aqueous S²⁻, for fresh crushed Pb- and As-containing pyrite. Moreover, aqueous S decreased after addition of U(VI), and a considerable amount of elemental sulfur was detected after the reaction. The SEM images showed that the reduction of aqueous U(VI) mainly occurs on pyrite surface at the Pb- and As-enrichment spots. It can be concluded that the solubility of pyrites could increase at impurities spots due to mineral lattice defects. This would lead to larger amount of reducing sulfur species, like S²⁻ and S₂²⁻, being released by the interface. Consequently, more U(VI) can be reduced and sorbed on impurities-rich spots. Therefore, we proposed that the reactivity of pyrite is largely dependent on the impurities hosted in the structure and reactive surface S²⁻ content resulting from the breaking of Fe-S bonds during grinding process.

6.1. Introduction

Remediation of uranium contamination resulting from mining and ore refinement has received extensive attention throughout the world. Uranium mainly exists as U(VI) and U(IV) in the ambient environment, and its solubility is largely dependent on the oxidation states. While tetravalent UO_2 , or a mixed valent oxide of U(IV) and U(VI), e.g., U_4O_9 , U_3O_7 , or U_3O_8 , is nearly non-soluble, hexavalent uranium (UO_2^{2+}) can form strong complexes with many inorganic ligands in particular carbonate [283], leading to a high mobility in the groundwater-rock system. The formation of ternary complexes of UO_2^{2+} and CO_3^{2-} with alkaline earth metals (Mg^{2+} , Ca^{2+} , Sr^{2+} and Ba^{2+}) can further enhance the solubility of U(VI) [284]. Sorption to solid particles and reduction of soluble U(VI) to U(IV) solid phases are the key geological processes that govern the immobilization of toxic uranium in the environment. Numerous studies have been performed to investigate the sorption behavior of U(VI) on various solid surfaces, such as metal oxyhydroxides [285, 286], SiO_2 [287], clays [288, 289], and organic matters [290, 291]. Due to the limited amount of sorption sites as well as the large influence of the solution pH value and composition on the sorption efficiency, reductive precipitation via biological and abiotic processes is considered as a more effective way for uranium attenuation. The bioreduction of soluble U(VI) to solid UO_2 using dissimilatory metal-reducing bacteria including sulfate-reducing bacteria (SRB) has been widely investigated [292-294], but reoxidation of the biogenic UO_2 by various oxidizing agents in the subsurface is also of importance [295, 296]. Fe(II)-bearing minerals are ubiquitous in the geologic environment. Abiotic reduction of aqueous U(VI) by surface-catalyzed Fe(II) [297, 298], green rust [299, 300], magnetite [18, 301-305], and mackinawite [306-308], has long been recognized.

As once-through fuel cycle is applied in many countries (e.g., Sweden, Finland, etc.), immobilization of uranium is of highly concern for the long-term storage of high-level radioactive waste (HLW) in a deep geological repository [309, 310]. Direct disposal of the spent nuclear fuel is also considered in China, since there is heavy water reactor in addition to the prevalent pressurized water reactor (PWR). The dissolution of the UO_2 matrix upon corrosion of the waste canister in the far future will cause the release of radio-toxic fission products and transuranic elements from spent nuclear fuel in contact with water. Therefore, maintenance of a reducing condition is essential for the safety of a future repository.

Pyrite (FeS_2), the Earth's most widespread and abundant sulfide mineral, is known to buffer reducing conditions at the repository conditions where it is present in host clay-rock as well as in near-field bentonite materials [311, 312]. Many studies have confirmed that pyrite is able to effectively immobilize redox-sensitive radionuclides such as ^{79}Se [108, 109, 112, 262, 313-315], ^{99}Tc [316-319], etc. Thermodynamically, UO_2 is the most stable phase in the pyrite-containing systems in a wide pH range from 0 to 14. The occurrence of U(VI) reduction on natural pyrite has been reported under acidic conditions (pH 3.6-6.1) over a short reaction time (e.g., 4 or 48 h), although the product observed was a hyperstoichiometric UO_{2+x} [99, 320]. Nevertheless, a recent study demonstrated that the reduction of aqueous U(VI) by pyrite was inhibited in most pH conditions, and partial reduction was only observed at pH 6.21-8.63 and 4.52-4.83 for synthetic and natural pyrite, respectively [98]. To date, factors influencing the reactivity of pyrite toward aqueous U(VI) remain unknown. It is generally accepted that the kinetics of redox reactions occurring at the mineral-water interface are largely dependent on the reactivity of surface sites [321]. Stoichiometrically, pyrite has a S/Fe ratio of 2, but the ideal chemistry is not encountered in natural specimens. Natural pyrites typically contain a host of minor and trace elements, such as As, Co, Ni, Cu, Pb, Zn, etc. The variability in the chemical composition can result in variation of physico-chemical properties [322], in particular the reactivity can be enhanced for As- and Co-doped pyrite [323]. Therefore, in order to better understand the role of pyrite on the mobility of toxic uranium in the environment, we investigate the influence of surface impurities on pyrite reactivity toward aqueous U(VI).

6.2. Materials and methods

6.2.1 Materials

Commercially available 1000 ppm $\text{UO}_2(\text{NO}_3)_2$ stock solution, dispersed in 2% HNO_3 matrix and used for the sorption experiments, was obtained from Sigma Aldrich. All other chemicals, e.g., $\text{FeCl}_2 \cdot 4\text{H}_2\text{O}$ and Na_2CO_3 , were purchased from Sigma Aldrich with analytical grade. Deionized water (18.2 $\text{M}\Omega \cdot \text{cm}$) was firstly degassed by purging with argon before using for solution preparation.

Three types of natural pyrite were collected for investigation. They are i) commercial lead-containing pyrite from Alfa Aesar chemical company, named Pb-pyrite, ii) arsenic-containing pyrite from the Jiguanshan ore mine (Tongling, China), here called As-pyrite, and iii) SiO_2 -coexisting pyrite from Anhui, China, named Si-pyrite. The As-pyrite and Si-pyrite blocks

were crushed, sieved, magnetically separated and washed, following the procedures mentioned in a previous study [313]. The obtained particle sizes were 1.5-4.8 mm, 0.13-0.15 mm, and 0.5-1.0 cm for Pb-pyrite, As-pyrite, and Si-pyrite, respectively. Subsequently, planetary ball mill (Pulverisette-7, Fritsch GmbH, Germany) was employed to grind the pyrite grains under N₂-atmosphere protection. Two kinds of pyrite powder were employed for sorption experiments. The first one with fresh surface (labelled as Type I pyrite) was prepared by washing the ground powder with 0.2 M HCl, degassed water and acetone for several times, and then dried and stored under anoxic conditions. The second one with fractured surface (labelled as Type II pyrite) was used directly from the ground powder without washing procedures.

The specific surface area of the ground pyrite powder was measured to be 0.6 ~ 0.9 m² g⁻¹ (Table S6.1) by BET N₂-absorption method. XRD analysis was used to characterize the phase components, while the main elements Fe and S as well as minor and trace elements (e.g., As, Co, Ni, Cu, Pb, etc.) in the pyrite were identified and quantified by inductively coupled plasma optical emission spectrometry (ICP-OES) after the digestion by aqua regia.

6.2.2 Batch sorption experiments

Two batches of sorption experiments were conducted at room temperature in 50 ml serum bottles under constant shaking in a N₂-filled glove box (O₂ < 2 ppm). Prior to introducing U(VI), the pyrite powder was equilibrated with 0.01 M NaCl at the given pH values for 2 days. Identical solid to liquid (S/L) ratio of 10 g L⁻¹ and an initial U(VI) concentration of 0.1 mM were applied to all reactors. The first batch (Batch I) experiments were performed at pH ~3.0, ~4.5, ~6.5, and ~9.5 using Type I pyrite powder. For the reactors at pH ~6.4 and ~9.5, extra 1.0 mM Na₂CO₃ was added to avoid U(VI) precipitation. Once adding the certain portion of UO₂(NO₃)₂ stock solution, a 5 mL aliquot of suspension was sampled and filtered through a 0.22 μm pore size membrane filters. Subsequently, the solution pH was quickly adjusted back to the given reaction pH values, using 0.1 or 1.0 M NaOH and HCl. At each defined time interval, the pH was measured and readjusted if necessary, and then a 5 mL aliquot of suspension was sampled by filtration. The Batch II experiments were performed following the same procedure of Batch I experiments, but using Type II pyrite for reaction instead. Controlled experiments in the absence of aqueous U(VI) were performed simultaneously.

The solution pH was measured by a combined glass Micro-pH electrode (Metrohm 6.0234.100) straight after its calibration by four pH standard solutions (i.e., pH 4.01, 7.00, 10.01, and 12.00) with manual temperature compensation. The sample filtrate for all reactors were analyzed by ICP-OES to determine the concentrations of total aqueous U, Fe, S, As, Co, Pb and Ni. Aqueous sulfide were analyzed by the methylene blue method [255]. Elemental sulfur was extracted by perchloroethylene and subsequent analyzed by high-performance liquid chromatography (HPLC) coupled with a UV/Visible detector [324]. The U(VI)-reacted pyrite in each reactor was collected by vacuum filtration through 0.22- μm nitrocellulose membrane, dried and stored in glove box, and took extreme care to prevent any possible sample oxidation for the subsequent solid characterization.

6.2.3 Spectroscopic and Microscopic Analyses

X-ray photoelectron spectroscopy (XPS) measurements were performed on the pristine Type I and Type II pyrite powder, and on the U(VI)-reacted pyrite from Batch I and Batch II sorption experiments. Samples were transported to the XPS facility in a N_2 -filled metallic jar, pasted flat on the double-face carbon tape in a glove bag, and then rapidly transferred into the XPS chamber under the protection of nitrogen. The XPS spectra were recorded using a Kratos AXIS Supra electron spectrometer. A monochromated Al $\text{K}\alpha$ source, a hybrid lens system providing an elliptic analysis area of $0.3 \times 0.8 \text{ mm}^2$, and a charge neutralizer were used. Pass energy was 160 eV for survey scans and 20 eV for regions. The binding energy (BE) scale was referenced to the C1s line of aliphatic carbon, which was set at 284.8 eV. The XPS data were processed using CasaXPS software.

Sorbed U speciation on Pb-pyrite at pH ~ 6.5 and ~ 9.5 were also characterized by U L_3 -edge (17166 eV) X-ray absorption near edge structure (XANES) spectroscopy analyses. The measurements were conducted at the SpLine Spanish CRG Beamline (BM25A) at the European Synchrotron Radiation Facility (ESRF), Grenoble, France. U L_3 -edge energy was calibrated by the K-edge excitation energy of an yttrium (17038 eV) metallic foil. Spectra references of solid U_3O_8 and U_4O_9 were from Kvashnina[264], while UO_2NO_3 , and UO_2 were from René[263] and Karsten[265], respectively. The dried samples were sealed double-side using Kapton tape in glove box, and then transferred in an anaerobic chamber to the synchrotron facility. All the samples were measured in fluorescence mode, except for the references which were prepared as pellets by diluting the solids in cellulose and measured in transmission mode. A Sirius liquid nitrogen cooled Si(Li) 13-multi-element solid state X-Ray

detector from e2v were used for data collection. During the measurement, samples were always under N₂ atmosphere protection. The Demeter software package was used for the data integration and reduction of XANES (Athena) [196]. A linear combination fit (LCF) was applied to the XANES spectra to identify and quantify the U solid speciation.

The morphology and chemical composition of U(VI)-reacted pyrite powder from Batch I and II experiments were characterized by scanning electron microscopy (SEM) using an energy dispersive X-ray spectrometer (EDX) analysis (Hitachi S4800).

6.3. Results and discussion

6.3.1 Pyrite Characterization

XRD analysis indicated that the Pb-pyrite and As-pyrite used for reaction were pure pyrite, while visible diffraction peaks of crystalline SiO₂ phase was observed for Si-pyrite. No other phase was detected (Figure S6.1). Because SiO₂ phase cannot be dissolved in aqua regia, ~8.1 wt % SiO₂ mineral inclusion was estimated based on the balance of mineral mass.

In addition to the main pyrite phase, ICP-OES analysis on the acid digestion solution revealed ~0.06 wt% Pb for Pb-pyrite (i.e., FeS₂Pb_{0.00060}), ~1.66 wt% As and ~0.07 wt% Pb for As-pyrite (i.e., FeS₂As_{0.027}Pb_{0.00070}), and ~0.06 wt% Pb for Si-pyrite (i.e., FeS₂Pb_{0.00059}), while other elements (Zn, V, Ti, Mn, Ba, Co, Cu, Cr, Bi, Cd, Ag, Ni, Sb, Mo, Ca) were below detection limits. As reported previously, arsenian pyrite may contain up to 10% As, and Pb-containing pyrite is generally arsenic-rich [322], thus the Pb and As impurities levels observed in this study are in the range found for natural pyrites.

XPS analysis was further employed to characterize the surface of Type I and Type II pyrite powder before reaction with aqueous U(VI). The results indicated that there was no apparent difference in the Fe2*p* and S2*p* spectra between these two types of pyrite (Figure S2). Particularly, no peak was observed at 168-169 eV that for the binding energy (BE) of SO₄²⁻ for Type II pyrite (Figure S6.2), suggesting that there was no surface oxidation during the grinding process. The presence of very weak signal at this BE for Type I Si-pyrite presumably was due to measurement noise or minor surface oxidation during transportation of XPS analysis.

6.3.2 Aqueous phase analysis for Type I pyrite suspension

The evolution of aqueous U, Fe and S for U(VI) reacted with Type I pyrite were monitored regularly and illustrated in Figure 6.1. Unexpectedly, the Pb and As impurities contained in the pyrite were not detected by ICP-OES in the filtrate, implying that these elements were really scarce in the pyrite structure. After a slight decrease in the first 24 hours, aqueous U(VI) remained nearly constant afterwards, while in contact with Pb- and As-pyrite at pH ~3.0 and ~4.5, indicating that there was no occurring redox reaction or that the reaction was too slow to be detected at acidic conditions. The continuous increase of aqueous Fe and S can be attributed to the non-oxidative dissolution of Pb- and As-pyrite. The $[S]_{\text{tot}}/[Fe]_{\text{tot}}$ ratios were much lower than 2.0, suggesting an excess release of surface iron compared to surface S at the experimental conditions.

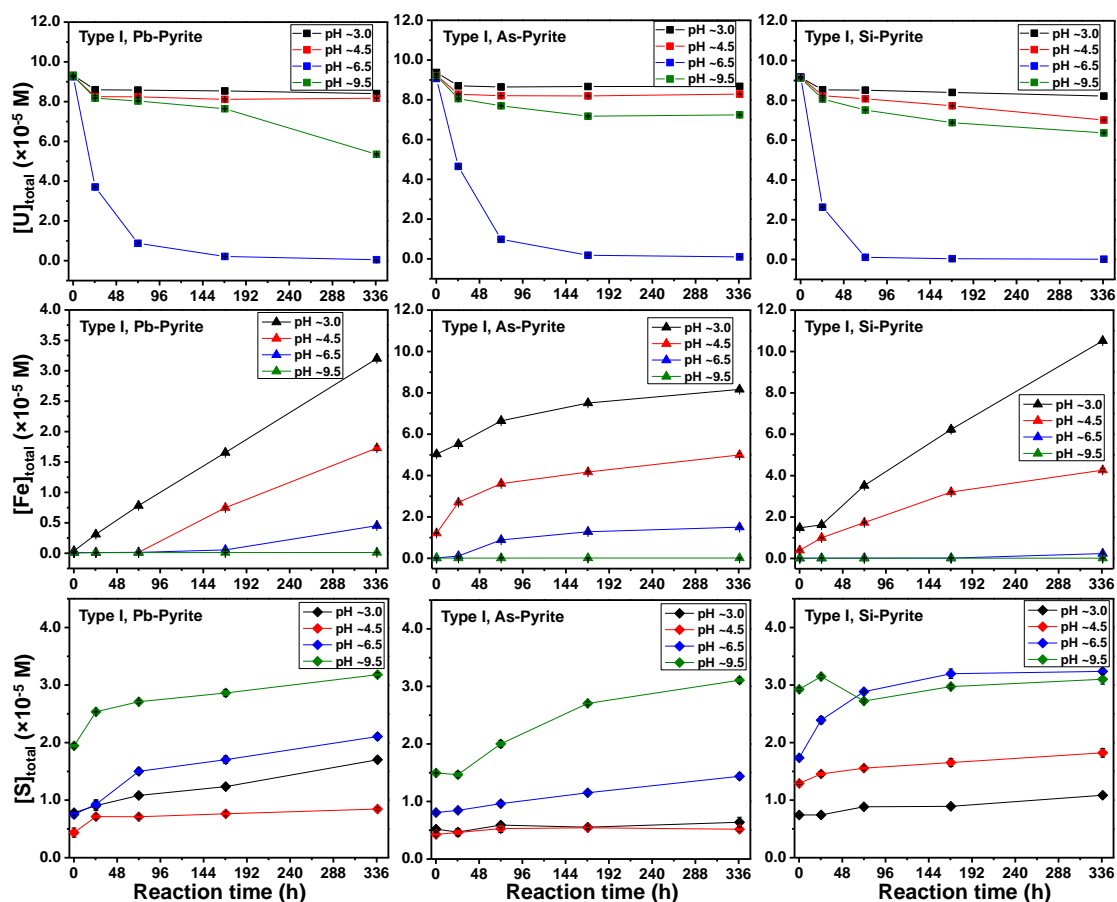


Figure 6.1. Concentration evolutions of total aqueous U, Fe and S in reactors of Type I pyrite.

At pH ~6.5 and ~9.5, aqueous U(VI) showed a gradual concentration decrease. Although the solubility of U(VI) is relatively low at these two pH conditions (Figure S3), we cannot exclude the possible occurrence of U(VI) reduction since spontaneous precipitation is a rapid process that should result in a sharp decrease in aqueous U(VI). Moreover, more aqueous S

was released compared to the reaction at pH ~3.0 and ~4.5, which further supported the possible occurrence of redox reaction since high pH is unfavorable for the non-oxidative dissolution of pyrite. In the presence of Si-pyrite, we can see the same trend, i.e., continuous decrease of aqueous U(VI) at all studied pHs, suggesting a possible U(VI) reduction. Meanwhile, aqueous S increased continuously with increasing reaction time.

Compared to the reaction of Pb-pyrite, more iron was released into the solution at pH ~3.0 and ~4.5 in the presence of As- and Si-pyrite. Since the reduction of U(VI) to U(IV) only consume two electrons, the release of large amount of aqueous Fe suggested a higher solubility of As- and Si-pyrite, which also implied a higher reactivity. The association of SiO₂ with natural minerals is frequent, and its impacts on the crystallinity, aggregation, particle surface composition, and overall chemical reactivity also have been reported for natural ferrihydrite [325, 326].

6.3.3 Aqueous phase analysis for Type II pyrite suspension

The solution data for U(VI) reacted with Type II pyrite are shown in Figure 6.2. Similarly, no Pb or As impurity, contained in pyrite, could be detected in the filtrate solution. In contrast to the reaction systems of Type I pyrite, in presence of Type II pyrite, aqueous U(VI) showed continuous decrease in Pb-pyrite suspension at all studied pHs. The gradual decrease of aqueous U(VI) can be attributed to U(VI) reduction, in particular for the reaction at pH ~3.0 and ~4.5 because the solubility of U(VI) is relatively high in these conditions (Figure S6.3). Noticeably, a relatively fast U(VI) decrease was observed within the first 24 hours, which can be mainly explained by the participation of surface S²⁻ to U(VI) reduction (see the discussion below). Along with the decrease in U(VI), aqueous Fe showed a continuous increase trend except for reaction at pH ~9.5. Unexpectedly, relatively high concentrations of aqueous total S (~2.4×10⁻⁴ M) were observed for all the reactions, and they remained fairly constant after a slight decrease in the first 24 hours. A high concentration of aqueous total S (2.5×10⁻⁴ M) was also observed in absence of aqueous U(VI) for the controlled experiments (Table S4). To the best of our knowledge, SO₄²⁻ is the most stable S species in aqueous solution. Because XPS analysis did not show the presence of SO₄²⁻ on the surface of Type II pyrite before reaction, the relatively high concentrations of aqueous S even in absence of aqueous U(VI) might be mainly explained by the oxidation of surface S²⁻ by surface Fe³⁺ upon contacting with solution. In reality, during the anoxic grinding process, the breaking of Fe-S bonds would result in an electron transfer from iron to sulfur, inducing the formation of S²⁻ and Fe³⁺ sites on pyrite

surface (see also XPS data in Figure S6.2) [327, 328]. Stoichiometrically, oxidation of S^{2-} by Fe^{3+} consumed more Fe^{3+} , which could result in an excess of S^{2-} surface species. Controlled experiments in absence of aqueous U(VI) confirmed the presence of aqueous S^{2-} for Type II Pb-pyrite, while aqueous S^{2-} was undetectable for Type I Pb-pyrite that had been acid washed (Table S6.4). Furthermore, the measured S^{2-} disappeared upon addition of aqueous U(VI) (Table S6.4). Perchloroethylene extraction and subsequent quantitative analysis by HPLC revealed that $\sim 0.85 \mu\text{M}$ of elemental sulfur was formed for Type II Pb-pyrite at pH ~ 4.5 (Table S6.4), which could account for the decrease of aqueous total S. Aqueous S^{2-} is reactive and its fast oxidation by e.g. aqueous Se(IV) in homogeneous system has been observed previously [329]. The participation of aqueous S^{2-} to U(VI) reduction could partially account for the faster reaction kinetics observed for Type II Pb-pyrite.

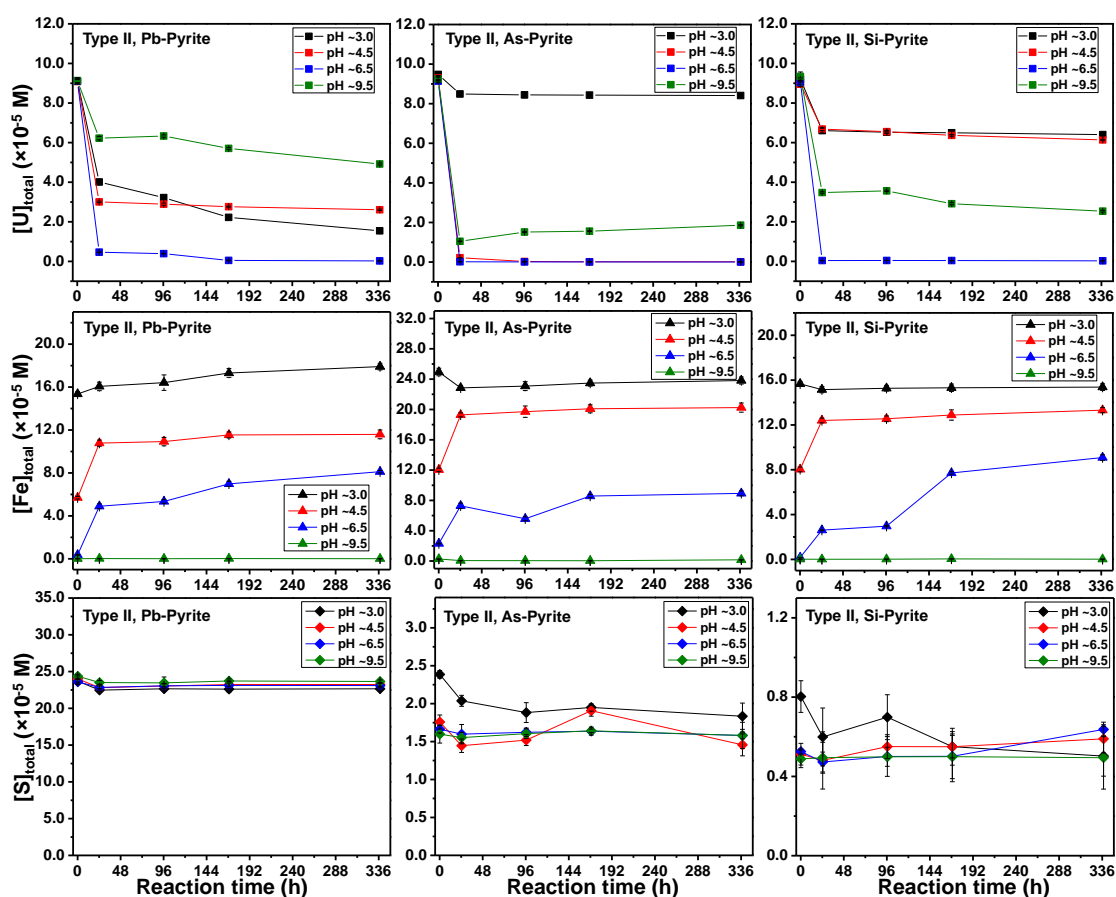


Figure 6.2. Concentration evolutions of total aqueous U, Fe and S for reactors of Type II pyrite.

For As-rich pyrite, aqueous U(VI) concentration at pH ~ 3.0 showed a small decrease within the first 24 hours and then remained constant. Conversely, aqueous U(VI) concentration decreased sharply to extremely low level in the first 24 hours when the reaction pH increased to ~ 4.5 and ~ 6.5 . Repeated experiments were performed and confirmed this sharp decrease of

aqueous U(VI) concentration at these pH levels (data not shown). Because the solubility of U(VI) is relatively high at pH ~4.5 and low at pH ~6.5 (Figure S6.3), it is most likely that the sharp decrease of U(VI) at pH ~4.5 was due to a reduction process, while spontaneous precipitation might mainly account for the U(VI) decrease at pH ~6.5. The controlled experiments indicated that a considerable amount of aqueous S^{2-} was present for Type II As-pyrite at pH ~4.5 (Table S6.4), which further supports the occurrence of U(VI) reduction. In accordance with the sharp decrease of U(VI), aqueous Fe concentration first increased and then remained almost constant at pH ~4.5 and ~6.5. At pH ~9.5, the concentration of U(VI) decreased sharply at the beginning of the experiment and then increased slightly throughout the reaction time. This might be also mainly explained by the spontaneous precipitation of U(VI) followed by a slight re-dissolution of the precipitate due to changes in solution pH. Given the presence of aqueous S^{2-} , we cannot exclude the possible occurrence of U(VI) reduction. The sharp decrease in aqueous Fe concentration from 1.775×10^{-4} M at $t = 0.2$ h to 5×10^{-7} M at $t = 24.5$ h could be attributed to the precipitation of Fe(III) oxyhydroxides due to the heterogeneous reduction of U(VI) [297, 298]. In contrast to Pb-pyrite, much lower level of aqueous S in As-pyrite-containing systems were found in all pH conditions investigated. This could be explained by a smaller increment of the specific surface area during grinding process, leading to a breaking of less Fe-S bonds. It is worth noting that $\sim 0.95 \mu\text{M } S^0$ was detected for the reaction at pH ~4.5 (Table S6.4). Therefore, the noticeable decrease of aqueous S in particular at pH ~3.0 could be explained by the formation of insoluble S^0 upon the oxidation of aqueous S^{2-} by U(VI). The generation of S^0 also has been observed for As-rich pyrite oxidation by aqueous Se(IV) in a previous work, and the results showed that the production of S^0 increased with decreasing pH [313].

Similar to Pb-pyrite, aqueous U(VI) decreased rapidly during the first 24 hours and then gradually decreased at pH ~3.0, ~4.5, and ~9.5 in presence of Type II Si-pyrite. These results are understandable because of the presence of aqueous S^{2-} in the early stage of the reaction. An apparent decrease in aqueous S total concentration in the first 24 hours further support this assumption. In contrast, for the reaction at pH ~6.5 aqueous U(VI) decreased to extremely low level in the first 24.5 hours, which could be mainly attributed to spontaneous precipitation of U(VI). Aqueous iron showed a similar evolution trend with that of As-pyrite, which could be explained similarly. Although Si-pyrite had the largest increment of surface area after grinding, the concentrations of aqueous S in presence of Si-pyrite were lower than that of Pb-pyrite and higher than that of As-pyrite. Presumably the presence of SiO_2 could

occupy some surface area, leading to less surface S^{2-} sites exposing to solution in comparison with Pb-pyrite.

6.3.4. XPS Surface features

XPS was used to characterize the speciation of uranium on pyrite surface. In line with the minor change of aqueous U(VI) concentration in solution, the surface uranium was too low to be detected on Type I Pb-pyrite samples at pH ~ 3.0 and ~ 4.5 , Type I As-pyrite samples at pH ~ 3.0 , ~ 4.5 and ~ 9.5 , and on Type I Si-pyrite samples at pH ~ 3.0 . Samples of Type I Si-pyrite at pH ~ 9.5 and Type II Si-pyrite at pH ~ 3.0 also showed weak XPS signal, thus they were not considered in the following discussion. The representative XPS spectra of U4f, Fe2p 3/2, and S2p for the samples of Type I Pb-pyrite and Type I As-pyrite at pH ~ 6.5 , and Type I Si-pyrite at pH ~ 4.5 are shown in Figure S1, and Type II Pb-pyrite at pH ~ 3.0 , Type II As-pyrite at pH ~ 4.5 , and Type II Si-pyrite at pH ~ 6.5 are shown in Figure 6.2. The XPS spectra for other samples are shown in Figure S6.5.

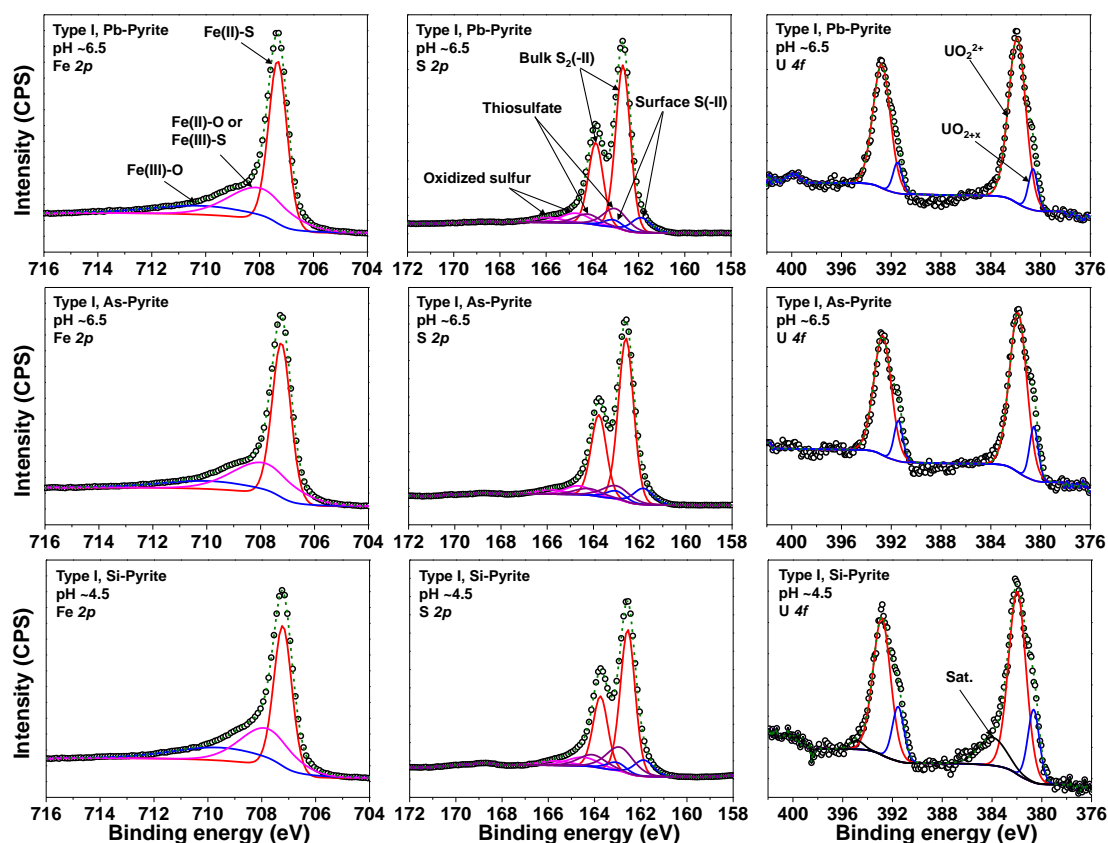


Figure 6.3. Fitted Fe(2p), S(2p) and U(4f) XPS spectra for U(VI)-reacted Type I pyrite.

The U4f spectra were fitted with a spin-orbit splitting of 10.89 eV, a fixed intensity ratio of 4:3 (4f 7/2:4f 5/2), and identical fwhm values (full width at half of maximum) for the doublet

peaks. With respect to Type I pyrite, the U $4f_{7/2}$ of Pb-pyrite sample at pH ~6.5 can be fitted with an intense peak at 381.9 eV and a very weak peak at 380.6 eV, corresponding to unreduced U(VI) and reduced U(IV), respectively. The sample of Pb-pyrite at pH ~9.5 can also be fitted with two contributors at 382.1 and 380.8 eV, respectively. The presence of two contributions indicated that U(VI) was partially reduced, resulting in a mixed valent oxide such as U_3O_8 . Nevertheless, the U(IV)/U(VI) ratios were much lower than 0.5 (Table 6.1), suggesting the simultaneous occurrence of spontaneous precipitation of U(VI). In addition to unreduced U(VI), the samples of As-pyrite at pH ~6.5 and Si-pyrite at pH ~4.5 and ~6.5 also showed peaks located at 380.5-380.8 eV, confirming the occurrence of U(VI) reduction. It is worth noting that the U(IV)/U(VI) ratio was higher at pH ~4.5 than that at pH ~6.5, which further confirmed the occurrence of U(VI) precipitation at higher pH.

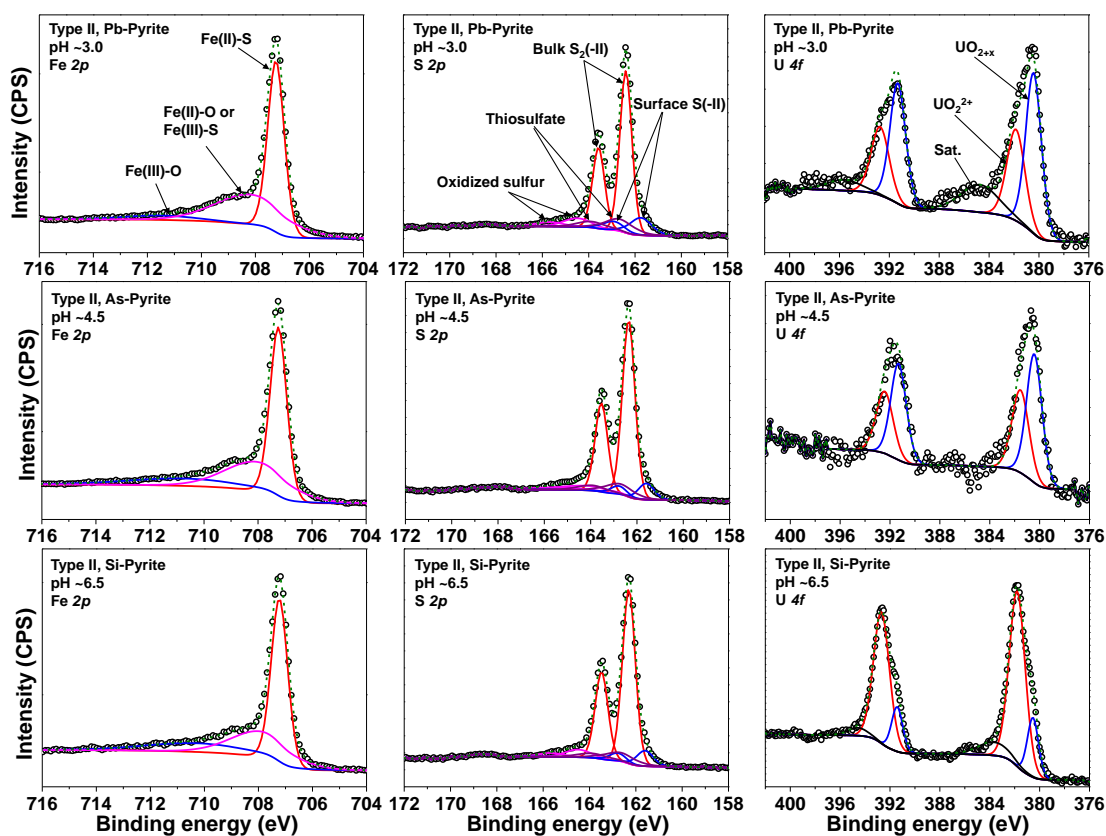


Figure 6.4. Fitted Fe(2p), S(2p) and U(4f) XPS spectra for U(VI)-reacted Type II pyrite.

The Fe2p spectra for U(VI)-reacted Type I pyrite can be fitted with three peaks located at 707.2 ± 0.1 , 707.9 ± 0.1 , and 709.7 ± 0.2 eV, corresponding to Fe(II)-S of pyrite, Fe(II)-O of hydrated Fe^{2+} [99, 330], and Fe(III)-S resulting from the breaking of Fe-S bonds at the pyrite surface [328, 331], respectively. Compared with the pristine pyrite, the Fe2p spectra of the U(VI)-reacted Type I pyrite were nearly identical. The S2p spectra were fitted with S2p 3/2

and S2p_{1/2} spin orbit doublets, with a fixed 2:1 intensity ratio and a 1.18 eV energy separation. In addition to the bulk S₂²⁻ dimers located at 162.6±0.1, the S2p spectra showed the presence of oxidized sulfur (e.g., sulfite, polysulfides or thiosulfate) and surface S²⁻ at 164.0±0.6 and 161.9 eV, respectively. These contributors were also observed for the pristine pyrite. After reaction with U(VI), the characteristic peak of SO₄²⁻ at 168-169 eV were not observed for all Type I pyrite.

Table 6.1. Summary of the fitted XPS data for U(VI)-reacted pyrite^a.

Pyrite	pH	Fe(III)-O	SO ₄ ²⁻	B.E.-UO ₂ ²⁺ (eV)	B.E.-UO _{2+x} (eV)	Area ratio- UO ₂ ²⁺ /UO _{2+x}
Type I Pb-	6.5	Y	N	381.88	380.60	7.59
Type I Pb-	9.5	Y	N	382.25	380.80	8.99
Type I As-	6.5	Y	N	381.80	380.53	5.85
Type I Si-	4.5	Y	N	381.96	380.65	3.76
Type I Si-	6.5	Y	N	381.86	380.65	2.67
Type II Pb-	3.0	Y	N	381.85	380.43	0.65
Type II Pb-	4.5	Y	N	381.86	380.42	1.67
Type II Pb-	6.5	Y	Y	381.85	380.43	1.90
Type II Pb-	9.5	Y	Y	382.03	380.44	4.35
Type II As-	3.0	Y	N	382.05	380.45	0.52
Type II As-	4.5	Y	N	381.54	380.42	0.70
Type II As-	6.5	Y	Y	382.23	380.47	1.79
Type II As-	9.5	Y	Y	382.13	380.45	8.96
Type II Si-	4.5	Y	N	382.32	380.55	0.43
Type II Si-	6.5	Y	N	381.71	380.44	5.03
Type II Si-	9.5	Y	N	381.79	380.53	4.21

^a Y indicates an observed signal, while N suggests no visible signal.

For Type II pyrite, in accordance with the significant decrease in aqueous U(VI) in solution, Pb-pyrite showed intense signal of surface uranium. The reduced U(IV) peak increased remarkably compared to Type I pyrite, with U(IV)/U(VI) ratios of 1.54, 0.55, 0.53, and 0.23 at pH ~3.0, ~4.5, ~6.5, and ~9.5, respectively. The increase in U(IV)/U(VI) ratio with decreasing pH suggested the formation of a more reduced uranium oxide at lower pH or the

simultaneous occurrence of U(VI) precipitation at higher pH. An apparent U(VI) reduction was also observed for As-pyrite at all investigated pH values. Similar to Pb-pyrite, the U(IV)/U(VI) ratios decreased with increasing pH, with ratio values of 1.94, 1.43, 0.56, and 0.11 at pH ~3.0, ~4.5, ~6.5, and ~9.5, respectively. The U(VI) reduction was observed for Si-pyrite at pH ~4.5, ~6.5, and ~9.5. Because of the low content of surface uranium, it is hard to determine the occurrence of U(VI) reduction at pH ~3.0 on Si-pyrite. Previous studies have demonstrated that the pH_{pzc} (point of zero charge) of pyrite and SiO_2 was around pH 2.0 [332] and 2.9 [333], respectively. Since UO_2^{2+} is the predominant species at pH ~ 3.0 [98], it is likely that electrostatic repulsion could prevent or slow down the U(VI) reduction at this pH condition.

After reaction with U(VI), no apparent differences were observed for the Fe2p and S2p spectra of Type II Pb-pyrite at pH ~3.0. However, at higher pH values, such as ~4.5, a weak peak at ~168.5 eV that is characteristic of SO_4^{2-} could be inferred, and it became clear when pH further increased to ~6.5 and ~9.5. Simultaneously, the Fe2p spectra showed an apparent increase in amplitude at ~710.2 eV, indicating the occurrence of Fe(III)-O compounds. Therefore, the precipitation of Fe(III) oxyhydroxide can account for the SO_4^{2-} detected at these pH conditions, since it has good affiliation toward many anions including SO_4^{2-} [334]. The formation of Fe(III) oxyhydroxide and the occurrence of sulfate were also observed for Type II As-pyrite at pH ~4.5, ~6.5, and ~9.5, but this was not clear for Si-pyrite. This might be explained by the formation of less Fe(III) oxyhydroxide and SO_4^{2-} in the Si-pyrite reaction systems, as confirmed by the solution data (Figures. 6.1 and 6.2) and XPS results (Figure S6.5).

6.3.5. XAS Characterization on uranium speciation

The XANES spectra of U(VI)-reacted Type I and Type II Pb-pyrite, and the reference XANES spectra for UO_2CO_3 , $UO_3 \cdot 2H_2O$, U_3O_8 , and U_4O_9 are shown in Figure 6.5. The results of LCF analysis of these spectra indicated that the combination of UO_2 and $UO_3 \cdot 2H_2O$ references gave good matches to the experimental spectra of samples from pH ~3.0 to ~9.5. Nevertheless, PHREEQC calculations using the NEA/OECD (2003) thermodynamic data base indicated that the solubility of schoepite is higher than 0.1 mM at $pH < 4.6$. The initial U(VI) loadings in the experiments were identical at 0.1 mM, indicating no schoepite precipitate occurred below pH 4.6 in our case. This suggested that the formed UO_{2+x} product has characteristics of both UO_2 and $UO_3 \cdot 2H_2O$. The presence of minor

$\text{UO}_2(\text{NO}_3)_2$ on Type I pyrite at pH ~6.5 and Type II pyrite at pH ~9.5 remains uncertain, since the error on the relative compositions, as calculated by the LCF procedure, is around 10–15% [313]. In line with XPS data, the linear combination fit shows that Type II pyrite at pH ~3.0 had the highest ratio of UO_2 , suggesting the formation a more reduced form at lower pH. In a word, the XANES results confirmed the occurrence of U(VI) reduction on Type I Pb-pyrite at pH ~6.5 and ~9.5, and Type II Pb-pyrite on the ~3.0 to ~9.5 pH range.

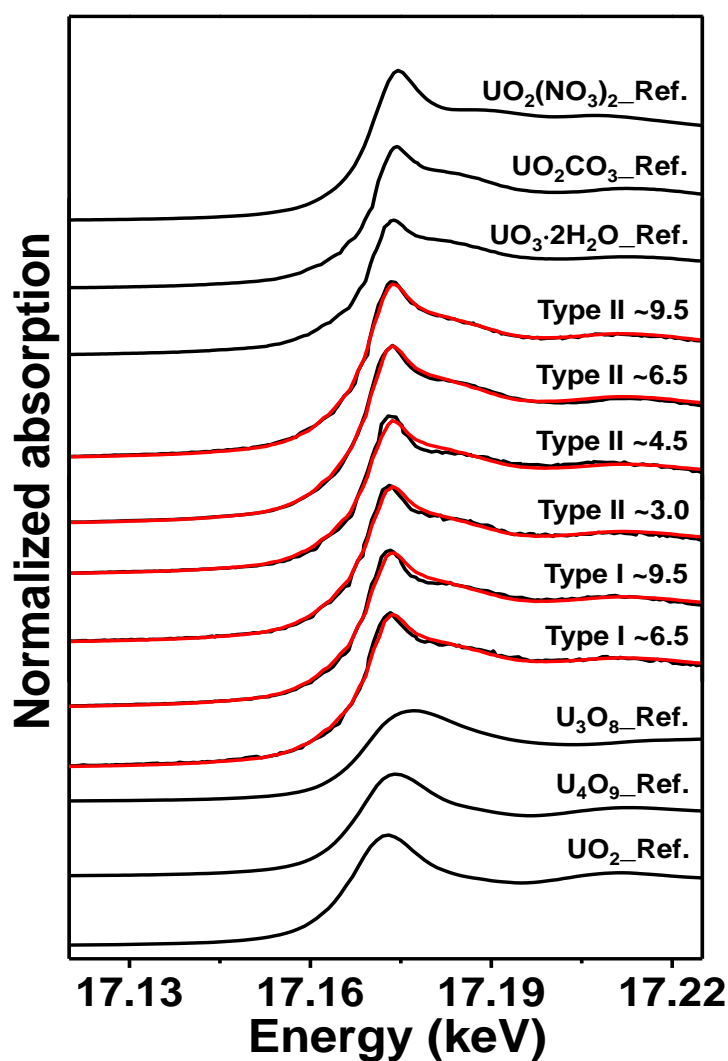


Figure 6.5. Normalized U L_3 -edge XANES spectra and the LCF results of U(VI)-reacted Pb-pyrite samples.

Table 6.2. LCF results of U L₃-edge XANES for identifying and quantifying uranium species (molar fraction) of U(VI)-reacted Pb-pyrite samples. Effects of pH and Fe(II) addition were investigated. Also reported is the concentration sum (Σ), which is not constrained to 100% for samples, and the value of the reduced χ square (χ_v^2), both indicating good matches to the experimental spectra. The error on the concentrations is estimated to be around 10–15%. Uncertainties are given by the number in brackets on the last digit(s), i.e., 14.4(1.5) represents 14.4±1.5.

ID	UO ₂ (%)	UO ₃ ·2H ₂ O (%)	UO ₂ CO ₃ (%)	UO ₂ (NO ₃) ₂ (%)	Σ (%)	χ_v^2 × 10 ⁻³
Type I ~6.5	14.4(1.5)	81.0(6.6)	-	3.5(5.9)	98.9	0.8
Type I ~9.5	19.2(1.7)	80.4(1.9)	-	-	99.6	1.0
Type II ~3.0	21.0(1.6)	79.1(6.7)	-	-	100.1	0.7
Type II ~4.5	14.8(1.9)	84.8(2.1)	-	-	99.6	1.2
Type II ~6.5	17.6(1.1)	84.5(1.2)	-	-	102.1	0.3
Type II ~9.5	14.1(1.2)	73.9(6.9)	4.0(7.8)	7.6(4.4)	99.6	0.2

6.3.6. SEM surface morphology

Following XPS and XAS analyses, SEM/EDX was used to image the surfaces of U(VI)-reacted pyrite and to determine the reactive sites where surface precipitates do occur. Representative SEM images for Type II Pb-, As-, and Si-pyrite after reaction with U(VI) are shown in Figure 6.6. The bright spots represent the enrichment of heavy metals. In addition to the main elements of Fe and S, the EDX spectra indicated the presence of U along with Pb for both Pb-pyrite and Si-pyrite, and with As for As-pyrite. Spots explorations on dark areas only showed the elements of Fe and S (Figure 6.6 A and B). These results indicate that U(VI) reduction mainly occurred at Pb- or As-enriched pyrite surface spots.

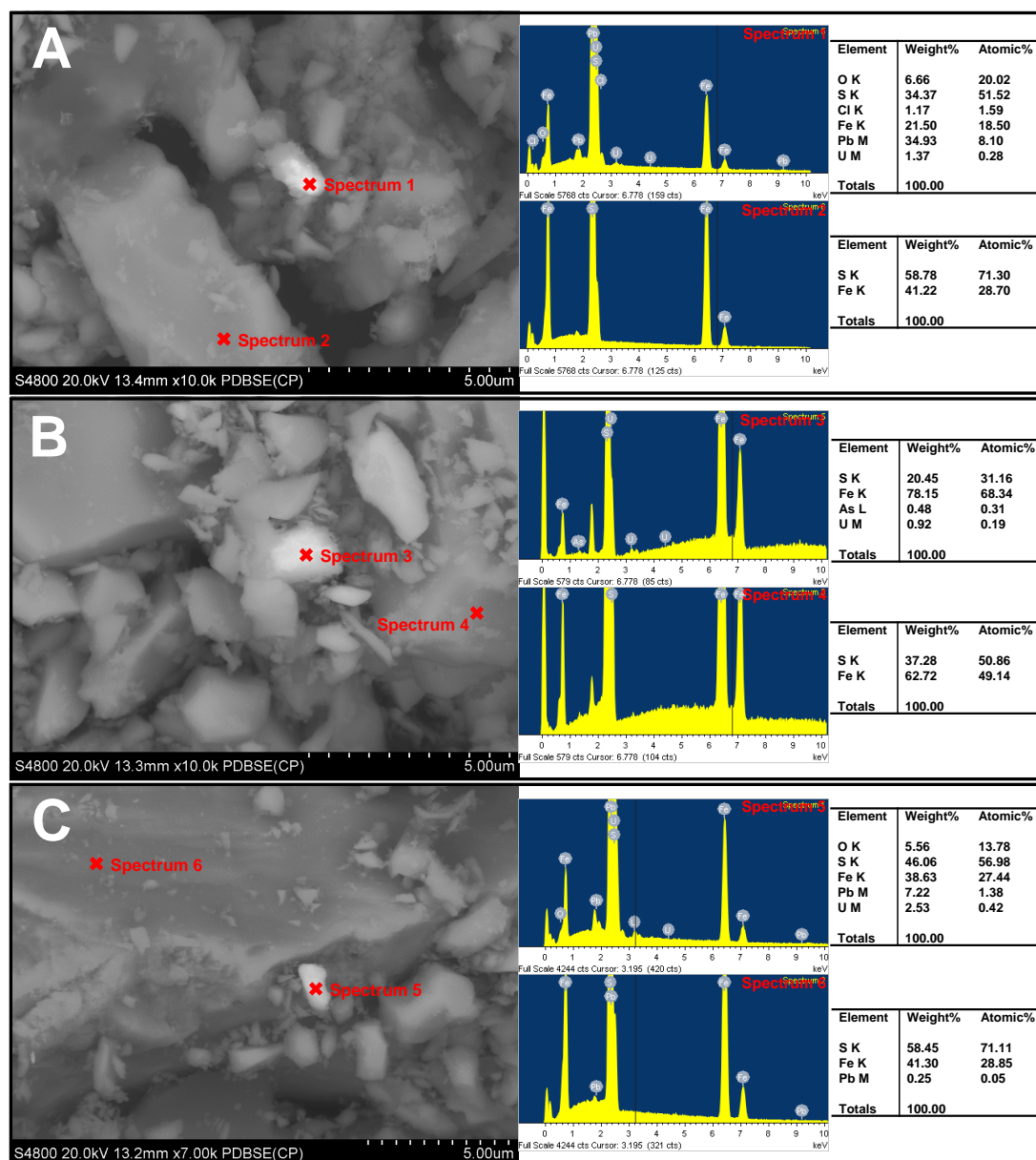


Figure 6.6. SEM images of (A) U(VI)-reacted Type II Pb-pyrite at pH ~6.5, (B) U(VI)-reacted Type II As-pyrite at pH ~3.0, and (C) U(VI)-reacted Type II Si-pyrite at pH ~6.5. The corresponding EDS spectra and elemental contents of selected spots are shown on the right of each SEM image.

6.3.7. Influencing factors on pyrite reactivity.

Both the results obtained of aqueous phase and on XPS data indicated that Type II pyrite (with unwashed surface) were much more reactive than Type I pyrite (with pre-washed surface) toward aqueous U(VI), i.e., the reactivity of pyrite was largely reduced by the surface acid wash. The occurrence of aqueous S^{2-} for Type II Pb- and As-pyrite and its disappearance following the formation of insoluble S^0 upon the addition of aqueous U(VI) demonstrate that surface S^{2-} generated by breaking Fe-S bond breaking during grinding could partially account

for the high Type II pyrite reactivity towards U(VI) reduction. However, reactive S^{2-} sites present on pyrite surface appear to be washed away by acid solution, leading to an absence of aqueous S^{2-} in Type I pyrite suspension and a nearly inert surface toward aqueous U(VI).

In addition, the SEM/EDX analysis further demonstrated that the Pb- and As-impurity-rich area on pyrite surface were the reactive sites for U(VI) reduction. Because XPS surface analyses showed that there was no apparent speciation difference between Type I and Type II pyrite, it is likely that the grinding process could expose more impurities-rich sites that could also partially account for the observed U(VI) reduction. Nevertheless, these impurities could be removed by several acid wash cycles, in particular for arsenic since it has the similar environment of arsenopyrite [335]. Unlike As impurity, pyrite lattice does not readily accommodate Pb at high concentration and the Pb content of pyrite was attributed to the presence of small scale inclusion of Pb-bearing mineral like galena [322]. Reduction of aqueous U(VI) by both galena and pyrite has been confirmed by Wersin et al (1994) [321]. When a 50 : 50 (w : w) mixture of pyrite and galena was used for reaction with U(VI), Aubriet et al. (2006) further demonstrated that galena was first oxidized and covered by PbO before U(VI) reduction by pyrite to occur [336]. This evidently supported that Pb-rich area on pyrite surface were the reactive sites for U(VI) reduction. Furthermore, preferential release of As impurity via arsenopyrite oxidation has previously been observed for As-rich pyrite oxidation by aqueous Se(IV) [313]. Therefore, we cannot exclude the possibility that the observed U(VI) reduction by Type II Pb- and As-pyrite occurred prevalently by reaction with galena and arsenopyrite, respectively.

6.4. Conclusions

The factors influencing the reactivity of pyrite toward aqueous U(VI) have been investigated. The results indicate that minor pyrite impurities such as As, Pb and Si play a significant role in the reactivity of the mineral, and the reduction of U(VI) mainly occurred at the Pb- and As-rich spots on pyrite surface. In addition, reactive S^{2-} can be generated on pyrite surface due to the breaking of Fe-S bonds during grinding process, which also can account for the reduction of aqueous U(VI). This study open new avenue in our understanding of the role of pyrite in governing the mobility of toxic uranium in the environment.

Supporting information

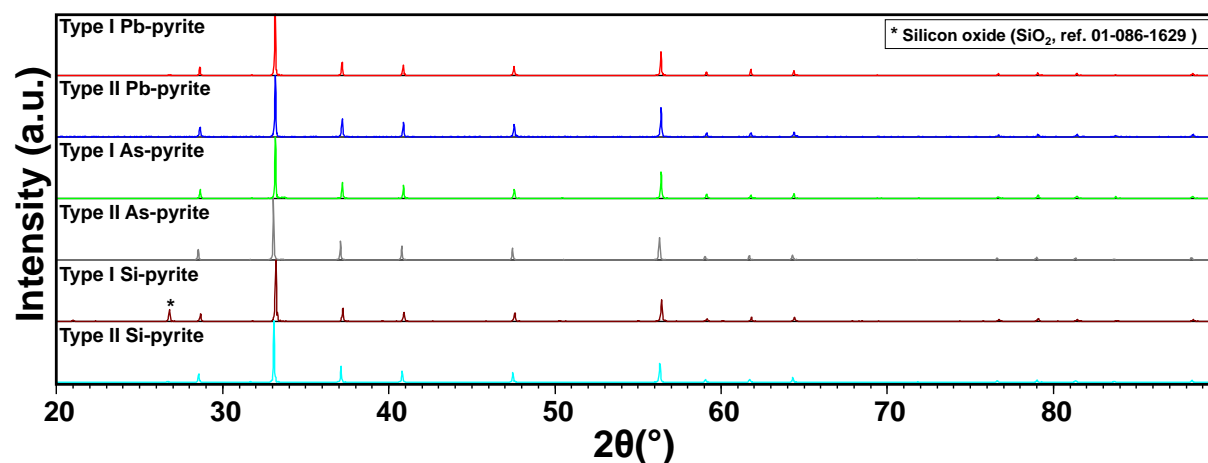


Figure S6.1. X-ray diffraction patterns of different types of pyrite. Diffraction peaks without marks belong to the pyrite signal and visible diffraction peak of SiO_2 is marked with the star symbol. Cu $K\alpha$ radiation at 1.5406 \AA is used.

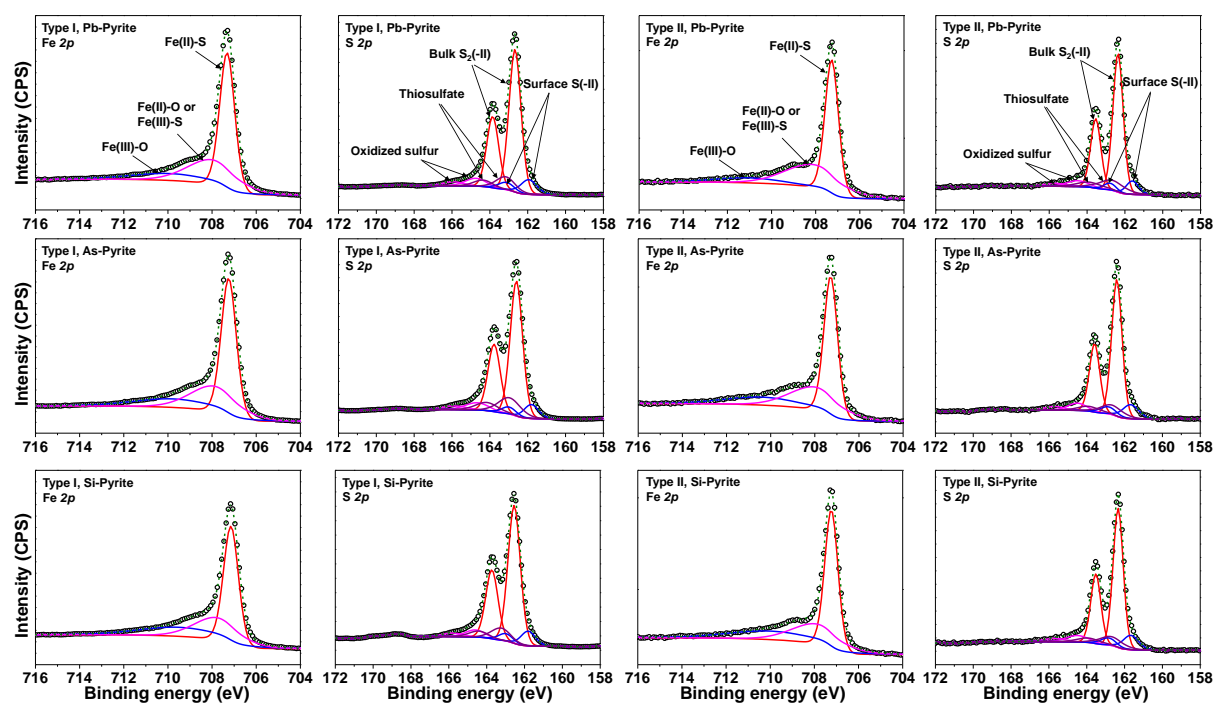


Figure S6.2. Fitted $\text{Fe}(2p)$ and $\text{S}(2p)$ XPS spectra for pristine pyrites.

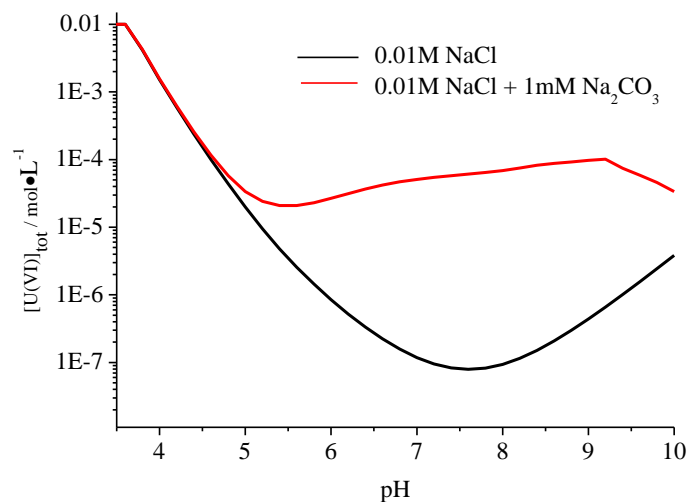


Figure S6.3. The solubility of schoepite as a function of pH in the presence of 0.01 M NaCl (black line) and 0.01 M NaCl + 1 mM Na₂CO₃ (red line). Calculations were performed by PHREEQC using the thermodynamic data for U from OECD/NEA (2003).

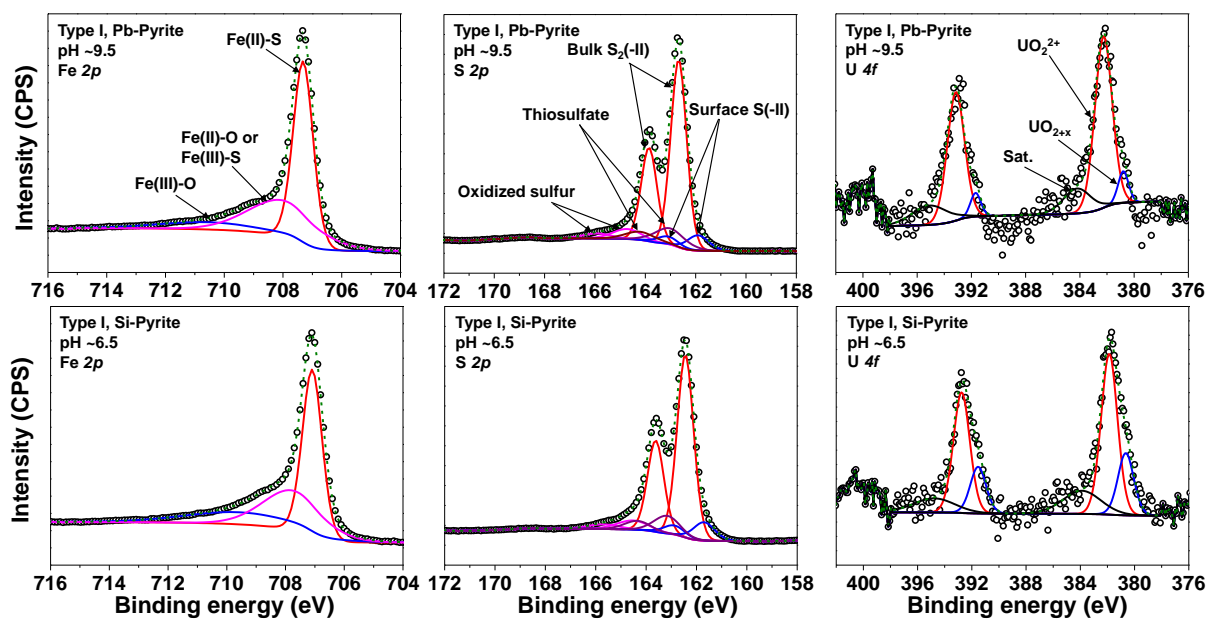


Figure S6.4. Fitted Fe(2*p*), S(2*p*) and U(4*f*) XPS spectra for reacted Type I pyrites.

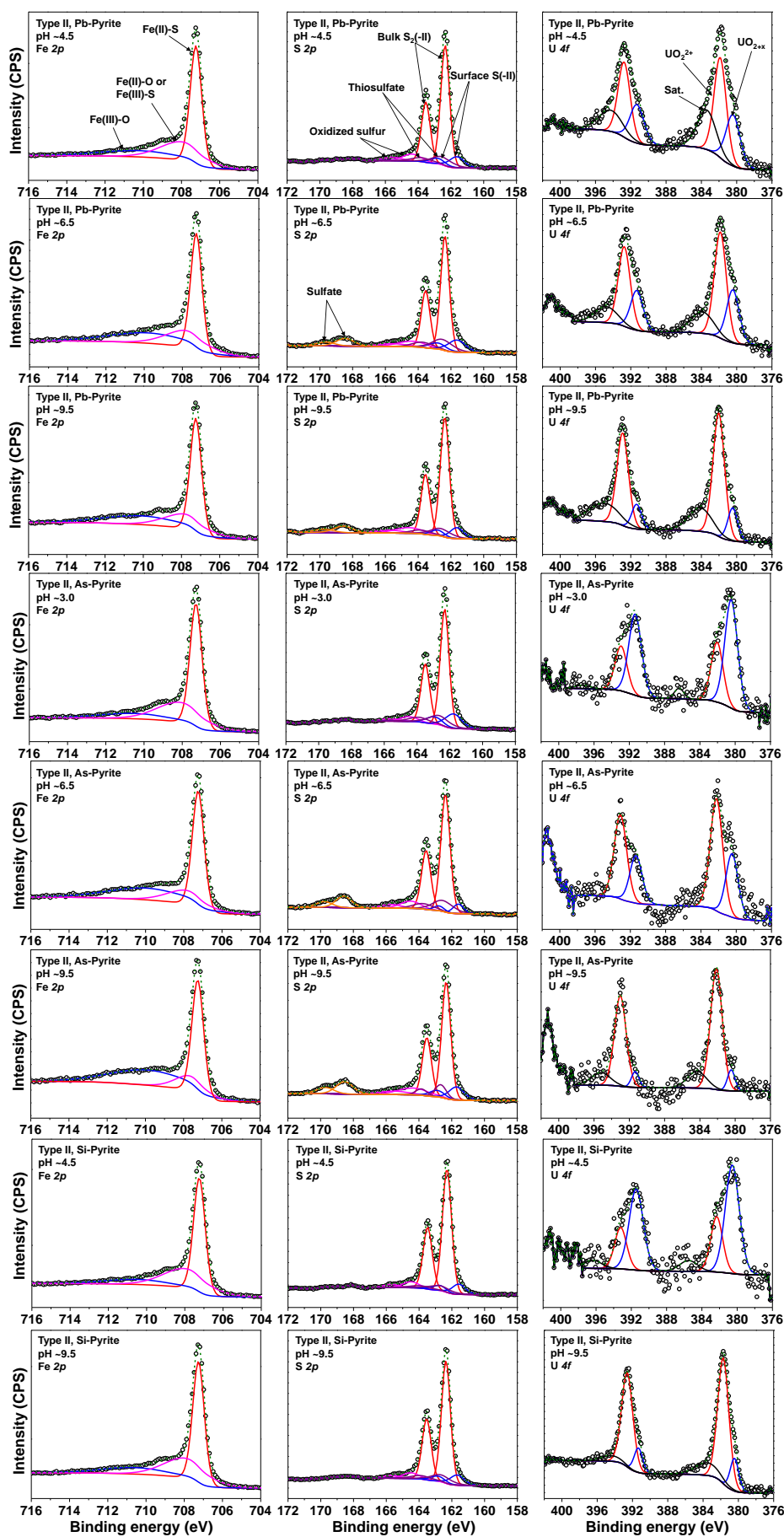


Figure S6.5. Fitted Fe(2p), S(2p) and U(4f) XPS spectra for reacted Type II pyrites.

Table S6.1. The specific surface area (SSA) of each ground pyrite powder

Pyrite type	SSA / m ² g ⁻¹
Pb-pyrite	0.8
As-pyrite	0.6
Si-pyrite	0.9

Table S6.2. Aqueous results of reactors with Type I pyrite. Uncertainties are given by the number in brackets on the last digit(s). Results with reaction time of 0 h in each reactor are from the sample taken after ~ 2 days pyrite equilibrium and just before the addition of U(VI). [U]_{tot} with 0.20 h reaction time can be considered as the initial [U(VI)] loading, approximately.

Pyrite	Time / h	pH	[U] _{tot} /mM	[Fe] _{tot} /mM	[S] _{tot} /mM	[As] _{tot} /mM
Type I Pb-pyrite	0.00	3.185	-	0.0004(1)	0.0078(4)	0.0018(0)
	0.20	3.060	0.0932(2)	0.0004(1)	0.0066(3)	0.0010(0)
	24.50	3.079	0.0860(1)	0.0031(1)	0.0090(8)	0.0009(0)
	72.00	3.076	0.0858(5)	0.0078(2)	0.0108(5)	0.0008(1)
	168.50	3.083	0.0854(2)	0.0166(2)	0.0123(3)	0.0009(1)
	337.00	3.074	0.0841(4)	0.0320(3)	0.0170(5)	0.0008(0)
Type I Pb-pyrite	0.00	4.608	-	0.0001(1)	0.0044(8)	0.0008(1)
	0.20	4.568	0.0928(1)	0.0001(1)	0.0046(3)	0.0007(1)
	24.50	4.545	0.0825(5)	0.0001(1)	0.0071(4)	0.0007(1)
	72.00	4.577	0.0824(4)	0.0001(1)	0.0071(3)	0.0007(1)
	168.50	4.520	0.0811(4)	0.0075(2)	0.0076(4)	0.0007(0)
	337.00	4.676	0.0817(1)	0.0173(4)	0.0085(2)	0.0007(1)
Type I Pb-pyrite	0.00	7.867	-	0.0001(1)	0.0075(5)	0.0010(1)
	0.20	6.445	0.0925(5)	0.0001(1)	0.0067(7)	0.0008(1)
	24.50	6.313	0.0371(1)	0.0001(1)	0.0093(8)	0.0007(1)
	72.00	6.069	0.0088(1)	0.0001(1)	0.0150(6)	0.0007(1)
	168.50	6.018	0.0021(1)	0.0006(1)	0.0170(7)	0.0008(1)
	337.00	6.580	0.0005(1)	0.0045(1)	0.0211(5)	0.0008(0)
Type I Pb-pyrite	0.00	9.281	-	0.0001(1)	0.0195(4)	0.0008(1)
	0.20	9.455	0.0930(2)	0.0001(1)	0.0172(5)	0.0007(1)

	24.50	9.324	0.0817(2)	0.0001(1)	0.0254(1)	0.0006(0)
	72.00	9.313	0.0803(1)	0.0001(1)	0.0271(2)	0.0007(1)
	168.50	9.355	0.0764(1)	0.0001(1)	0.0286(6)	0.0006(2)
	337.00	9.393	0.0535(3)	0.0001(1)	0.0318(4)	0.0007(1)
	0.00	3.346	-	0.0504(10)	0.0052(4)	0.0007(0)
	0.20	3.067	0.0938(5)	0.0499(8)	0.0055(1)	0.0006(1)
Type I As-pyrite	24.50	3.007	0.0870(2)	0.0553(3)	0.0047(6)	0.0007(1)
	72.00	2.983	0.0865(1)	0.0665(2)	0.0059(4)	0.0006(1)
	168.50	3.012	0.0867(1)	0.0751(3)	0.0055(4)	0.0006(1)
	337.00	3.014	0.0868(1)	0.0817(7)	0.0064(9)	0.0006(1)
	0.00	4.868	-	0.0121(1)	0.0043(3)	0.0018(1)
	0.20	4.492	0.0925(3)	0.0136(2)	0.0039(2)	0.0013(0)
Type I As-pyrite	24.50	4.623	0.0828(3)	0.0270(2)	0.0046(6)	0.0013(1)
	72.00	4.643	0.0821(1)	0.0361(7)	0.0053(7)	0.0012(1)
	168.50	4.409	0.0820(3)	0.0417(4)	0.0054(2)	0.0011(1)
	337.00	4.495	0.0829(1)	0.0500(8)	0.0052(4)	0.0011(0)
	0.00	7.404	0.0000(5)	0.0001(1)	0.0081(2)	0.0011(1)
	0.20	6.442	0.0907(1)	0.0001(1)	0.0060(2)	0.0011(1)
Type I As-pyrite	24.50	6.320	0.0465(1)	0.0011(1)	0.0085(3)	0.0011(1)
	72.00	6.262	0.0098(1)	0.0089(3)	0.0096(5)	0.0012(0)
	168.50	6.221	0.0018(1)	0.0128(2)	0.0115(3)	0.0012(1)
	337.00	6.626	0.0010(1)	0.0151(2)	0.0144(5)	0.0015(0)
	0.00	9.297	-	0.0001(1)	0.0150(0)	0.0011(0)
	0.20	9.524	0.0922(7)	0.0001(1)	0.0085(3)	0.0011(1)
Type I As-pyrite	24.50	9.487	0.0806(3)	0.0001(1)	0.0147(5)	0.0011(1)
	72.00	9.432	0.0770(2)	0.0001(1)	0.0200(6)	0.0013(1)
	168.50	9.352	0.0718(3)	0.0001(1)	0.0270(3)	0.0020(1)
	337.00	9.287	0.0724(4)	0.0001(1)	0.0311(5)	0.0017(1)
	0.00	3.304	-	0.0148(1)	0.0074(4)	0.0006(1)
	0.20	3.044	0.0915(2)	0.0145(2)	0.0077(5)	0.0005(1)
Type I Si-pyrite	24.50	3.097	0.0853(2)	0.0162(2)	0.0074(4)	0.0006(1)
	72.00	3.104	0.0851(2)	0.0352(5)	0.0088(4)	0.0005(1)
	168.50	3.144	0.0840(2)	0.0623(14)	0.0089(2)	0.0005(1)
	337.00	3.248	0.0822(1)	0.1052(4)	0.0109(5)	0.0004(1)
Type I	0.00	4.722	-	0.0039(1)	0.0129(2)	0.0008(1)

Si-pyrite	0.20	4.427	0.0917(1)	0.0040(2)	0.0126(5)	0.0006(1)
	24.50	4.410	0.0824(1)	0.0100(2)	0.0146(4)	0.0006(1)
	72.00	4.493	0.0808(5)	0.0173(3)	0.0156(4)	0.0007(0)
	168.50	4.539	0.0773(1)	0.0321(2)	0.0165(7)	0.0006(1)
	337.00	4.885	0.0701(3)	0.0427(7)	0.0182(8)	0.0005(0)
Type I Si-pyrite	0.00	7.179	-	0.0001(1)	0.0174(3)	0.0022(1)
	0.20	6.438	0.0917(3)	0.0001(1)	0.0155(6)	0.0012(1)
	24.50	6.210	0.0263(2)	0.0001(1)	0.0239(6)	0.0011(1)
	72.00	6.314	0.0011(1)	0.0001(1)	0.0288(2)	0.0010(0)
	168.50	6.207	0.0004(1)	0.0001(1)	0.0320(8)	0.0011(1)
	337.00	6.936	0.0002(1)	0.0024(1)	0.0324(5)	0.0012(0)
Type I Si-pyrite	0.00	9.245	-	0.0001(1)	0.0293(3)	0.0008(1)
	0.20	9.532	0.0912(3)	0.0001(1)	0.0200(2)	0.0008(1)
	24.50	9.448	0.0807(5)	0.0001(1)	0.0315(2)	0.0009(1)
	72.00	9.348	0.0751(1)	0.0001(1)	0.0272(2)	0.0007(1)
	168.50	9.357	0.0688(2)	0.0001(1)	0.0297(2)	0.0008(0)
	337.00	9.383	0.0636(3)	0.0001(1)	0.0310(9)	0.0009(0)

Table S6.3. Aqueous results of reactors with Type II pyrite. Uncertainties are given by the number in brackets on the last digit(s). Results with reaction time of 0 h in each reactor are from the sample taken after ~ 2 days pyrite equilibrium and just before the addition of U(VI). $[U]_{\text{tot}}$ with 0.20 h reaction time can be considered as the initial $[U(VI)]$ loading, approximately.

Pyrite	Reaction time / h	pH	$[U]_{\text{tot}}$ /mM	$[Fe]_{\text{tot}}$ /mM	$[S]_{\text{tot}}$ /mM	$[As]_{\text{tot}}$ /mM
Type II Pb-pyrite	0.00	3.185	-	0.1536(22)	0.2370(26)	0.0011(2)
	0.20	2.989	0.0913(10)	0.1566(59)	0.2292(34)	0.0007(1)
	24.50	2.949	0.0401(1)	0.1606(40)	0.2247(21)	0.0006(1)
	96.50	2.997	0.0322(3)	0.1641(72)	0.2265(32)	0.0005(1)
	169.00	2.985	0.0223(4)	0.1731(41)	0.2261(40)	0.0005(1)
	337.50	3.021	0.0155(1)	0.1791(31)	0.2266(28)	0.0003(0)
Type II Pb-pyrite	0.00	4.432	-	0.0570(13)	0.2400(40)	0.0003(2)
	0.20	4.413	0.0909(13)	0.0846(36)	0.2336(39)	0.0003(1)
	24.50	4.345	0.0301(4)	0.1078(29)	0.2281(47)	0.0003(2)
	96.50	4.481	0.0289(5)	0.1092(39)	0.2304(29)	0.0003(0)

	169.00	4.517	0.0277(2)	0.1154(28)	0.2323(48)	0.0003(1)
	337.50	4.495	0.0261(3)	0.1159(41)	0.2324(25)	0.0002(2)
Type II Pb-pyrite	0.00	6.213	-	0.0037(1)	0.2360(34)	0.0002(2)
	0.20	6.568	0.0910(9)	0.0732(31)	0.2347(43)	0.0002(0)
	24.50	6.588	0.0047(1)	0.0490(22)	0.2284(21)	0.0002(1)
	96.50	6.527	0.0039(1)	0.0535(16)	0.2306(30)	0.0002(1)
	169.00	6.055	0.0005(2)	0.0699(23)	0.2312(50)	0.0003(2)
	337.50	6.367	0.0003(0)	0.0812(11)	0.2310(31)	0.0003(3)
Type II Pb-pyrite	0.00	9.428	-	0.0001(0)	0.2436(27)	0.0002(1)
	0.20	9.421	0.0913(16)	0.0808(28)	0.2386(50)	0.0001(1)
	24.50	9.211	0.0622(8)	0.0003(0)	0.2350(27)	0.0001(1)
	96.50	9.235	0.0633(5)	0.0002(0)	0.2346(81)	0.0001(1)
	169.00	9.199	0.0571(4)	0.0003(0)	0.2372(28)	0.0001(1)
	337.50	9.214	0.0492(5)	0.0002(0)	0.2366(22)	0.0002(1)
Type II As-pyrite	0.00	3.047	-	0.2494(50)	0.0239(5)	0.0002(2)
	0.20	2.951	0.0948(13)	0.2502(89)	0.0225(9)	0.0000(1)
	24.50	2.912	0.0849(4)	0.2285(33)	0.0204(7)	0.0001(0)
	96.50	2.922	0.0845(14)	0.2308(59)	0.0188(13)	0.0001(1)
	169.00	2.945	0.0843(4)	0.2348(40)	0.0195(5)	0.0001(2)
	337.50	2.996	0.0841(7)	0.2382(47)	0.0183(17)	0.0001(1)
Type II As-pyrite	0.00	4.524	-	0.1205(21)	0.0176(9)	0.0001(0)
	0.20	4.587	0.0930(13)	0.1872(36)	0.0221(18)	0.0002(2)
	24.50	4.511	0.0022(1)	0.1929(26)	0.0145(9)	0.0005(2)
	96.50	4.593	0.0003(1)	0.1971(75)	0.0152(7)	0.0008(1)
	169.00	4.432	0.0002(0)	0.2009(53)	0.0191(7)	0.0009(2)
	337.50	4.508	0.0002(1)	0.2025(60)	0.0146(14)	0.0008(2)
Type II As-pyrite	0.00	6.189	-	0.0231(4)	0.0166(5)	0.0010(1)
	0.20	6.343	0.0914(9)	0.1748(24)	0.0218(2)	0.0007(2)
	24.50	6.278	0.0002(0)	0.0728(35)	0.0160(13)	0.0008(3)
	96.50	6.288	0.0001(1)	0.0557(25)	0.0162(6)	0.0008(1)
	169.00	6.413	0.0001(0)	0.0858(21)	0.0164(5)	0.0012(0)
	337.50	6.496	0.0001(0)	0.0893(32)	0.0158(4)	0.0010(1)
Type II As-pyrite	0.00	9.211	-	0.0027(0)	0.0160(12)	0.0004(2)
	0.20	9.552	0.0925(10)	0.1775(47)	0.0207(14)	0.0003(2)
	24.50	9.537	0.0105(2)	0.0005(0)	0.0155(7)	0.0005(1)

	96.50	9.548	0.0152(2)	0.0005(0)	0.0160(6)	0.0007(1)
	169.00	9.472	0.0156(2)	0.0004(0)	0.0164(2)	0.0009(1)
	337.50	9.495	0.0186(3)	0.0016(0)	0.0158(17)	0.0012(0)
	0.00	3.113	-	0.1567(22)	0.0080(8)	0.0001(1)
	0.20	2.914	0.0921(6)	0.1581(32)	0.0095(19)	0.0001(1)
Type II Si-pyrite	24.50	2.918	0.0661(12)	0.1515(28)	0.0060(15)	0.0002(1)
	96.50	2.920	0.0653(5)	0.1527(25)	0.0070(11)	0.0002(1)
	169.00	2.972	0.0650(9)	0.1532(33)	0.0055(6)	0.0002(1)
	337.50	2.987	0.0640(7)	0.1538(30)	0.0050(10)	0.0002(1)
	0.00	4.567	-	0.0803(21)	0.0051(5)	0.0002(1)
	0.20	4.485	0.0895(11)	0.1166(25)	0.0070(8)	0.0002(1)
Type II Si-pyrite	24.50	4.572	0.0668(8)	0.1240(21)	0.0048(14)	0.0001(1)
	96.50	4.419	0.0656(7)	0.1255(26)	0.0055(6)	0.0002(1)
	169.00	4.445	0.0637(4)	0.1288(46)	0.0055(9)	0.0002(1)
	337.50	4.532	0.0614(3)	0.1332(23)	0.0059(7)	0.0001(0)
	0.00	6.458	-	0.0017(0)	0.0053(1)	0.0001(1)
	0.20	6.322	0.0904(9)	0.1043(18)	0.0077(11)	0.0001(1)
Type II Si-pyrite	24.50	6.408	0.0004(0)	0.0261(4)	0.0047(5)	0.0002(1)
	96.50	6.596	0.0005(0)	0.0297(5)	0.0050(10)	0.0001(2)
	169.00	6.405	0.0004(1)	0.0771(10)	0.0050(11)	0.0002(1)
	337.50	6.487	0.0003(1)	0.0909(24)	0.0064(4)	0.0002(2)
	0.00	9.539	-	0.0002(0)	0.0049(4)	0.0001(1)
	0.20	9.557	0.0934(23)	0.1000(31)	0.0077(12)	0.0001(0)
Type II Si-pyrite	24.50	9.512	0.0348(4)	0.0001(0)	0.0049(8)	0.0001(1)
	96.50	9.497	0.0356(3)	0.0002(0)	0.0050(5)	0.0002(1)
	169.00	9.445	0.0291(5)	0.0004(0)	0.0050(13)	0.0001(1)
	337.50	9.380	0.0254(4)	0.0002(0)	0.0049(16)	0.0002(3)

Table S6.4. Determination of sulfide species concentration in reactors at pH ~4.5. MBS represents methylene-blue-detectable sulfur, including total S(-II) species (e.g., S²⁻, S_n²⁻, and H₂S). Uncertainties are given by the number in brackets on the last digit(s), while uncertainties for [S⁰] are not given due to the unquantifiable extraction efficiency. Results with reaction time of 0 h in each reactor are from the sample taken after ~ 2 days pyrite equilibrium and just before the addition of U(VI). [U]_{tot} with 0.20 h reaction time can be considered as the initial [U(VI)] loading, approximately.

Pyrite	Time / h	pH	[U] _{tot} /mM	[Fe] _{tot} /mM	[S] _{tot} /mM	[MBS] /mM	[S ⁰] / μM
Type I Pb-pyrite	0.00	4.438	-	0.0005(1)	0.0046(3)	0.0001(1)	0 ^b
	0.20	4.494	0.0816(2)	0.0007(2)	0.0040(5)	nd ^a	nd ^a
	71.50	4.486	0.0746(3)	0.0016(2)	0.0082(6)	0.0001(1)	0 ^b
Type I As-pyrite	0.00	4.478	-	0.0215(4)	0.0043(2)	0.0003(1)	0 ^b
	0.20	4.507	0.0833(1)	0.0239(3)	0.0051(2)	nd	nd ^a
	71.50	4.522	0.0741(1)	0.0394(4)	0.0114(3)	0.0002(5)	0.2128
Type II Pb-pyrite	0.00	4.504	-	0.0658(5)	0.2497(26)	0.0016(1)	0.0922
	0.20	4.498	0.0796(1)	0.0923(7)	0.2467(32)	nd	nd ^a
	71.50	4.498	0.0360(1)	0.1151(7)	0.2372(31)	0.0003(1)	0.8462
Type II As-pyrite	0.00	4.501	-	0.1242(6)	0.0244(8)	0.0085(3)	0.2186
	0.20	4.494	0.0830(2)	0.1641(5)	0.0481(8)	nd	nd ^a
	71.50	4.502	0.0002(1)	0.1984(5)	0.0152(4)	0.0003(1)	0.9546

^a nd: not determined.

^b “0” means that no retention peak of S⁰ is visible for this sample.

General conclusions

Retention of MoO_4^{2-} on AFm phases.

As minor but highly reactive phases present in hydrated cement, AFm phases, such as AFm- SO_4 ($[\text{Ca}_4\text{Al}_2(\text{OH})_{12}]^{2+} \cdot \text{SO}_4^{2-} \cdot m\text{H}_2\text{O}$) and AFm- Cl_2 ($[\text{Ca}_4\text{Al}_2(\text{OH})_{12}]^{2+} \cdot (\text{Cl}^-)_2 \cdot m\text{H}_2\text{O}$), have been considered as effective phases for the remediation of aquatic environments, to remove anionic contaminants mainly through anion exchange mechanisms. Here, a detailed molecular view of sorption mechanisms of MoO_4^{2-} onto AFm phases was reported, showing that other uptake mechanisms — edge adsorption, interfacial dissolution-precipitation — are at play and control the anion uptake under environmentally-relevant conditions. This contrasts to the classical view of anionic exchange as the main retention mechanism.

Advanced modelling (using PHREEQC code) of aqueous data shows that the sorption isotherm can be interpreted by three retention mechanisms with increasing Mo loadings, including two types of edge sites complexes, formation of the new AFm phase (i.e., AFm- MoO_4), and CaMoO_4 precipitation.

Meanwhile, as shown by Mo K-edge XANES data, Mo geometry evolves from tetrahedral to octahedral on the edge, and back to tetrahedral coordination at higher Mo loadings when precipitation of AFm- MoO_4 and CaMoO_4 predominates.

From TEM-EDX and HE-XRD analysis, octahedrally incorporated Mo(VI) on the edge was shown destabilize the edge structure of AFm phases, followed by co-precipitation of Mo-bearing katoite.

An anion insertion process on both AFm phases was also followed by in-situ time-resolved synchrotron-based XRD, remarkably agreeing with the sorption isotherm interpretation.

This work puts all these mechanisms in perspective, offering a new insight into the complex interplay of anion uptake mechanisms by AFm phases, by using changes in Mo geometry as powerful molecular-scale probe.

SeO_3^{2-} uptake by CaAl LDH.

Layered double hydroxides (LDHs), lamellar mixed hydroxides with a generic chemical formula $[\text{M}^{\text{II}}_{6-x}\text{M}^{\text{III}}_x\text{O}_6]^{x+}(\text{A}^{n-})_{x/n} \cdot m\text{H}_2\text{O}$, are anion exchangers with a strong potential to scavenge anionic contaminants in aquatic environments in the alkaline pH range where they are stable. AFm phases belong to the family of CaAl LDHs, in which M^{II} and M^{III} are Ca^{II}

and Al^{III} cations. In this study, a linear relationship between hydrated anion radius and basal spacing of CaAl LDHs in solution is established for the first time, via investigating by TRHE-XRD the inter-layer distance and intercalated anion complexation environment in four CaAl LDHs (i.e., Cl⁻, SO₄²⁻, SeO₃²⁻, and MoO₄²⁻ saturated CaAl LDHs).

PHREEQC modelling of batch sorption isotherms shows that precipitation of AFm-SeO₃ is the dominant mechanism controlling the retention of SeO₃²⁻ at medium loadings, reconfirming the retention mechanism of new AFm phase formation put forward in MoO₄²⁻ study. AFm-Cl₂ shows much stronger affinity ($R_d \sim 17800 \text{ L kg}^{-1}$) for SeO₃²⁻ than AFm-SO₄ ($R_d \sim 705 \text{ L kg}^{-1}$), probably due to their smaller particle size and the lower charge thus easier exchangeable, of the intercalated anion of AFm-Cl₂.

At stoichiometric SeO₃²⁻ loading, the newly formed AFm-SeO₃ phase in solution results in two layer-to-layer distances, i.e., $11.03 \pm 0.03 \text{ \AA}$ and $9.93 \pm 0.06 \text{ \AA}$, indicated by in-situ time-resolved XRD.

Besides, Se K-edge, Mo K-edge, and S K-edge EXAFS spectra indicate inner-sphere complexation of intercalated SeO₃²⁻, outer-sphere complexation of intercalated MoO₄²⁻ and SO₄²⁻ with the Ca-Al-O layers of AFm-SeO₃, AFm-MoO₄, and AFm-SO₄, respectively.

With the layer-to-layer distance of $11.03 \pm 0.03 \text{ \AA}$, a remarkable linear relationship between the sizes of hydrated intercalated anions (i.e., Cl⁻, SO₄²⁻, MoO₄²⁻, and SeO₃²⁻) obtained from PDF analysis of experiment data and basal spacing of corresponding AFm phases is established. The results confirm the co-existence of unconstrained and bonded SeO₃²⁻ in the interlayer space of AFm phases.

Contrary to AFm-SeO₃ with ISC bonded SeO₃²⁻, the phase with OSC intercalated SeO₃²⁻ is kinetically favored but thermodynamically unstable under over exposure to selenite corrosion.

This work offers new insights into a fast but reliable approach to determine the complexation environment of intercalated anions via XRD analyses.

Determination of Eh values imposed by steel corrosion products in cement-based media.

For reinforced cementitious barriers in nuclear waste repositories, Eh is of great essence to the migration behaviors of redox-sensitive RNs, and will be largely controlled by the corrosion of embedded steel. Reductive immobilization of RNs on the steel (i.e., Fe⁰) and its corrosion couples (e.g., magnetite/hematite and magnetite/goethite) is another key retardation factor.

Here, we develop a new approach to obtain the Eh values based on XANES results and on the Nernst equation.

Oxidized RNs (U^{VI} , Se^{IV} , Mo^{VI} , and Sb^V) were employed as species probes in hyperalkaline cement pore water. Fe^0 , magnetite/hematite, and magnetite/goethite show a good affinity towards RNs, resulting in decreasing K_d order for $U > Sb > Se > Mo$ under both N_2 and H_2 atmosphere.

LCF of XANES spectra was used to identify and quantify reduced species of sorbed U, Se, and Sb, present as UO_2 , U_4O_9 , $FeSe$, $FeSe_2$, Se^0 , Sb^0 , and Sb_2O_3 . The presence of H_2 did not obviously enhance the removal rate of aqueous RNs, but it promoted the formation of the most reduced species, e.g., $FeSe$ or Sb^0 . From experiment-based Pourbaix diagrams, $UO_2(OH)_4^{2-}$, SeO_3^{2-} , MoO_4^{2-} , and $Sb(OH)_6^-$ are the predominated aqueous species, respectively, and their concentrations can be treated as the total aqueous RNs concentrations.

Using Nernst equation, experimental Eh values are obtained, which are remarkably close together and center around -450 mV at pH ~13.5 for both Fe^0 and Fe-(hydr)oxides couples. This Eh value appears to be controlled by amorphous $Fe(OH)_2/Fe(OH)_3$ or $(Fe_{1-x}Ca_x)(OH)_2/Fe(OH)_3$ couple, which presence among corrosion product was confirmed by PDF analysis of HE-XRD patterns.

This approach could pave the way for describing the Eh gradient in reinforced concrete or any other solid or biological materials where direct Eh measurements are not feasible.

RNs sorption behaviors on hydrated Fe-bearing CEM-V/A cement.

Deep geological storage in clay rich host rocks is foreseen in France for low- and intermediate-level radioactive waste (L/ILW). CEM-V/A cement, containing 25% blast furnace slag and 25 % fly ash, is the preferred cement type and possesses advantages of longer internal high pH conditions and better resistance to sulfate attack. In this work, sorption behaviors of RNs (i.e., U^{VI} , Se^{IV} , Mo^{VI} , and Sb^V) on pristine CEM-V/A hardened cement paste (HCP), Fe phases-bearing (i.e., NZVI, magnetite, hematite, and goethite) HCP, and separated hydration products of reinforced cement (e.g., C-S-H, ettringite, AFm, Fe^0 , mackinawite, etc.) in cement pore water (pH ~13.5) were investigated, aiming to uncover potential active sorption sites in reinforced HCP.

Hydrated NZVI-bearing CEM-V/A cement has the highest RNs removal efficiency and the pristine hydrated cement had a better uptake performance than Fe-(hydr)oxides-bearing

cement. S K-edge XANES analysis reveals the existence of reducing S species, e.g., sulfide and possible FeS₂, which may act as reductants for RNs. All the types of cement showed a strong affinity towards Sb(V) and U(VI), resulting in decreasing R_d order of Sb > U > Se > Mo.

Clarkeite-type colloidal nanoparticles formation and hereafter adsorption on cement could be the predominated U(VI) sorption mechanisms, while co-precipitation with Ca²⁺ could be the most effective uptake path for Sb(V).

LCF of Se K-edge XANES spectra indicate that Se(IV) uptake was attributed to complexation with Ca-sites and reductive precipitation by NZVI and sulfide. Besides, PDF analysis of HEXRD patterns shows that after SeO₃²⁻ corrosion, NZVI would completely transformed into Fe(OH)₂ and tetrahedron-octahedron iron bridging of magnetite would collapse due to the oxidation by Se(IV).

No reduction of molybdate can be detected. Mo K-edge XAS uncovered that AFm-SO₄ and Fe⁰ were the two most effective phases for MoO₄²⁻ removal in reinforced cement.

According to the microprobe mapping, U concentrated on the surface of Ca-rich phases while Mo had strong correlation with Fe phases. Fe⁰ always showed strong affinity to all RNs, while hydrated cement phases had a certain selectivity (e.g., RNs' complexation ability with Ca).

The influence of surface impurities on the reactivity of pyrite toward aqueous U(VI).

Iron sulfides, such as pyrite (FeS₂), are widely present not only in CEM-V/A cement, but also in claystone and granitic rock natural barriers, as potential scavengers for RNs in nuclear waste repositories. The factors influencing pyrite reactivity toward aqueous U(VI) were investigated in this study. The results indicated that the minor impurities of As, Pb and Si generally hosted in pyrite play a significant role in the reactivity of pyrite, and the reduction of U(VI) mainly occurred at the Pb- and As-rich spots on pyrite surface. In addition, reactive S²⁻ can be generated on pyrite surface due to the breaking of Fe-S bonds during grinding process, which also can account for the reduction of aqueous U(VI). The findings of this study can improve our understanding regarding the role of pyrite in governing the mobility of toxic uranium in the environment.

Perspectives

Dissolution of spent nuclear fuel (UO₂) in silica-rich fluids.

Uranium in spent nuclear fuel is principally in the form of uraninite (UO_{2+x}), of which dissolution and diffusion is vital to the safety evaluation of repositories. Coffinite, USiO₄, is an important alteration mineral of uraninite in contact with silica-rich groundwater in a reducing environment, but its unexpected occurrence via uraninite coffinitization is in long-term discussions. Recently, its thermodynamic properties were constrained, suggesting the thermodynamic metastability of coffinite with respect to uraninite plus quartz[337]. Typically, uranium solubility in the repository environment is derived from the dissolution of UO₂ and further oxidation into U(VI) regularly[338]. The formation of a series of secondary phases, like coffinite nanoparticles, would influence uranium concentrations during diffusion. Thus, it is of importance to better understand the process of coffinitization, and the consequences on mobility of uranium in granite/claystone system.

Uranium(VI) colloidal nanoparticles in cement leachate.

Dissolution of uraninite in spent nuclear fuel is always accompanied with oxidation, resulting in the mobile uranium forms, hexavalent uranium species. A recent work reported that U(VI) can form nano-sized U(VI) colloids (i.e., clarkeite-like phases) with alkali and alkaline-earth cations in cement leachate (pH 10-13) and the nanoparticles are stable in aqueous phase for even several years[259]. This would potentially enhance the mobility of U(VI) under hyperalkaline conditions. Thus, in cementitious environments a potential new mechanism for U(VI) to be transported as a colloidal phase is proposed. Migration behavior of these U(VI) colloids through the interface of cement/granite or cement/claystone is worth better knowing.

Sorption behaviors of RN oxyanions on LDHs' surface.

AFm phases in HCP can be considered as effective phases to remove anionic RN contaminants. In Chapter 2, we use MoO₄²⁻ as a “structural probe” to investigate the potential sorption sites on CaAl LDHs and also the related uptake mechanisms with increasing surface coverage: two types of edge surface sites complexation—tetrahedral and octahedral complexation on the edge, interlayer anion exchange leading to formation of AFm-MoO₄, and finally, decomposition of LDHs structures turning into CaMoO₄ precipitation. Here, Mo was selected as special probe, because it belongs to transition metals (for which an observation of

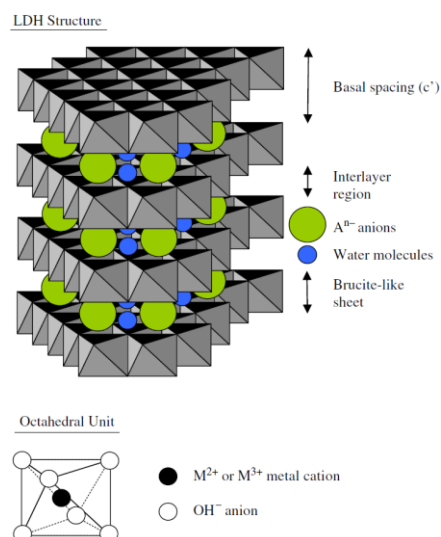
pre-edge peak in XANES spectrum is possible) and has two types of coordination symmetry (i.e., octahedral and tetrahedral symmetry), which can be distinguished easily by XANES. These features allowed us to probe the two types of edge sites under low Mo loading. Conversely, whether these two types of edge sites are functionally different for other RN anions or not should be checked experimentally. However, we can hypothesize that, for other oxyanions to present a similar sorption behavior on M^{II} - M^{III} LDHs edge sites, they should have:

- possible octahedral coordination symmetry
- comparable atomic radii to M^{II} and M^{III} (lattice mismatch, or in this case, O-O distances, are typically a discriminating factor)
- good affinity to M^{II}

For most oxyanions, at least the three sorption mechanisms, including surface sorption, anion exchange, and LDH decomposition/co-precipitation, should be at work as increasing oxyanions coverage. Under environmentally-relevant conditions (e.g., for nuclear waste disposal), removal of trace amounts of anionic contaminants should occur mainly by surface sorption mechanisms, rather than anion exchange. Besides, it would be intriguing to know the sorption behaviors of RN oxyanions on LDHs' surface. For instance, sorption behaviors of MoO_4^{2-} and SeO_3^{2-} (in Chapter 3) are differing, with the latter non-specializing on the edge. These should possess distinct bonding strengths and the strong binding strength provided by structural incorporation would lead to a low contaminant bioavailability. This work provides also a conceptual framework for improving toxic oxyanion leaching regulation for CaAl LDHs containing materials, such as fly- and bottom-ashes.

Intercalated anion's size vs. LDHs' basal spacing.

The correlation between intercalated anions and layer-to-layer distances of LDHs (e.g., hydrocalumite[211], hydrotalcite[212, 213, 215], etc.) has attracted extensive attentions. The study in Chapter 3 aims to give a detailed discussion on the structural configurations of intercalated anions of CaAl LDHs and their basal spacing from a molecular level. For the first time, a remarkable linear relationship unwraps the correlation in the case of 100%



humidity using the hydrated anion's radius obtained experimentally. With this linear relationship, structural configurations of intercalated anions could be predicted preliminarily, even as well as the structural stability of the corresponding phases. Regarding CaAl LDHs, by subtracting the thickness of Brucite-like sheet ($\sim 2.0 \text{ \AA}$ for the Ca-Al-O sheet, shown in the above figure[174]), the diameters of hydrated OSC intercalated anions are nearly the same with space of interlayer region. It suggests that most interlayer water molecules are employed for intercalated anions' hydration, similar to the hydration state of anions in solution. This work provides also an insight into kinetic vs. thermodynamic control on preferred configurations of anions, potentially forming inner-sphere complexes (e.g., SeO_3^{2-} , SO_3^{2-} , and AsO_2^-) when they are subject to the uptake by LDHs via anion exchange mechanisms. Predictions can be made that linear relationships may also exist in other LDH-analogous structures.

Sorption competition of RNs on corrosion products of reinforced Fe^0 .

In Chapter 4, experimental Eh values are obtained using Nernst equation, which identically point out a center value of $\sim -450 \text{ mV}$ at $\text{pH} \sim 13.5$ for both Fe^0 and its corrosion products of Fe-(hydr)oxides couples. As discussed in our previous work[339], when redox sensitive elements are introduced together they do compete for electrons, the one with the highest Eh° being reduced first, the other RNs being reduced – if ever, i.e. if electrons are still available – in order of decreasing Eh° . In the present, it is meaningful to test this hypothesis with cement pore water suspension of steel corrosion products. Indeed, co-existence of RNs is more likely a real RNs leakage situation. Till now, preliminary work has been done on RNs sorption competition, showing that the competition occurred not only on redox reactions, related to the redox potential, but firstly on the limited surface sites (e.g., Ca-sites and Fe-sites), related to the sites' affinity for RNs. These lead to the more complicated sorption competition behaviors of RNs (e.g., U, Se, Mo, Sb).

Synchrotron-based X-ray analysis of Fe^0 -reinforced cement cores.

Interactions between the steel, steel corrosion products, cement hydrates, and RNs are of importance to the performance of reinforced cementitious structures in repositories. For instance, Eh will be mainly influenced by the interface between the corroded steel and cement pastes. The released soluble iron will diffuse outside and will probably be trapped in cement hydrates. Besides, it is also not clear whether RN precipitation will occur at the interface or within the hydrated cement. Furthermore, the inclusion of RNs in cement hydrates could lead

to phase transformations. Apart from the microprobe analysis described in Chapter 5, several synchrotron-based X-ray imaging techniques can also be powerful tools applying for further investigation on hardened cement cores.

X-ray diffraction micro-tomography (XRD-CT) can be used to characterize the different phases forming at the corroded steel - cement interface, in the presence or absence of RNs. Hydrated cement paste can be described by XRD-CT technique [340] at the micron scale. Here, spatial distributions of the corroded steel - cement interface and the bulk corroded cement phases after contacting with RNs can also be obtained, providing a visualized proof to active sites for RNs immobilization. Besides, layers of corrosion phases on the steel can be probed “in-situ” by micro-XRD[341]. That a significant part of corroded Fe is potentially transported away from the corrosion interface also has direct contributions to the Eh.

The approach for Eh determination described in Chapter 4 appears to be a reliable method to compute Eh in concrete, but also in other (e.g., biological) systems where local Eh direct measurement is not feasible. This could pave the way for RNs speciation mapping in real reinforced concrete blocks and further description of the Eh gradient. Spatially-resolved studies of the RN speciation as a function of distance to the steel/NZVI, at a submicro scale, can be achieved by micro-XANES. It will be a powerful tool to probe the “in-situ” gradient of Fe oxidation states in the steel corrosion layers and the molar fractions of RNs species. Spatial resolutions of the resulting Eh gradient depend on the sizes of X-ray beam scanning pixels: ~ μm level.

U(VI) retention on synthetic trace elements doped pyrite.

Pyrite, as a reducing buffer, is ubiquitously present as a minor component in the argillite host rock in France, in granitic host rock in China and Scandinavia, and also might exist in slag used in CEM-V/A cement. Several factors are critical to the reactivity of pyrite, such as the minor element impurities in pyrite lattice and the fracture resulting Fe(III) and S(-II) on pyrite surface. As discussed in Chapter 6, sulfide on the unwashed surface of fractured pyrite is mainly responsible for the strong reductive ability towards U(VI). Besides, the impurity sites (e.g., As- and Pb-) on different types of pyrite could result in more dissolved sulfide, due to crystallographic defects, thus collective U reduction and precipitation on the sites. Systematic study on impurities effects can be performed by synthesizing a series of nano-sized pyrite with impurities, such as As-, Co-, Ni-doped pyrite[128]. With synthetic nano-sized pyrite, effects of surface S(-II) and Fe(III), resulting from structural fracture, can be excluded.

Thermodynamic predictions of secondary phases in cementitious repositories.

The safety of deep geologic nuclear waste repositories should be evaluated for at least thousands of years. Under the geologic time scale, alkali leachate of freshly hydrated Portland cement can interact with rock forming minerals, likely initiating the dissolution of aluminosilicate minerals in the adjacent rock and promoting the formation of secondary minerals, such as zeolite. Formation process of zeolites and their affinity towards RNs are of great essence in the context of long time scale[342]. However, their stability and the conditions of formation or dissolution are largely unknown due to the variable composition of cations (Ca, Na, K), Al/Si ratios, H₂O contents and structural variability of zeolites. Till now, no/very little experimental solubility and thermodynamic data are available. Thermodynamic data (solubility, Gibbs free energy, enthalpy and entropy) of different zeolites, including synthetic and natural zeolites, could close an important gap in thermodynamics and be helpful for long-term performance predictions of cementitious repositories.

References

1. Vuori, S., *The environmental and ethical basis of the geological disposal of long-lived radioactive waste*. ATS Ydintekniikka, 1995. **24**(3): p. 16-17.
2. AGENCY, I.A.E., *Estimation of Global Inventories of Radioactive Waste and Other Radioactive Materials*. IAEA TECDOC Series. 2008, Vienna: INTERNATIONAL ATOMIC ENERGY AGENCY.
3. Grambow, B., *Geological Disposal of Radioactive Waste in Clay*. Elements, 2016. **12**(4): p. 239-245.
4. Deng, Y.F., et al., *Laboratory hydro-mechanical characterisation of Boom Clay at Essen and Mol*. Physics and Chemistry of the Earth, Parts A/B/C, 2011. **36**(17): p. 1878-1890.
5. Amann, F., et al., *Geomechanical behaviour of Opalinus Clay at multiple scales: results from Mont Terri rock laboratory (Switzerland)*. Swiss Journal of Geosciences, 2017. **110**(1): p. 151-171.
6. Krishnamoorthy, T., R. Nair, and T. Sarma, *Migration of radionuclides from a granite repository*. Water resources research, 1992. **28**(7): p. 1927-1934.
7. Price, R. and S. Bauer. *Analysis of the elastic and strength properties of Yucca Mountain tuff, Nevada*. in *The 26th US Symposium on Rock Mechanics (USRMS)*. 1985. American Rock Mechanics Association.
8. OECD/NEA, *Engineered Barrier Systems and the Safety of Deep Geological Repositories*. OECD Publishing.
9. Grambow, B., *Mobile fission and activation products in nuclear waste disposal*. Journal of Contaminant Hydrology, 2008. **102**(3-4): p. 180-186.
10. Altmann, S., *'Geo'chemical research: A key building block for nuclear waste disposal safety cases*. Journal of Contaminant Hydrology, 2008. **102**(3-4): p. 174-179.
11. Dossier, A., *Argile*. Safety Evaluation of a Geological Repository. ANDRA Report Series, 2005.
12. Duro, L., et al., *Assessment of the evolution of the redox conditions in a low and intermediate level nuclear waste repository (SFRI, Sweden)*. Applied Geochemistry, 2014. **49**: p. 192-205.
13. Nóvoa, X.R., *Electrochemical aspects of the steel - concrete system. A review*. Journal of Solid State Electrochemistry, 2016. **20**(8): p. 2113-2125.
14. Gouda, V.K., *Corrosion and Corrosion Inhibition of Reinforcing Steel: I. Immersed in Alkaline Solutions*. British Corrosion Journal, 1970. **5**(5): p. 198-203.
15. Yan, S., et al., *Uranium(VI) Removal by Nanoscale Zerovalent Iron in Anoxic Batch Systems*. Environmental Science & Technology, 2010. **44**(20): p. 7783-7789.
16. Liger, E., L. Charlet, and P. Van Cappellen, *Surface catalysis of uranium (VI) reduction by iron (II)*. Geochimica et Cosmochimica Acta, 1999. **63**(19): p. 2939-2955.
17. Missana, T., U. Maffiotte, and M. Garcia-Gutierrez, *Surface reactions kinetics between nanocrystalline magnetite and uranyl*. Journal of Colloid and Interface Science, 2003. **261**(1): p. 154-160.
18. Scott, T.B., et al., *Reduction of U(VI) to U(IV) on the surface of magnetite*. Geochimica Et Cosmochimica Acta, 2005. **69**(24): p. 5639-5646.
19. Sherman, D.M., C.L. Peacock, and C.G. Hubbard, *Surface complexation of U(VI) on goethite (α -FeOOH)*. Geochimica et Cosmochimica Acta, 2008. **72**(2): p. 298-310.
20. Duff, M.C., J.U. Coughlin, and D.B. Hunter, *Uranium co-precipitation with iron oxide minerals*. Geochimica et Cosmochimica Acta, 2002. **66**(20): p. 3533-3547.

21. Min, X., et al., *Fe₃O₄@ZIF-8: a magnetic nanocomposite for highly efficient UO₂²⁺ adsorption and selective UO₂²⁺/Ln³⁺ separation*. *Chemical Communications*, 2017. **53**(30): p. 4199-4202.
22. Fernandez-Martinez, A. and L. Charlet, *Selenium environmental cycling and bioavailability: a structural chemist point of view*. *Reviews in Environmental Science and Bio/Technology*, 2009. **8**(1): p. 81-110.
23. López de Arroyabe Loyo, R., et al., *Immobilization of Selenite on Fe₃O₄ and Fe/Fe₃C Ultrasmall Particles*. *Environmental Science & Technology*, 2008. **42**(7): p. 2451-2456.
24. Kirsch, R., et al., *Reduction of antimony by nano-particulate magnetite and mackinawite*. *Mineralogical Magazine*, 2008. **72**(1): p. 185-189.
25. Mitsunobu, S., Y. Takahashi, and Y. Terada, *μ -XANES Evidence for the Reduction of Sb(V) to Sb(III) in Soil from Sb Mine Tailing*. *Environmental Science & Technology*, 2010. **44**(4): p. 1281-1287.
26. Scheinost, A.C., et al., *Quantitative antimony speciation in shooting-range soils by EXAFS spectroscopy*. *Geochimica et Cosmochimica Acta*, 2006. **70**(13): p. 3299-3312.
27. Zhou, Z., et al., *The Removal of Antimony by Novel NZVI-Zeolite: the Role of Iron Transformation*. *Water, Air, & Soil Pollution*, 2015. **226**(3): p. 76.
28. Mitsunobu, S., et al., *Behavior of Antimony(V) during the Transformation of Ferrihydrite and Its Environmental Implications*. *Environmental Science & Technology*, 2013. **47**(17): p. 9660-9667.
29. Huang, Y.H., C. Tang, and H. Zeng, *Removing molybdate from water using a hybridized zero-valent iron/magnetite/Fe(II) treatment system*. *Chemical Engineering Journal*, 2012. **200–202**: p. 257-263.
30. Xu, N., C. Christodoulatos, and W. Braida, *Modeling the competitive effect of phosphate, sulfate, silicate, and tungstate anions on the adsorption of molybdate onto goethite*. *Chemosphere*, 2006. **64**(8): p. 1325-1333.
31. Das, S. and M. Jim Hendry, *Adsorption of molybdate by synthetic hematite under alkaline conditions: Effects of aging*. *Applied Geochemistry*, 2013. **28**: p. 194-201.
32. Michel, F.M., et al., *The Structure of Ferrihydrite, a Nanocrystalline Material*. *Science*, 2007. **316**(5832): p. 1726-1729.
33. Gustafsson, J.P., *Modelling molybdate and tungstate adsorption to ferrihydrite*. *Chemical Geology*, 2003. **200**(1–2): p. 105-115.
34. Börsig, N., et al., *Uptake mechanisms of selenium oxyanions during the ferrihydrite-hematite recrystallization*. *Geochimica et Cosmochimica Acta*, 2017. **206**: p. 236-253.
35. Lothenbach, B. and A. Nonat, *Calcium silicate hydrates: Solid and liquid phase composition*. *Cement and Concrete Research*, 2015. **78**: p. 57-70.
36. Matschei, T., B. Lothenbach, and F.P. Glasser, *Thermodynamic properties of Portland cement hydrates in the system CaO–Al₂O₃–SiO₂–CaSO₄–CaCO₃–H₂O*. *Cement and Concrete Research*, 2007. **37**(10): p. 1379-1410.
37. Baur, I., et al., *Dissolution-precipitation behaviour of ettringite, monosulfate, and calcium silicate hydrate*. *Cement and Concrete Research*, 2004. **34**(2): p. 341-348.
38. Matschei, T., B. Lothenbach, and F.P. Glasser, *The AFm phase in Portland cement*. *Cement and Concrete Research*, 2007. **37**(2): p. 118-130.
39. Aimoz, L., et al., *Structural Insight into Iodide Uptake by AFm Phases*. *Environmental Science & Technology*, 2012. **46**(7): p. 3874-3881.
40. Ochs, M., D. Mallants, and L. Wang, *Cementitious Materials and Their Sorption Properties*, in *Radionuclide and Metal Sorption on Cement and Concrete*. 2016, Springer. p. 5-16.

41. Iwaida, T., et al., *Structure alteration of CSH (calcium silicate hydrated phases) caused by sorption of caesium*. Radiochimica Acta, 2002. **90**(9-11): p. 677-681.
42. Tits, J., et al., *The uptake of Eu (III) and Th (IV) by calcite under hyperalkaline conditions*, 2002, Paul Scherrer Institut.
43. Schlegel, M.L., et al., *Mechanism of europium retention by calcium silicate hydrates: an EXAFS study*. Environmental science & technology, 2004. **38**(16): p. 4423-4431.
44. Poiteau, I., et al., *Sorption mechanisms of Eu³⁺ on CSH phases of hydrated cements*. Journal of Colloid and Interface Science, 2001. **236**(2): p. 252-259.
45. Ochs, M., D. Mallants, and L. Wang, *Sorption Values for Chlorine and Iodine, in Radionuclide and Metal Sorption on Cement and Concrete*. 2016, Springer International Publishing: Cham. p. 17-44.
46. Noshita, K., et al., *Categorization of cement hydrates by radionuclide sorption mechanism*. MRS Online Proceedings Library Archive, 2000. **663**.
47. Poiteau, I., et al., *Reproducibility of the uptake of U (VI) onto degraded cement pastes and calcium silicate hydrate phases*. Radiochimica Acta, 2004. **92**(9-11): p. 645-650.
48. Wieland, E., et al., *Macro- and micro-scale studies on U(VI) immobilization in hardened cement paste*. Journal of Radioanalytical and Nuclear Chemistry, 2010. **286**(3): p. 793-800.
49. Evans, N.D.M., *Binding mechanisms of radionuclides to cement*. Cement and Concrete Research, 2008. **38**(4): p. 543-553.
50. Chatterji, S., *Mechanism of the CaCl₂ attack on portland cement concrete*. Cement and Concrete Research, 1978. **8**(4): p. 461-467.
51. Abdelrazig, B.E.I., et al., *The solution chemistry and early hydration of ordinary portland cement pastes with and without admixtures*. Thermochemica Acta, 1999. **340-341**: p. 417-430.
52. Ito, R., et al., *Removal of insoluble chloride from bottom ash for recycling*. Waste Management, 2008. **28**(8): p. 1317-1323.
53. Grishchenko, R.O., A.L. Emelina, and P.Y. Makarov, *Thermodynamic properties and thermal behavior of Friedel's salt*. Thermochemica Acta, 2013. **570**: p. 74-79.
54. Dermatas, D. and X. Meng, *Utilization of fly ash for stabilization/solidification of heavy metal contaminated soils*. Engineering Geology, 2003. **70**(3-4): p. 377-394.
55. Hassett, D.J., D.F. Pflughoeft-Hassett, and L.V. Heebink, *Leaching of CCBs: observations from over 25 years of research*. Fuel, 2005. **84**(11): p. 1378-1383.
56. Talero, R., et al., *Comparative and semi-quantitative XRD analysis of Friedel's salt originating from pozzolan and Portland cement*. Construction and Building Materials, 2011. **25**(5): p. 2370-2380.
57. Izquierdo, M. and X. Querol, *Leaching behaviour of elements from coal combustion fly ash: An overview*. International Journal of Coal Geology, 2012. **94**: p. 54-66.
58. Baur, I. and C.A. Johnson, *Sorption of Selenite and Selenate to Cement Minerals*. Environmental Science & Technology, 2003. **37**(15): p. 3442-3447.
59. Wu, Y., et al., *Effective removal of selenate from aqueous solutions by the Friedel phase*. Journal of Hazardous Materials, 2010. **176**(1-3): p. 193-198.
60. Bonhoure, I., et al., *Uptake of Se(IV/VI) oxyanions by hardened cement paste and cement minerals: An X-ray absorption spectroscopy study*. Cement and Concrete Research, 2006. **36**(1): p. 91-98.
61. Choi, W.-H., et al., *Properties of synthetic monosulfate as a novel material for arsenic removal*. Journal of Hazardous Materials, 2012. **227-228**(0): p. 402-409.
62. Prince, W., M. Espagne, and P.C. Aitcin, *Ettringite formation*. Cement and Concrete Research, 2003. **33**(5): p. 635-641.

63. Moore, A.E. and H.F.W. Taylor, *Crystal structure of ettringite*. Acta Crystallographica Section B, 1970. **26**(4): p. 386-393.
64. Guo, B., K. Sasaki, and T. Hirajima, *Selenite and selenate uptaken in ettringite: Immobilization mechanisms, coordination chemistry, and insights from structure*. Cement and Concrete Research, 2017. **100**: p. 166-175.
65. Guo, B., K. Sasaki, and T. Hirajima, *Characterization of the intermediate in formation of selenate-substituted ettringite*. Cement and Concrete Research, 2017. **99**: p. 30-37.
66. Zhang, M. and E.J. Reardon, *Removal of B, Cr, Mo, and Se from Wastewater by Incorporation into Hydrocalumite and Ettringite*. Environmental Science & Technology, 2003. **37**(13): p. 2947-2952.
67. Cornelis, G., T. Van Gerven, and C. Vandecasteele, *Antimony leaching from uncarbonated and carbonated MSWI bottom ash*. Journal of hazardous materials, 2006. **137**(3): p. 1284-1292.
68. Choi, W.H., et al., *Development of a novel process for arsenic(V) removal from water using Fe- ettringite*. Desalination and Water Treatment, 2014. **52**(4-6): p. 712-718.
69. Jiménez, A. and M. Prieto, *Thermal Stability of Ettringite Exposed to Atmosphere: Implications for the Uptake of Harmful Ions by Cement*. Environmental Science & Technology, 2015. **49**(13): p. 7957-7964.
70. Taylor, H.F.W., C. Famy, and K.L. Scrivener, *Delayed ettringite formation*. Cement and Concrete Research, 2001. **31**(5): p. 683-693.
71. Cornelis, G., et al., *Leaching mechanisms of oxyanionic metalloid and metal species in alkaline solid wastes: A review*. Applied Geochemistry, 2008. **23**(5): p. 955-976.
72. Saikia, N., S. Kato, and T. Kojima, *Behavior of B, Cr, Se, As, Pb, Cd, and Mo present in waste leachates generated from combustion residues during the formation of ettringite*. Environmental toxicology and chemistry, 2006. **25**(7): p. 1710-1719.
73. Glasser, F., *Characterisation of the barrier performance of cements*. MRS Online Proceedings Library Archive, 2002. **713**.
74. Hillier, S., et al., *Hydrogarnet: A Host Phase for Cr(VI) in Chromite Ore Processing Residue (COPR) and Other High pH Wastes*. Environmental Science & Technology, 2007. **41**(6): p. 1921-1927.
75. Paikaray, S., M.J. Hendry, and J. Essilfie-Dughan, *Controls on arsenate, molybdate, and selenate uptake by hydrotalcite-like layered double hydroxides*. Chemical Geology, 2013. **345**: p. 130-138.
76. Liu, R., R.L. Frost, and W.N. Martens, *Absorption of the selenite anion from aqueous solutions by thermally activated layered double hydroxide*. Water Research, 2009. **43**(5): p. 1323-1329.
77. Das, J., et al., *Studies on Mg/Fe Hydrotalcite-Like-Compound (HTlc)*. Journal of Colloid and Interface Science, 2002. **251**(1): p. 26-32.
78. Palmer, S.J., A. Soisonard, and R.L. Frost, *Determination of the mechanism(s) for the inclusion of arsenate, vanadate, or molybdate anions into hydrotalcites with variable cationic ratio*. Journal of Colloid and Interface Science, 2009. **329**(2): p. 404-409.
79. Lothenbach, B. and F. Winnefeld, *Thermodynamic modelling of the hydration of Portland cement*. Cement and Concrete Research, 2006. **36**(2): p. 209-226.
80. Aurelio, G., et al., *Structural study of selenium(IV) substitutions in calcite*. Chemical Geology, 2010. **270**(1): p. 249-256.
81. Heberling, F., et al., *A thermodynamic adsorption/entrapment model for selenium(IV) coprecipitation with calcite*. Geochimica et Cosmochimica Acta, 2014. **134**: p. 16-38.
82. Renard, F., et al., *Selenium incorporation into calcite and its effect on crystal growth: An atomic force microscopy study*. Chemical Geology, 2013. **340**: p. 151-161.

83. Fernández-González, A., et al., *Miscibility in the CaSO₄·2H₂O–CaSeO₄·2H₂O system: Implications for the crystallisation and dehydration behaviour*. *Chemical Geology*, 2006. **225**(3): p. 256-265.
84. Trotignon, L., H. Peycelon, and X. Bourbon, *Performance assessment of CEM-I and CEM-V concrete engineered barriers in a clayey geological medium*.
85. Gaucher, E., et al., *ANDRA underground research laboratory: interpretation of the mineralogical and geochemical data acquired in the Callovian–Oxfordian formation by investigative drilling*. *Physics and Chemistry of the Earth, Parts A/B/C*, 2004. **29**(1): p. 55-77.
86. Metz, V., B. Kienzler, and W. Schübler, *Geochemical evaluation of different groundwater–host rock systems for radioactive waste disposal*. *Journal of Contaminant Hydrology*, 2003. **61**(1): p. 265-279.
87. Baeyens, B., et al., *In situ physico-chemical characterization of Boom Clay*. *Radioact. Waste Manage. Nucl. Fuel Cycle*, 1985. **6**(3-4): p. 391-408.
88. Vaughan, D.J. and C.L. Corkhill, *Mineralogy of Sulfides*. *Elements*, 2017. **13**(2): p. 81-87.
89. Hunger, S. and L.G. Benning, *Greigite: a true intermediate on the polysulfide pathway to pyrite*. *Geochem. Trans*, 2007. **8**(1): p. 1.
90. Lan, Y. and E.C. Butler, *Monitoring the transformation of mackinawite to greigite and pyrite on polymer supports*. *Applied Geochemistry*, 2014. **50**: p. 1-6.
91. Kirsch, R., et al., *Reduction of antimony by nano-particulate magnetite and mackinawite*, in *Mineralogical Magazine* 2008. p. 185.
92. Qi, C., et al., *Environmental geochemistry of antimony in Chinese coals*. *Science of The Total Environment*, 2008. **389**(2): p. 225-234.
93. Scott, T., O.R. Tort, and G. Allen, *Aqueous uptake of uranium onto pyrite surfaces: reactivity of fresh versus weathered material*. *Geochimica et Cosmochimica Acta*, 2007. **71**(21): p. 5044-5053.
94. Wersin, P., et al., *Interaction between aqueous uranium (VI) and sulfide minerals: spectroscopic evidence for sorption and reduction*. *Geochimica et Cosmochimica Acta*, 1994. **58**(13): p. 2829-2843.
95. Eglizaud, N., et al., *Uranium (VI) interaction with pyrite (FeS₂): Chemical and spectroscopic studies*. *Radiochimica Acta*, 2006. **94**(9-11): p. 651-656.
96. Bruggeman, C. and N. Maes, *Uptake of uranium (VI) by pyrite under boom clay conditions: influence of dissolved organic carbon*. *Environmental science & technology*, 2010. **44**(11): p. 4210-4216.
97. Aubriet, H., B. Humbert, and M. Perdicakis, *Interaction of U (VI) with pyrite, galena and their mixtures: a theoretical and multitechnique approach*. *Radiochimica Acta*, 2006. **94**(9-11): p. 657-663.
98. Yang, Z., et al., *Inhibition of U(VI) Reduction by Synthetic and Natural Pyrite*. *Environmental Science & Technology*, 2014. **48**(18): p. 10716-10724.
99. Descostes, M., et al., *Uptake of uranium and trace elements in pyrite (FeS₂) suspensions*. *Geochimica Et Cosmochimica Acta*, 2010. **74**(5): p. 1551-1562.
100. Moyes, L.N., et al., *Uranium uptake from aqueous solution by interaction with goethite, lepidocrocite, muscovite, and mackinawite: An X-ray absorption spectroscopy study*. *Environmental science & technology*, 2000. **34**(6): p. 1062-1068.
101. Hyun, S.P., et al., *Uranium (VI) reduction by iron (II) monosulfide mackinawite*. *Environmental science & technology*, 2012. **46**(6): p. 3369-3376.
102. Troyer, L.D., Y. Tang, and T. Borch, *Simultaneous reduction of arsenic (V) and uranium (VI) by mackinawite: role of uranyl arsenate precipitate formation*. *Environmental science & technology*, 2014. **48**(24): p. 14326-14334.

103. Veeramani, H., et al., *Abiotic reductive immobilization of U (VI) by biogenic mackinawite*. Environmental science & technology, 2013. **47**(5): p. 2361-2369.
104. Gallegos, T.J., et al., *Uranium(VI) Interactions with Mackinawite in the Presence and Absence of Bicarbonate and Oxygen*. Environmental Science & Technology, 2013. **47**(13): p. 7357-7364.
105. Naveau, A., et al., *Interactions of aqueous selenium(-II) and (IV) with metallic sulfide surfaces*. Environmental Science & Technology, 2007. **41**(15): p. 5376-5382.
106. Breynaert, E., C. Bruggeman, and A. Maes, *XANES-EXAFS analysis of solid-phase reaction products formed upon contacting Se(IV) with FeS₂ and FeS*. Environmental Science & Technology, 2008. **42**(10): p. 3595-3601.
107. Kang, M., et al., *Redox reaction of aqueous selenite with As-rich pyrite from Jiguanshan ore mine (China): Reaction products and pathway*. Applied Geochemistry, 2014. **47**(0): p. 130-140.
108. Kang, M.L., et al., *Effect of pH on Aqueous Se(IV) Reduction by Pyrite*. Environmental Science & Technology, 2011. **45**(7): p. 2704-2710.
109. Curti, E., L. Aimoz, and A. Kitamura, *Selenium uptake onto natural pyrite*. Journal of Radioanalytical and Nuclear Chemistry, 2013. **295**(3): p. 1655-1665.
110. Scheinost, A.C. and L. Charlet, *Selenite Reduction by Mackinawite, Magnetite and Siderite: XAS Characterization of Nanosized Redox Products*. Environmental Science & Technology, 2008. **42**(6): p. 1984-1989.
111. Scheinost, A.C., et al., *X-ray absorption and photoelectron spectroscopy investigation of selenite reduction by Fe-II-bearing minerals*. Journal of Contaminant Hydrology, 2008. **102**(3-4): p. 228-245.
112. Charlet, L., et al., *Nanocomposite Pyrite-Greigite Reactivity toward Se(IV)/Se(VI)*. Environmental Science & Technology, 2012. **46**(9): p. 4869-4876.
113. Diener, A., et al., *Structure of selenium incorporated in pyrite and mackinawite as determined by XAFS analyses*. Journal of Contaminant Hydrology, 2012. **Accepted**.
114. Kang, M., et al., *The influence of pH and reaction time on the formation of FeSe₂ upon selenite reduction by nano-sized pyrite-greigite*. Radiochimica Acta, 2016. **104**(9): p. 649-656.
115. Helz, G.R., T.P. Vorlicek, and M.D. Kahn, *Molybdenum scavenging by iron monosulfide*. Environmental science & technology, 2004. **38**(16): p. 4263-4268.
116. Helz, G.R., et al., *New model for molybdenum behavior in euxinic waters*. Chemical Geology, 2011. **284**(3): p. 323-332.
117. Erickson, B.E. and G.R. Helz, *Molybdenum(VI) speciation in sulfidic waters*. Geochimica et Cosmochimica Acta, 2000. **64**(7): p. 1149-1158.
118. Xu, N., C. Christodoulatos, and W. Braida, *Adsorption of molybdate and tetrathiomolybdate onto pyrite and goethite: effect of pH and competitive anions*. Chemosphere, 2006. **62**(10): p. 1726-1735.
119. Bostick, B.C., S. Fendorf, and G.R. Helz, *Differential adsorption of molybdate and tetrathiomolybdate on pyrite (FeS₂)*. Environmental science & technology, 2003. **37**(2): p. 285-291.
120. Vorlicek, T.P., et al., *Capture of molybdenum in pyrite-forming sediments: role of ligand-induced reduction by polysulfides*. Geochimica et Cosmochimica Acta, 2004. **68**(3): p. 547-556.
121. Freund, C., et al., *The effect of a thiol-containing organic molecule on molybdenum adsorption onto pyrite*. Geochimica et Cosmochimica Acta, 2016. **174**: p. 222-235.
122. Dahl, T.W., et al., *Molybdenum reduction in a sulfidic lake: Evidence from X-ray absorption fine-structure spectroscopy and implications for the Mo paleoproxy*. Geochimica et Cosmochimica Acta, 2013. **103**: p. 213-231.

123. Chappaz, A., et al., *Does pyrite act as an important host for molybdenum in modern and ancient euxinic sediments?* *Geochimica et Cosmochimica Acta*, 2014. **126**: p. 112-122.
124. Rosso, K.M. and D.J. Vaughan, *Sulfide Mineral Surfaces*. *Reviews in Mineralogy and Geochemistry*, 2006. **61**(1): p. 505-556.
125. Rosso, K.M. and D.J. Vaughan, *Reactivity of Sulfide Mineral Surfaces*. *Reviews in Mineralogy and Geochemistry*, 2006. **61**(1): p. 557-607.
126. Nesbitt, H., et al., *Sulfur and iron surface states on fractured pyrite surfaces*. *American Mineralogist*, 1998. **83**(9-10): p. 1067-1076.
127. Rimstidt, J.D. and D.J. Vaughan, *Pyrite oxidation: a state-of-the-art assessment of the reaction mechanism*. *Geochimica et Cosmochimica Acta*, 2003. **67**(5): p. 873-880.
128. Lehner, S., et al., *The effect of As, Co, and Ni impurities on pyrite oxidation kinetics: An electrochemical study of synthetic pyrite*. *Geochimica et Cosmochimica Acta*, 2007. **71**(10): p. 2491-2509.
129. Ma, B., et al., *The reductive immobilization of aqueous Se(IV) by natural pyrrhotite*. *Journal of Hazardous Materials*, 2014. **276**(0): p. 422-432.
130. Kennedy, B.A., *Surface mining*. 1990: SME.
131. Uddin, M.K., *A review on the adsorption of heavy metals by clay minerals, with special focus on the past decade*. *Chemical Engineering Journal*, 2017. **308**: p. 438-462.
132. Kubota, T., et al., *Removal of radioactive cesium, strontium, and iodine from natural waters using bentonite, zeolite, and activated carbon*. *Journal of Radioanalytical and Nuclear Chemistry*, 2013. **296**(2): p. 981-984.
133. Montavon, G., E. Alhajji, and B. Grambow, *Study of the interaction of Ni²⁺ and Cs⁺ on MX-80 bentonite; Effect of compaction using the "capillary method"*. *Environmental Science & Technology*, 2006. **40**(15): p. 4672-4679.
134. de Pablo, L., M.L. Chávez, and M. Abatal, *Adsorption of heavy metals in acid to alkaline environments by montmorillonite and Ca-montmorillonite*. *Chemical engineering journal*, 2011. **171**(3): p. 1276-1286.
135. MBADCAM, J.K., S.G. ANAGHO, and J.N. NSAMI, *Kinetic and equilibrium studies of the adsorption of lead (II) ions from aqueous solution onto two Cameroon clays: Kaolinite and smectite*. *Journal of Environmental Chemistry and Ecotoxicology*, 2011. **3**(11): p. 290-297.
136. Gupta, S.S. and K.G. Bhattacharyya, *Immobilization of Pb (II), Cd (II) and Ni (II) ions on kaolinite and montmorillonite surfaces from aqueous medium*. *Journal of environmental management*, 2008. **87**(1): p. 46-58.
137. Wu, T., et al., *Effect of organic matter on ¹²⁵I diffusion in bentonite*. *Journal of Radioanalytical and Nuclear Chemistry*, 2015. **303**(1): p. 255-260.
138. Tachi, Y. and K. Yotsuji, *Diffusion and sorption of Cs⁺, Na⁺, I⁻ and HTO in compacted sodium montmorillonite as a function of porewater salinity: Integrated sorption and diffusion model*. *Geochimica et Cosmochimica Acta*, 2014. **132**: p. 75-93.
139. Glaus, M.A., et al., *Comparative study of tracer diffusion of HTO, ²²Na⁺ and ³⁶Cl⁻ in compacted kaolinite, illite and montmorillonite*. *Geochimica et Cosmochimica Acta*, 2010. **74**(7): p. 1999-2010.
140. Wang, X. and Z. Tao, *Diffusion of ⁹⁹TcO₄⁻ in compacted bentonite: Effect of pH, concentration, density and contact time*. *Journal of radioanalytical and nuclear chemistry*, 2004. **260**(2): p. 305-309.
141. Zhao, Y., Z. Guo, and J. Xu, *⁹⁹TcO₄⁻ diffusion and sorption in compacted GMZ bentonite studied by capillary method*. *Journal of Radioanalytical and Nuclear Chemistry*, 2013. **298**(1): p. 147-152.

142. Wu, T., et al., *Salt effects on Re(VII) and Se(IV) diffusion in bentonite*. Applied Clay Science, 2017. **141**: p. 104-110.
143. Wang, Z., et al., *pH effect on Re(VII) and Se(IV) diffusion in compacted GMZ bentonite*. Applied Geochemistry, 2016. **73**: p. 1-7.
144. Montavon, G., et al., *Interaction of selenite with MX-80 bentonite: Effect of minor phases, pH, selenite loading, solution composition and compaction*. Colloids and Surfaces A: Physicochemical and Engineering Aspects, 2009. **332**(2-3): p. 71-77.
145. Missana, T., U. Alonso, and M. García-Gutiérrez, *Experimental study and modelling of selenite sorption onto illite and smectite clays*. Journal of Colloid and Interface Science, 2009. **334**(2): p. 132-138.
146. Charlet, L., et al., *Electron transfer at the mineral/water interface: Selenium reduction by ferrous iron sorbed on clay*. Geochimica et Cosmochimica Acta, 2007. **71**(23): p. 5731-5749.
147. Peak, D., U.K. Saha, and P.M. Huang, *Selenite Adsorption Mechanisms on Pure and Coated Montmorillonite: An EXAFS and XANES Spectroscopic Study*. Soil Science Society of America Journal, 2006. **70**(1): p. 192-203.
148. Wang, H., et al., *Sorption of Se(IV) on Fe- and Al-modified bentonite*. Journal of Radioanalytical and Nuclear Chemistry, 2015. **303**(1): p. 107-113.
149. Atia, A.A., *Adsorption of chromate and molybdate by cetylpyridinium bentonite*. Applied Clay Science, 2008. **41**(1): p. 73-84.
150. Orucoglu, E. and S. Hacıyakupoglu, *Bentonite modification with hexadecylpyridinium and aluminum polyoxy cations and its effectiveness in Se(IV) removal*. Journal of Environmental Management, 2015. **160**: p. 30-38.
151. Muir, B., et al., *The removal of molybdates and tungstates from aqueous solution by organo-smectites*. Applied Clay Science, 2017. **136**: p. 8-17.
152. Van Loon, L.R., J.M. Soler, and M.H. Bradbury, *Diffusion of HTO, $^{36}\text{Cl}^-$ and $^{125}\text{I}^-$ in Opalinus Clay samples from Mont Terri*. Journal of Contaminant Hydrology, 2003. **61**(1): p. 73-83.
153. Idemitsu, K., et al., *Diffusion behavior of selenite in purified bentonite*. Progress in Nuclear Energy, 2016. **92**: p. 279-285.
154. Tian, W., et al., *The effect of ionic strength on the diffusion of ^{125}I in Gaomiaozhi bentonite*. Journal of Radioanalytical and Nuclear Chemistry, 2013. **295**(2): p. 1423-1430.
155. Van Loon, L.R., M.A. Glaus, and W. Müller, *Anion exclusion effects in compacted bentonites: towards a better understanding of anion diffusion*. Applied Geochemistry, 2007. **22**(11): p. 2536-2552.
156. Wang, J., *High-level radioactive waste disposal in China: update 2010*. Journal of Rock Mechanics and Geotechnical Engineering, 2010. **2**(1): p. 1-11.
157. Ström, A., et al., *Site descriptive modelling during characterization for a geological repository for nuclear waste in Sweden*. Applied Geochemistry, 2008. **23**(7): p. 1747-1760.
158. Kojo, M., *The Strategy of Site Selection for the Spent Nuclear Fuel Repository in Finland*, in *The Renewal of Nuclear Power in Finland*, M. Kojo and T. Litmanen, Editors. 2009, Palgrave Macmillan UK: London. p. 161-191.
159. He, J., et al., *Migration of $^{75}\text{Se(IV)}$ in crushed Beishan granite: Effects of the iron content*. Journal of Hazardous Materials, 2017. **324**: p. 564-572.
160. Jan, B.Y.-L., S.-C. Tsai, and Y.-Y. Li, *Determination of sorption and diffusion parameters of Se(IV) on crushed granite*. Journal of Radioanalytical and Nuclear Chemistry, 2014. **301**(2): p. 365-371.

161. Videnská, K., et al., *Effect of grain size on the sorption and desorption of SeO₄²⁻ and SeO₃²⁻ in columns of crushed granite and fracture infill from granitic water under dynamic conditions*. Journal of Radioanalytical and Nuclear Chemistry, 2013. **298**(1): p. 547-554.
162. Shih, Y.-H., et al., *Determination of sorption and diffusion parameters of ⁹⁹Tc in crushed granite using through-diffusion experiments*. Journal of Radioanalytical and Nuclear Chemistry, 2017. **311**(2): p. 1111-1116.
163. Li, C., et al., *The influence of pH on the sorption and diffusion of ⁹⁹TcO₄⁻ in Beishan granite*. Radiochimica Acta International journal for chemical aspects of nuclear science and technology, 2012. **100**(7): p. 449-456.
164. Ikonen, J., et al., *Sorption and diffusion of selenium oxyanions in granitic rock*. Journal of Contaminant Hydrology, 2016. **192**: p. 203-211.
165. GUO, Z.-J., et al., *Adsorption of Se (IV) onto Beishan granite*. Acta Physico-Chimica Sinica, 2011. **27**(9): p. 2222-2226.
166. Chen, T.S., M ; Li, C; Tian, W; Liu, X; Wang, L; Wang, X; Liu, C, *The influence of temperature on the diffusion of I-125(-) in Beishan Granite*. RADIOCHIMICA ACTA, 2010.
167. Li, C., et al., *Effects of ionic strength and humic acid on ⁹⁹TcO₄⁻ sorption and diffusion in Beishan granite*. Journal of Radioanalytical and Nuclear Chemistry, 2012. **293**(3): p. 751-756.
168. Lu CJ; Liu CL; Chen T; Wang J; Wang XY; Su R; Sun JY; Yang RX; Zhang XS; Liu, C., *Determination of the effective diffusion coefficient for ¹²⁵I(-) in Beishan granite*. RADIOCHIMICA ACTA, 2008.
169. Ghosh-Dastidar, A., et al., *Selenium Capture Using Sorbent Powders: Mechanism of Sorption by Hydrated Lime*. Environmental Science & Technology, 1996. **30**(2): p. 447-452.
170. Peak, D., *Adsorption mechanisms of selenium oxyanions at the aluminum oxide/water interface*. Journal of Colloid and Interface Science, 2006. **303**(2): p. 337-345.
171. Ippolito, J.A., K.G. Scheckel, and K.A. Barbarick, *Selenium adsorption to aluminum-based water treatment residuals*. Journal of Colloid and Interface Science, 2009. **338**(1): p. 48-55.
172. Baik, M.H., W.J. Cho, and P.S. Hahn, *Sorption of U(VI) onto granite surfaces: A kinetic approach*. Journal of Radioanalytical and Nuclear Chemistry, 2004. **260**(3): p. 495-502.
173. Baik, M.H., S.P. Hyun, and P.S. Hahn, *Surface and bulk sorption of uranium(VI) onto granite rock*. Journal of Radioanalytical and Nuclear Chemistry, 2003. **256**(1): p. 11-18.
174. Goh, K.-H., T.-T. Lim, and Z. Dong, *Application of layered double hydroxides for removal of oxyanions: A review*. Water Research, 2008. **42**(6-7): p. 1343-1368.
175. Álvarez-Ayuso, E. and H.W. Nugteren, *Purification of chromium(VI) finishing wastewaters using calcined and uncalcined Mg-Al-CO₃-hydrotalcite*. Water Research, 2005. **39**(12): p. 2535-2542.
176. Chubar, N., *EXAFS and FTIR studies of selenite and selenate sorption by alkoxide-free sol-gel generated Mg-Al-CO₃ layered double hydroxide with very labile interlayer anions*. Journal of Materials Chemistry A, 2014. **2**(38): p. 15995-16007.
177. Oestreicher, V., M. Jobbágy, and A.E. Regazzoni, *Halide Exchange on Mg(II)-Al(III) Layered Double Hydroxides: Exploring Affinities and Electrostatic Predictive Models*. Langmuir, 2014. **30**(28): p. 8408-8415.

178. Huang, P.-P., et al., *MgAl layered double hydroxides with chloride and carbonate ions as interlayer anions for removal of arsenic and fluoride ions in water*. RSC Advances, 2015. **5**(14): p. 10412-10417.
179. Dijkstra, J.J., H.A. van der Sloot, and R.N.J. Comans, *The leaching of major and trace elements from MSWI bottom ash as a function of pH and time*. Applied Geochemistry, 2006. **21**(2): p. 335-351.
180. Blissett, R.S. and N.A. Rowson, *A review of the multi-component utilisation of coal fly ash*. Fuel, 2012. **97**: p. 1-23.
181. Snellings, R., G. Mertens, and J. Elsen, *Supplementary Cementitious Materials*. Reviews in Mineralogy and Geochemistry, 2012. **74**(1): p. 211-278.
182. Wu, Y.-H., et al., *Recycling of Sustainable Co-Firing Fly Ashes as an Alkali Activator for GGBS in Blended Cements*. Materials, 2015. **8**(2): p. 784.
183. Yao, Z.T., et al., *A comprehensive review on the applications of coal fly ash*. Earth-Science Reviews, 2015. **141**: p. 105-121.
184. <http://www.greenpeace.org/eastasia/press/releases/climate-energy/2010/coalash-en-pr/>.
185. O'Connor, G.A., et al., *A Modified Risk Assessment to Establish Molybdenum Standards for Land Application of Biosolids Although employees of the USEPA were involved in the preparation of this document, it has not had the USEPA's peer and policy review, and does not necessarily reflect the views of the agency*. Contribution of the Florida Agric. Exp. Stn. Journal Ser. no. R-07599. Journal of Environmental Quality, 2001. **30**(5).
186. Geng, C., et al., *Contamination investigation and risk assessment of molybdenum on an industrial site in China*. Journal of Geochemical Exploration, 2014. **144, Part B**: p. 273-281.
187. Mushtaq, A., M. Iqbal, and A. Muhammad, *Management of radioactive waste from molybdenum-99 production using low enriched uranium foil target and modified CINTICHEM process*. Journal of Radioanalytical and Nuclear Chemistry, 2009. **281**(3): p. 379-392.
188. Lindgren, M., M. Pettersson, and M. Wiborgh, *Correlation factors for C-14, Cl-36, Ni-59, Ni-63, Mo-93, Tc-99, I-129 and Cs-135. In operational waste for SFR 1*, 2007, Swedish Nuclear Fuel and Waste Management Co.
189. Bildstein, O. and F. Claret, *Stability of clay barriers under chemical perturbations*. Developments in Clay Science, 2015: p. 155-188.
190. Borg, S., et al., *An XAS study of molybdenum speciation in hydrothermal chloride solutions from 25–385 °C and 600 bar*. Geochimica et Cosmochimica Acta, 2012. **92**: p. 292-307.
191. Tournassat, C., et al., *Modeling specific pH dependent sorption of divalent metals on montmorillonite surfaces. A review of pitfalls, recent achievements and current challenges*. American Journal of Science, 2013. **313**(5): p. 395-451.
192. Parkhurst, D.L. and C. Appelo, *User's guide to PHREEQC (Version 2): A computer program for speciation, batch-reaction, one-dimensional transport, and inverse geochemical calculations*.
193. Giffaut, E., et al., *Andra thermodynamic database for performance assessment: ThermoChimie*. Applied Geochemistry, 2014. **49**: p. 225-236.
194. Hammersley, A., et al., *Two-dimensional detector software: from real detector to idealised image or two-theta scan*. International Journal of High Pressure Research, 1996. **14**(4-6): p. 235-248.

195. Juhas, P., et al., *PDFgetX3: a rapid and highly automatable program for processing powder diffraction data into total scattering pair distribution functions*. Journal of Applied Crystallography, 2013. **46**(2): p. 560-566.
196. Ravel, B. and M. Newville, *ATHENA, ARTEMIS, HEPHAESTUS: data analysis for X-ray absorption spectroscopy using IFEFFIT*. Journal of Synchrotron Radiation, 2005. **12**(4): p. 537-541.
197. Ankudinov, A., A. Nesvizhskii, and J. Rehr, *Dynamic screening effects in x-ray absorption spectra*. Physical Review B, 2003. **67**(11): p. 115120.
198. Wang, Y. and H. Gao, *Compositional and structural control on anion sorption capability of layered double hydroxides (LDHs)*. Journal of Colloid and Interface Science, 2006. **301**(1): p. 19-26.
199. Farley, K.J., D.A. Dzombak, and F.M.M. Morel, *A surface precipitation model for the sorption of cations on metal oxides*. Journal of Colloid and Interface Science, 1985. **106**(1): p. 226-242.
200. Nadeau, P., et al., *Interstratified clays as fundamental particles*. Science, 1984. **225**: p. 923-925.
201. Baquerizo, L.G., et al., *Hydration states of AFm cement phases*. Cement and Concrete Research, 2015. **73**: p. 143-157.
202. Essington, M.E., *Calcium molybdate solubility in spent oil shale and a preliminary evaluation of the association constants for the formation of CaMoO₄(aq), KMoO₄(aq), and NaMoO₄(aq)*. Environmental Science & Technology, 1990. **24**(2): p. 214-220.
203. Tournassat, C., et al., *Nanomorphology of montmorillonite particles: Estimation of the clay edge sorption site density by low-pressure gas adsorption and AFM observations*. American Mineralogist, 2003. **88**(11-12): p. 1989-1995.
204. Mesbah, A., et al., *Crystal Structures and Phase Transition of Cementitious Bi-Anionic AFm-(Cl-, CO₃)²⁻) Compounds*. Journal of the American Ceramic Society, 2011. **94**(1): p. 262-269.
205. Li, F. and X. Duan, *Applications of Layered Double Hydroxides*, in *Layered Double Hydroxides*, X. Duan and D.G. Evans, Editors. 2006, Springer Berlin Heidelberg: Berlin, Heidelberg. p. 193-223.
206. Shi, Z., et al., *Role of calcium on chloride binding in hydrated Portland cement–metakaolin–limestone blends*. Cement and Concrete Research, 2017. **95**: p. 205-216.
207. Rayman, M.P., *Food-chain selenium and human health: emphasis on intake*. British Journal of Nutrition, 2008. **100**(2): p. 254-268.
208. Chen, F.R., P.C. Burns, and R.C. Ewing, *Se-79: geochemical and crystallo-chemical retardation mechanisms*. Journal of Nuclear Materials, 1999. **275**(1): p. 81-94.
209. You, Y., G.F. Vance, and H. Zhao, *Selenium adsorption on Mg–Al and Zn–Al layered double hydroxides*. Applied Clay Science, 2001. **20**(1–2): p. 13-25.
210. Mandal, S., S. Mayadevi, and B.D. Kulkarni, *Adsorption of Aqueous Selenite [Se(IV)] Species on Synthetic Layered Double Hydroxide Materials*. Industrial & Engineering Chemistry Research, 2009. **48**(17): p. 7893-7898.
211. Taylor, H., *Crystal structures of some double hydroxide minerals*. Mineralogical Magazine, 1973. **39**(304): p. 377-389.
212. Miyata, S., *The syntheses of hydrotalcite-like compounds and their structures and physico-chemical properties I: The systems Mg²⁺-Al³⁺-NO₃⁻, Mg²⁺-Al³⁺-Cl⁻, Mg²⁺-Al³⁺-ClO₄⁻, Ni²⁺-Al³⁺-Cl⁻ and Zn²⁺-Al³⁺-Cl⁻*. Clays and Clay Minerals, 1975. **23**: p. 369-375.
213. Miyata, S., *Anion-exchange properties of hydrotalcite-like compounds*. Clays and Clay Minerals, 1983. **31**(4): p. 305-311.

214. Hou, X., et al., *Hydration, expansion, structure, and dynamics of layered double hydroxides*. American Mineralogist, 2003. **88**(1): p. 167-179.
215. Wang, J., et al., *Molecular Modeling of the Structure and Energetics of Hydrotalcite Hydration*. Chemistry of Materials, 2001. **13**(1): p. 145-150.
216. Hou, X. and R.J. Kirkpatrick, *Interlayer Structure and Dynamics of ClO_4^- Layered Double Hydroxides*. Chemistry of Materials, 2002. **14**(3): p. 1195-1200.
217. Ma, B., et al., *Evidence of Multiple Sorption Modes in Layered Double Hydroxides Using Mo As Structural Probe*. Environmental Science & Technology, 2017. **51**(10): p. 5531-5540.
218. Marty, N., C.M. and S. Grangeon, *Dissolution kinetics of AFm-Cl as a function of pH at room temperature*, in *14ème Colloque du Groupe Français des Argiles* 2016: Poitiers, France.
219. Hammersley, A.P., et al., *Two-dimensional detector software: From real detector to idealised image or two-theta scan*. High Pressure Research, 1996. **14**(4-6): p. 235-248.
220. Aquilanti, G., et al., *Operando characterization of batteries using x-ray absorption spectroscopy: advances at the beamline XAFS at synchrotron Elettra*. Journal of Physics D: Applied Physics, 2017. **50**(7): p. 074001.
221. Séby, F., et al., *A critical review of thermodynamic data for selenium species at 25°C*. Chemical Geology, 2001. **171**(3-4): p. 173-194.
222. Grangeon, S., et al., *X-ray diffraction: a powerful tool to probe and understand the structure of nanocrystalline calcium silicate hydrates*. Acta Crystallographica Section B, 2013. **69**(5): p. 465-473.
223. Bookin, A. and V. Drits, *Polytype diversity of the hydrotalcite-like minerals. I. Possible polytypes and their diffraction features*. Clays and Clay Minerals, 1993. **41**(5): p. 551-557.
224. Allmann, R., *Refinement of the hybrid layer structure $[\text{Ca}_2\text{Al}(\text{OH})_6]^{+}[\text{1/2}\text{SO}_4 \cdot 3\text{H}_2\text{O}]^{-}$* . Neues Jahrbuch für Mineralogie Monatshefte, 1977. **1977**: p. 136-143.
225. Renaudin, G., et al., *Structural phase transition and high temperature phase structure of Friedels salt, $3\text{CaO} \cdot \text{Al}_2\text{O}_3 \cdot \text{CaCl}_2 \cdot 10\text{H}_2\text{O}$* . Cement and Concrete Research, 1999. **29**(12): p. 1937-1942.
226. Van Cappellen, P., et al., *A surface complexation model of the carbonate mineral-aqueous solution interface*. Geochimica et Cosmochimica Acta, 1993. **57**(15): p. 3505-3518.
227. Wang, X., et al., *Sulfate Local Coordination Environment in Schwertmannite*. Environmental Science & Technology, 2015. **49**(17): p. 10440-10448.
228. Bruni, F., et al., *Aqueous solutions of divalent chlorides: Ions hydration shell and water structure*. The Journal of Chemical Physics, 2012. **136**(6): p. 064520.
229. Mancinelli, R., et al., *Hydration of Sodium, Potassium, and Chloride Ions in Solution and the Concept of Structure Maker/Breaker*. The Journal of Physical Chemistry B, 2007. **111**(48): p. 13570-13577.
230. Eklund, L. and I. Persson, *Structure and hydrogen bonding of the hydrated selenite and selenate ions in aqueous solution*. Dalton Transactions, 2014. **43**(17): p. 6315-6321.
231. Powell, D.H., et al., *The hydration structure around chloride ions in aqueous solution*. Faraday Discussions of the Chemical Society, 1988. **85**(0): p. 137-146.
232. Marcus, Y., *A simple empirical model describing the thermodynamics of hydration of ions of widely varying charges, sizes, and shapes*. Biophysical Chemistry, 1994. **51**(2): p. 111-127.

233. Vchirawongkwin, V., B.M. Rode, and I. Persson, *Structure and Dynamics of Sulfate Ion in Aqueous Solution An ab initio QMCF MD Simulation and Large Angle X-ray Scattering Study*. The Journal of Physical Chemistry B, 2007. **111**(16): p. 4150-4155.
234. Georgieva, V., S. Genieva, and L. Vlaev, *Comparative study of the electro-transport characteristics of chalcogenate and chalcogenite ions in aqueous solutions*. Physics and Chemistry of Liquids, 2009. **47**(5): p. 530-541.
235. Johansson, G. and R. Caminiti, *The hydration of tungstate and molybdate ions in aqueous solution*. Zeitschrift für Naturforschung A, 1986. **41**(11): p. 1325-1329.
236. Vlaev, L.T. and S.D. Genieva, *Electron Transport Properties of Ions in Aqueous Solutions of Sodium Selenite*. Journal of Structural Chemistry. **45**(5): p. 825-831.
237. Landais, P., *Advances in geochemical research for the underground disposal of high-level, long-lived radioactive waste in a clay formation*. Journal of Geochemical Exploration, 2006. **88**(1): p. 32-36.
238. Truche, L., et al., *Experimental reduction of aqueous sulphate by hydrogen under hydrothermal conditions: Implication for the nuclear waste storage*. Geochimica et Cosmochimica Acta, 2009. **73**(16): p. 4824-4835.
239. Truche, L., et al., *Kinetics of pyrite to pyrrhotite reduction by hydrogen in calcite buffered solutions between 90 and 180 °C: Implications for nuclear waste disposal*. Geochimica et Cosmochimica Acta, 2010. **74**(10): p. 2894-2914.
240. Antunes, R.A., I. Costa, and D.L.A.d. Faria, *Characterization of corrosion products formed on steels in the first months of atmospheric exposure*. Materials Research, 2003. **6**: p. 403-408.
241. LINDBERG, R.D. and D.D. RUNNELLS, *Ground Water Redox Reactions: An Analysis of Equilibrium State Applied to Eh Measurements and Geochemical Modeling*. Science, 1984. **225**(4665): p. 925-927.
242. Stumm, W. and J.J. Morgan, *Aquatic chemistry: chemical equilibria and rates in natural waters*. Vol. 126. 2012: John Wiley & Sons.
243. Hofstetter, T.B., A. Neumann, and R.P. Schwarzenbach, *Reduction of Nitroaromatic Compounds by Fe(II) Species Associated with Iron-Rich Smectites*. Environmental Science & Technology, 2006. **40**(1): p. 235-242.
244. Gorski, C.A., et al., *Redox properties of structural Fe in clay minerals. 1. Electrochemical quantification of electron-donating and-accepting capacities of smectites*. Environmental science & technology, 2012. **46**(17): p. 9360-9368.
245. Gorski, C.A., et al., *Redox properties of structural Fe in clay minerals. 2. Electrochemical and spectroscopic characterization of electron transfer irreversibility in ferruginous smectite, SWa-1*. Environmental science & technology, 2012. **46**(17): p. 9369-9377.
246. Gorski, C.A., et al., *Redox properties of structural Fe in clay minerals: 3. Relationships between smectite redox and structural properties*. Environmental science & technology, 2013. **47**(23): p. 13477-13485.
247. MACE, N., et al., *Préparation et caractérisations des PCH CEM V/A ROMBAS dans le cadre du GL CTEC*. CEA technical report, 2015.
248. Kanel, S.R., et al., *Removal of Arsenic(III) from Groundwater by Nanoscale Zero-Valent Iron*. Environmental Science & Technology, 2005. **39**(5): p. 1291-1298.
249. Dixit, S. and J.G. Hering, *Comparison of Arsenic(V) and Arsenic(III) Sorption onto Iron Oxide Minerals: Implications for Arsenic Mobility*. Environmental Science & Technology, 2003. **37**(18): p. 4182-4189.
250. Matijević, E. and P. Scheiner, *Ferric hydrous oxide sols: III. Preparation of uniform particles by hydrolysis of Fe (III)-chloride, -nitrate, and-perchlorate solutions*. Journal of Colloid and Interface Science, 1978. **63**(3): p. 509-524.

251. Penners, N. and L. Koopal, *Preparation and optical properties of homodisperse haematite hydrosols*. *Colloids and Surfaces*, 1986. **19**(2): p. 337-349.
252. Cornell, R.M. and U. Schwertmann, *The iron oxides: structure, properties, reactions, occurrences and uses*. 2006: John Wiley & Sons.
253. Silvester, E., et al., *Redox potential measurements and Mössbauer spectrometry of Fe II adsorbed onto Fe III (oxyhydr) oxides*. *Geochimica et Cosmochimica Acta*, 2005. **69**(20): p. 4801-4815.
254. Didier, M., et al., *Adsorption of Hydrogen Gas and Redox Processes in Clays*. *Environmental Science & Technology*, 2012. **46**(6): p. 3574-3579.
255. Wan, M., et al., *Occurrence of Surface Polysulfides during the Interaction between Ferric (Hydr)Oxides and Aqueous Sulfide*. *Environmental Science & Technology*, 2014. **48**(9): p. 5076-5084.
256. Farrow, C., et al., *PDFfit2 and PDFgui: computer programs for studying nanostructure in crystals*. *Journal of Physics: Condensed Matter*, 2007. **19**(33): p. 335219.
257. Zhao, X., et al., *An overview of preparation and applications of stabilized zero-valent iron nanoparticles for soil and groundwater remediation*. *Water Research*, 2016. **100**: p. 245-266.
258. Gorman-Lewis, D., et al., *Solubility measurements of the uranyl oxide hydrate phases metaschoepite, compreignacite, Na-compreignacite, becquerelite, and clarkeite*. *The Journal of Chemical Thermodynamics*, 2008. **40**(6): p. 980-990.
259. Bots, P., et al., *Formation of Stable Uranium(VI) Colloidal Nanoparticles in Conditions Relevant to Radioactive Waste Disposal*. *Langmuir*, 2014. **30**(48): p. 14396-14405.
260. Johnson, C.A., et al., *Solubility of antimony and other elements in samples taken from shooting ranges*. *Journal of Environmental Quality*, 2005. **34**(1): p. 248-254.
261. Scheinost, A.C., et al., *X-ray absorption and photoelectron spectroscopy investigation of selenite reduction by FeII-bearing minerals*. *Journal of Contaminant Hydrology*, 2008. **102**(3-4): p. 228-245.
262. Liu, X., et al., *Selenide retention onto pyrite under reducing conditions*. *Radiochimica Acta*, 2008. **96**(8): p. 473-479.
263. Bès, R., et al., *Use of HERFD-XANES at the U L3- and M4-Edges To Determine the Uranium Valence State on [Ni(H₂O)₄]3[U(OH,H₂O)(UO₂)₈O₁₂(OH)₃]*. *Inorganic Chemistry*, 2016. **55**(9): p. 4260-4270.
264. Kvashnina, K., et al., *Chemical state of complex uranium oxides*. *Physical review letters*, 2013. **111**(25): p. 253002.
265. Opel, K., et al., *Study of the solubility of amorphous and crystalline uranium dioxide by combined spectroscopic methods*. *Radiochimica Acta*, 2007. **95**(3): p. 143-149.
266. Sandberg, P., *Critical evaluation of factors affecting chloride initiated reinforcement corrosion in concrete*. Report TVBM 3068, 1995.
267. Kinniburgh, D. and D. Cooper, *PhreePlot: Creating graphical output with PHREEQC*. 2011.
268. Langmuir, D., *Aqueous environmental geochemistry*. Vol. 549. 1997: Prentice Hall Upper Saddle River, NJ.
269. Burnol, A., et al., *Decoupling of arsenic and iron release from ferrihydrite suspension under reducing conditions: a biogeochemical model*. *Geochemical Transactions*, 2007. **8**: p. 12-12.
270. Spadini, L., et al., *Structure and stability of Cd²⁺ surface complexes on ferric oxides: I. Results from EXAFS spectroscopy*. *Journal of Colloid and Interface Science*, 1994. **168**(1): p. 73-86.

271. Mayant, C., et al., *Surface site density, silicic acid retention and transport properties of compacted magnetite powder*. Physics and Chemistry of the Earth, Parts A/B/C, 2008. **33**(14–16): p. 991-999.
272. Chivot, J., *Thermodynamique des produits de corrosion*. Sciences et Techniques Series, ANDRA, 2004: p. 4.
273. Gómez-Lopera, S.A., R.C. Plaza, and A.V. Delgado, *Synthesis and Characterization of Spherical Magnetite/Biodegradable Polymer Composite Particles*. Journal of Colloid and Interface Science, 2001. **240**(1): p. 40-47.
274. Cornell, R. and U. Schwertmann, *The iron oxides*. VCH-Verlagsgesellschaft, 1996, Weinheim, Germany.
275. Steefel, C.I. and P. Van Cappellen, *A new kinetic approach to modeling water-rock interaction: The role of nucleation, precursors, and Ostwald ripening*. Geochimica et Cosmochimica Acta, 1990. **54**(10): p. 2657-2677.
276. Skriver, H.L. and N. Rosengaard, *Surface energy and work function of elemental metals*. Physical Review B, 1992. **46**(11): p. 7157.
277. Wang, L., D. Jacques, and P. De Cannière, *Effects of an alkaline plume on the Boom Clay as a potential host formation for geological disposal of radioactive waste*. External Report SCK•CEN-ER-28, SCK•CEN, Belgium, 2010.
278. Kosakowski, G. and U. Berner, *The evolution of clay rock/cement interfaces in a cementitious repository for low- and intermediate level radioactive waste*. Physics and Chemistry of the Earth, Parts A/B/C, 2013. **64**: p. 65-86.
279. Grangeon, S., et al., *Quantitative X-ray pair distribution function analysis of nanocrystalline calcium silicate hydrates: a contribution to the understanding of cement chemistry*. Journal of Applied Crystallography, 2017. **50**(1): p. 14-21.
280. Baquerizo, L.G., T. Matschei, and K.L. Scrivener, *Impact of water activity on the stability of ettringite*. Cement and Concrete Research, 2016. **79**: p. 31-44.
281. Proux, O., et al., *FAME: a new beamline for X-ray absorption investigations of very-diluted systems of environmental, material and biological interests*. Physica Scripta, 2005. **2005**(T115): p. 970.
282. Mylon, S.E. and G. Benoit, *Subnanomolar Detection of Acid-Labile Sulfides by the Classical Methylene Blue Method Coupled to HPLC*. Environmental Science & Technology, 2001. **35**(22): p. 4544-4548.
283. Bargar, J.R., R. Reitmeyer, and J.A. Davis, *Spectroscopic confirmation of uranium(VI)-carbonate adsorption complexes on hematite*. Environmental Science & Technology, 1999. **33**(14): p. 2481-2484.
284. Dong, W.M. and S.C. Brooks, *Determination of the formation constants of ternary complexes of uranyl and carbonate with alkaline earth metals (Mg²⁺, Ca²⁺, Sr²⁺, and Ba²⁺) using anion exchange method*. Environmental Science & Technology, 2006. **40**(15): p. 4689-4695.
285. Guo, Z.J., Y. Li, and W.S. Wu, *Sorption of U(VI) on goethite: Effects of pH, ionic strength, phosphate, carbonate and fulvic acid*. Applied Radiation and Isotopes, 2009. **67**(6): p. 996-1000.
286. Wang, Z.M., et al., *Adsorption of Uranium(VI) to Manganese Oxides: X-ray Absorption Spectroscopy and Surface Complexation Modeling*. Environmental Science & Technology, 2013. **47**(2): p. 850-858.
287. Comarmond, M.J., et al., *The Sorption Processes of U(VI) onto SiO₂ in the Presence of Phosphate: from Binary Surface Species to Precipitation*. Environmental Science & Technology, 2016. **50**(21): p. 11610-11618.
288. Joseph, C., et al., *Sorption of U(VI) onto Opalinus Clay: Effects of pH and humic acid*. Applied Geochemistry, 2013. **36**: p. 104-117.

289. Zheng, J., et al., *Surface complexation modeling of U(VI) sorption on GMZ bentonite in the presence of fulvic acid*. *Radiochimica Acta*, 2017. **105**(1): p. 33-41.
290. Cumberland, S.A., et al., *Uranium mobility in organic matter-rich sediments: A review of geological and geochemical processes*. *Earth-Science Reviews*, 2016. **159**: p. 160-185.
291. Mikutta, C., et al., *Tetra- and Hexavalent Uranium Forms Bidentate-Mononuclear Complexes with Particulate Organic Matter in a Naturally Uranium Enriched Peatland*. *Environmental Science & Technology*, 2016. **50**(19): p. 10465-10475.
292. Yi, Z.J., *Microbial removal of uranyl by sulfate reducing bacteria in the presence of Fe (III) (hydr)oxides*. *Journal of Environmental Radioactivity*, 2010. **101**(9): p. 700-705.
293. Zhang, P., et al., *Dynamic Succession of Groundwater Sulfate-Reducing Communities during Prolonged Reduction of Uranium in a Contaminated Aquifer*. *Environmental Science & Technology*, 2017. **51**(7): p. 3609-3620.
294. Sani, R.K., et al., *Reduction of uranium(VI) under sulfate-reducing conditions in the presence of Fe(III)-(hydr)oxides*. *Geochimica Et Cosmochimica Acta*, 2004. **68**(12): p. 2639-2648.
295. Sani, R.K., et al., *Reoxidation of reduced uranium with iron(III) (hydr)oxides under sulfate-reducing conditions*. *Environmental Science & Technology*, 2005. **39**(7): p. 2059-2066.
296. Komlos, J., et al., *Real-time speciation of uranium during active bioremediation and U(IV) reoxidation*. *Journal of Environmental Engineering-Asce*, 2008. **134**(2): p. 78-86.
297. Chakraborty, S., et al., *U(VI) Sorption and Reduction by Fe(II) Sorbed on Montmorillonite*. *Environmental Science & Technology*, 2010. **44**(10): p. 3779-3785.
298. Jeon, B.H., et al., *Chemical reduction of U(VI) by Fe(II) at the solid-water interface using natural and synthetic Fe(III) oxides*. *Environmental Science & Technology*, 2005. **39**(15): p. 5642-5649.
299. O'Loughlin, E.J., S.D. Kelly, and K.M. Kemner, *XAFS Investigation of the Interactions of U-VI with Secondary Mineralization Products from the Bioreduction of Fe-III Oxides*. *Environmental Science & Technology*, 2010. **44**(5): p. 1656-1661.
300. O'Loughlin, E.J., et al., *Reduction of Uranium(VI) by mixed iron(II/iron(III) hydroxide (green rust): Formation of UO₂ nanoparticles*. *Environmental Science & Technology*, 2003. **37**(4): p. 721-727.
301. Yuan, K., et al., *Uranium reduction on magnetite: Probing for pentavalent uranium using electrochemical methods*. *Geochimica Et Cosmochimica Acta*, 2015. **156**: p. 194-206.
302. Veeramani, H., et al., *Products of abiotic U(VI) reduction by biogenic magnetite and vivianite*. *Geochimica Et Cosmochimica Acta*, 2011. **75**(9): p. 2512-2528.
303. Skomurski, F.N., et al., *Heterogeneous reduction of U(6+) by structural Fe(2+) from theory and experiment*. *Geochimica Et Cosmochimica Acta*, 2011. **75**(22): p. 7277-7290.
304. Rovira, M., et al., *Interaction of uranium with in situ anoxically generated magnetite on steel*. *Journal of Hazardous Materials*, 2007. **147**(3): p. 726-731.
305. Missana, T., M. Garcia-Gutierrez, and V. Fernandez, *Uranium(VI) sorption on colloidal magnetite under anoxic environment: Experimental study and surface complexation modelling*. *Geochimica Et Cosmochimica Acta*, 2003. **67**(14): p. 2543-2550.
306. Veeramani, H., et al., *Abiotic Reductive Immobilization of U(VI) by Biogenic Mackinawite*. *Environmental Science & Technology*, 2013. **47**(5): p. 2361-2369.

307. Bi, Y.Q., et al., *Oxidative dissolution of UO₂ in a simulated groundwater containing synthetic nanocrystalline mackinawite*. *Geochimica Et Cosmochimica Acta*, 2013. **102**: p. 175-190.
308. Hyun, S.P., et al., *Uranium(VI) Reduction by Iron(II) Monosulfide Mackinawite*. *Environmental Science & Technology*, 2012. **46**(6): p. 3369-3376.
309. Ferry, C., et al., *Specific outcomes of the research on the spent fuel long-term evolution in interim dry storage and deep geological disposal*. *Journal of Nuclear Materials*, 2006. **352**(1-3): p. 246-253.
310. Schmeide, K., et al., *Interaction of U(VI) with Aspo diorite: A batch and in situ ATR FT-IR sorption study*. *Applied Geochemistry*, 2014. **49**: p. 116-125.
311. Gaucher, E.C., et al., *Modelling the porewater chemistry of the Callovian-Oxfordian formation at a regional scale*. *Comptes Rendus Geoscience*, 2006. **338**(12-13): p. 917-930.
312. Beaucaire, C., et al., *Regional fluid characterisation and modelling of water-rock equilibria in the Boom clay Formation and in the Rupelian aquifer at Mol, Belgium*. *Applied Geochemistry*, 2000. **15**(5): p. 667-686.
313. Kang, M., et al., *Redox reaction of aqueous selenite with As-rich pyrite from Jiguanshan ore mine (China): Reaction products and pathway*. *Applied Geochemistry*, 2014. **47**: p. 130-140.
314. Diener, A., et al., *Structure of selenium incorporated in pyrite and mackinawite as determined by XAFS analyses*. *Journal of Contaminant Hydrology*, 2012. **133**: p. 30-39.
315. Bruggeman, C., et al., *Selenite reduction in Boom clay: Effect of FeS₂, clay minerals and dissolved organic matter*. *Environmental Pollution*, 2005. **137**(2): p. 209-221.
316. Bruggeman, C., A. Maes, and J. Vancluysen, *The identification of FeS₂ as a sorption sink for Tc(IV)*. *Physics and Chemistry of the Earth*, 2007. **32**(8-14): p. 573-580.
317. Huo, L.J., et al., *Reductive immobilization of pertechnetate in soil and groundwater using synthetic pyrite nanoparticles*. *Chemosphere*, 2017. **174**: p. 456-465.
318. Peretyazhko, T.S., et al., *Pertechnetate (TcO₄⁻) reduction by reactive ferrous iron forms in naturally anoxic, redox transition zone sediments from the Hanford Site, USA*. *Geochimica Et Cosmochimica Acta*, 2012. **92**: p. 48-66.
319. Maes, A., et al., *Evidence for the interaction of technetium colloids with humic substances by X-ray absorption spectroscopy*. *Environmental Science & Technology*, 2004. **38**(7): p. 2044-2051.
320. Eglizaud, N., et al., *Uranium(VI) interaction with pyrite (FeS₂): Chemical and spectroscopic studies*. *Radiochimica Acta*, 2006. **94**(9-11): p. 651-656.
321. Wersin, P., et al., *Interaction between aqueous uranium(VI) and sulfide minerals - spectroscopic evidence for sorption and reduction*. *Geochimica Et Cosmochimica Acta*, 1994. **58**(13): p. 2829-2843.
322. Abraitis, P.K., R.A.D. Patrick, and D.J. Vaughan, *Variations in the compositional, textural and electrical properties of natural pyrite: a review*. *International Journal of Mineral Processing*, 2004. **74**(1-4): p. 41-59.
323. Lehner, S. and K. Savage, *The effect of As, Co, and Ni impurities on pyrite oxidation kinetics: Batch and flow-through reactor experiments with synthetic pyrite*. *Geochimica Et Cosmochimica Acta*, 2008. **72**(7): p. 1788-1800.
324. McGuire, M.M. and R.J. Hamers, *Extraction and quantitative analysis of elemental sulfur from sulfide mineral surfaces by high-performance liquid chromatography*. *Environmental Science & Technology*, 2000. **34**(21): p. 4651-4655.
325. Stewart, B.D., et al., *Reactivity of Uranium and Ferrous Iron with Natural Iron Oxyhydroxides*. *Environmental Science & Technology*, 2015. **49**(17): p. 10357-10365.

326. Jones, A.M., et al., *The effect of silica and natural organic matter on the Fe(II)-catalysed transformation and reactivity of Fe(III) minerals*. *Geochimica Et Cosmochimica Acta*, 2009. **73**(15): p. 4409-4422.
327. Nesbitt, H.W., et al., *Sulfur and iron surface states on fractured pyrite surfaces*. *American Mineralogist*, 1998. **83**(9-10): p. 1067-1076.
328. Murphy, R. and D.R. Strongin, *Surface reactivity of pyrite and related sulfides*. *Surface Science Reports*, 2009. **64**(1): p. 1-45.
329. Ma, B., et al., *The reductive immobilization of aqueous Se(IV) by natural pyrrhotite*. *Journal of Hazardous Materials*, 2014. **276**: p. 422-432.
330. Eggleston, C.M., J.J. Ehrhardt, and W. Stumm, *Surface structural controls on pyrite oxidation kinetics: An XPS-UPS, STM, and modeling study*. *American Mineralogist*, 1996. **81**(9-10): p. 1036-1056.
331. Elsetinow, A.R., et al., *Oxidation of {100} and {111} surfaces of pyrite: Effects of preparation method*. *American Mineralogist*, 2000. **85**(3-4): p. 623-626.
332. Bebie, J., et al., *Surface charge development on transition metal sulfides: An electrokinetic study*. *Geochimica Et Cosmochimica Acta*, 1998. **62**(4): p. 633-642.
333. Sverjensky, D.A., *Zero-point-of-charge prediction from crystal chemistry and solvation theory* *Geochimica Et Cosmochimica Acta*, 1994. **58**(14): p. 3123-3129
334. Rietra, R., T. Hiemstra, and W.H. van Riemsdijk, *Sulfate adsorption on goethite*. *Journal of Colloid and Interface Science*, 1999. **218**(2): p. 511-521.
335. Le Pape, P., et al., *Arsenic Incorporation in Pyrite at Ambient Temperature at Both Tetrahedral S-I and Octahedral Fe-II Sites: Evidence from EXAFS-DFT Analysis*. *Environmental Science & Technology*, 2017. **51**(1): p. 150-158.
336. Aubriet, H., B. Humbert, and M. Perdicakis, *Interaction of U(VI) with pyrite, galena and their mixtures: a theoretical and multitechnique approach*. *Radiochimica Acta*, 2006. **94**(9-11): p. 657-663.
337. Guo, X., et al., *Thermodynamics of formation of coffinite, USiO₄*. *Proceedings of the National Academy of Sciences*, 2015. **112**(21): p. 6551-6555.
338. Mesbah, A., et al., *Coffinite, USiO₄, Is Abundant in Nature: So Why Is It So Difficult To Synthesize?* *Inorganic Chemistry*, 2015. **54**(14): p. 6687-6696.
339. Couture, R.-M., et al., *On-off mobilization of contaminants in soils during redox oscillations*. *Environmental science & technology*, 2015. **49**(5): p. 3015-3023.
340. Voltolini, M., et al., *Understanding cement hydration at the microscale: new opportunities from 'pencil-beam' synchrotron X-ray diffraction tomography*. *Journal of Applied Crystallography*, 2013. **46**(1): p. 142-152.
341. Schlegel, M.L., et al., *Anodic Activation of Iron Corrosion in Clay Media under Water-Saturated Conditions at 90 °C: Characterization of the Corrosion Interface*. *Environmental Science & Technology*, 2010. **44**(4): p. 1503-1508.
342. Lothenbach, B., E. Bernard, and U. Mäder, *Zeolite formation in the presence of cement hydrates and albite*. *Physics and Chemistry of the Earth, Parts A/B/C*, 2017. **99**: p. 77-94.

Sorption of radionuclides in reinforced cementitious barriers

Sorption and redox reactions of radionuclides (RNs) are critical processes for a nuclear waste disposal repository safety assessment. In geological repositories, these processes may occur in (i) canister (steel) corrosion layer, (ii) reinforced concrete, e.g. on hydrated cement and (iii) argillite, e.g. on pyrite and clays or granite. Both steel corrosion products and pyrite act as local reducing buffers, controlling the redox potential (Eh) and thus the sorption behavior of redox-sensitive RNs. In contrast, sorption of RNs not involving redox processes may occur on clays, iron oxides and cement hydration products, and often involve surface adsorption, ion exchange, or co-precipitation processes. In this PhD thesis, minor but highly reactive cementitious AFm phases (AFm-Cl₂ or AFm-SO₄ solids, belonging to CaAl LDHs) were employed to adsorb MoO₄²⁻ and SeO₃²⁻ at various surface loadings. A combination of PHREEQC chemical equilibrium modelling and synchrotron-based X-ray techniques (e.g., in-situ time-resolved XRD, PDF, and XAFS) reveals that multiple sorption sites, including two types of edge sites, interlayer ion exchange sites, and a Ca-rich phase precipitation, are active processes in the RNs retention on AFm phases. A linear relationship is shown to link AFm basal spacing and hydrated intercalated anion radius. Co-sorption of U and Mo on Fe⁰-reinforced hydrated cement-core has also been investigated by micro-probe mapping, showing U to be instantly immobilized by cement materials while Mo is preferentially sorbed on Fe reaction products. The Eh value prevailing in concrete is hard to be determined. Here, redox-sensitive RNs (e.g., U^{VI}, Se^{IV}, Mo^{VI}, and Sb^V) are employed as probes, to measure in-situ Eh values, by computing the Nernst equation in the following way. Reduced species concentration were measured based on the total concentration of reductively precipitated RN and on speciation among these reduced species as obtained by LCF analysis of XANES data. The experimentally determined Eh values obtained that way were remarkably closed for all RNs with centered values of -446.4±78.0 mV for cement pore water (CPW) equilibrated with Fe⁰ and values of -346 to -509 mV for CPW equilibrated with corrosion products Fe-oxides couples (magnetite/hematite or magnetite/goethite) at pH ~13.5. Neither the Eh value computed for these couples or for Fe⁰/Fe(OH)₂ match these data. Instead, the redox potential appear to be controlled by amorphous Fe(OH)₂/Fe(OH)₃ or (Fe_{1-x},Ca_x)(OH)₂/Fe(OH)₃ couples. Finally, within clay or granite far field, several factors may critically affect the surface reactivity of pyrites, namely element impurities in pyrite lattice and presence of Fe³⁺ and S²⁻ at the pyrite surface. Element impurities and presence of S²⁻ on the pyrite surface were shown to largely speed up U(VI) reduction. The experimental results obtained above could provide fundamental data for the safety assessment of nuclear waste disposal.

Sorption de radionucléides dans des barrières cimentaires renforcées

La sorption et les réactions redox des radionucléides (RN) sont des processus critiqués pour une évaluation de la sécurité des dépôts de déchets nucléaires. Dans les dépôts géologiques, ces procédés peuvent se produire dans (i) une couche de corrosion (acier), (ii) un béton armé, par exemple, sur le ciment hydraté et (iii) l'argillite, sur la pyrite et les argiles ou le granit. Les produits de corrosion de l'acier et la pyrite agissent comme des tampons de réduction locaux, contrôlant le potentiel redox (Eh) et donc le comportement de sorption des RN sensibles au redox. En revanche, la sorption de RN n'impliquant pas de processus redox peut se produire sur des argiles, des oxydes de fer et des produits d'hydratation de ciment et impliquent souvent des processus d'adsorption de surface, d'échange d'ions ou de co-précipitations. Dans cette thèse de doctorat, des phases d'AFm cimentaires mineures, mais hautement réactives (acides gras AFm-Cl₂ ou AFm-SO₄, appartenant aux LDH CaAl) ont été utilisées pour adsorber MoO₄²⁻ et SeO₃²⁻ à diverses charges de surface. Une combinaison de la modélisation de l'équilibre chimique PHREEQC et des techniques de rayons X à base de synchrotron (par exemple, XRD, PDF et XAFS résolus dans le temps) révèle que les sites de sorption multiples, y compris deux types de sites de bord, des sites d'échange d'ions intercalaires et une précipitation de phase riche en Ca, sont des processus actifs dans la rétention des RN sur les phases AFm. Une relation linéaire permet de lier l'espacement basal AFm et le rayon d'anion intercalé hydraté. La co-sorption de U et Mo sur le ciment-ciment hydraté renforcé par Fe⁰ a également été étudiée par cartographie micro-sonde, montrant que U doit être immobilisé instantanément par des matériaux de ciment tandis que Mo est préférentiellement sorbé sur des produits de réaction de Fe. La valeur Eh prédominant dans le béton est difficile à déterminer. Ici, les RN sensibles à la réduction rénale (par exemple, U^{VI}, Se^{IV}, Mo^{VI} et Sb^V) sont utilisées comme sondes, pour mesurer les valeurs Eh in-situ, en calculant l'équation de Nernst de la manière suivante. La concentration des espèces réduites a été mesurée en fonction de la concentration totale de RN précipitée par réduction et de la spéciation parmi ces espèces réduites, tel qu'obtenu par l'analyse LCF des données XANES. Les valeurs Eh déterminées expérimentalement obtenues de cette façon étaient remarquablement fermées pour toutes les RN avec des valeurs centrées de -368 à -524 mV pour l'eau de pore de ciment (CPW) équilibrée avec Fe⁰ et des valeurs de -346 à -509 mV pour CPW équilibrées avec des produits de corrosion Fe - couples d'oxydes (magnetite / hématite ou magnetite / goethite) à pH ~ 13,5. Ni la valeur Eh calculée pour ces couples ni pour Fe⁰ / Fe(OH)₂ correspond à ces données. Au lieu de cela, le potentiel redox semble être contrôlé par le couple amorphe Fe(OH)₂/Fe(OH)₃ or (Fe_{1-x},Ca_x)(OH)₂/Fe(OH)₃. Enfin, dans le domaine de l'argile ou du granit, plusieurs facteurs peuvent affecter réactivité superficielle des pyrites, à savoir les impuretés élémentaires dans le réseau de pyrite et de la présence de Fe³⁺ et S²⁻ à la surface de la pyrite. Les impuretés des éléments et la présence de S²⁻ sur la surface de la pyrite ont largement accéléré la réduction des U (VI). Les résultats expérimentaux obtenus ci-dessus pourraient fournir des données fondamentales pour l'évaluation de la sécurité de l'élimination des déchets nucléaires.